Dissertation

submitted to the
Combined Faculty of Natural Sciences and Mathematics
of the Ruperto Carola University Heidelberg, Germany
for the degree of
Doctor of Natural Sciences

Presented by

Lic. Vilma Jimenez Sabinina

born in Moscow, Russia

Oral examination: November 27th 2018

Analysis of the Architecture of the Nuclear Pore Complex by 3D super-resolution fluorescence microscopy

Referees: Dr. Martin Beck

Prof. Dr. Ed C. Hurt

Part of the technical work described in this thesis has been published:

Li, Y., Mund, M., Hoess, P., Deschamps, J., Matti, U., Nijmeijer, B., Jimenez Sabinina, V., Ellenberg, J., Schoen, I., Ries, J. (2018). Real-time 3D single-molecule localization using experimental point spread functions. *Nat Methods 2018 May 05. volume 15, pages 367–369. doi: 10.1038/nmeth.4661*.

Strauss, S., Nickels, P. C., Strauss, M. T., Jimenez Sabinina, V., Ellenberg, J., Carter, J. D., Gupta, S., Janjic, N.,and Jungmann, R. (2018). Modified aptamers enable quantitative sub-10-nm cellular DNA-PAINT imaging. *Nat Methods 2018 Aug 20. Epub ahead of print. doi: 10.1038/s41592-018-0105-0.*

This work was carried out at the European Molecular Biology Laboratory in Heidelberg from October 2014 to July 2018 under the supervision of Dr. Jan Ellenberg.

Acknowledgments

First and foremost, I would like to thank my supervisor Jan Ellenberg, for giving me the opportunity to carry out my PhD work in his lab and for his constant support and guidance throughout my time at EMBL.

I would also like to thank all of the past and present Ellenberg lab members for their daily support and for creating such a fun and warm-hearted working atmosphere. Thank you Anna, Arina, Shotaro, Judith, Manu, Julia, Øvind, Isabell, Nike, Yu, Merle, Franzi, Bea, Jeremy, Yin, Antonio, Julius, J-K, Sandra, Moritz, Andrea, Birgit, Bianca, Nathalie, Steffi and Adele, for being such amazing labmates and for always being there for me. I would like to especially thank Bianca for teaching me all the basics of cell and molecular biology and for all the technical support she provided during my PhD studies, J-K and Julius for all their theoretical and programming advise, Steffi for all her guidance regarding the management of my collaborations and projects and the Nup-Club (Shotaro, Arina, Antonio and Jeremy) for stimulating scientific discussions.

I want to thank all the members of my Thesis Advisory Committee: Martin Beck, Jonas Ries and Ed Hurt, for their insightful comments, advise and discussions that have shaped my PhD project throughout the last three years. I am especially grateful to Martin Beck and Ed Hurt for reviewing this Thesis and to Jonas Ries and Harald Herrmann-Lerdon for forming part of my Defense Committee.

I am very grateful to my collaborators Shyamal Mosalaganti and Martin Beck for their guidance with the analysis of my work, Mark Bates for his valuable advice on SMLM and 4Pi-SMLM and Philipp Höß and Jonas Ries for their help and guidance with super-resolution microscopy at EMBL. I would also like to thank all the members of the ALMF and all the people at EMBL who supported me throughout my PhD time.

I would also like to thank BIF for supporting my PhD work and conference attendance and especially thank the wonderful BIF community and friends for creating such motivating and inspiring retreats, courses and events.

Thanks to my friends and EMBL family who made my PhD experience so much fun. Thank you Nelly, Maria, Jessi, Sourabh, Jørgen, Lukas, Mariana, Emiliano, Paola, Natalie, Irma and Lore for your friendship, for sharing so much laughter and creating so many memorable moments. Gracias Dani, Diana, Lalo y Hugo por formar parte de mi familia en EMBL, por todos sus consejos, apoyo y cariño constante.

Por último y más importante, agradezco infinitamente a toda mi familia, especialmente a mis padres por su fortaleza, apoyo, motivación y amor incondicional. Gracias Katia por tu enorme cariño y respaldo. Гера, спасибо тебе за всю твою поддержку и заботу.

Summary

Nuclear pore complexes (NPCs), embedded in the two nuclear membranes, are the unique gateways that mediate all the traffic between the nucleus and the cytoplasm. In higher eukaryotes, each NPC is composed of multiple copies of approximately 30 different proteins termed nucleoporins and has a mass of over 100 MDa.

In recent years, substantial effort has been devoted to the structural and functional characterization of this essential molecular machine in eukaryotic cells. Even though a pseudo-atomic model of the scaffold of the NPC has been produced, many details of the structure still remain elusive due to the enormous size, complexity and conformational dynamics of the NPC. In addition, we have little structural understanding of how such a large machine is assembled and what dynamic structural changes underlie its functions.

During my PhD work, I established a methodology that can determine the 3D architecture of the NPC by combining single-molecule localization microscopy in a 4Pi detection scheme with computational classification and 3D single particle averaging. This new approach is able to resolve the structure of the NPC with molecular specificity and nano-scale resolution *in situ* in human cells.

I here present the reconstruction of a 3D molecular map that integrates both scaffold and flexible nucleoporins and that allows us to address dynamic components of the NPC that have been inaccessible for atomic resolution methods to date. My findings indicate that the peripheral regions of the NPC can assume very different conformational states and that even the overall scaffold structure of the NPC is more flexible than previously assumed. The methodology I have established opens the exciting possibility to address novel structural, functional and assembly aspects of this fundamental cellular machine and can be applied to interrogate the 3D architecture of other large protein complexes and organelles inside cells.

Zusammenfassung

Kernporen, eingelassen in die zwei Membranen des Zellkerns, sind die einzigartigen, als Tore fungierenden Proteinkomplexe, die den gesamten Verkehr zwischen dem Zellkern und dem Zytoplasma vermitteln. In höheren Eukaryoten besteht jede Pore aus mehreren Kopien von etwa 30 verschiedenen Proteinen, die als Nukleoporine bezeichnet werden, und hat eine Masse von über 100 MDa.

In den letzten Jahren wurden erhebliche Anstrengungen unternommen, um diese essentielle molekulare Maschine in eukaryotischen Zellen strukturell und funktionell zu charakterisieren. Obwohl ein pseudo-atomares Modell des Kernporengerüsts erstellt werden konnte, bleiben viele Details der Struktur aufgrund der enormen Größe, Komplexität und Konformationsdynamik des NPCs weiterhin schwer erfassbar. Darüber hinaus haben wir wenig strukturelles Verständnis darüber, wie ein solch großer Proteinkomplex entsteht und welche dynamischen und strukturellen Veränderungen seinen Funktionen zugrunde liegen.

Während meiner Doktorarbeit habe ich eine Methodik entwickelt, die in der Lage ist, die 3D-Architektur der Kernpore durch die Kombination von Einzelmolekül-Lokalisierungsmikroskopie in einem 4Pi-Detektionssschema mit computergestützter Klassifizierung und 3D-Einzelpartikel-Mittelung zu bestimmen. Mit diesem Ansatz gelingt es, die Struktur der Poree mit molekularer Spezifität und mit einer Auflösung von wenigen Nanometern in situ in menschlichen Zellen zu erfasssen.

Als Ergebnis erhält man die Rekonstruktion einer 3D-Molekülkarte, die sowohl Gerüst- als auch flexible Nukleoporine integriert und es uns ermöglicht, auch dynamische Teile der Kernpore zu adressieren, die für atomare Auflösungsmethoden bisher nicht zugänglich waren. Meine Ergebnisse zeigen, dass die peripheren Regionen der Pore sehr unterschiedliche Konformationszustände annehmen können und dass sogar die Gerüststruktur der Pore flexibler ist als bisher angenommen. Die von mir entwickelte Methode

eröffnet die aufregende Möglichkeit, neuartige strukturelle, funktionale und Enstehungsaspekte dieser fundamentalen zellulären Maschine zu untersuchen und kann dazu verwendet werden, die 3D-Architektur anderer großer Proteinkomplexe und Organellen in Zellen zu untersuchen und zu verstehen.

Table of contents

1 Introduction

1.1 The eukaryotic nucleus

1.1.1 The nuclear envelope

Eukaryotic cells are defined by the presence of a nucleus. This protective membrane compartment shelters the cell’s genome and insulates the nucleoplasm from the cytoplasm for specific biochemical and molecular processes. The cell nucleus is encircled by a nuclear envelope (NE), which is a double membrane sheet composed of the inner nuclear membrane (INM) and the outer nuclear membrane (ONM). The INM and ONM meet at multiple regions of the NE and serve as templates for the assembly of proteinaceous membrane pores. These pores house the unique machinery responsible for the cells’ nucleocytoplasmic exchange, called the nuclear pore complex (NPC) (Fig. 1-1 A). In metazoa, the NE is supported on the nuclear side by a meshwork of intermediate filament proteins, called the nuclear lamina consisting of A-type and B-type lamins. The linker of the nucleoskeleton and cytoskeleton (LINC) complexes physically link the cytoskeleton to the nuclear lamina, preserving the structural and functional integrity of the NE (reviewed in Starr and Fridolfsson, 2010). The NE is a highly dynamic structure and its remodeling is fundamental for cell division, growth and differentiation.

1.1.2 The organization of the NE

The NE is a specialized continuation of the endoplasmic reticulum (ER). However, the spatially proximal ONM and INM are functionally distinct and comprise a different set of proteins that is typically not found in the ER (Fig. 1-1 B).

The ONM accommodates a variety of integral membrane proteins that possesses a Klarsicht, ANC-1, Syne Homology-domain (KASH). The KASH domain can interact with the Sad1p/ UNC-84-domian (SUN) of proteins of the INM in the periplasmic space of the NE and in this way creates a LINC complex. The ONM-localized nuclear envelope spectrin repeat proteins (Nesprins) connect the LINC complex to the cytoskeleton, allowing the transmission of forces across the NE.

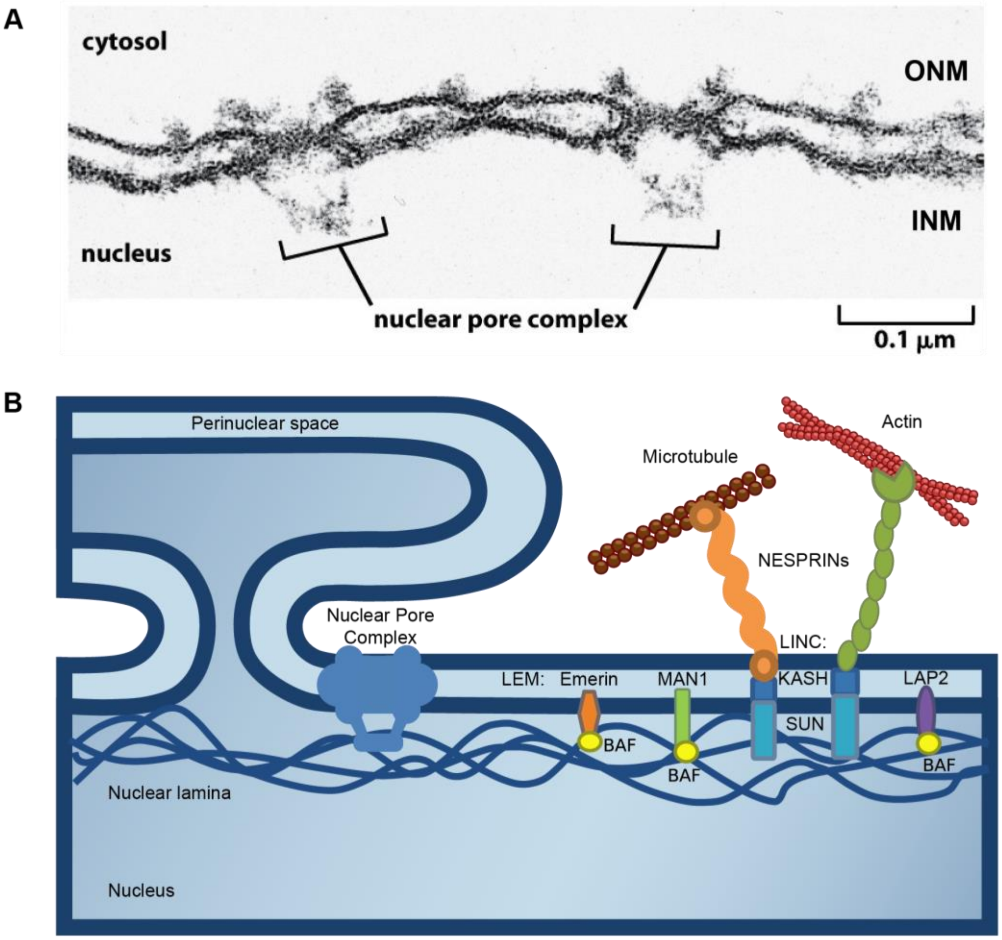

FIGURE 1-1. The composition of the nuclear envelope. A) Side-view electron micrograph illustrating the continuity of the inner and outer nuclear membrane and embbeded NPCs (adapted from Molecular Biology of the Cell, Alberts, 2002). **B)** Schematic representation of proteins of the NE. The nuclear pore complex (NPC) spans across the INM and ONM. INM proteins, including SUN, LAP2, Emerin, MAN1, are mostly associated with the nuclear lamina. Emerin, LAP2 and MAN1 harbor a LEM domain which interacts with BAF (barrier-to-autointegration factor), a chromatin-binding protein. The INM protein SUN interacts with KASH at the perinuclear space to form the LINC complex. The nuclear lamina forms a meshwork underlying the inner nuclear membrane (adapted from Ya-Hui Chi, 2009).

The INM houses a large diversity of proteins that play crucial roles in governing nuclear and chromatin organization, DNA repair and transcriptional control (reviewed in Katta et al., 2014). Two conserved INM protein domains, including the SUN and lap2-emerin-MAN1 (LEM) families, depend on lamins and other lamin-associated proteins to maintain the structural integrity of the nucleus.

1.1.3 The nuclear pore complex

The Nuclear pore complex is the unique gate that connects the ONM with the INM to allow selective nucleocytoplasmic transport. The NPC is a massive molecular machine, it reaches a molecular mass of about 120 MDa in vertebrates (Reichelt et al., 1990) and of about 60 MDa in yeast (Rout and Blobel, 1993), making it the largest non-polymeric protein complex inside cells. The key structural elements that compose the NPC are a cytoplasmic ring, a nucleoplasmic ring, an inner ring, as well as two asymmetric regions called the nuclear basket and cytoplasmic filaments (Fig 1-2). Despite its high molecular mass, proteomic analysis revealed that the NPC is actually composed only by about 30 different proteins (Cronshaw et al., 2002), known as nucleoporins (Nups). The NPC has an eight-fold symmetric structure, due to which each Nup is present in copies of multiples of eight, giving rise to over 500 Nups per pore. In vertebrates, almost all Nups are soluble, except for three transmembrane proteins (pom121, gp210 and Ndc1) that play key roles in attaching the pore to the NE. The stable anchoring of the NPC to the lamina in mammalian cells prevents their mobility within the NE (Daigle et al., 2001).

Structurally, the over 30 Nups have only a small set of domains, limited to β-propellers, α-helical solenoids, phenyl-alanine-glycine (FG) repeats, coiled-coiled and transmembrane domains (Alber et al., 2007a). Multiple different Nups create biochemically stable subcomplexes that are thought to work as functionally related building blocks of the pore (Schwartz, 2005). The vertebrate NPC can therefore be divided into three major subcomplexes, that provide the main mass of the pore, called the Nup107, Nup93 and Nup62 subcomplexes (Amlacher et al., 2011), which localize symmetrically relative to the central membrane plane. The Nup107 and Nup93 subcomplexes form three stacked rings (nucleoplasmic, cytoplasmic and inner ring) that compose the structural scaffold of the NPC (Fig. 1-2 A), while the Nup62 subcomplex has an important role in selective transport. In addition, the cytoplasmic filaments and the nuclear basket, which are large filament-like structures that extrude towards the cytoplasm and nucleoplasm, respectively, complete the principal structural elements of the pore (Schwartz, 2016) (Fig. 1-2 B-C).

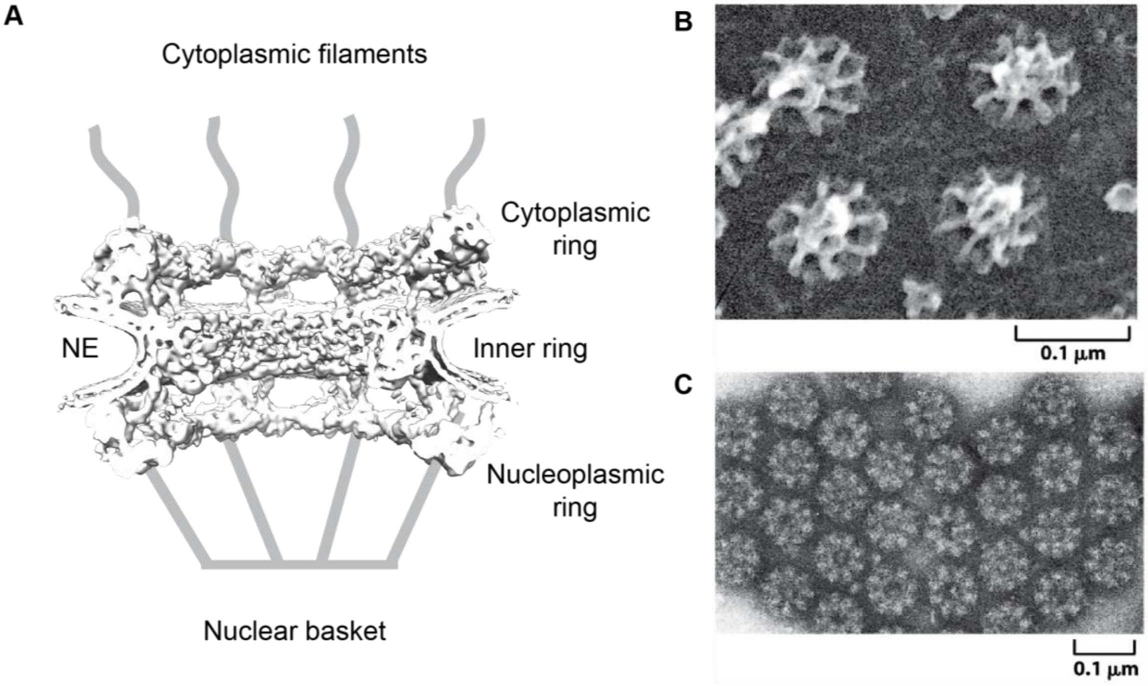

FIGURE 1-2. Overall architecture of the Nuclear Pore Complex. A) Schematic representation of the NPC containing a side-view cryo-ET reconstruction of the scaffold region (adapted from von Appen, 2015). **(B-C)** Scanning electron micrograph of the nuclear and cytoplasmic side, respectively, of the nuclear envelope of a *Xenopus laevis* oocyte (adapted from Molecular Biology of the Cell, Alberts, 2002)

The evolutionary origin of the NPC has been hypothesized to be common with vesicle coat complexes, such as COPI, COPII and Clathrin. Initially, this theory was supported by computational and biochemical analysis, that found that both NPCs and vesicle coats comprise similar elements of protein structures – mainly β-propellers and α-helical solenoids (Devos et al., 2004). Moreover, the specific arrangement of a β-propeller followed by an α-helical solenoid seems to be unique to members of either the NPC or vesicle coating complexes, which share the common function of bending and stabilizing membrane curvatures. Further similarities, such as sharing the dual-function protein Sec13 that has been known to be a member of both NPC and COPII complexes (reviewed in D'Angelo and Hetzer, 2008), support the common ancestry hypothesis. Finally, high-resolution structural studies found that several Nups (Nup85, Nup96, Nup93 and Nup107) and coat proteins (Sec31 and Sec16) that have less sequence similarity between each other, contain a conserved tripartite element called the ancestral coatomer element 1 (ACE1) (Brohawn et al., 2008), which provides additional structural evidence of evolution from a common ancestor.

1.1.4 Transport through the nuclear pore complex

The NPCs have evolved to exchange material across the NE with very high speed and selectivity. It has been estimated that an individual pore can transport around 100 MDa/s of macromolecular cargoes (Ribbeck and Görlich, 2001). While ions, metabolites and molecules smaller than ~40 kDa can diffuse across the NE, larger molecules (e.g. mRNAs, tRNAs and proteins) need to be actively transported (Görlich and Kutay, 1999) (Fig.1-3 A). Each particular class of macromolecule is transported in a distinct way depending on their intrinsic transport signal. These signals are recognized by a large family of soluble nuclear transport receptors (NTRs) known as karyopherins in yeast (Mosammaparast and Pemberton, 2004) and also termed importins and exportins in mammals (Weis, 1998), depending on their transport direction.

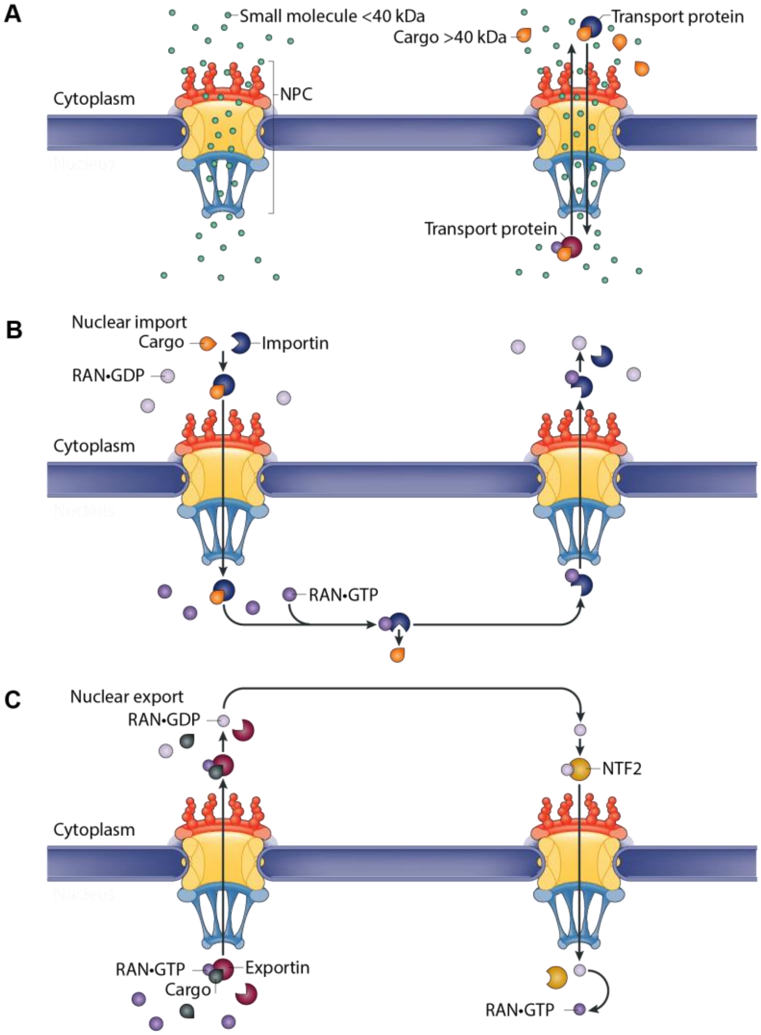

FIGURE 1-3. Transport through the NPC. A) Schematic representation of nuclear transport. Molecules smaller than 40kDa transit through the nuclear pore by passive diffusion. Larger cargoes bind to nuclear transport receptors that recognize nuclear localization sequences and nuclear export sequences. **B)** Schematic representation of nuclear import. During import, importins bind to their cargo and pass through the central transport channel of the NPC. Inside the nucleus, the binding of RAN·GTP, causes a conformational change that allows cargo release. Finally, the bound complex of importin·RAN·GTP translocates back to the cytoplasm. C) Schematic representation of nuclear export. Exportins bind to the cargo and RAN·GTP in the nucleus and move through the NPC to the cytoplasm. RAN induced GTP hydrolysis dissociates the complex. The resulting RAN·GDP complex interacts with the nuclear transport factor NTF2 to translocate back to the nucleus. **A) - C)** (adapted from Raices, 2012)

Vertebrates have at least twenty different transport receptors, whereas fourteen have been identified in yeast (Fried and Kutay, 2003). Transport receptors have a comparable molecular weight (~100-150 kDa) and they also possess a similar domain structure; this includes an N-terminal Ran-binding domain, a central Nup-binding domain and a C-terminal cargo-binding domain (Yuh and Blobel, 2001). Most of them recognize their cargo directly, however, in some cases an adaptor protein is needed. Bound macromolecules are then carried through the central channel of the NPC and released in the respective target compartment. This active translocation process requires energy, which usually derives from GTP hydrolysis.

Here, a member of the Ras-related GTPase superfamily – Ran, consumes GTP, and interacts with transport receptors in order to regulate the association and dissociation of receptor-cargo complexes. The directionality of cargo binding and release is dictated by the concentration gradient of Ran-GTP. In the nucleus, Ran-GTP is highly abundant due to chromatin-bound Ran-guanine nucleotide exchange factor (Ran-GEF) (Smith et al., 2002). In the cytoplasm, Ran-GTP is quickly hydrolyzed to GTP by the cytoplasmic filament-bound Ran-GTP-activating protein (Ran-GAP) and because of this, has a much lower concentration in this compartment (Wente and Rout, 2010).

During import, importins bind to its cargo in the cytoplasm where RanGTP levels are low, mediate the interaction of the complex with the NPC and move across the pore. Once the importin-cargo complex has reached the nuclear side of the pore, binding of Ran-GTP will stimulate the release of the cargo from the complex into the nucleus. The importin-Ran-GTP complex is then recycled back to the cytoplasm. Upon reaching the cytoplasm, GTP hydrolysis of Ran will free the importin and allow it to interact with the next cargo to start a new import cycle (Fig.1-3 B). A similar process takes place during export; in this case, Ran-GTP binding enhances the affinity of the exportins to its cargo in the nucleus. The exportin-cargo-Ran-GTP ternary complex translocates through the NPC and dissociates through GTP hydrolysis in the cytoplasmic side. Ran is further returned to the nucleoplasm via its exclusive import receptor NTF2 (Moore and Blobel, 1994) (Fig.1-3 C). The actual transfer through the pore does not depend on energy consumption, but rather on diffusion and due to this has no directionality. The shifts in Ran affinity provide sufficient energy for cargo release and asymmetric GTP hydrolysis/exchange between nucleus and cytoplasm establishes the concentration gradients for cargo proteins.

During transport, all transport receptors bind transiently to Nups that occupy the central channel of the NPC, called phenylalanine-glycine (FG)-Nups that are natively disordered. Even though FG-Nups provide binding sites for transport receptors with which they mediate active transport through the pore, FG-Nups are also fundamental structural components for the formation of the selective barrier of the NPC (Patel et al., 2007). To explain the selective gating of the NPC, different models have been proposed. The “virtual gating” model suggests that both sides of the NPC channel, filled with FG-Nups, create a highly selective entropic barrier for large molecules. Transport receptors would be able to overcome this entropic barrier by transiently binding to different FG-domains throughout the channel. This model provides a significant kinetic advantage for cargo-karyopherin complex displacement and views the pore as a catalyst that lowers the activation energy for transportation (Rout et al., 2003). A second model, termed the “polymer brush” model suggest that long non-interacting hydrophobic FG-Nups block the pore channel but can be pushed aside by karyopherin-cargo complexes (Macara, 2001). Structural observations form atomic force microscopy experiments, identified that *in vitro*-purified FG-filaments can extend and collapse by addition of a karyopherin that binds to their anchoring sites, supporting the idea of FG-Nups acting like polymer brushes that can contribute to the entropic barrier of the pore (Lim et al., 2006, 2007). In contrast to the two previous kinetic models, the “selective phase” model proposes the formation of a dense interacting meshwork or hydrogel of disordered hydrophobic FG repeats within the central channel of the NPC (Ribbeck and Görlich, 2001). On one hand, the mesh size of the FG-repeat gel would mechanically restrict access to macromolecules. On the other hand, the binding of transport receptors to FG-repeats would transiently replace the FG-FG interactions, effectively dissolving them in the FG-phase, and allowing the receptor-cargo complex to have exclusive access to the central channel of the pore. A similar selective phase hypothesis could be formulated based on a liquid phase rather than a hydrogel model of FG-repeats.

Understanding which model describes best how the permeability barrier of the NPC actually works remains a central question in the field. In yeast, nucleoporin Nsp1 was shown to form a hydrogel-like structure *in vitro* based on hydrophobic interactions and displays selective properties that resemble the gating behavior of the NPC (Frey and Görlich, 2007; Frey et al., 2006). However, this gel-like state was produced under non-native and harsh concentrations and in vivo evidence for the existence of such a hydrogel is still lacking. Another study shows that under more physiological conditions, Nsp1 mostly fails to form FG-interactions with other FG-Nups and only few interactions were detected in the central channel of the pore (Patel et al., 2007). These results support a new combined two-gate model architecture, where a “selective gate” is formed by interacting FG-repeats within the center of the NPC channel and a “virtual gate” of non-interacting FG-Nups at the periphery (reviewed in (Weis, 2007)). In conclusion, a unifying model consistent with all experimental observations and interpretations about how the architecture of the selective gate of the NPC functions, remains elusive.

1.1.5 Nuclear pore complex biogenesis

The assembly of hundreds of proteins into a large macromolecular complex embedded in the NE, as the biogenesis of NPC, is a fascinating example of molecular self-assembly that remains a challenging process to decipher. In higher eukaryotes that undergo an open mitosis, the NPC assembles at two different stages during the cell cycle: during mitosis and interphase (Fig.1-4). First, at the end of mitosis, after the nuclear envelope has broken down to allow microtubules to access and attach to chromosomes, the NE together with the NPCs reform around the segregated chromosomes. This type of NPC biogenesis, termed postmitotic assembly, occurs in a very short time window at the end of mitosis to ensure that the new nucleus can rapidly import essential proteins to enter the next phase of the cell cycle.

Second, during interphase, when preparing for the next round of cell division, the number of NPCs roughly doubles homeostatically with nuclear and cellular growth. This second biogenesis pathway, termed interphase assembly, requires the challenging insertion of newly forming NPCs into an already sealed NE. The NPCs generated in both processes are indistinguishable, but the mechanisms leading to their formation seem to differ (Antonin et al., 2008; Otsuka and Ellenberg, 2017).

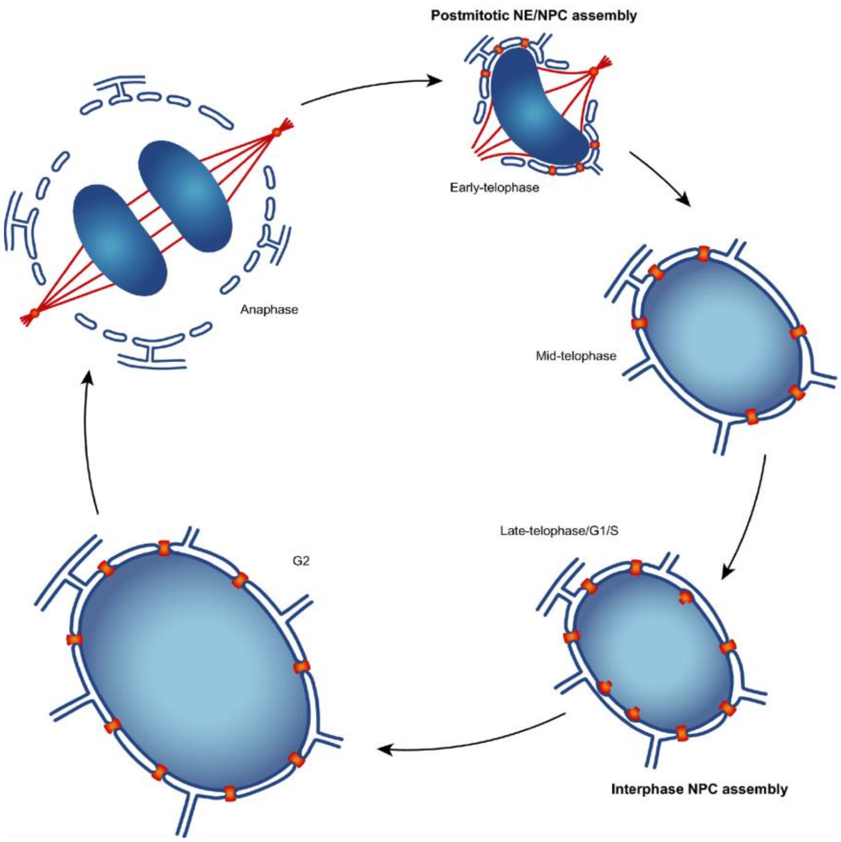

FIGURE 1-4. Nuclear pore complex biogenesis. The NPC assembles at two different stages of the cell cycle. During anaphase and telophase, the nuclear membranes assemble on chromatin (blue gradient) together with the nuclear pore complexes (NPCs, orange) in a process called postmitotic assembly. Next, during nuclear growth after telophase, the NPCs assemble de novo into a sealed double membrane with a different assembly mechanism termed interphase assembly (adapted from Otsuka, 2018).

Postmitotic NPC assembly begins shortly after the onset of anaphase in a highly organized sequential manner. Live cell imaging of mammalian cells revealed that this process also occurs in a small temporal window; within ~15 minutes after anaphase onset, NPCs have fully assembled and established a transport-competent nucleus (Dultz et al., 2008; Otsuka et al., 2014). Initial studies using *Xenopus* egg extracts as an *in vitro* system have revealed the order in which Nups are recruited to form a mature NPC and proposed a stepwise model for how postmitotic assembly may be achieved. First, ELYS, a DNA-binding protein and component of the nuclear ring of the pore, binds to the surface of DNA and recruits the Nup107 subcomplex, a major component of the cytoplasmic and nucleoplasmic rings, which together may act as seeding point for postmitotic assembly. Membranes are subsequently recruited to the chromatin resulting in the local enrichment of NE-specific proteins, including the transmembrane Nup Pom121 (Antonin et al., 2005). The subsequent recruitment of the Nup93 complex would then be mediated by its membrane-associated nucleoporins, Nup53 and Nup155 (Vollmer et al., 2012), which further promote the incorporation of Nup188 and Nup205 to complete the structural backbone of the NPC. Next, the recruitment of FG-repeat containing nucleoporins of the Nup62 subcomplex establishes selective transport in the central channel. Finally, the peripheral Nups are incorporated to establish a fully assembled NPC. While the capacity of nuclear import is rapidly reestablished during postmitotic assembly, the nuclear envelope remains permeable for passive diffusion for the first couple of hours after mitosis (Dultz et al., 2009).

The order of assembly of Nups has also been studied by in human cell lines at different cell cycle stages, which consistently revealed that ELYS, the Nup107 complex and Nup153 are recruited at early times after anaphase onset compared to cytoplasmic Nups that come later at telophase (reviewed in Otsuka and Ellenberg, 2017). In addition, recent structural work has revealed that postmitotic assembly originates by the radial dilatation of preexisting small openings within the membrane (Otsuka et al., 2018) that likely originate from closing fenestrae in the mitotic ER. The initial postmitotic structural intermediate contains dense material in the center of the membrane. After radial dilation has stopped, the central channel continues to mature until the transport competence is established (Fig.1-5 A). The association of Nups with chromatin and the interactions between many of them are regulated by the ratio of importin β to the small GTPase Ran. The RanGTP-dependent release of Nups from the import receptors is a fundamental step in the early NPC assembly which coordinates the spatial positioning of the assembly sites (reviewed in Dasso, 2002). Parallel to this, the local NE environment is remodeled during postmitotic assembly to incorporate nascent NPCs. Postmitotic dephosphorylation drives nuclear membrane coverage by regulating a large number of interactions between INM proteins and chromatin (reviewed in Ungricht and Kutay, 2017).

While the order of postmitotic assembly is now well characterized and some initial insights into the structural intermediates have been revealed, understanding which are the molecular components that drive the initial self-assembly and membrane dilation, and by what highly ordered cooperative mechanism is such an efficient process achieved (assembly of 2500 pores in 5 min), remains a mystery.

In contrast to postmitotic NPC assembly, interphase assembly occurs within a fully assembled NE and thus requires that the newly forming pores be inserted into a double membrane. Interphase assembly events occur more sporadically from the beginning of G1 to the end of the G2 phase, making it experimentally very challenging to capture these rare assembly events and to distinguish them from the large number of NPCs already formed after mitosis. However, live cell imaging studies, performed on human cell lines, were able to capture and compare the temporal order of assembly of a few specific molecular components of the pore during both postmitotic and interphase assembly. These studies report that the NPC assembly during interphase lasts on average one order of magnitude more than during mitosis and differs in the order of integration of Nups (e.g. Pom121 and the Nup107 complex show an inverted order of recruitment), providing evidence on mechanistic differences between the two assembly pathways (Dultz et al., 2008; Dultz and Ellenberg, 2010). Further studies performed in human cell lines and with reconstituted nuclei from *Xenopus* egg extracts, have identified molecular players that guide the insertion of assembling NPCs during interphase, which involve (i) members of the ER-membrane bending protein family of Reticulons (RTNs) and Yop1/DP1 (Dawson et al., 2009), (ii) the domain of Nup133 in charge of membrane curvature sensing (Doucet et al., 2010) (iii) the confinement of Pom121 to the INM (Funakoshi et al., 2011), (iv) the presence of the cytoskeleton-interacting INM protein Sun1 (Talamas and Hetzer, 2011), (v) the dimerization and membrane deforming activity of Nup53 (Vollmer et al., 2012) and (vi) the recruitment of the Nup107 complex by Nup153 to the INM (Vollmer et al., 2015). Moreover, *in situ* structural evidence has captured interphase assembly intermediates in both human and rat cells (Otsuka et al., 2016). In this study, live cell correlated EM tomography revealed the asymmetrical fusion of interphase NPC assembly; an inside-out evagination of the INM expands in width and depth until fusing with the flat ONM

(Fig.1-5 B). Interphase intermediates, present inside the dome-shape evagination, already contained a pre-formed 8-fold symmetric nuclear ring structure. While the static intermediates of interphase assembly have now been structurally characterized, it still remains unclear which specific molecular players are present at each stage of the inside-out evagination process, which stands out as a current important question in the field.

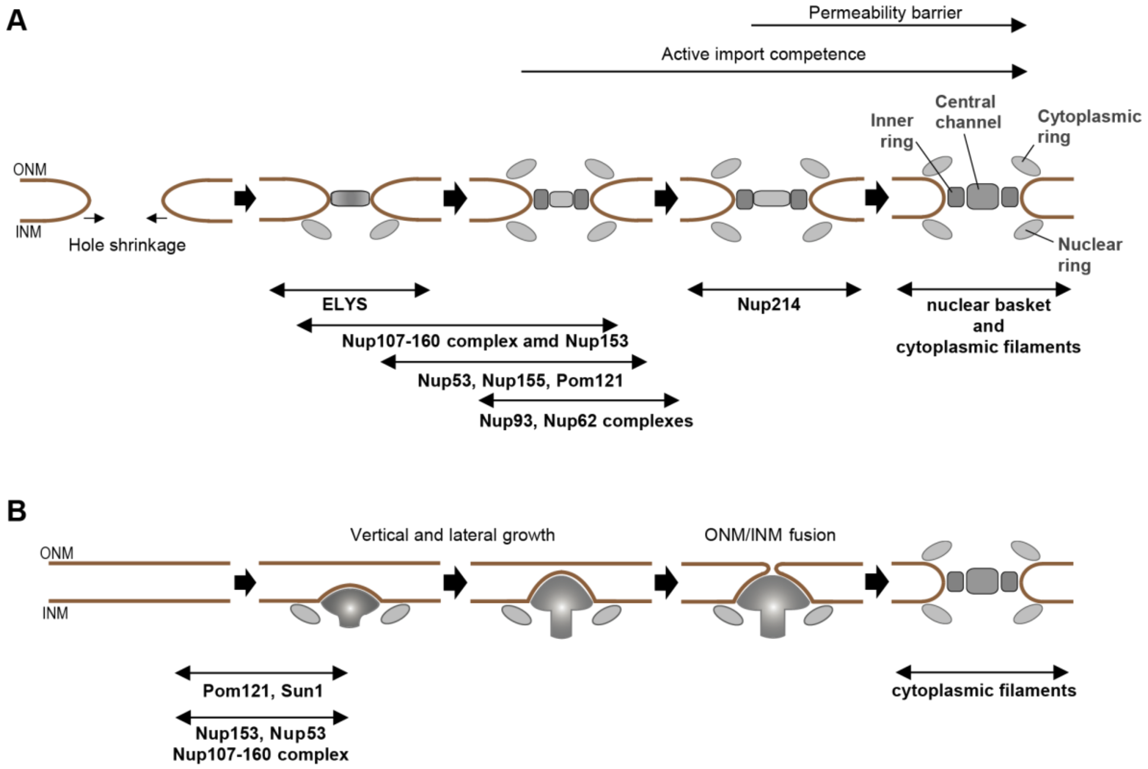

FIGURE 1-5. Two models of NPC assembly. A) The postmitotic assembly of the NPC initiates by radial dilations of small membrane openings. Initial postmitotic structural intermediates contain densely packed material in the center of the membrane hole as well as the nuclear ring. The central density continues to maturate even after the membrane dilation stops, and the NPC gradually obtains permeability barrier function against small proteins. Molecular players involved in individual steps of the assembly are indicated below. ONM, outer nuclear membrane; INM, inner nuclear membrane. **B)** Interphase NPC assembly initiates by an inside-out extrusion of the nuclear membrane. The interphase structural intermediate is a dome-shaped evagination of the INM. The structure of the nuclear ring can be found underneath the INM from the beginning and grows in size vertically and laterally until it fuses with the flat ONM. Molecular players in individual steps of the assembly are indicated (adapted from Otsuka and Ellenberg, 2017).

1.2 Structure of the nuclear pore complex

1.2.1 NPC components

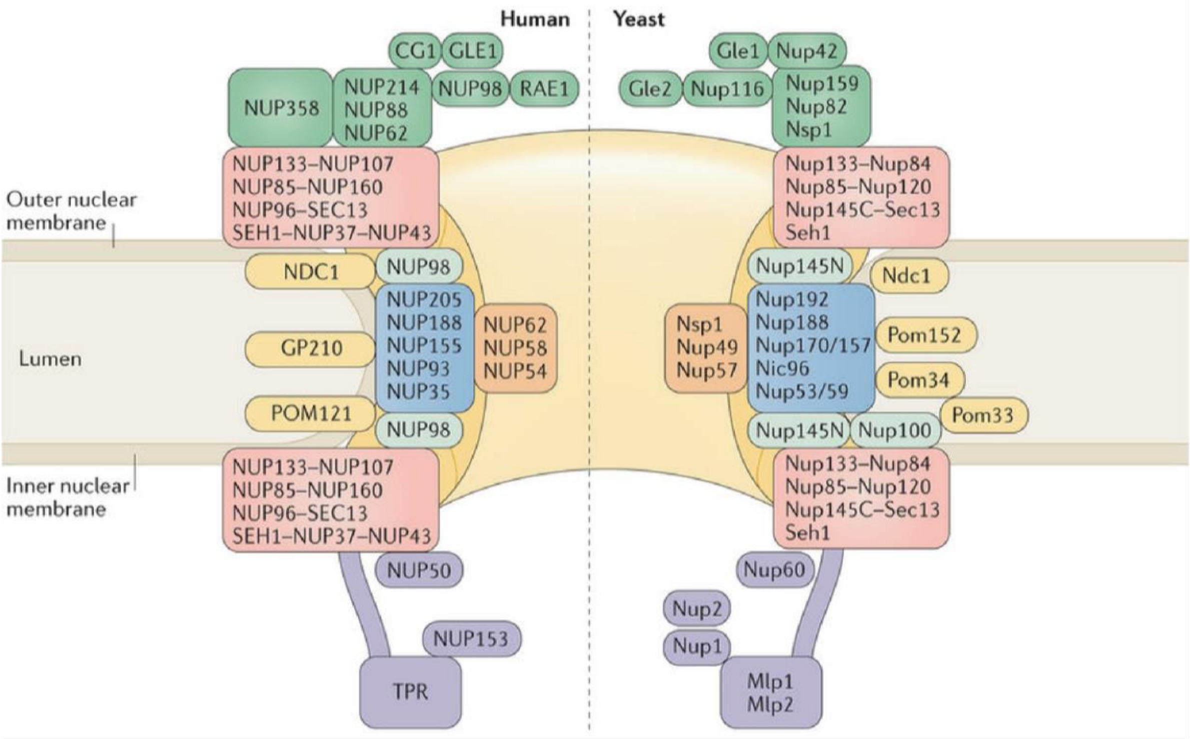

FIGURE 1-6. Organization of nucleoporins. Schematic representation of the organization of yeast and human Nups. NUPs subcomplexes are shown as colour-coded boxes and are superimposed onto the general NPC architecture. The vertebrate Nup107/ yeast 84-subcomplexes is shown in red; the inner ring complex is in blue; the transmembrane NUPs are in yellow; the NUP62 complex (the nucleoskeletal-like 1 (Nsp1) complex in yeast) is in orange; cytoplasmic complexes are in green; and nuclear basket complexes are in purple. (adapted from Beck and Hurt, 2017)

Counterintuitively to its enormous size, the NPC is formed by only about 30 different nucleoporins. Initially, the composition of the NPC was dissected in yeast by biochemical and genetic studies. The release of the yeast and some higher eukaryote genomes in the 90's opened up the possibility to identify further putative nucleoporins through their shared conserved motifs (Doye and Hurt, 1997). Finally, mass spectrometry studies on enriched NPC fractions, in both yeast and vertebrate cells, allowed the characterization of a near complete set of member- and some associated-proteins of the pore (Cronshaw et al., 2002; Rout et al., 2000a). Biochemical studies revealed that Nups are organized into subcomplexes, giving rise to the modular nature of the pore (Schwartz, 2005). These subcomplexes serve as basic blocks that build up the architecture of NPC (Fig.1.6).

Most nucleoporins are structurally conserved between yeast, mammals and plants, yet their conservation has been less evident outside these three phylogenetic groups. More recent comparative genomic analysis were able to trace back all major NPC subcomplexes to the Last Eukaryotic Common Ancestor (LECA) (Neumann et al., 2010). Similar phylogenetic studies support the hypothesis of the presence of a NPC-like machine in the LECA and propose that the pore has evolved within strong structural constrains while being highly adaptive at the sequence level (Mans et al., 2004). Despite the high structural and functional similarity between NPCs across species, the number and density of pores in the nuclear envelope varies greatly between different organisms and cell types. In vertebrates, the average nucleus contains between 2000-5000 pores with a density of ~15 pores/μm^2, while the yeast cell has as little as 200 pores but reaches a density of ~12 pores/μm^2 (Winey et al., 1997). Contrastingly, a *Xenopus* oocyte can reach as many as 50 million pores per nucleus with a density of ~60 pores/μm^2 (Cordes et al., 1995). Moreover, different human cell lines have been reported to embed different densities of pores in their nuclei. The human HeLa cell line has been reported to contain around 10 pores/μm^2 (Otsuka et al., 2016) while the osteosarcoma U2OS cell line only around 5 pores/μm^2 (Maimon et al., 2012). The different number and density of pores present in each cell type might be linked to the differences in transport requirement. NPC composition also varies between organisms, cell types, cell cycle phases and developmental stages (D’Angelo et al., 2012).

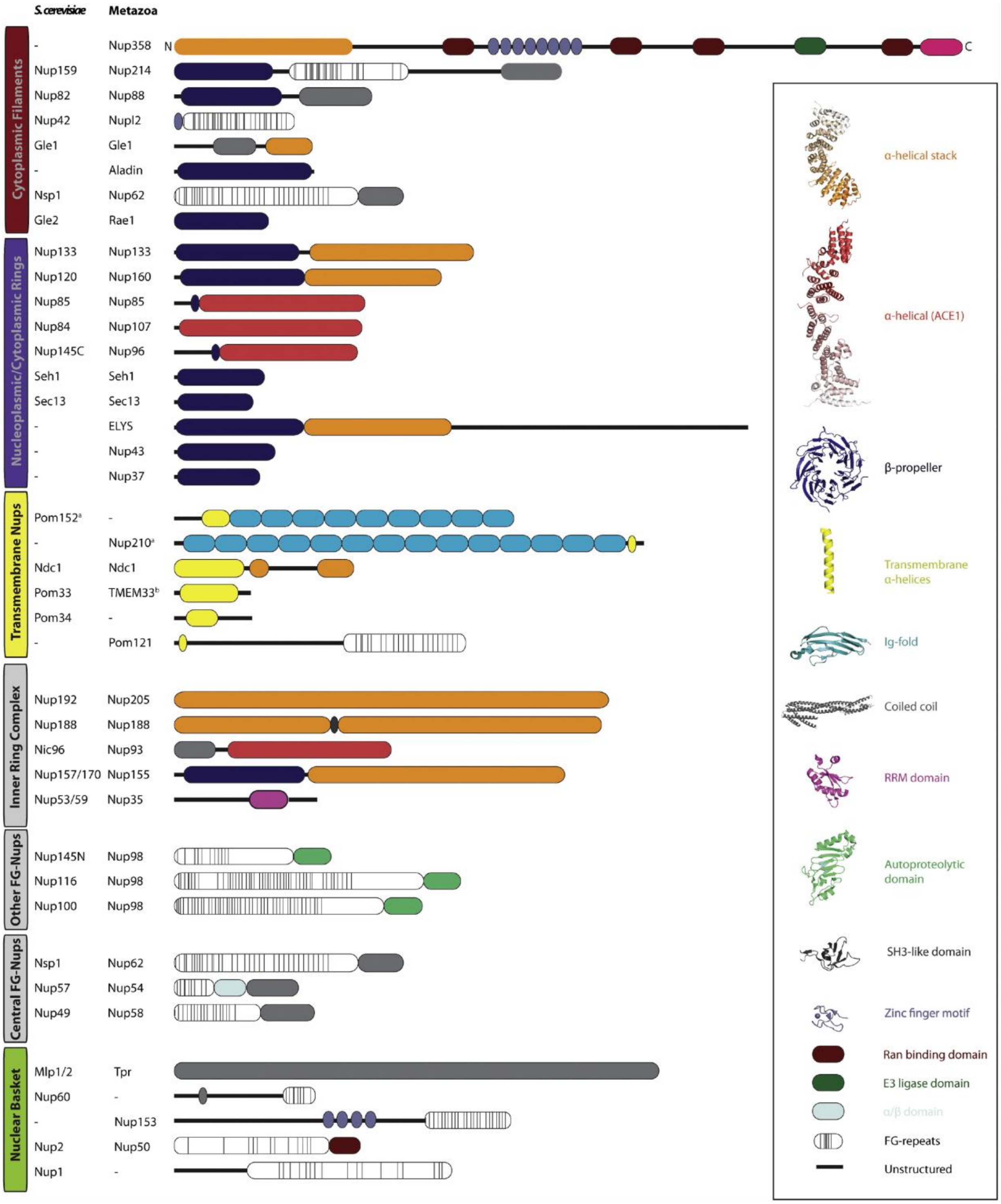

FIGURE 1-7. Domain elements in nucleoporins. Nups are built up from a small set of architectural elements. Yeast (S. cerevisiae) and metazoa nucleoporins are ordered according to the subcomplexes they belong to. Domain elements are color coded and illustrated by representative crystal structures. Illustration length represents the approximate relative molecular weight of each Nup (adapted from Schwartz, 2016).

Vertebrate nucleoporins possess distinct molecular masses, which range from approximately 50 to 358 kDa (Cronshaw et al., 2002). With some exceptions, the distinctive name of each nucleoporin was selected according to two parameters: the first part indicates if the protein is a soluble (Nup) or a transmembrane (Pom) protein and the subsequent part makes reference to its molecular weight. Due to the different molecular masses that Nups possess in distinct organisms there is no universal nomenclature for nucleoporins across species. Nups are confined to a particular location and function through specific domains and structural motifs (Fig.1-7). Nups are usually subdivided in three general classifications. The first class is composed of scaffold Nups that contain α-solenoid and β-propeller motifs and are structural components of the pore. The second class is represented by transmembrane Nups that are characterized by their membrane-anchoring capacity and which contain membrane-spanning helices and cadherin folds in their secondary structure (Onischenko et al., 2009). The third class corresponds to barrier Nups, whose main feature is the presence of phenylalanine-glycine (FG)-repeats. Barrier Nups can be further classified into central FG-Nups that have a crucial role during nucleocytoplasmic transport (Lim et al., 2008), cytoplasmic FG-Nups and nuclear FG-Nups. Homology modeling indicates that 38% of all Nup motifs are α-solenoid folds, followed by 29% of FG-repeats and 16% to β-propeller folds. Other types of motifs constitute, individually, less than 5% of the Nup secondary structure landscape (Devos et al., 2006). The limited amount of predicted motif types present within the NPC suggest that the overall structure and function of the NPC has evolved through extensive gene duplication from an ancient precursor set of only a few protein types.

From early on, it was observed that the NPC has an eight-fold symmetry (Gall, 1967; Hinshaw et al., 1992). However, characterizing the stoichiometry of Nups that constitute the observed NPC symmetry remained a challenge until recently. It had been suggested that nucleoporins should be present in copies of multiples of eight in order to assemble an octagonal structure. Initially, based on semi-quantitative immunological assays in yeast (Rout et al., 2000a) and proteomic analysis in vertebrates (Cronshaw et al., 2002), it was estimated that 16 to 32 copies of the scaffold Nups should be present in each individual NPC. More recent work using targeted mass spectrometry in isolated nuclei of human HeLa cell lines (Ori et al., 2013) and super-resolution microscopy in live yeast (Mi et al., 2015) revealed the relative stoichiometry of subcomplexes within fully assembled NPCs (Fig. 1-8). Ori and colleagues used a strategy combining orthogonal approaches to calibrate the obtained stoichiometries to absolute numbers of Nup copies per NPC. First, they counted the number of extracted nuclei using flow cytometry. Once the total number of nuclei was established, they quantified the copies of the scaffold Nup107 from the determined population of nuclei. Next, using cryo-electron tomography and fluorescence microscopy, they determined the density of NPC and the surface area on the nucleus, respectively, in HeLa cell lines. Taken together, from these measurements, Ori and colleagues estimated an average of 37±14 Nup107 copies per NPC. Finally, to independently cross-validate this estimation, they used super-resolution microscopy on mEos2-tagged Nup107 HeLa cell lines to count the number of mEos2-Nup107 fusion protein copies per NPC and arrived at a conclusion that supported the presence of 32 copies. Then, taking Nup107 as a calibration baseline, Ori and colleagues calculated the relative abundance of all human Nups within the NPC based on mass spectrometry. These results show that the major scaffold components of the pore share a comparable stoichiometry of 32 copies per NPC, with the exception of ELYS and Seh1 that presented a sub-stoichiometric abundance. While the lower copy number of ELYS can be explained by its proposed exclusive occurrence on the nucleoplasmic side of the pore, the sub-stoichiometric abundance of Seh1, which is present at both faces of the pore, remains puzzling.

Nucleoporin stoichiometry has shown to be more dynamic and complex than previously considered. Nucleoporins have been shown, for example, to group into three different dynamic classes, ranging from very stable Nups with low dissociation rates to highly dynamic Nups with high dissociation rates (Rabut et al., 2004). In addition, Nup mRNA expression levels vary across different tissue culture cells and affect the ultimate composition of NPCs (Ori et al., 2013). Also, NPC stoichiometry is regulated at both the transcriptional and post-transcriptional level and fluctuates in space and time throughout the cell cycle (Ori et al., 2016). The changes in NPC composition have also been shown to have functional relevance during cell differentiation and in disease (reviewed in (Raices and D'Angelo, 2012)). Studies using *in vitro* differentiation models discovered that the variation of the transmembrane nucleoporin Gp210 is essential for myogenesis and neural differentiation in mice (D'Angelo et al., 2012). Moreover, the cytoplasmic filament Nup358 has a comparable role in myogenesis; the up-regulation of Nup358 gene expression levels is required for differentiation (Asally et al., 2011). Asally and colleagues correlated the observed increase in Nup358 mRNA expression during myogenesis with structural changes within the NPC that they detected with atomic force microscopy. Further studies on cardiomyocyte differentiation also connected the variation at the gene expression level of different Nups with changes at the structural level of the NPC, suggesting a potential involvement of the NPC in heart formation (Perez-Terzic et al., 1999, 2003). These similar findings provide evidence for the dynamic nature of the NPC and for the role of its composition and remodeling during differentiation, however, the mechanism by which Nups act to promote tissue development remains uncharacterized.

Loss-of-function mutations of several Nups are lethal for developing organisms (Lupu et al., 2008; Zhang et al., 2008), which is in agreement with their essential role for cell survival and during cell differentiation. As a result of their tissue-specific composition, mutations of specialized Nups cause distinct alterations in particular types of organs. For example, mutation of Nup155, which is overrepresented in the heart, liver and muscle tissue, triggers cardiac diseases (Zhang et al., 2008). A missense mutation in Nup62 was found in autosomal recessive infantile bilateral striatal necrosis (Basel-Vanagaite et al., 2006) and mutations causing the mislocalization of the Nup Aladin is associated with the rare autosomal recessive disorder called triple A syndrome (Huebner et al., 2004). These studies exemplify the impact that NPC composition has on the regulation of cellular processes and its involvement in cardiac, immune and nervous system diseases.

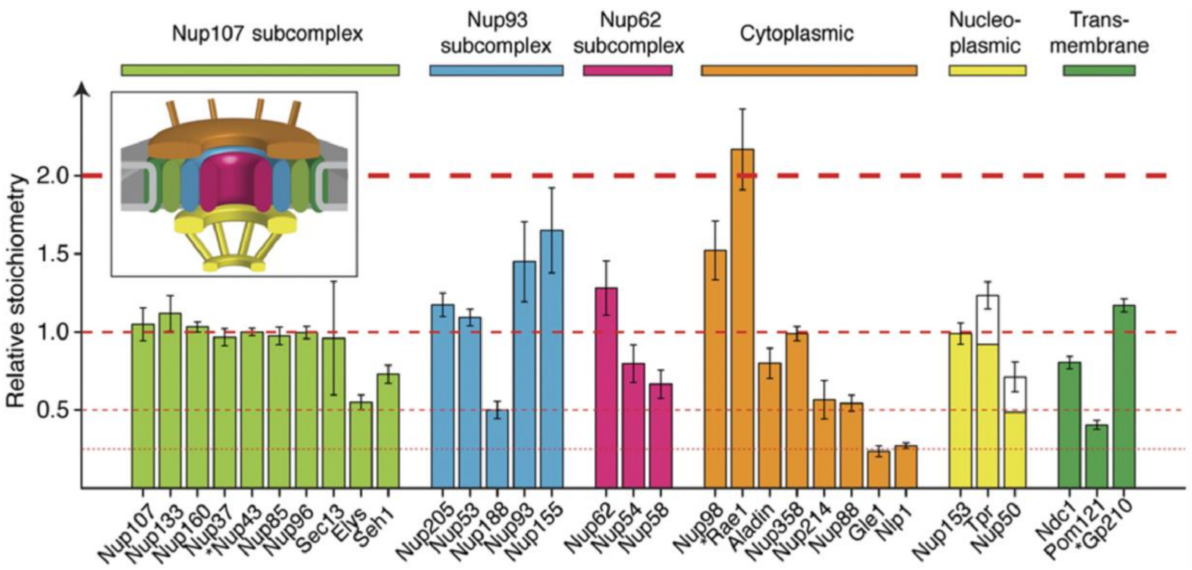

FIGURE 1-8. NPC Stoichiometry. The abundances of all Nups were determined by targeted proteomics. The relative stoichiometries are presented as median light to heavy ratio±median absolute deviation (across four biological replicates and multiple independent measurements). Nups are color-coded according to the subcomplex they belong to or according to their predicted localization in the NPC (inset). All abundance levels are normalized to the Nup107 subcomplex and the major abundance steps (multiples of Nup107) are indicated with dashed red lines (adapted from Ori, 2013).

1.2.2 Scaffold nucleoporins and subcomplexes

Scaffold Nups constitute the stable symmetric platform of the NPC. Most of the scaffold Nups have a low turnover rate and stay incorporated in the pore through the entire life span of the cell (D’Angelo et al., 2009; Daigle et al., 2001; Rabut et al., 2004). The majority of scaffold Nups contain an α-solenoid fold, a β-propeller fold, or a combination of both (Devos et al., 2006). The scaffold of the NPC constitutes different symmetric structural elements at both nuclear and cytoplasmic sides of the NE; two separated outer-rings (subdivided into a nuclear- and cytoplasmic-ring), two closely positioned inner rings at the NPC equator and two linker regions that connect both outer- and inner-rings with each other (reviewed in (Grossman et al., 2012)).

Depending on the location and properties of the scaffold Nups, they can be categorized into outer-ring Nups, inner-ring Nups and linker Nups. From biochemical studies, it became evident that the structural elements of the scaffold of the pore are further subdivided into smaller subcomplexes (Dabauvalle et al., 1990; Finlay et al., 1991; Lutzmann et al., 2002). Outer-ring Nups build the Nup84 subcomplex in yeast and Nup107 subcomplex in vertebrates while inner-ring Nups compose the yeast Nic96 and vertebrate Nup93 subcomplex.

1.2.2.1 Yeast Nup84 / vertebrate Nup107 subcomplex

The yeast Nup84 and vertebrate Nup107 subcomplex, also known as the Y-shaped-subcomplex, is one of the two largest subcomplexes that constitute the scaffold of the NPC. The Y-shaped-subcomplex is an evolutionarily conserved subcomplex and embodies seven and ten outer-ring Nups in yeast and vertebrates, respectively (Lutzmann et al., 2002; Ori et al., 2013). The Nup107 subcomplex is composed of Nup107, Nup133, Nup160, Nup96, Nup85, Nup43, Nup37, Seh1, ELYS and Sec13, while the yeast homologue is composed of Nup84, Nup85, Nup133, Nup120, Nup145C, Seh1 and Sec13 (reviewed in (Siniossoglou et al., 2000)) (Fig. 1-6). The Y-shape-subcomplex has a total molecular mass of around 600kDa in yeast and 1000kDa in vertebrates. This subcomplex is essential for the proper function of the cell, as several studies have shown that that depletion of any of the constitutional members of the Y-shape-subcomplex results in abnormal nuclear morphology, absence of NPC formation and stalling of mRNA export (Boehmer et al., 2003; Walther et al., 2003).

The first structural insights into the heptameric yeast Nup84 subcomplex were obtained from negatively stained specimen of the entire subcomplex and from its dimeric and trimeric partial complexes that were analyzed in 2D by EM (Lutzmann et al., 2002; Siniossoglou et al., 2000), revealing a 40 nm long Y-shaped structure. Later on, 3D reconstructions of single-particle EM confirmed the previously observed Y-shaped architecture of the reconstituted Nup84 heptamer and identified two different conformations present within the analyzed particles (Kampmann and

Blobel, 2009). The superimposition of the two detected conformational states of the Y-shape-subcomplex uncovered two distinct hinge regions, suggesting a high flexibility of this scaffold subcomplex (Fig.1-9 A-C). In addition, by docking previously available crystal structures into the 3D EM maps, the relative arrangement of outer-ring Nups was identified within the Y-shaped-subcomplex. The obtained structure contains a 45nm long stem with two 10-15nm arms, where Nup120 occupies the longer arm, Nup85 and Seh1 the second shorter arm and Nup133, followed by Nup84, Sec13 and finally Nup145C the foot (Kampmann and Blobel, 2009). Furthermore, the additional docking of the heterotrimeric Sec13-Nup145C-Nup84 subcomplex revealed that the structural changes between the different Y-shape-subcomplex conformations occur at the Nup145C-Nup84 interface (Nagy et al., 2009) (Fig.1-9 C).

Following the developments in recombinant protein production and reconstitution of the Y-shaped-subcomplex, the individual Nups have been successfully crystalized in different parts over the last decade. The docking of the obtained crystal structures to available EM maps provides a comprehensive atomic resolution map of the entire Y-shape-subcomplex (reviewed in (Grossman et al., 2012)). The atomic resolution map highlights two resemblances between the NPC and the COPII machinery. First, the high structural similarity found between the bifunctional vesicle coating protein Sec13 and Seh1 (Fath et al., 2007). Second, the helical domains of Nup84, Nup85 and Nup145C that fall into a group called ancestral coatomer element 1 (ACE1), due to their similarity to the COPII machinery (Whittle and Schwartz, 2010). In conclusion, the structural likeness of Nups and the helical elements of the ACE1 subgroup, provide strong evidence that the vesicle coating system is evolutionary related to the components of the Y-shape-subcomplex.

In more recent years, two independent groups have accomplished the crystallization of an almost fully assembled Y-shape-subcomplex. First, the crystal structure of a heterohexameric subcomplex, including the yeast Nup84, Nup85, Nup120, Nup145C, Sec13 and Seh1, was solved at a resolution of 7.4Å (Stuwe et al., 2015a).

Stuwe and colleagues used high-affinity synthetic antibodies as crystallization chaperones to stabilize the heptameric complex. At the same time, the heterotetrameric subcomplex, composed by the Nup120, Nup145C, Nup85 and Sec13 from the thermophilic fungus *M. thermophila*, was resolved at a 4.1Å resolution and was further assembled with the available crystal structures of missing Nups to create a composed Y-shape-subcomplex map (Kelley et al., 2015).

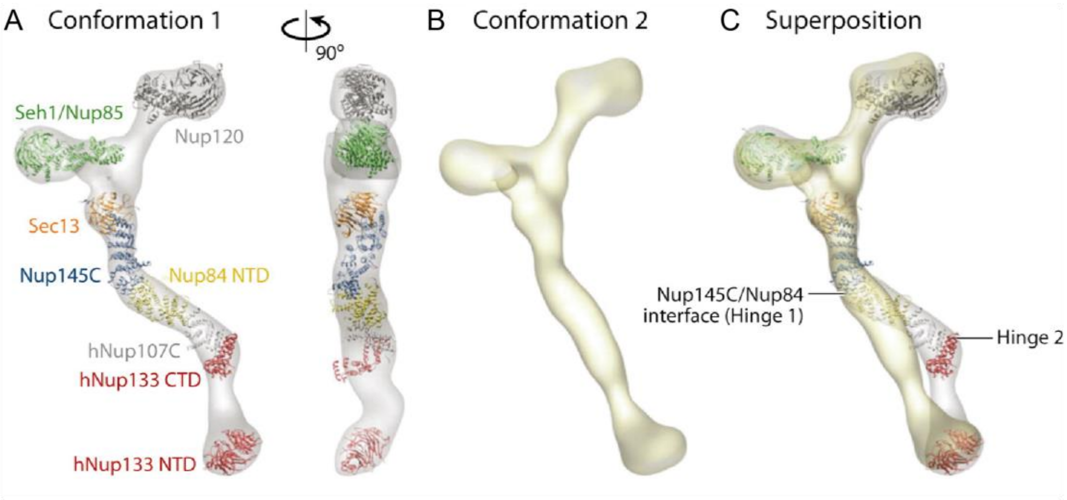

FIGURE 1-9. Two conformations of the Y-shape-subcomplex. A) EM reconstruction of Conformation 1 of the Y-shape-subcomplex with docked crystal structures. To the right, the rotated view is illustrated. **B)** EM reconstruction of Conformation 2 of the Y-shape-subcomplex. The two hinge regions are completely extended, forming an almost entirely straight stem compared with Conformation 1. **C)** The superimposition of both conformations. The kink region at the Nup145C/Nup84 interface is indicated and was used for the structural alignment. The superimposition shows the differences in interface, which correspond to a hinge in the heptamer stem (adapted from Nagy, 2009 and Grossmann, 2012). Abbreviations: EM, electron microscopy; NTD, N-terminal domain; CTD, C-terminal domain.

1.2.2.2 Yeast Nic96 / vertebrate Nup93 subcomplex

The yeast Nic96 and vertebrate Nup93 subcomplex, also known as the inner-ring subcomplex (IRC) composes the central part of the scaffold of the pore. This subcomplex is the second major component of the scaffold of the NPC. In yeast it comprises the nucleoporins Nic96, Nup192, Nup145, Nup170, Nup53 and 188

(Fischer et al., 2015; Grandi et al., 1997; Hawryluk-Gara et al., 2005, 2008; Stuwe et al., 2015b). In addition, the structured coiled-coil domains of Barrier Nups (Nup49, Nup57 and Nsp1) form a stable complex, called the channel nucleoporin heterodimer (CNT), which also takes part of the IRC subcomplex (Chug et al., 2015; Stuwe et al., 2015b). The vertebrate inner-ring subcomplex homologs are Nic96, Nup205, Nup145, Nup155, Nup35 and 188. This subcomplex is thought to serve as an anchoring platform for the FG-Nups of the central channel of the pore (Alber et al., 2007a; Amlacher et al., 2011; Kim et al., 2018; Kosinski et al., 2016; Schrader et al., 2008) (Fig.1-10 A-B).

In recent years, extensive progress has been made both with X-ray crystallography and EM, for the structural understanding of the inner-ring components of the NPC (Hoelz et al., 2016), however to resolve the structure and interaction map at single-residue resolution will still require substantial effort.

The yeast Nic96 and vertebrate Nup93 subcomplex share the same structural scaffold motifs with the Y-shape-subcomplex components (i.e. α- solenoid and β-propeller folds) (Devos et al., 2006). In addition to the computationally predicted structural motifs, crystal structures of inner-ring Nups have exposed a number of distinct fold types that were previously unforeseen and with no structural homologs present in available databases (Schrader et al., 2008).

The yeast Nup170 and vertebrate Nup157 resemble the Y-shaped-subcomplex component Nup133, as they both combine an N-terminal β-propeller with an α-helical stack domain to form a curved shaped structure (Amlacher et al., 2011; Flemming et al., 2009; Lutzmann et al., 2005; Whittle and Schwartz, 2009). Interestingly, Nup170 adopts different conformations under distinct biochemical environments, suggesting a variety of mechanical forces acting on Nup170 at specific molecular positions (Lin et al., 2016).

Finally, the crystal structures of the conserved Nup192 and Nup188 subunits derived from the thermophilic fungus *C. thermophiles* (Amlacher et al., 2011) and the subunit Nup192 from *S.cerevisiae* (Sampathkumar et al., 2013), revealed a S-like structure made of stacks of HEAT repeats, that resembles the shape of known transport receptors and vesicle coating proteins. The full-length superimposed structure of Nup192 reveals that its binding sites for Nup53 and Nic96 are respectively located at the top and bottom of the protein, around 140 Å apart (Lin et al., 2016).

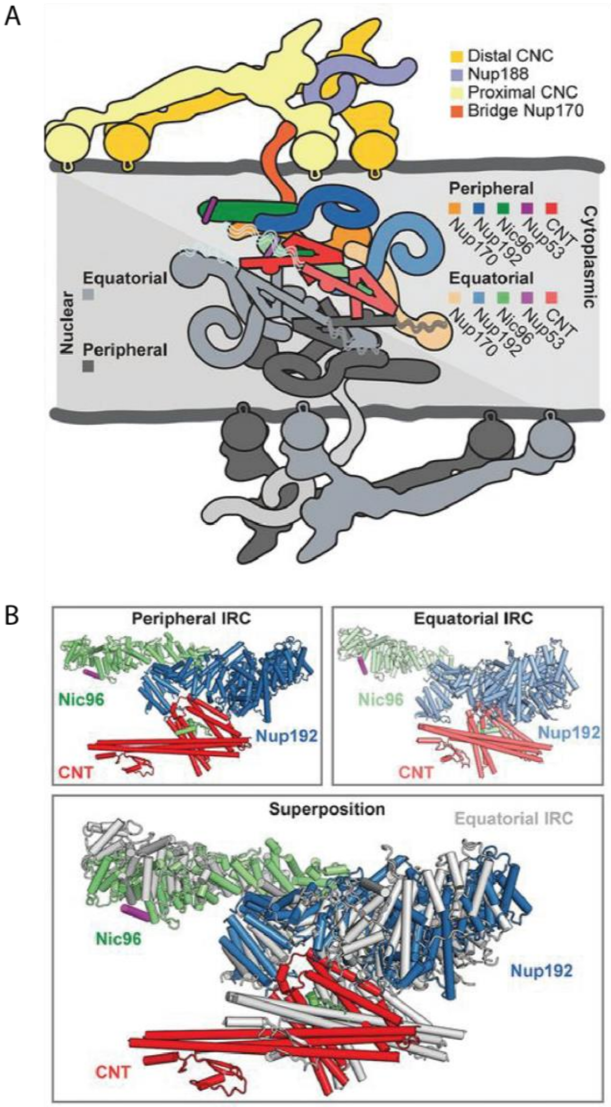

FIGURE 1-10. Schematic of Inner-ring A) Illustation of the arrangement of inner-ring Nups in a cross-sectional view and the interactions that take place with the Y-shape-subcomplex (yellow). The proteins corresponding to the nuclear side of the spoke are colored in gray for simplicity. All Nups and specific subcomplexes are color-coded. **B)** Struture of the inner-ring subcomplex (IRC). Equatorial and peripheral IRCs adopt similar conformations. Superimposed image is shown (adapted from Lin, 2016). Abbreviations: CNC, coat nucleoporin complex; CNT, channel nucleoporin heterodimer

The protein-protein interaction network of the inner-ring has been widely studied (Amlacher et al., 2011; Hawryluk-Gara et al., 2008; Kosinski et al., 2016; Lin et al., 2016; Onischenko et al., 2009; Stuwe et al., 2015a, 2015b) and shows more plasticity compared to the interaction network of the Y-shape-subcomplex. While the outer-ring of the scaffold of the pore uses extensive surface contacts, the inner ring proteins are mainly bridged by flexible sequences of linker Nups (Fig. 1-10 A). The specific interaction of the large scaffold domain of Nic96, Nup170, Nup188, and Nup92 to the long, intrinsically disordered sequences of linker Nups, is held together by extensive interfaces of α-helical domains (Hoelz et al., 2011a; Stuwe et al., 2015a). In addition, Nic96 is essential for the attachment of the Nsp1-Nup49-Nup57 heterodimer (Stuwe et al., 2015b), thus Nic96 has been proposed to serve as an important assembly sensor of the scaffold of the NPC.

1.2.2.3 Models of organization of the Scaffold of the NPC throughout time

During the past two decades, the structural details of the isolated Y-shape-subcomplex and reconstituted inner-ring components have been carefully characterized, however, understanding how these subcomplexes are positioned and orientated within the entire scaffold of the NPC remained a mystery until not long ago. A primary challenge for solving this problem relied on the differences in resolution available at the time for EM density maps and the crystal structures, which prevented the direct docking of the Y-shape-subcomplex into the outer-ring and the yeast Nic96/vertebrate Nup93 into the inner-ring of the NPC. Initially, based on diverse auxiliary data, several models have been proposed throughout the course of time, which gave hints at how the scaffold of the NPC might be organized. More recent technological developments have pushed the limits of recombinant protein production, reconstitution and resolution of both light and electron microscopy and provided new complementary evidence as to how the entire scaffold of the NPC is structured. However, the architectural details of more flexible and unstructured regions of the NPC remain elusive.

One of the initial models was proposed by the Hoelz and Blobel group and was named the “Fence-like coat” model. This model is based on evidence derived from different crystal structures, biochemical and *in vivo* studies that highlight the resemblance between COPII components and Nups (reviewed in (Hoelz et al., 2011b)). First, the observation that both Sec13-Nup145C and Seh1-Nup85 hetero-dimers can form elongated hetero-octameric structures (Debler et al., 2008; Seo et al., 2009), suggested that the Y-shaped-subcomplex could be positioned horizontally within the scaffold of the NPC. Second, the unstructured N-terminus of Nup133 has been observed to interact with the central α-helical domain of Nup120, suggesting an arrangement that could form a stacked ring like structure (Seo et al., 2009). Taking this information together, the “Fence-like coat” model makes the assumption that the Y-shape-subcomplex is positioned as horizontal vertical poles in the assembled NPC, resulting in a cylindrical scaffold (Fig.1-11 A). This scaffold accommodates 32 copies of each scaffold Nup into four rings, stacked in an antiparallel manner.

While the overall dimensions of the proposed model were in accordance with the experimentally determined size of the yeast NPC and with the relative positions of scaffold Nups within the Y-shape-subcomplex, more recent experimental evidence discredited the vertical architecture proposed in the “Fence-like coat” model. Two independent groups resolved the crystal structure of the heterotrimeric complex composed of Nup84-Nup145C-Sec13 and showed that the interaction between Nup84 and Nup145C is stabilized by crown-to-crown interactions (Brohawn and Schwartz, 2009; Nagy et al., 2009). The Schwarz group argued that these findings go in disagreement with the “fence-like coat” model, as the crown-to-crown interaction presented in the heterotrimeric complex require the same interface that was proposed to stabilize the vertical poles of the model (e.g. Nup145C homodimerization). In response to this discrepancy, the Hoelz and Blobel group interpreted the observed promiscuity of Nup145C (i.e. interaction with Nup145C or Nup84) as evidence of the presence of different conformational states and proposed, in addition to the vertical architecture of the NPC, a dynamic character to the “fence-like coat” model (Hoelz et al., 2011b).

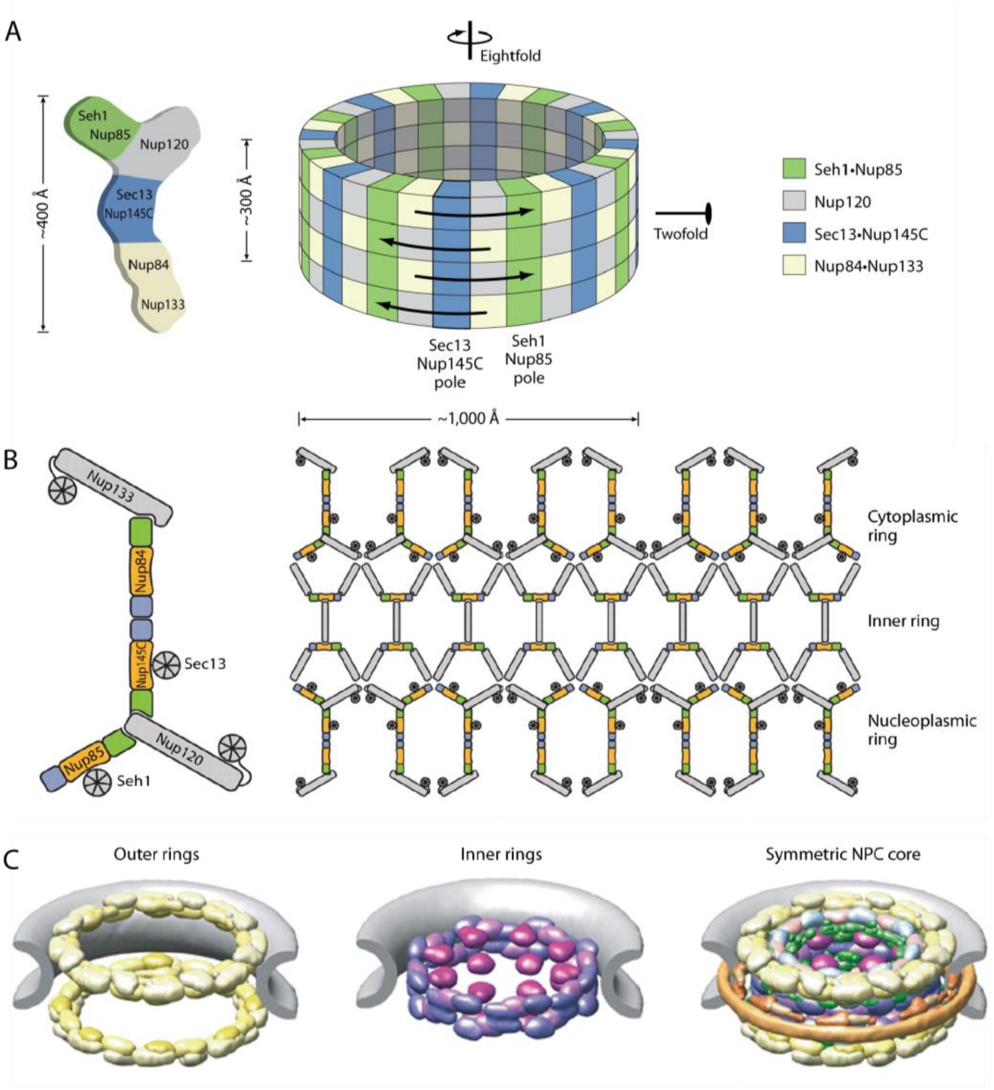

FIGURE 1-11. Initial models of the scaffold of the NPC. A) Schematic representation of the “fence-like” model . Approximate localization of the seven nucleoporins of the Y-shape-subcomplex (left). Eight heptamers are circumferentially arranged in a head-to-tail fashion in four stacked rings, thereby forming a cylindrical scaffold (right). **B)** Schematic representation of the “lattice” model.

In this model the Y-shape-subcomplex is orientated vertically, in a head-to-head orientation along the equatorial plane. **C)** Schematic representation of the “computational” model. This model predicts 16 Y-shape-subcomplexes composing two separate rings, one in the nucleoplasmic and one in the cytoplasmic side. Between the two outer-rings, two inner-rings are sandwiched, forming a compact cylinder across the NE. **A)-C)** (adapted from Hoelz, 2011)

The Schwartz group proposed a different model for how the Y-shape-subcomplex could be organized within the scaffold of the NPC. This model was also based on similarity observations between the NPC scaffold and the lattice-like architecture of the COPII coat and was termed the “lattice” model of the NPC (Brohawn et al., 2009). The observation that Nup145C interacts with Sec13 in a similar manner as the COPII outer coat component Sec31 with Sec13, by a β-propeller composed by two interaction partners (see section 1.2.2.1; Structure of the Y-shape-subcomplex), lead to the hypothesis that the same building-block principles might guide COPII and NPC architecture.

The edge element of the COPII cage is arranged of Sec31-Sec13 heterodimers (Fath et al., 2007). Four edge elements meet, by the interaction of the N-terminal β-propellers of Sec31, to form a vertex. The variable number of edge elements and their adjusting angular interactions create vesicles of different sizes (Stagg et al., 2008). Based on structural evidence that four scaffold Nups share an ACE1 domain with Sec31 and that Nup84-Nup145C heterodimers form an analogous crown-to-crown interaction to Sec31-Sec13 heterodimers, the Schwartz group proposed a model where similar edge elements and vertexes conform the scaffold of the NPC in a lattice-like organization (Brohawn et al., 2008, 2009). In addition, given that Nup133 does not share the ACE1 domain, they proposed that this Nup might serve as a termination element (Boehmer et al., 2008). Taken together, the “lattice” model contemplates two peripheral outer rings formed by eight copies of the Y-shape-subcomplex each. Within the scaffold of the pore, each Y-shape-subcomplex is orientated vertically, in a head-to-head orientation along the equatorial plane, and with Nup133 terminal elements facing outwards (Bilokapic and Schwartz, 2012) (Fig.1-11 B).

An alternative “computational” model was proposed by the Sali group, which makes use of integrative modeling to encompass biophysical and proteomic data available at the time (Alber et al., 2007a, 2007b). The Sali group used known information about the size, symmetry, localization and interactions between Nups and made assumptions about their absolute stoichiometry to create restraints for their

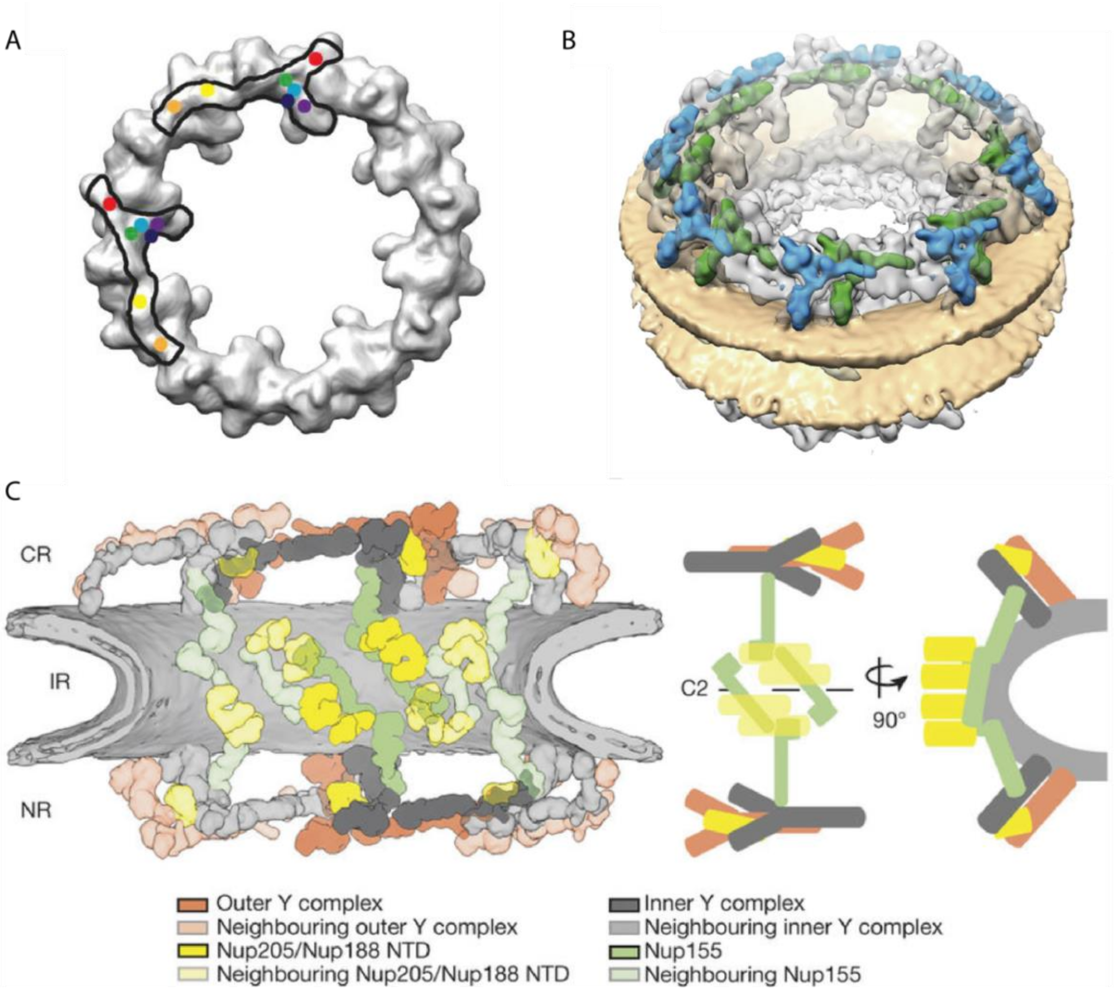

FIGURE 1-12. Subsequent models of the scaffold of the NPC. A) The two possible arrangements of the Y-shape-subcomplexes traced in the electron density of the cytoplasmic ring of the nuclear pore complex are shown. Measurements were obtained with super-resolution microscopy. The dots represent the measured radial position of individual Nups (adapted from Szymborska, 2013). **B)** EM reconstruction showing the stereoview of the optimized fit of the two vertices of the Y-shape-subcomplex per subunit in the cytoplasmic ring (protein in transparent gray, membranes in yellow, the two fitted vertices per subunit in green and blue) (adapted from Bui, 2013). **C)** Schematic representation of the side-view of the human nuclear pore scaffold. New insights into the organization of the inner-ring subcomplex members are shown. (adapted from von Appen, 2015). Abbreviations: NTD, N-terminal domain.

computational analysis. In their resulting “computational” model, 16 Y-shape-subcomplexs form two separate rings, one in the nucleoplasmic and one in the cytoplasmic side. Between the two outer-rings, two inner-rings are sandwiched, forming a compact cylinder across the NE (Fig.1-11 C). In more recent years, using refined structural information of the Nup84-subcomplex obtained by the Rout group (Fernandez-Martinez et al., 2012), the “computational” model, in addition, predicted that the outer-rings of the scaffold of the NPC are formed by head-to-tail arrangements of Y-shape-subcomplexes.

While the “computational” model predicts a head-to-tail arrangement of the Y-shape-subcomplex within the outer-ring of the NPC, how the subcomplexes’ arms are orientated within the scaffold of the NPC was left under debate. In order to tackle this question, the Ellenberg group used 2D super-resolution microscopy combined with single particle averaging to rotationally position all Y-shape-subcomplex Nups within the outer-ring of the NPC, with a precision bellow one nanometer (Szymborska et al., 2013). The resulting 2D map supports a head-to-tail arrangement of the Y-shape-subcomplex and in addition provided direct evidence of the orientation of the subcomplex within the scaffold of the NPC (Fig.1-12 A). Moreover, when comparing the proposed orientation of the subcomplex with EM maps available at the time, the Ellenberg group found two different positions where the Y-shape-subcomplex could fit. This study also demonstrates the value of using super-resolution technologies for the study of large protein complexes such as the NPC.

During the same period of time, the Beck group used an integrative approach based on single-particle EM, crosslinking mass spectrometry and the first cryo-ET map with a resolution that provided sufficient information to position multiple copies of the Y-shape-subcomplex structure into the outer-rings of the NPC (Bui et al., 2013). The 3D EM map was obtained from isolated NEs of human tissue culture cells. By searching for the structural signature of the isolated human Y-shaped-subcomplex vertex, the Beck lab revealed, for the first time, the 32 subunits that conform the fully assembled scaffold of the NPC. Moreover, the Y-shaped-subcomplexes are arranged as two concentric, mildly shifted rings on both the cytoplasmic and nucleoplasmic sides of the NE (Fig.1-12 B). Furthermore, the Beck group reported a cryo-EM map of the NPC scaffold with a resolution down in the 2-nm range that was achieved by using a direct electron detector hardware (von Appen and Beck, 2015). In this refined map of the scaffold of the NPC new protein interfaces within the Y-shaped-subcomplex were revealed, as well as initial insights into the organization of the inner-ring subcomplex members. In addition, the human Nup358 was shown to have an unexpected role in the Y-shape-subcomplex oligomerization (Fig.1-12 C).

More recently, the refined structure of the human inner-ring of the scaffold of the NPC has been uncovered by combined efforts of the Beck and Hoelz group (Kosinski et al., 2016; Lin et al., 2016). While the Beck group resolved a refined architectural map of the inner-ring of the pore, the Hoelz group provided the structures of the reconstituted inner-ring components and determined the interactions between them. By using molecular modeling and combining the results of both groups, the first model that explains the majority of the electron density of the scaffold of the pore is reached (reviewed in (Beck and Hurt, 2017)). This model proposes that the inner-ring of the scaffold of the NPC is composed by four horizontally stacked, slightly shifted, intermingling rings (Fig1-13 A). Initial evidence comes from the systematic fitting of the Nup205 and Nup188 N-terminal domains, which revealed that these inner-ring Nups are positioned parallel to the NE, which supports the described four-ring organization (von Appen and Beck, 2015). In addition, the previously published Nup62-Nup58-Nup54 heterodimer (Chug et al., 2015; Stuwe et al., 2015b), the C-terminal domain of Nup205 (Stuwe et al., 2015b) and Nup62 and Nup93 complex interactions (Fischer et al., 2015; Stuwe et al., 2015b) were docked into the tomographic map, strongly defending the proposed model. From the fully assembled inner-ring, one can observe 32 copies of each Nup205, Nup93, Nup155 and Nup62 and 16 copies of Nup155 that connect to the outer-ring of the scaffold of the NPC. The discovered architectural principles of how the inner-ring is organized, resemble the Y-shape-subcomplex organization within the outer-ring of the scaffold of the pore, and highlight the suspected evolutionary relationship between the NPC modules (Fig1-13 A).

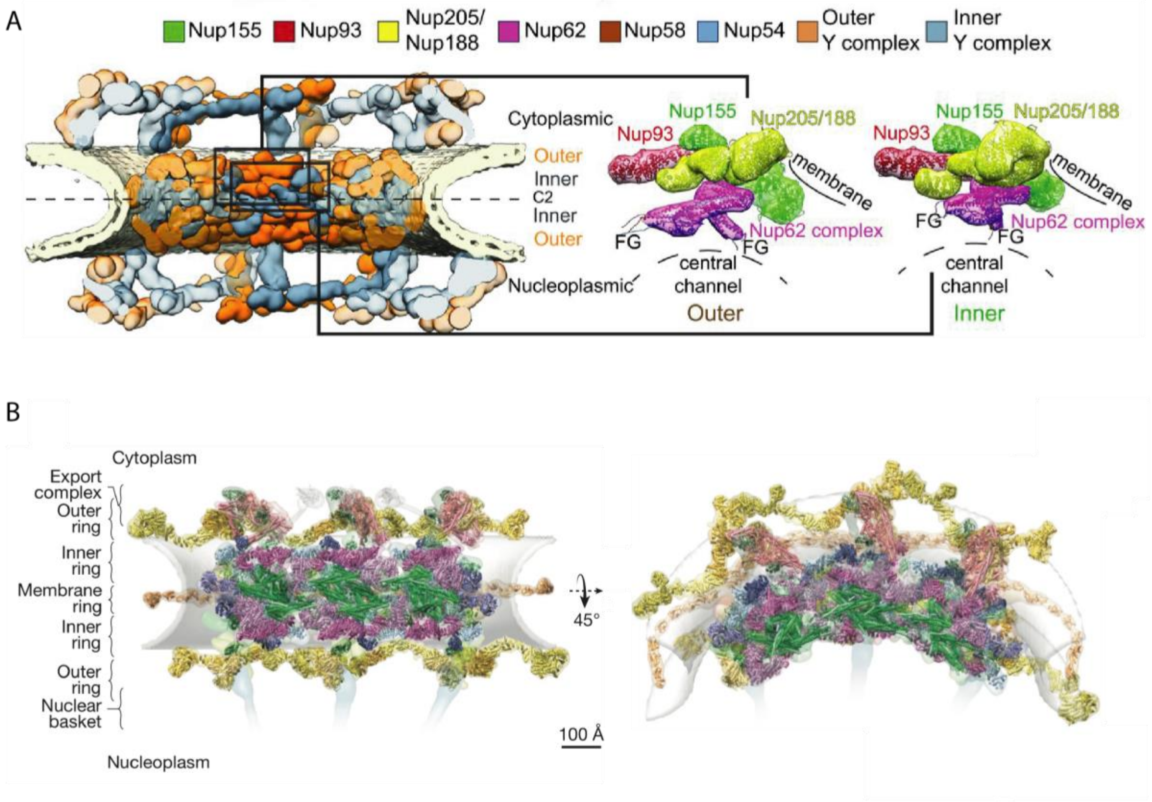

FIGURE 1-13. Current models of the scaffold of the NPC. A) Complete structure of the human NPC and its components shown in side-view. Inner (gray) and outer (orange) copies of the Y complex (top and bottom) and the inner-ring (middle) are shown in comparison. The configurations of the outer and inner copies of the inner-ring conformation are shown enlarged on the right. FG repeat domains can readily reach out into the central channel (adapted from Kosinski, 2016). **B)** Complete structure of the yeast NPC and its components shown in different orientations. Both outer and inner-ring run continuously between the scaffold of the NPC (adapted from von Kim, 2018). Abbreviations: NTD, N-terminal domain; F, phenylalanine; G, glycine.

The latest study carried by the Rout and Sali groups, reconstructed a 3D map of the entire yeast Scaffold of the NPC (Kim et al., 2018) (Fig1-13 B). Some novel features appear in this tomographic reconstruction as the organization of the transport machinery, which confirms the existence of a previously reported large central transporter with two high-density ‘lobes’ connected by a narrower ‘waist’ of lower density (Akey and Goldfarb, 1989). These densities suggest how the distribution of FG repeats could be positioned within the transport channel of the NPC. In addition, this study also highlights the differences and similarities between yeast and human

NPCs. One example of a difference between the scaffolds of the yeast and human pores, is that the yeast scaffold encompasses 16 copies of the outer-ring and inner-ring components instead of the 32 shown in human. However the overall architecture of the yeast and human scaffold retain gross structural similarities and allows the drawing of equal conclusions as to how the different subcomplexes are accommodated within the pore.

Finally, the Beck group has expanded the structural characterization of the NPC to other eukaryotic kingdoms, by investigating and reconstructing the symmetric core of the algal NPC (Mosalaganti et al., 2018). This study revealed unexpected differences in architecture and oligomerization states between the algal and human NPC, providing novel evidence of the structural variation of the NPC between species.

1.2.3 Transmembrane nucleoporins

Transmembrane (TM) Nups anchor the scaffold of the NPC to the NE. In yeast, the TM module consists of four membrane binding proteins: Ndc1, Pom152, Pom35 and Pom33 (Chadrin et al., 2010; Aitchison and Rout, 2012). Ndc1 is the only TM Nup universally conserved in eukaryotes (Mansfeld et al., 2006; Stavru et al., 2006) and together with Pom121 and gp210 compose the vertebrate set of membrane-spanning Nups. TM Nups are constituted by a varying number of TM α-helices with diverse topology. TM α-helices are the key structural component that enables TM Nups to bind to the pore membrane.

The yeast Pom152 contains a cadherin fold (Rout et al., 2000b) that might help stabilize the curvature of the pore membrane, by bridging the interaction of the INM with the ONM at the perinuclear space (Devos et al., 2006; Wheelock and Johnson, 2003). The homolog of the yeast pom152, the vertebrate gp210, in addition to its anchoring capacities, has an essential role during NPC disassembly and NE breakdown (reviewed in Grossman et al., 2012). Phosphorylation of gp210 is an early step during NE breakdown that guides lamin disassembly (Galy et al., 2008).

The TM Nup Ndc1 is essential for proper NPC assembly and is also required for the targeting of ALADIN to the NPC (Yamazumi et al., 2009). The interaction network of Ndc1 has been well characterized in yeast. The cytosolic domain of Ndc1 establishes pairwise interactions with Pom34 and Pom152, suggesting the coexistence of two different subcomplexes. However, the recruitment of each of these components to the NPC occurs independently, as silencing of one TM Nup does not affect the recruitment of others (Onischenko et al., 2009).

Finally, in vertebrates, Pom121 plays a crucial role in anchoring the NPC to the pore membrane and is indispensable for both mitotic and interphase NPC assembly (Shaulov et al., 2011). The N-terminal cytosolic domain of Pom121 directly binds to the β-propeller regions of Nup155 and Nup160, creating an interface between the NPC scaffold and the pore membrane (Mitchell et al., 2010). During interphase NPC assembly, Pom121 accumulates at the assembly site prior to scaffold Nups, suggesting an important function during interphase assembly initiation (Doucet and Hetzer, 2010; Dultz and Ellenberg, 2010).

1.2.4 Barrier nucleoporins

Barrier Nups create the selective gate that controls all nucleocytoplasmic transport through the NPC. Barrier Nups contain multiple FG-repeats with a typical spacing of about 20 amino acids, creating FG stretches and thus are termed FG Nups (reviewed in (Lemke, 2016)). The long stretches of FG-repeats form intrinsically disordered regions (Denning et al., 2003), and comprise one-third of the pore volume; extending all the way from the cytoplasm to the nucleoplasm. Strikingly, phylogenetic analysis identified only limited conservation between the FG-repeat regions (Ando et al., 2013). In addition, the regions separating the FG repeats are lacking conservation features as well, but are largely hydrophilic and contain multiple serine residues in tandem. FG Nups have been shown to provide interaction sites for transport receptors to facilitate transport of soluble cargo proteins (Frey and Görlich, 2007; Isgro and Schulten, 2007a, 2007b). These binding sites create low-affinity but high-specificity interactions with transport receptors (Schwoebel et al., 1998; Strawn et al., 2004). Moreover, the crystal structure of the transport receptor importin β reveals interaction with five FG domains. Mutation of importin β' interaction sites reduced nuclear protein import and thus provides direct evidence of the functional significance of these interactions (Bayliss et al., 2000).

In yeast, barrier nucleoporins are composed of Nsp1, Nup57 and Nup49 (Grandi et al., 1993, 1995a; Suntharalingam and Wente, 2003), while in vertebrates these are Nup62, Nup54 and Nup58 (Buss and Stewart, 1995; Grandi et al., 1997; Hu et al., 1996; Hülsmann et al., 2012).

Some barrier Nups can exist in different stable subcomplexes and be present at different positions within the NPC channel. For example, the yeast Nsp1/vertebrate Nup62 nucleoporin forms a stable trimeric subcomplex with the yeast Nup57-Nup49/vertebrate Nup54-Nup58 barrier Nups and is a crucial component of the transport machinery (Chug et al., 2015). This subcomplex interacts with the inner-ring of the NPC via the yeast Nic96/vertebrate Nup96 subcomplex (Grandi et al., 1995b; Schrader et al., 2008; Stuwe et al., 2015b). In addition, this Nup forms a stable subcomplex together with the yeast Nup82/vertebrate Nup88 (Bailer et al., 2001; Grandi et al., 1995a) and yeast Nup159/vertebrate Nup214 at the cytoplasmic face of the pore (Alber et al., 2007a; Belgareh et al., 1998).

The yeast Nsp1/vertebrate Nup62 subcomplex is a conserved stable assembly of three barrier Nups: the yeast Nsp1-Nup57-Nup49 and vertebrate Nup62-Nup54-Nup58 (Chug et al., 2015). All components share a similar structural organization, containing an ordered region of around 150-200 residues that are predicted to form 3-4 α-helical regions surrounded by stretches of FG repeats (Devos et al., 2006; Hu et al., 1996; Sharma et al., 2015). The members of this subcomplex interact with each other through their conserved coiled-coil domains (Ulrich et al., 2014).

The yeast Nsp1/vertebrate Nup62 subcomplex is positioned symmetrically at the central channel of the NPC and is responsible for the formation of the permeability barrier. The subcomplex is attached to the inner-ring of the scaffold of the pore by interacting with the N-terminal domain of the yeast Nic96/vertebrate Nup93 (Grandi et al., 1995b), and is required for proper protein transport. Based on this evidence, a model has been proposed for the ultrastructural arrangement of the yeast Nsp1/vertebrate Nup62 subcomplex, where the yeast Nic96/vertebrate Nup93 forms a T-shaped conformation together with the structured domain of yeast Nsp1/vertebrate Nup62 subcomplex, also called the channel nucleoporin heterodimer, and extrudes the FG-repeat domains towards the central channel (see section 1.2.2.2) (Lin et al., 2016; Schrader et al., 2008).

The developments in recombinant protein production and reconstitution of the yeast Nsp1/vertebrate Nup62 subcomplex provided new hypothesis as to how the subcomplex could be organized within the transport channel of the pore. The reconstitution of the yeast Nsp1 subcomplex *in vitro*, revealed a 150kDa subcomplex with a 1:1:1 stoichiometry (Schlaich et al., 1997). Schlaich and colleagues show that the yeast Nup57 has the role of the organizing seed, as Nup49 and Nsp1 independently bind to it to form the subcomplex. In addition, they also show that Nsp1 specifically interacts through two-heptad repeat regions of its C-terminal domain.

Originally, the *in vitro* reconstitution of the vertebrate Nup62 subcomplex revealed a ring-like structure with a diameter of ~15nm that resembles the central channel of the pore (Guan et al., 1995). More recent structural studies have identified that the reconstituted vertebrate subcomplex has a dynamic nature and is likely to undergo constant structural rearrangements (Melčák et al., 2007; Solmaz et al., 2011, 2013). The Melčák and Blobel group determined the crystal structures of the Nup54-Nup58 and Nup54-Nup62 components and found that the Nup54-Nup58 heterodimer forms a flexible ring that can undergo rearrangements of about 20-40nm. In addition, the Nup54-Nup62 heterodimer projects alternatively up and down from the midplane ring. This group proposes an alternative model where the described rings formed by the Nup62 subcomplex can dilate and constrict the nulcear pore channel and have named this configuration the “ring cycle” model (Sharma et al., 2015; Solmaz et al., 2013).

1.2.5 The cytoplasmic filaments

A set of different Nups are localized exclusively at the cytoplasmic face of the NPC and are referred to as the cytoplasmic filaments. These elongated filaments are anchored disordered polypeptides that provide docking sites for transport receptors and thus play an important role in nucleocytoplasmic transport and are essential for RNA export. In yeast, the cytoplasmic filaments are mainly composed of the FG-Nups Nup82, Nup159 and barrier Nup Nsp1. In addition the cytoplasmic filaments can interact with the FG-Nups Nup42, Nup145N, Nup116 and Nup100 at the cytoplasmic side (Fernandez-Martinez et al., 2016). In vertebrates, the cytoplasmic filaments are mainly composed of Nup88, Nup214 and Nup358/RanBP2 and in addition can interact with the FG-Nups Nup98 and Nup62 at the cytoplasmic side as well (Hoelz et al., 2011b) (Fig.1-6).

The yeast cytoplasmic filaments are mainly composed of Nup82 and Nup159 and provide docking sites for mRNA export factors. Given that mRNA export factors are stably attached to the cytoplasmic filaments, they can be regarded as part of the NPC (Hoelz et al., 2011a). The structure of Nup159 exhibits an uncommon asymmetric seven-bladed β-propeller at its N-terminal domain (Weirich et al., 2004). While the structure of the vertebrate homolog Nup214 preserves the asymmetric core, it contains in addition extended loops and a 30-residue C-terminal segment that folds back and binds into the β-propeller’s bottom region (Napetschnig et al., 2007).

This N-terminal domain is involved in RNA export, as in yeast it has been shown to interact with the RNA helicase Dbp5 that is further regulated by the binding of Gle1 (Montpetit et al., 2011). In yeast, Gle1 can also recruit the FG-Nup Nup42 and together become part of the yeast cytoplasmic filaments (Strahm et al., 1999). In vertebrates, Nup214 has been shown to tightly interact with the nuclear export receptor CRM1 via its FG-repeat fragments (Port et al., 2015), providing further evidence of its involvement with the mRNA export machinery.

The yeast Nup159-Nup82 heterodimer can further recruit the FG-Nup Nup116 or another of its homologs Nup100 and Nup145N (Bailer et al., 2000; Stuwe et al., 2012; Yoshida et al., 2011). These Nups have a similar architecture and share a specific type of FG-domain; the repetitive tetrapeptide “GLFG” repeat motif. In addition, Nup100 and Nup116 also possess a Gle2 binding sequence (GLEBS) for the mRNA export factor Gle2 to attach (Bailer et al., 1998) and in this way participate in the mRNA export mechanism. Finally, the latter FG-Nups also interact with inner-ring Nup192 and thus have been suggested to help anchoring the cytoplasmic filaments to the scaffold of the pore (Fischer et al., 2015; Stuwe et al., 2015b).

The crystallization of the yeast cytoplasmic nucleoporins has been challenging due to their flexibility and intrinsically disordered domains. However, recent work form the Rout and Sali lab solved the structure of the yeast trimeric complex composed of the two main cytoplasmic filament Nups Nup82 and Nup159, bound to the multipositional barrier Nup Nsp1 (Fernandez-Martinez et al., 2016) by using integrative modeling approaches (Alber et al., 2007b). The integrative structural analysis determined that the trimeric subcomplex is anchored to the cytoplasmic face of the pore via interactions with the Y-shaped-subcomplex. In addition, the combined structural and functional mapping of the trimeric subcomplex suggests that the yeast mRNA export and remodeling machinery is surprisingly positioned over the NPC’s central channel rather than in the distal filaments per se as previously thought.

The vertebrate cytoplasmic filaments contain a large additional nucleoporin termed Nup358/RanBP2, which is specific to higher eukaryotes and has no homolog in yeast. Nup358/RanBP2 attaches to the scaffold of the NPC with its N-terminal domains and serves as binding site for the transport factors Ran and RanGAP1 (Matunis et al., 1996; Yaseent and Blobel, 1999). The Blobel group provided evidence of the important role that these binding events have for the assembly and disassembly of transport receptors during transport. In addition, this Nup also has SUMO ligase activity and together with the coenzyme factor Ubc9 incorporates SUMO modifiers to specific targets at the cytoplasmic side of the NPC (Reverter and Lima, 2005).

The cytoplasmic vertebrate nucleoporin Nup358/RanBP2 contains four 150-residue domains that contribute to the binding of Ran. Structural analysis of the complex of Nup358 bound to Ran and the non-hydrolisable version of GTP, revealed that the GTPase domain of Ran and its C-terminal region wraps and interacts with the pleckstrin-homology domain of Nup358/RanBP2 (Vetter et al., 1999). This molecular embrace mechanism has been suggested to trigger the dissociation of Ran from transport factors and facilitates GTP hydrolysis needed for transportation (see section 1.1.4).

The crystal structures of the N- and C-terminal domains of Nup358/RanBP2 have been solved by the Hoelz Lab (Kassube et al., 2012; Lin et al., 2013) (Fig.1-14 A-B). The N-terminal domain contains an α-helical domain that harbors three central tetratricopeptide repeats (TPRs) in a non-canonical conformation (lacking the characteristic peptide-binding groove). Kassube and colleagues demonstrated that the N-terminal domain of Nup358/RanBP2 has the capability of binding to single-stranded RNA in solution and proposed a role for it in the remodeling of mRNPs (Kassube et al., 2012) (Fig. 1-14 B). The C-terminal domain contains a cyclophilin-like fold with an uncharacteristic active site. Lin and colleagues showed that this active site cavity mediates a weak association with the human immunodeficiency virus-1 capsid protein *in vitro*, supporting a role for this domain in viral infection (Lin et al., 2013) (Fig. 1-14 B).

More recent structural studies performed by the Beck lab have identified that Nup358/RanBP2 has an unanticipated role in the oligomerization of the Y-shape-subcomplexes of the cytoplasmic ring of the pore scaffold (von Appen and Beck, 2015). In this study, von Appen and collegues demonstate that the silencing of Nup358/RanBP2 abolishes one of the two double rings that composes the cytoplasmic outer-ring of the pore.

Finally, in vertebrates, the function that the yeast Nup116, Nup100 and Nup145N provide, are carried out by a single FG-Nup called Nup98. The cytoplasmic Nup98 contains a GLEBS motif that can interact with the vertebrate homolog of Gle2, the Ribonucleic acid export 1 (Rae1) (Bailer et al., 1998; Ren et al., 2010). The vertebrate Nup98 can localize symmetrically to both sides of the NPC and associates both with the cytoplasmic Nup88 and with the Y-shaped-subcomplex member Nup96 through its C-terminal domain (Griffis, 2003). Given that the same terminal domain is used for both interactions, Nup88 and Nup96 compete for Nup98 binding, which results in a distribution where Nup98 is present mainly in a complex with Nup88 on the cytoplasmic side and with the Y-shape-subcomplex mainly in the nucleoplasmic side of the pore (Ratner et al., 2007).

1.2.6 The nuclear basket

The nuclear basket is one of the least characterized structural regions of the NPC and is thought to be composed out of eight elongated filaments that converge into a distal ring in the nucleoplasmic side of the pore (Goldberg and Allen, 1992). The Nups that form part of the nuclear basket typically possess FG-repeats, α-helical domains and combined α/β-regions (Cook et al., 2007). In yeast, the nuclear basket is composed of three FG-Nups: Nup1, Nup2, Nup60, and two export factors: Mlp1 and Mlp2 (Rout et al., 2000b). While in vertebrates only two FG-Nups: Nup50 (Nup2 homolog) and Nup153 (Nup60 homolog), and a single export factor called Tpr (Mlp1-2 homolog) (Grossman et al., 2012) (Fig.1-6).

The components of the nuclear basket are highly dynamic and are thought to exchange continuously, as opposed to scaffold Nups (D’Angelo et al., 2009; Rabut et al., 2004). The nuclear basket has been shown to interact with components of the nuclear lamina, for example in vertebrates, Nup153 interacts specifically with lamin B3 (Smythe et al., 2000), and has been suggested to play a role in the assembly of the lamina and NE. Finally, the nuclear basket also interacts with SUMO-modifying agents though Nup153’s FG-domains (Chow et al., 2012).

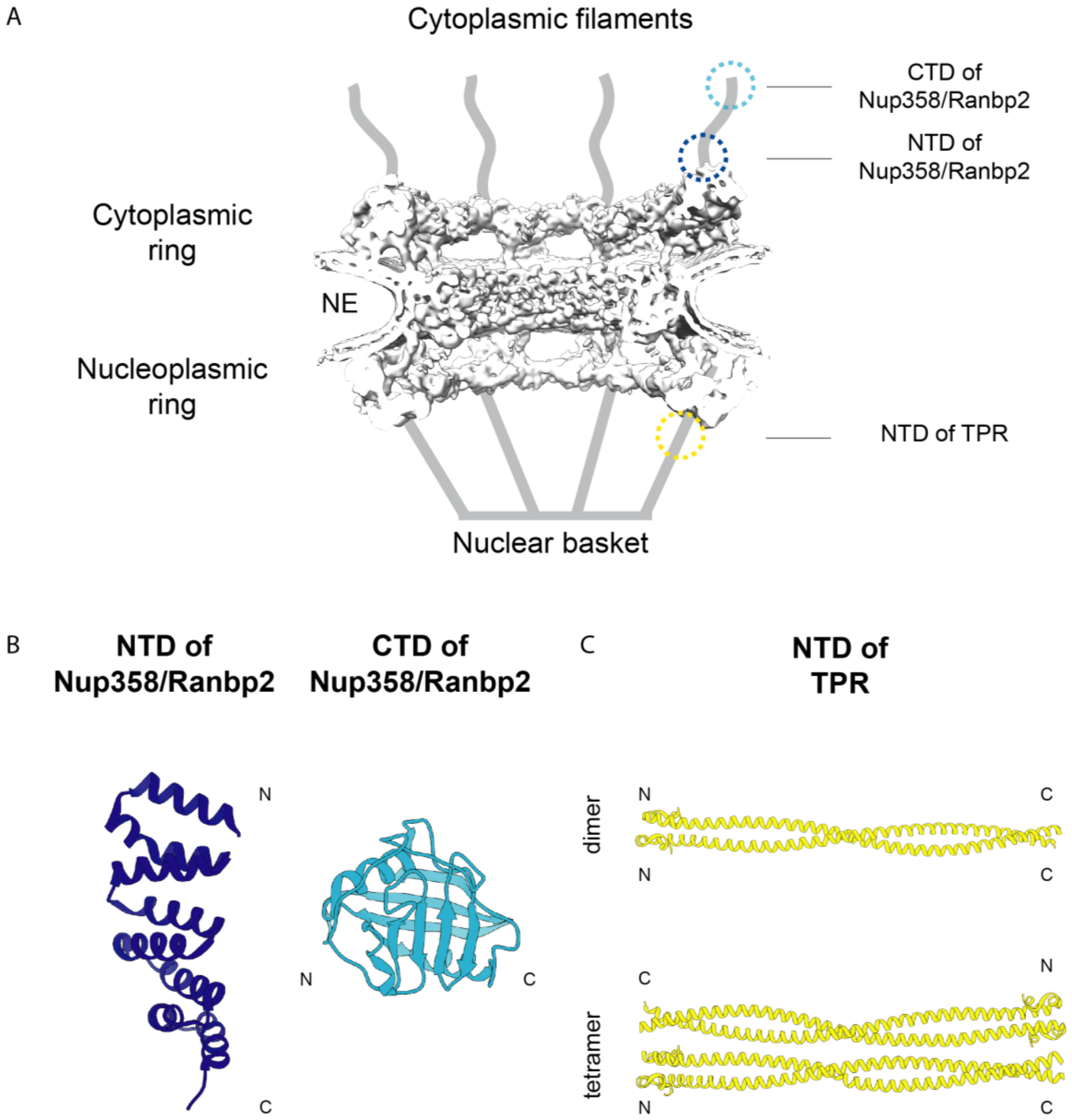

FIGURE 1-14. Available crystal structures of Nup358/RanBP2 and TPR. A) Schematic representation of the NPC containing a side-view cryo-ET reconstruction of the scaffold region (adapted from von Appen, 2015). The predicted positions of the N-terminal domain (NTD) and C-terminal domain (CTD) of Nup358/RanBP2 and of the N-terminal domain (NTD) of TPR are illustrated (dashed line circles). **B)** The crystal structures of the NTD of Nup358/RanBP2 (PDB: 4GA0; left) and of the CTD of Nup358/RanBP2 (PDB: 4I9Y; right) are shown (adapted from Kassube, 2012 and Lin, 2013). **C)** The crystal structures of the NTD of TPR (2–142) in a parallel coiled-coil dimer arrangement (PDB:5TVB; upper panel) and the further oligomerized antiparallel tetramerc arrangement (PDB:5TVB; lower panel) (adapted from Pal, 2017). Abbreviation: N: N-terminus and C: C-terminus.

The yeast Nup2/vertebrate Nup50 is located at the nuclear side of the central gated channel, is involved in transport receptor recycling and cargo release during nuclear import that is mediated by importin α/β (Matsuura et al., 2003). Further studies also demonstrate its role during the bidirectional transport of importin α (Solsbacher et al., 2000).

The vertebrate homolog of Mlp1-2, Tpr, is thought to be the main architectural component that forms the nuclear basket, while Nup153 has been suggested to link the nuclear basket to the scaffold of the pore (Krull et al., 2004). In addition, Nup153 has been linked to the formation of the transport barrier on the nucleoplasmic side of the pore, given their high content of FG-domains.

Tpr is a 270 kDa protein that constitutes the major mass of the nuclear basket. This Nup contains a long coiled-coil N-terminal region and a highly acidic and post-translationally modified C-terminal domain (Nakano et al., 2010; Rajanala et al., 2014). The crystal structure of the first 142 residues (out of ~1600 amino acids) of the long Tpr protein shows a continuous α-helical stretch that folds into a tetramer (Pal et al., 2017) (Fig.1-14 A, C). These results provide evidence of the ability of TPR’s N-terminus to dimerize *in vitro*, however, if this conformation has biological relevance remains unclear. To understand the organization of the nuclear basket further, it will be important to have an ultrastructural understanding of its architecture and link it to the described functions. Given the large size and flexibility of the nuclear basket components, it will remain a challenge to resolve crystal structures or EM maps of its conformations.

In summary, the recent integration of high-resolution technologies has characterized the symmetric core of the NPC in human (von Appen et al., 2015; Bui et al., 2013; Kosinski et al., 2016), yeast (Kim et al., 2018) and algal cells (Mosalaganti et al., 2018) in great detail. While it has been widely accepted that the structure and function of the NPC is highly conserved between species, substantial differences in the stoichiometry and architecture (Kim et al., 2018; Mosalaganti et al., 2018; Rajoo et al., 2018) have recently been discovered, suggesting that the plasticity of the NPC structure has functional and evolutionary significance. To further investigate both the inherent flexibility of the symmetric core and of the still uncharacterized unstructured asymmetric regions of the pore, new technologies that can capture the variability and dynamics of this essential machine are needed. The advances in fluorescent light microscopy, which can circumvent the diffraction limit of light, could be key technologies for obtaining more information about the structural plasticity and the related functions of the NPC.

1.3 Super-resolution microscopy

Light microscopy has been a fundamental tool for the comprehension and advancement of biological sciences. Since the 17th century, scientists have made breakthrough discoveries with help of optical microscopy, among these, Robert Hooke (1638-1703) who coined the biological meaning of “cell” and Antoni van Leeuwenhoek (1632-1723) who first described the existence of microorganisms (Gest, 2004). While the technological advances have produced more sophisticated microscopes throughout time, they all share the same fundamental limitation; the maximum achievable resolution is limited by the diffraction of light. Before the recent development of super-resolution microscopy circumvented, for the first time, this long-standing barrier, it was assumed that the resolution of optical microscopes was fundamentally limited by the diffraction of light, which was described and formulated by Verdet, Abbe and Rayleigh (Abbe, 1873; Rayleigh, 1896; Verdet, 1869). Abbe’s criterion of resolution states that the light of wavelength λ, focused by an objective of numerical aperture of $n \cdot \sin \alpha < 1$ (where n is the refractive index of the medium and α is half of the collection angle of the objective), cannot distinguish objects closer than the distance $d = \lambda/(2n \sin \alpha)$, given that diffraction fuses each individual image into a single blur spot (Hell, 2009). In practice, this criterion states that light cannot be focused more sharply than to a spot of approximately 200 nm in diameter and 700 nm in depth and thus cannot distinguish between two molecules that are closer than 200 nm from each other in the lateral plane and 700 nm in the axial plane. Given that most cellular processes take place at the molecular level at nanometer-scales, many fundamental molecular processes and cellular architectures have remained beyond the reach of conventional light microscopy. Over the last decades, several new imaging technologies have been developed that circumvent the diffraction limit of light and are collectively called super-resolution microscopy (SRM) techniques. These technologies are enabling the study of diverse cellular processes and structures at the nanometer-scale (Sydor et al., 2015).

The common denominator between many of the different SRM techniques is that individual fluorophores can be manipulated into different photo-physical states, and thus can be visualized independently. The differences between these technologies rely on how one manipulates the photo-physical states that fluorophores possess. In the following sections, I will describe three main super-resolution microscopy techniques, which are Structured illumination microscopy, Stimulated emission depletion microscopy and Single-molecule localization microscopy.

1.3.1 Structured illumination microscopy

Structured illumination microscopy (SIM) is based on illumination of the sample with striped patterns of light (Gustafsson, 2000). This pattern is usually an interference pattern created by the illumination of two opposing beams. When illuminating the fine structures of the sample with the coarse interference patterns, the resulting fluorescence image contains information about the sample structure convolved with the excitation pattern and point spread function of the microscope. In addition, the pattern interferes with the high spatial frequency features of the sample and results in an additional pattern called Moiré fringes. With this additional pattern information, structures below the diffraction limit of light are introduced into the diffraction-limited passband and encoded in the image (Heintzmann and Gustafsson, 2009). However, it is not sufficient to have a single image to extract the high spatial frequency information from the convolved image. Multiple images from phase-shifted excitation patterns have to be recorded in order to sample the desired field of view and recover the information encoded in the Moiré fringes. After processing all the phase-shifted images with specialized algorithms, the high-frequency information can be extracted to produce a reconstructed image with a lateral and axial resolution that is approximately twofold better than the diffraction-limited image both in 2D and 3D (Fig.1-15 A) (Gustafsson et al., 2008).

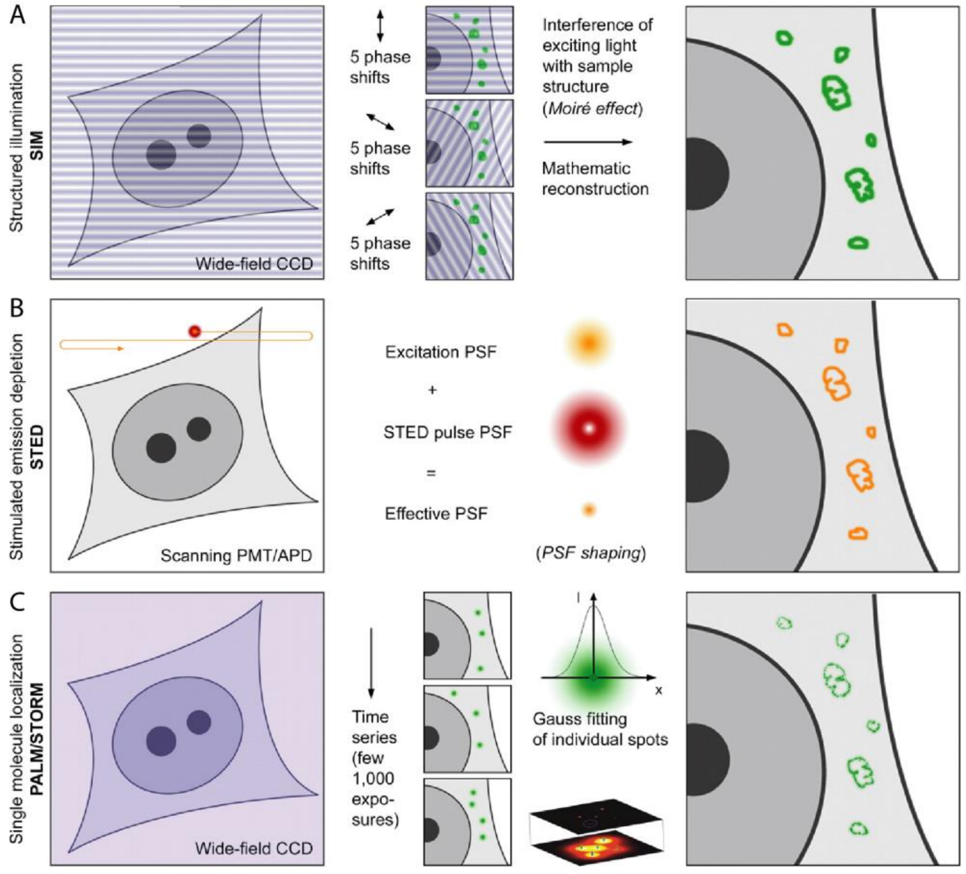

FIGURE 1-15. Super-resolution microscopy. A) In SIM the sample is excited by a nonuniform wide-field illumination. This illumination is combined with the sample sub-diffraction information and generates moiré fringes. A mathematical reconstruction allows the reconstruction of high-resolution images with doubled resolution in xy compared with wide-field resolution. **B)** In STED microscopy the sample is scanned with two overlapping laser beams. The first laser excites the fluorophores and the second longer wavelength laser drives the fluorophores back to the dark state by the process of stimulated emission, generating a donut-shaped energy distribution, from which only a small volume of light can be emitted. Here the PSF is shaped to a volume smaller than the diffraction limit. **C)** In Single molecule localization microscopy only a low number of fluorophores are in the *on* state. These molecules are detected as diffraction-limited spots and their lateral position is determined by gaussian fitting. **A)-C)** (adapted from Schermelleh, 2011).

An advantage of this technology over other SRM techniques is that it does not depend on the photo-physics of the fluorophores and thus standard labeling technologies for antibodies, fluorescent proteins and organic dyes can be used to stain the samples. Consequently, multicolor imaging can also easily be implemented with SIM. In addition, the speed of SIM relies directly on how fast the striped excitation patterns can be generated and uses a comparatively low light dosage, making this technology compatible with live cell imaging (Shao et al., 2011).

To achieve a gain beyond the two-fold resolution improvement with SIM, additional implementations have been suggested. A strategy called saturated structured illumination microscopy (SSIM) uses the nonlinear response after illumination with the striped pattern of light (Gustafsson, 2005). This method allowed an improvement of resolution of about four times, however uses a high light dose and can rapidly bleach conventional fluorophores and is not compatible with live cell imaging. Other forms of nonlinear response have been published, including the use of dyes with photo-physical properties in non-linear SIM (NL-SIM) that also allows a comparable improvement in resolution to SSIM, but with a lower light dosage needed (Rego et al., 2012).

Finally, the most recent implementations of SIM combined with ultra-thin lattice lightsheet microscopy (i.e. Bessel-beam) (Chen et al., 2014) and additionally with NL-SIM with TIRF objectives (Li et al., 2015) have majorly increased the capabilities and applications of SIM. In these methods, the generated light sheet compensates for some of the sample damage due to high light dosages and provides an improved resolution compared to standard SIM methods.

1.3.2 Stimulated emission depletion microscopy

Stimulated emission depletion microscopy (STED) is a method that uses the photo-physical properties of fluorophores in order to confine the excitation volume below the diffraction limit (Hell and Wichmann, 1994; Klar and Hell, 1999; Klar et al., 2000).

STED makes use of the different states in which fluorophores can exist; the fluorescent (*on*) state and the dark (*off*) state, connected by a transition switch between the fluorescent singlet state S_1 and the ground state S_0 (Hell, 2003). During excitation, the transition switch ($S_0 \rightarrow S_1$) makes the dye fluorescent, however the STED beam induces the opposite transition ($S_1 \rightarrow S_0$) to turn the dye off. The STED beam has a doughnut shape with zero intensity at the very center that is generated by a phase plate. In this way, the STED beam induces a doughnut shape *off* state transition and an *on* state transition at the zero intensity center; creating a sub-diffraction limited excitation beam (Fig.1-15 B). Importantly, the switch to the *off* state in STED has to be reversible and protects the fluorophores from photo-damage. In addition, the effective excited volume gets smaller with higher beam intensity, which allows for fine-tuning of the desired resolution. The typical lateral resolution that one can achieve with STED in biological samples is around 20-70 nm (Sydor et al., 2015). With this technique, two objects that would normally be blurred to a single spot (see section 1.3) can be resolved as individual objects by scanning through the sample and switching them independently *on* and *off*.

STED can also be extended to the third dimension by creating a STED beam with a hollow sphere (Hein et al., 2008). In this work, the Hell lab demonstrated that 3D STED could improve the axial resolution by a factor of three compared to conventional microscopy. However, given the high light dosage needed to transition to the *off* state STED, photobleaching can occur and special photo-stable dyes need to be used.

Finally, a more recent extension of STED has been created, that can achieve accurate performance with lower light intensities and is called Reversible saturable optical fluorescence transitions (RESOLFT) (Hofmann et al., 2005). This technique makes use of the *cis-trans* isomerization of reversible photoswitchable proteins and a light dose eight times lower than conventional STED. RESOLFT achieves a comparable lateral resolution of around 50 nm and due to the low light dosage and fast recording developments is much more compatible with live cell imaging (Chmyrov et al., 2013), however good performance suitable dyes that can be used in living cells are still scarce.

1.3.3 Single molecule localization microscopy

Single molecule localization microscopy (SMLM) also uses the photo-physical properties of fluorophores to resolve diffraction-limited objects, however, in this method the transition switches between *off* and *on* states (see section 1.3.2) are propagated stochastically through the whole field of view. Moreover, SMLM relies on the ability to precisely localize the individual stochastically blinking fluorophores through the entire field of view and from thousands of such scarcely populated blinking images generate the final sub-diffraction resolution image. Three groups independently developed the main principles underlying SMLM: (i) Eric Betzig's group developed PALM (Betzig et al., 2006), (ii) Xiaowei Zhuang's group STORM (Rust et al., 2006) and (iii) Michael Mason's group fPALM (Hess et al., 2006).

In SMLM all fluorophores are stochastically switching between the *on* and the *off* states, so only a small subset of molecules will be observed at the same time. To sample all of the molecules present in the image, several thousands of images have to be recorded until each molecule has blinked and the maximal photon yield is exhausted. Each of the fluorophores is detected as a diffraction-limited spot, as in conventional microscopy. However, given the *a priori* knowledge that the visualized diffraction-limited spot comes from an individual fluorophore source and not the blurred image of multiple tightly spaced fluorophores (see section 1.3), the exact position of the single fluorophore can be assigned to the center of the signal with much higher precision than the diffraction-limited resolution. After acquisition, the position or localization of each individual fluorophore can be determined by fitting a Point spread function (PSF) model to the fluorescent signal and the coordinates of individual fluorophore positions are combined to reconstruct the super-resolved image (Fig.1-15 C).

SMLM can be performed with a variety of fluorophores. Initially, the *on-off* transition needed for SMLM was demonstrated by using photoactivatable proteins (e.g. paGFP) as in PALM (Betzig et al., 2006) and fPALM (Hess et al., 2006). Subsequently, this transition was also obtained with photoswitchable dye pairs (e.g. Cy3-Cy5) as in STORM (Rust et al., 2006) and then with the direct use of individual photoswitchable dyes (e.g. Cy5 and Alexa 647) (Heilemann et al., 2008) as in and GSDIM (Fölling et al., 2008). Lately, multiple reversible photoswitchable and irreversible photoconvertible proteins are being developed (reviewed in (Zhou and Lin, 2013)), which is rapidly expanding the repertoire of fluorophores suitable for SMLM in biological samples.

1.3.3.1 Resolution in SMLM

SMLM images have been reported to reach a lateral resolution of around 10-30 nm (Sydor et al., 2015), which is superior to the resolution that can be obtained with STED microscopy. It is however difficult to calculate the real resolution of SMLM images, as there are three main factors influencing the resolution of the super-resolved images; the precision of the computationally determined positions, the labeling density of the sample and the stability of the imaging system (Patterson et al., 2010).

First, the uncertainty of the position estimation is termed localization precision$_{x,y}$, and can be derived by the Gaussian approximation. Here, the best possible localization precision is given by the following equation:

$$\sigma_{xy} \geq \frac{s}{\sqrt{N}}$$

where σ_{xy} is the lateral localization precision, *s* is the width of the PSF and *N* the number of photons/molecule (Chacko et al., 2013). In practice, this means that brighter fluorophores (i.e. higher number of emitted photons) can be localized more precisely than dim ones, as well as in-focus molecules (i.e smaller PSF size) can be localized more precisely than out-of-focus ones.

Secondly, the density of localizations follows the Nyquist criterion, where in order to resolve two objects spaced at a distance *d*, the space has to be sampled at least in $\frac{d}{2}$ intervals. For SMLM this means that for a desired resolution, for example of 10nm, each dye molecule should be spaced no more than 5 nm apart from each other. Due to this, a high labeling density is essential to obtain the best possible resolution with SMLM.

Finally, the last factor affecting resolution is the sample drift that is produced by mechanical instabilities of the imaging system in the nanometer range over long acquisition times. In order to reduce the system drift, several hardware and software solutions have been implemented, including temperature-controlled chambers, focus-lock for axial stability during data acquisition, customized sample holders, etc. However, given the long acquisition time needed in SMLM, it is almost impossible to use hardware to fully stop the mechanical instabilities over such a long time frame. This is why, in addition to the hardware solutions mentioned above, SMLM images are also drift-corrected after acquisition. Multiple drift-correction algorithms have been developed; however, the most common approaches rely on using fiducial markers or the auto-correlation of the localizations over time (Bates et al., 2012; Huang et al., 2008).

1.3.3.2 3D SMLM

SMLM methods have been extended to also improve the estimation of the axial position fluorophores and are collectively called 3D SMLM techniques. 3D SMLM typically can achieve an axial resolution of about 10-75nm (Sydor et al., 2015). There are different ways to encode and extract with high precision the axial position of fluorophores. The most commonly used techniques rely on the shape of the PSF to extract the axial position of the fluorophore; either by introducing additional optical elements in the light path to change the shape of the PSF at different heights (e.g. astigmatic STORM (Huang et al., 2008), double helix PSF (Pavani et al., 2009)), or by imaging from two focal planes at the same time (biplane (Juette et al., 2008)). These methods share the advantage of being more accessible in use, however, their axial resolution is worse by at least a factor of 3 than their lateral resolution.

Alternative 3D SMLM methods have been developed, which can provide an isotropic resolution (i.e. similar lateral and axial resolution) and belong to the family of interferometric methods; iPALM (Shtengel et al., 2009) and 4Pi-SMLM (Aquino et al., 2011). These methods share the basic principle that the fluorescent photons are collected from two opposing objectives, travel through opposing detection legs and self-interfere at a beam splitter. Here, the difference in path lengths directly depends on the axial position of the fluorophore and by analyzing the detected interference pattern (i.e. constructive and destructive) from different phase delays, the precise axial position of fluorophores can be determined (Fig.1-16). Given that the interference pattern is periodic, the axial position of fluorophores can be only determined at half the wavelength of the emitted light (e.g. around a thickness of ~250nm), limiting the applicability of these methods to thin samples. Within the 4Pi-STORM modality, two different strategies have been developed to circumvent the periodicity restriction. The first strategy exploits the fact that the phase difference between opposite wavefronts varies more slowly at the outer parts when moving out-of focus, which encodes information of the axial position over a range larger than half the wavelength of the emitted light (Aquino et al., 2011). The second strategy relies on the axial sample scanning (W-4Pi-SMLM (Huang et al., 2016)), which extends the imaging capabilities to whole cells with a volumetric reconstruction of around 10 nm isotropically in 10 µm-thick samples. While the interferometric methods provide a much superior axial resolution to comparable 3D SMLM techniques, these methods are technically very demanding and due to this are not extensively used.

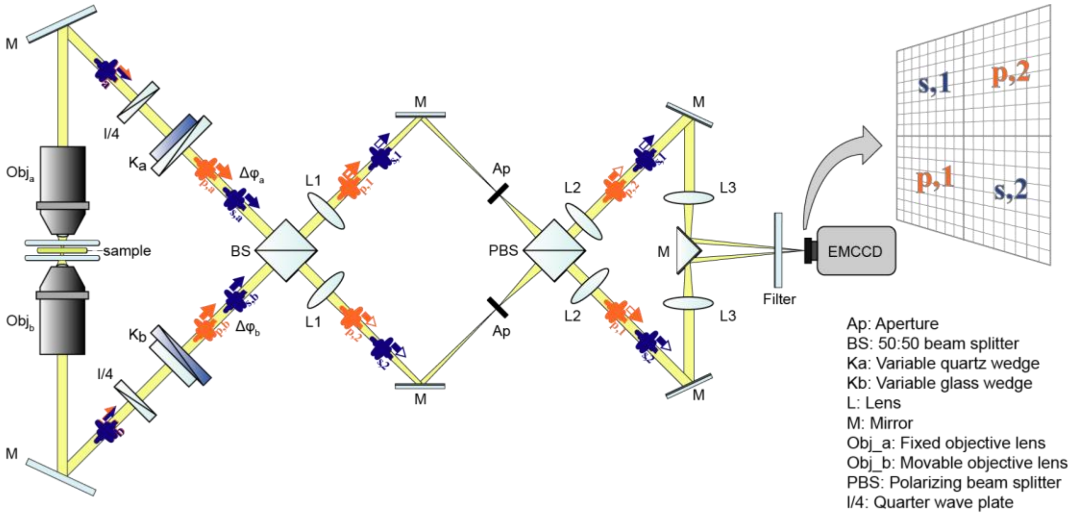

FIGURE 1-16. 4Pi-SMLM. The sample is sandwiched between coverslips and excited trough two opposing objectives. Light travels through opposite legs (a and b) of the 4Pi cavity, which consists of two dichroic mirrors, two quarter-wave plates (λ/4), two modified Babinet-Soleil compensators (Ka and Kb) and a neutral beam splitter (BS). Light is separated into s- and p-polarization states (sa, pa, sb and pb) and phase differences (Δϕa, Δϕb) are introduced. After self-interference at the beam splitter (PBS), four interference patterns s1, s2, p1, p2 are produced. The resulting image pairs p1 and s1, and p2 and s2 are separated by tilted mirrors to four detection channels and detected in individual quadrants of a single camera chip (adapted from Aquino, 2011)

Finally, a third conceptually distinct method has recently been developed, which obtains 3D information from surface-generated fluorescence (Bourg et al., 2015; Deschamps et al., 2014). Here, similar to TIRF microscopy, the emitters close to the glass coverslip contain an evanescent field. This near-field fluorescence, also called supercritical-angle fluorescence, is dependent on the emitter’s distance to the coverslip and thus can be used to estimate the axial position of the fluorophore. These techniques can obtain high axial resolution but are limited to a depth of only a few 100 nm.

In more practical terms, the selection of a particular 3D SMLM technique is guided by balancing the desired localization precision, the depth of the region of interest and the feasibility of the imaging system. For my doctoral work, it was critical to obtain high isotropic resolution information and given that my region of interest is constrained to thin regions (i.e. around 200nm), I decided to implement 4Pi-STORM microscopy and therefore will further discuss its implementations in Chapter 2.

1.3.3.3 Multi-color SMLM

Multi-color SMLM imaging requires the independent detection of differentially labeled molecules under study. Different strategies have been developed over the course of time to allow accurate and feasible multi-color SMLM acquisition. An initial approach uses two dyes with separate excitation and emission spectra, which are recorded either sequentially of simultaneously using different excitation and detection configurations of the imaging system (Bock et al., 2007; van de Linde et al., 2009). This approach is less complicated as it can be used with a broad selection of fluorophores, however, the final super-resolved images from the distinct colors have to be carefully registered after acquisition, as chromatic differences might be present. In addition, if the acquisition is performed sequentially, longer imaging time is required and larger effects from mechanical instabilities can be present.

Alternatively, the simultaneous acquisition of different fluorophores can be obtained by using the same excitation wavelength but detecting different emission spectra (Lampe et al., 2012; Testa et al., 2010). In this ratio-metric approach, the dye pairs have to be carefully selected to allow the described spectral overlap. Here, the sample is excited with a single laser and the emitted light separated into two detection paths by a dichroic mirror. The emission spectra of such similar fluorophores will partially overlap and each fluorophore will be visible in each detector with different intensities. Based on the ratio of the signal intensities in each detector, the color can be assigned to each specific fluorophore. This method provides the advantage of fast acquisition times and bypasses the shifts that can arise from wavelength-dependent differences. However, the selection of dyes is more restrictive and due to the inherent spectral overlap of the technique, a cross talk of around 10-20% can be expected in the resulting images.

A follow-up approach from the original STORM technique (Rust et al., 2006), coined the activator-reported approach, uses dye pairs, where one acts as an “activator” dye and the second as a photoswitchable “reporter” dye (Bates et al., 2007). In this approach the activator dye is excited with its appropriate wavelength and facilitates the photo-activation of the reporter dye, which is then detected through the indirect excitation of the activator dye. In addition, by using the same reporter dye in combinatorial pairing with different activator dyes, one can separate the different colors (i.e. differentially labeled molecules) through different excitation wavelengths but detect the same emission spectra of the reporter dye. The activator-reporter approach has been demonstrated to separate up to six colors and achieve a lateral resolution of around 20 nm (Bates et al., 2012). An advantage of this technique is the absence of chromatic aberrations, given that the same reporter dye is used for detecting different colors and no further registration steps are needed for image reconstruction. However, particular dye pairs are needed (e.g. demonstrated with Cyanine dyes and derivatives) at specific ratios and different excitation lasers have to be incorporated into the imaging system.

Finally, a recent multi-color approach has been demonstrated, which relies on the synchronous identification of the emission spectra and positions of individual PSFs in order to separate individual colors simultaneously (Zhang et al., 2015). This approach, called spectrally resolved STORM (SR-STORM) enables cross-talk-free imaging of up to four different dyes that are spaced 10 nm from each other in the emission spectra. An advantage of this approach is the feasibility of dye selection and throughput, while a disadvantage is the requirement for a dual-objective scheme (Xu et al., 2012) for decoupling the spatial and spectral information simultaneously.

Choosing the most suitable multi-color approach for SMLM is guided by the possibilities for modifications of the employed imaging system, the compatibility of the required probes and dyes with the biological sample, the degree of crosstalk that is permitted for interpretation and the labeling density of the sample that is required. For my doctoral studies, I have implemented both activator-reporter and ratio-metric approaches and therefore will discuss their characteristics and performance further in Chapter 2.

1.4 Structure determination by averaging

In the field of electron tomography (ET) low-resolution 3D volumes (i.e. tomograms) are reconstructed from 2D projection images of a tilt series from a biological sample. The macromolecular and organelle structures that are present in a large number of copies within tomograms can be further extracted, aligned and averaged to increase the signal-to-noise ratio and overall resolution of the underlying 3D structure (Briggs, 2013). This approach, called subtomogram averaging, has been widely used in the last two decades to determine the structure and spatial distribution of macromolecular assemblies' *in situ* using electron microscopy.

A small set of studies in the field of SRM have implemented some of the general principles underlying subtomogram averaging to improve the signal-to-noise ratio and overall precision of super-resolved images. These studies have demonstrated that the implementation of averaging combined with SRM is a powerful tool for high-resolution mapping of macromolecular assemblies *in situ*, as shown with the nuclear pore complex (Broeken et al., 2015; Szymborska et al., 2013), centrosomes (Burns et al., 2015) and viruses (Lelek et al., 2012). It is important to note however, that these studies mostly focused on 2D SRM and made use of averaging to obtain high-resolution information of the static regions of the molecular assemblies under study.

In the course of my doctoral work, I have expanded the implementation of subtomogram averaging combined with 3D SRM to gain insights not only into the static regions of molecular assemblies but also to map a more flexible and variable architecture captured with SRM. Because of this, I will present the main general principles of subtomogram averaging in the following section and will discuss the implementation of my work in Chapter 2.

1.4.1 General principles of subtomogram averaging

In subtomogram averaging the main workflow consists of iterative averaging and alignment steps to obtain a final averaged image with superior signal-to-noise ratio. Here all subtomograms are aligned to a reference through a cross-correlation based scoring function. Subsequently, the aligned subtomograms will be averaged to produce the next reference to which all subtomograms will be aligned again in an iterative process. The iteration of this process will continue until no further improvement in alignment is obtained (W. Wan, 2016).

In order to align the subtomograms, the reference is masked (constrains the volume to the region of interest) and rotated in different orientations at defined angles and compared to each filtered subtomogram (removes high-resolution noise) with cross-correlation functions (CC). After identifying the best orientation for alignment, all subtomograms are rotated accordingly and averaged to generate the subsequent reference (Figure 1-17).

1.4.2 Alignment by angular search

There are different algorithms that can be used for subtomogram alignment, however I will give a description of the concepts behind the alignment by angular search, given that this is the approach that I implemented throughout this study. Here, the rotational search space is defined by three Euler angles. During alignment, in each rotational step the similarity between the reference and individual particle will be calculated by CC in Fourier space. The peak of the resulting 3D CC volume contains information about the CC score and CC peak position. The best CC score in the rotational search space will determine the rotation and the highest CC peak will dictate the translation needed for alignment. After all optimal rotations and translations have been determined, they will be applied to all the subtomograms and summed to produce the next refined reference (Fig.1-17) (W. Wan, 2016).

In this method, a priori information can be used to confine both the rotational search (e.g. rough size of the subunit or the underlying symmetry) and to the translational shifts (e.g. applying masks to the CC volume). In addition, to an increase of alignment precision, the data should be low-pass filtered to remove noise and masked to remove regions that do not contain information about the object of interest.

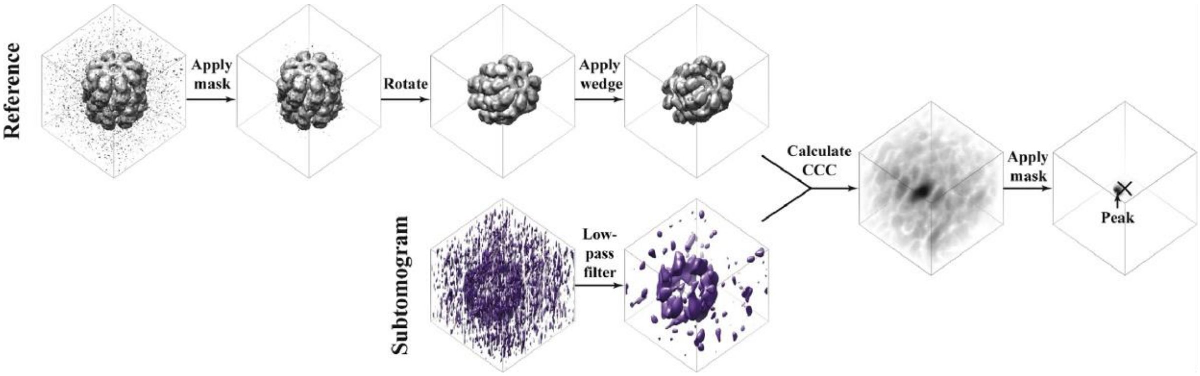

FIGURE 1-17. Subtomogram averaging and alignment by angular search. The reference structure is colored in grey and the subtomogram in purple. The reference is masked and rotated. A wedge mask is applied. The subtomogram is filtered to remove noise and compared to the reference by cross-correlation. The CCC function can be further masked to limit the range of shifts and the peak is identified. The rotation of the reference in which the highest CCC value is identified determines the rotation and the position of the CCC peak determines the translation (the X-mark denotes the center of the box and the arrow indicates the CCC peak). Illustrated by using eight- fold symmetric thermosomes as example images. Density maps were calculated from a crystal structure (PDB ID: 3j1b) (adapted from Wan, 2016).

1.5 Research goals

Since the discovery of pores embedded in the NE by electron microscopy in the 50’s, the architecture of this essential eukaryotic protein complex has been extensively studied. Initially, substantial progress was achieved with X-ray crystallography, where individual Nups and specific sub-complexes were resolved. In parallel, electron microscopy provided the first 3D reconstructions of the NPC and identified the underlying eight-fold rotational symmetry. However, up to this point, it remained challenging to dock the available crystal structures to EM density maps due to the gap in resolution of the two methods. Recently, the technical advances of cryo-ET have pushed the resolution to approximately 2 nm/ 20 Å; allowing the integration of biochemical and structural information obtained *in vitro* with 3D density maps obtained *in situ*. Through this divide and conquer strategy, recent studies have characterized the structural composition of the outer and inner ring of the scaffold of the NPC in great detail (Bui et al., 2013; Kim et al., 2018; Kosinski et al., 2016; Lin et al., 2016), showing how the different building blocks that compose the static architecture of the pore follow the same basic structural principles.

Although the central scaffold of the NPC is now well characterized from an average static perspective, atomic resolution methods have not been able to assess the variability nor the flexibility of this enormous and dynamic machinery. Due to this, the structural characterization of the NPC in the context of its different functional and assembly states has remained challenging.

In my PhD work, I proposed that 3D SRM would provide complementary information regarding the variability of the scaffold of the NPC and, in addition, would allow the mapping of the flexible components of the pore that have remained inaccessible for atomic resolution methods. 3D SRM has the advantage of combining molecular specificity and high signal to noise of the fluorescent label, which can capture the underlying variability and flexibility of molecular components, with high-resolution imaging. From the available repertoire of SRM techniques, I decided to implement SMLM, as this approach currently provides the best resolution in 3D, compared to other available 3D SRM techniques.

The first aim of my PhD work was to establish and optimize the labeling and imaging conditions to obtain high quality single and dual-color SMLM images of NPCs with 2D SMLM and 3D SMLM (4Pi-STORM). The single and dual-color optimizations used for 2D SMLM and 4Pi-SMLM imaging were performed in collaboration with Dr. Mark Bates at the Department of NanoBiophotonics at the

Max Plank Institute for Biophysical Chemistry in Göttingen. During this time, I screened for the best labeling strategy and dye selection for single and double color SMLM. The optimizations were all performed on genome-edited human cell lines in which all copies of the respective Nup of interest were tagged by inserting a SNAP-tag (Keppler et al., 2003) into the endogenous gene loci to obtain maximal fluorophore labeling. The results of these experiments are presented in section 2.1.

Using the experimental methods I initially optimized, I further assessed the 3D structural organization of four different scaffold Nups with 3D SMLM. In order to characterize the structural organization of the selected Nups, I developed a computational pipeline in collaboration with Drs. Shyamal Mosalaganti and Martin Beck at the European Molecular Biology Laboratory in Heidelberg. This pipeline implements averaging and alignment routines (described in section 1.4.) which increase the signal-to-noise ratio of the fluorescent labels of my datasets and allow a precise estimation of the 3D position and symmetry of the Nups of interest. The developed 3D SMLM averaging pipeline and resulting 3D reconstructions of scaffold Nups are presented in sections 2.2 and 2.3, respectively.

Furthermore, I investigated the underlying architectural variability and flexibility of scaffold Nups with aid of both statistical methods and topological data analysis tools for unsupervised classification. My results revealed that scaffold Nups comprise an unexpected broad constitutional variability and positional flexibility that has previously not been accounted for. These efforts are also presented in section 2.3.

Having successfully established a 3D SMLM averaging pipeline that would systematically resolve the structural organization of scaffold Nups and developed analysis tools to uncover their inherent flexibility, I expanded these methodologies to study the flexible organization of two asymmetrically positioned Nups that form part of the cytoplasmic filaments and nuclear basket. Given the inherent flexibility of the Nups of interest, I predicted to observe a larger number of conformational states for these Nups. In order to resolve, without bias, the different conformational states detected in the 3D SMLM images of flexible Nups; I relied on the developed methodologies for unsupervised classification prior to averaging. My results revealed that flexible Nups have an intricate 3D organization that reflects the dynamic nature of these regions of the pore. Surprisingly, I also discovered that the architecture of the nuclear basket is highly scattered across the vertical axis and does not unite in a single distal ring as previously hypothesized. These results are presented in section 2.4.

Finally, after successfully determining the architecture of individual Nups with 3D SMLM, which led to the discovery of the inherent variability and characterization of the different conformational states present in the NPC, I developed a strategy to position the Nup of interest into a unique comprehensive molecular 3D map. These technological developments are presented in section 2.5. The resulting proof-of-principle 3D molecular map, generated from dual-color 3D SMLM data, can integrate any positions and conformational states of the Nups of interest. This holistic model will further allow the interpretation of remaining questions in the field, such as the structural changes that the NPC undergoes during functional perturbations and assembly state intermediates. In addition, the developed methodology provides a new framework for architectural determination that can serve as a paradigm for other macromolecular assemblies.

2 Results

2.1 *In situ* 3D organization of the NPC revealed by localization microscopy

At the start of my doctoral work, an initial pseudo-atomic model of the scaffold of the human NPC was produced, which proposed how the Y-shape-subcomplex could be positioned and orientated (Bui et al., 2013). During the course of my doctoral work, higher-resolution density maps of the scaffold of the NPC have allowed the characterization of the structural composition of the outer and inner ring of the NPC in even greater detail (von Appen et al., 2015; Kim et al., 2018; Kosinski et al., 2016; Lin et al., 2016). However, even though most of the scaffold of the NPC is now well characterized from an averaged static perspective, scaffold nucleoporins that localize asymmetrically (i.e. only associate with the nucleoplasmic or cytoplasmic face) blur out within the reconstructed cryo-ET density maps and their positioning still awaits confirmation. For instance, this is the case of nucleoporin ELYS, which has been characterized as a member of the Y-shape-subcomplex but due to its asymmetric localization to the nuclear ring (reviewed in (Hoelz et al., 2011a)), available NPC electron densities have been insufficient to determine its exact position and orientation. Current EM models predict the position of its β-propellers in the proximity of its known interfaces to Nup160 (von Appen and Beck, 2015). In addition, existing NPC models depict an averaged conformation of the NPC architecture and struggle to obtain information about the likely structural flexibility within the scaffold of NPCs (Kim et al., 2018). Finally, due to the inherent flexibility of the nuclear basket and the cytoplasmic filaments, the architecture of these peripheral regions of the pore remains uncharacterized. Therefore, during my PhD work, I hypothesized that current 3D SRM technologies could provide complementary high-resolution information about specific NPC components inside the cell and capture their different conformations. Pursuant to the specific aims of my research study, implementing high resolution 3D SRM of the human NPC *in situ* would allow me to characterize i) asymmetrically localized nucleoporins (e.g. ELYS), ii) the variability within the scaffold of the pore and iii) the architecture and localization of flexible peripheral nucleoporins.

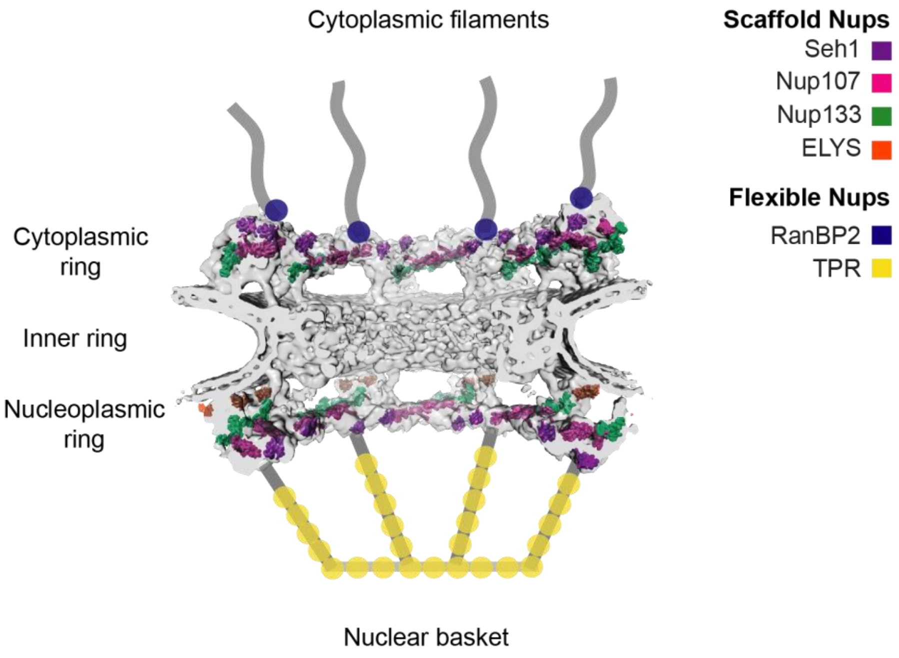

FIGURE 2-1. Positioning of targeted Nucleoporins. A model describing the architecture of the NPC with the predicted positions of the scaffold Nups and the hypothesized positiond of the flexible Nups under study. This model incorporates the isosurface view (cut in half) of the core-region of the human NPC (EMDB 3103; light grey) and the schematic representation of the nuclear basket and cytoplasmic filaments (grey), which are the least characterized structural regions of the NPC. In the symmetrical core-region of the NPC, the estimated positions (docked crystal structures) of the nucleoporins Seh1 (purple), Nup107 (pink) and Nup133 (green) are shown (Bui et al., 2013). The position of the β-propeller of the Nup ELYS (orange) has been predicted by crosslinking experiments and computational modeling (Bui et al., 2013, von Appen et al., 2015). The position of the cytoplasmic Nup RanBP2 (blue) is hypothesized to be adjacent to the cytoplasmic ring of the pore (Bui et al., 2013). Finally, the nucleoplasmic Nup Tpr (yellow) is hypothesized to compose the main architectural element that holds the nuclear basket (Krull et al., 2004).

In order to investigate the above mentioned gaps in our knowledge about the architecture of the NPC, I designed a strategy where the targeting of a carefully selected set of six nucleoporins; three symmetrically positioned scaffold Nups (Seh1, Nup107, Nup133), one asymmetrically positioned scaffold Nup (ELYS) and two flexible peripheral Nups (Nup358/RanBP2 and Tpr) (Fig.2-1) in human cell lines with single- and dual-color 3D SRM would provide sufficient information to tackle the above mentioned aims i-iii. In addition, preserving a constant reference nucleoporin during dual-color 3D SRM imaging should allow me to create a comprehensive 3D molecular map that integrates all relative positions of both the scaffold and flexible regions of the NPC.

To map the molecular positions of the Nups of interest (NOI) (Fig.2-1) with the highest possible precision that 3D SRM technologies provided at the start of my PhD work, I selected the implementation of the 4Pi-SMLM (see Chapter 1: 1.3.3.2 and Fig.1-16). To access the only available 4Pi-SMLM system at the time, we established a collaboration with Dr. Mark Bates and Prof. Dr. Stefan Hell at the Department of NanoBiophotonics at the Max Plank Institute for Biophysical Chemistry in Göttingen.

2.1.1 SMLM labeling strategies for the NPC

All SMLM imaging systems, including the 4Pi-SMLM used in the study, rely on high quality sample labeling, where the macromolecular complex of interest is densely and specifically tagged with photoswitchable fluorescent probes. To label the protein of interest with a SMLM compatible fluorescent probe, a range of different exogenous and endogenous labeling strategies have been developed, all of which have their advantages as well as disadvantages. However, the main desired characteristics for achieving a high-quality sample for SMLM include a high degree of labeling, low background, a small size of the label to reduce the risk of functional perturbation and achieve the minimal offset to the protein domain of interest and compatibility with a wide choice of available fluorophores for multicolor imaging. The most commonly used strategies include (i) indirect labeling (e.g. the use of antibodies or nanobodies against the protein of interest (Ries et al., 2012)) and (ii) direct labeling (e.g. fusion of fluorescent proteins or fusion self-labeling enzymes (Koch et al., 2018)).

One of the initial goals of my PhD work was to evaluate, compare and select the best performing labeling strategies for the 3D mapping of the NPC architecture with 4Pi-SMLM. Previously, only indirect labeling strategies (i.e. both antibodies and nanobodies against fluorescent proteins (such as GFP) had been implemented in 2D SMLM for the study of the architecture of the NPC (Löschberger et al., 2012; Szymborska et al., 2013). Direct labeling strategies (i.e. imaging of the fusion protein mEos2) had been used in 2D SMLM for determining the stoichiometry of nucleoporins within the human NPC (Ori et al., 2013). As my desired labeling strategy would had need to enable the use of diverse fluorophores for multicolor imaging with reduced offset to the protein of interest for accurate 3D mapping (see section 2.1), I selected a direct labeling strategy based on fusion self-labeling enzymes (e.g. SNAP- or Halo-tag (Keppler et al., 2003; Los and Wood, 2006)), as these permit the covalent bonding of a variety of dyes suitable for SMLM with a minimal offset. Therefore, I included the SNAP-tag system in my repertoire of possible tagging strategies in addition to indirect labeling strategies. To systematically compare indirect labeling strategies and avoid the variability in specificity and affinity between different antibodies and nanobodies, I compared them against the same GFP-tagged NOI. To evaluate the performance of the labeling systems under consideration, I consistently used the organic dye Alexa Fluor (AF) 647 as a readout, as this dye has proven to exhibit extremely good photo-switching properties for SMLM (Dempsey et al., 2011).

Moreover, in order to maximize the efficiency of the SMLM labeling strategies under consideration, I decided to use homozygous genome-editing technologies (i.e. ZFN or CRISPR/Cas9) (Koch et al., 2018) in human cell lines (HeLa and U2OS) to fully replace the endogenous NOI with the tagged version (GFP and SNAP-tag). All genome-edited cell lines used in this work were generated together with my colleagues Dr. Birgit Koch, Bianca Nijmeijer and Moritz Kueblbeck (for details see Chapter 4: Materials and methods).

Given the above discussed rationale, the experimental conditions that I used to evaluate and compare the set of labeling systems for the study of the NPC architecture with 4Pi-SMLM are:

A. HeLa Kyoto cells, endogenously expressing mEGFP-Nup107, stained with α-GFP antibody and secondary antibody (F(ab')2 fragment) coupled to AF647.
B. HeLa Kyoto cells, endogenously expressing mEGFP-Nup107, stained with α-GFP nanobody directly coupled to AF647.
C. U2OS cells, endogenously expressing SNAP-Nup107, labeled with benzylguanine (BG)-AF647.

The 4Pi-SMLM images of nuclear pores in all tested experimental conditions (Fig.2-2 A-C) revealed the characteristic ring-shape structure that has been previously reported for scaffold Nups and allowed for qualitative comparison between conditions. The specificity and density of labeling, low background and the size of the used probe primarily guided the qualitative evaluation of the sample labeling.

Staining with an α-GFP antibody (Fig.2-2 A) gave the highest density of labeling, likely arising from the amplification of the AF647 signal by the use of primary and secondary polyclonal antibodies. However, this condition exhibited the presence of background labeling and due to the large size of antibodies, this technique incorporates a substantial offset to the NOI of ~25nm, which shifts the obtained position of the NOI for the accurate 3D mapping NPC. Staining with an α-GFP nanobody (Fig.2-2 B) gave a lower density of labeling comparing to the sample labeled with the α-GFP antibody. This condition also exhibited the presence of background but due to the small size of the nanobody (~10 times smaller than an antibody), it reduces the offset to the NOI to ~8nm. Finally, Labeling of the SNAP-tag (Fig.2-2 C) shows high specificity but a low density of labeling compared to previous conditions, likely arising from the lack of amplification of the AF647 signal produced by the one-to-one stoichiometry of the self-labeling SNAP tag with the covalently bound AF647 dyes per NOI. Nevertheless, this condition revealed very

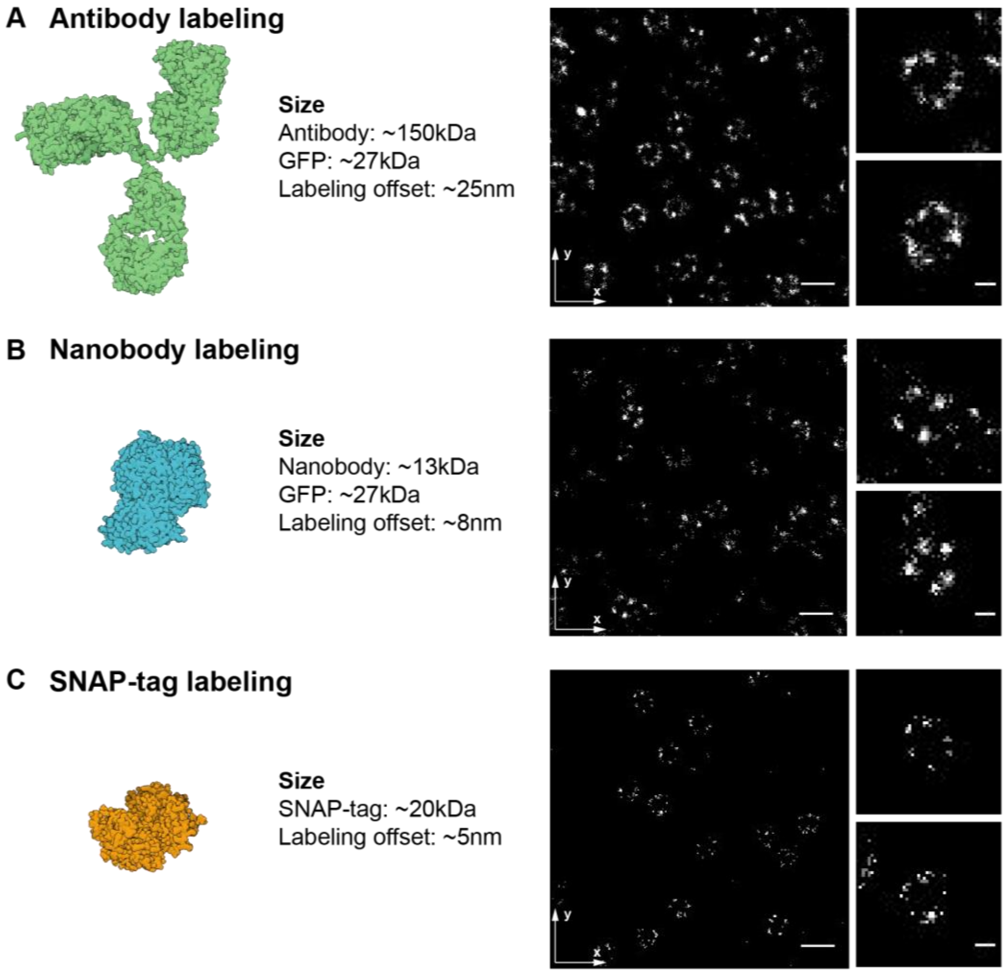

FIGURE 2-2. Selection of NPC labeling strategy. Schematic representation of three different labeling startegies. The isosurface-rendered density maps were created from the crystal structure of an antibody (PDB: 1IGT), a GFP:nanobody (PDB: 3G9A) and a SNAP-tag (PDB: 3KZY). The respective molecular weights and estimated labeling offsets are indicated. A representative 1.75 μm^2 area of the lower surface of the nucleus (scale bars indicate 200 nm) and two exemplary pores (scale bars indicate 50 nm) are shown for **A)** HeLa Kyoto cell, endogenously expressing mEGFP-Nup107, labeled with anti-GFP antibody and a secondary antibody conjugated to AF 647. **B)** HeLa Kyoto cell, endogenously expressing mEGFP-Nup107, labeled with anti-GFP nanobody directly coupled to AF 647. **C)** U2OS cell, endogenously expressing SNAP-Nup107, labeled with BG- AF 647.

low background labeling and due to the small size and direct covalent bonding to the dye, reduces the offset to the NOI to around ~5nm, which best approximates the obtained position of the NOI for the accurate 3D mapping NPC. Taken together, I decided to apply direct labeling based on SNAP-tag for the systematic mapping of the NOI, as this strategy revealed a higher specificity, lower background and better approximation to the ground-truth position of the NOI, compared to the indirect labeling strategies.

As described in 2.1, in order to assemble a comprehensive 3D molecular map of the NOI, I rely on a relative pair-wise positioning of the NOI together with a reference Nup labeled with one of the alternative labeling systems describedabove. Based on the qualitative performance of the compared labeling strategies, I decided to use antibody labeling as the system for the reference Nup, as this system provided a higher density of labeling compared to nanobodies and given that this labeling strategy will only be used as a reference to position the NOIs relative to each other, its large size will not affect the positioning precision of the rest of the NOI labeled with SNAP-tag. Thus, a direct anti-ELYS antibody was selected as a reference and its labeling performance is discussed in 2.1.2. Further evaluations and optimizations of labeling strategies for multicolor 4Pi-SMLM are discussed in 2.5.1.

2.1.2 4Pi-SMLM imaging of the NPC

After having selected the most favorable labeling strategies for the systematic mapping of the NOI, my next immediate goal was to optimize the embedding medium and acquisition conditions for 4Pi-SMLM imaging to study the underlying 3D architecture of the NOI.

The organic dyes used in SMLM, including AF647 can undergo light-induced reversible transitions between *on* and *off* states (see 1.3.3). However, not only the chemical properties of the fluorophore are important to achieve a good photoswitching behavior; its immediate molecular environment has also been shown to play an important role (Vogelsang et al., 2010). Due to this, special blinking buffers are used to enhance the blinking behavior and stabilize the reversible *off* state to prevent photobleaching. A variety of studies have identified a range of buffer conditions that induce the photoswitching of different organic dyes (Dempsey et al., 2011; Lehmann et al., 2016; Olivier et al., 2013a, 2013b; Vaughan et al., 2012; Vogelsang et al., 2010). Most of the commonly used blinking buffers contain redox active molecules (e.g. primary thiol) and an oxygen scavenging system. The organic dye AF647, for example has been reported to present good photoswitching behaviors in the presence of a primary thiol (e.g. mercaptoethylamine (MEA) and β-mercaptoethanol (βME)) and with oxygen removal (Dempsey et al., 2011). To optimize the embedding medium and imaging conditions for 4Pi-SMLM, I compared the use of blinking buffers that contain either MEA or βME and preserved oxygen removal (see Chapter 4: Materials and methods for details on buffer composition). It is important to note that the objective geometry within 4Pi-SMLM (Aquino et al., 2011) requires the embedding of the sample in-between two coverslips, which are positioned in-between two opposing objectives (Fig.2-3 A). Due to the particular 4Pi-SMLM embedding of the sample, the narrow space in-between the coverslips tolerates only ~ 30µl of blinking buffer, thus it was important to test which buffer composition would favor a good photoswitching behavior of AF647 in combination with the optimized SNAP-tag labeling condition from 2.1.1 for a prolonged time in the strictly reduced volume needed for 4Pi-SMLM.

Consistent with previous reports, AF647 presented good photoswitching behavior with both primary thiols and the initially obtained 4Pi-SMLM images showed comparable characteristics. However, given the restricted volume of the embedding medium, I further compared their performance over longer periods of time. After a period of 3h, AF647 deteriorated significantly its photoswitching behavior in the presence of βME compared to MEA. Thus, for the particular embedding needed in for 4Pi-SMLM, MEA is the thiol of preference for longer acquisition times and was used in all single-color 4Pi-SMLM imaging presented in this work.

The 4Pi-SMLM images presented in this work were always taken from the bottom of the cell's nucleus (Fig.2-3 A). Usually, in SMLM based techniques specimens are imaged with epifluorescence illumination. However, this type of illumination generally produces high background signal, arising primarily from out-of-focus fluorophores. For specimens near the cell surface, which are positioned close to the coverslip (~200 nm), the incidence angle of the illumination light can be adjusted to allow total internal reflection (TIRF), which provides superior signal-to-noise ratio by reducing the out-of-focus background (Bates et al., 2013a). However, given that the NOIs are positioned further than 200 nm away from the coverslip, TIRF illumination cannot be implemented. To optimize the 4Pi-SMLM imaging of the NOI with reduced background, I relied on the strategy of illuminating the sample with a highly inclined beam of excitation light termed "HiLo" instead (Tokunaga et al., 2008). This strategy, similar to TIRF, increases the signal-to-noise ratio, allowed high quality single-molecule detection and provided an imaging framework for future acquisitions.

After 4Pi-SMLM imaging, the lateral position of individual molecules is further determined by fitting the center of single molecule photon emissions, while the axial position is determined from the self-interference of the detected light from four different phase delays as the intensity ratios between the corresponding detection channels. The resulting three-dimensional image is further corrected for drift that arises from the inherent mechanical instabilities of the microscope during the long single molecule blinking acquisition. For more detailed information about the lateral and axial position determination in 4Pi-SMLM data, correction for lateral drift and image reconstruction see Chapter 4: Materials and methods and referenced literature (e.g. (Aquino et al., 2011)). All the 4Pi-SMLM images used in this work were rendered with a 7-nm voxel size and assigned with an 8-bit grayscale value, based on the number of localizations per rendered voxel. The reconstructed 4Pi-SMLM images with the described labeling, embedding and imaging optimizations resulted in high quality NPC images of the bottom of the cell's nucleus (Fig.2-3 B).

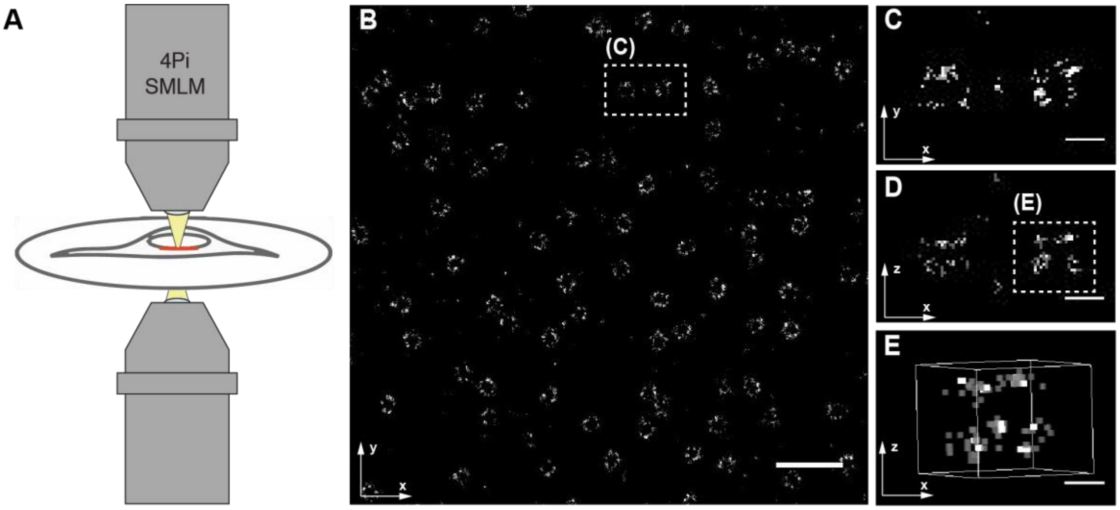

FIGURE 2-3. 4Pi-SMLM imaging of the Nuclear Pore Complex. A) Schematic representation of the 4Pi-SMLM objective geometry and sample imaging. In this set-up the sample is mounted between two coverslips and imaged through two opposing objectives (Aquino et al., 2011). In all experiments, the selected focal plane corresponds to the botton of the cell's nucleus (red). **B)** A representative 4Pi-SMLM image of the lower surface of the nucleus with embedded NPCs. Axial sum-projection 4Pi-SMLM image of endogenously tagged SNAP-Nup107 U2OS cell line labeled with BG-A647. **C)** top-view and **D)** side-view 4Pi-SMLM magnifications of the NPCs that are embedded in the lower surface of the nucleus **E)** 3D rendering of side-view volume containing a single NPC where both nuclear- and cytoplasmic rings of the NPCs are observed. Scale bars, 500 nm (B), 100 nm (C,D) and 50 nm (E).

The magnified top-view 4Pi-SMLM image of the scaffold SNAP-Nup107 (Fig.2-3 C) showed the characteristic ring-like architecture of scaffold nucleoporins, which have been previously reported with 2D SMLM techniques (Löschberger et al., 2012; Szymborska et al., 2013). Moreover, the corresponding magnified side-view 4Pi-SMLM image and 3D rendering of an individual pore (Fig.2-3 D-E) clearly revealed the underlying dual-ring architecture. This arrangement is consistent with the proposed positions of Nup107, as a Y-shape-subcomplex member, forming part of both nucleoplasmic and cytoplasmic rings of the pore (von Appen and Beck, 2015; Bui et al., 2013).

2.2 3D averaging of 4Pi-SMLM NPC particles

To extract quantitative 3D information about the spatial positioning of the NOI from 4Pi-SMLM images, I decided to integrate information of hundreds of single NPC 3D image volumes of a particular NOI in a 3D averaging routine. Averaging methods are useful analysis tools as they combine information from a large number of copies of a particular macromolecular complex of interest, to increase the signal-to-noise ratio and overall resolution of the underlying 3D structure of the macromolecule of interest (Briggs, 2013). While averaging methods have been heavily used in the last decades in the field of EM tomography to determine the structure of macromolecular complexes *in situ*, its implementation in the field of SRM is still very novel and the algorithms are often very specific to the macromolecular assemblies of interest (see 1.4). I therefore set out to develop a general methodological pipeline for the 3D averaging of SMLM images and optimized it by using both the SNAP-Nup107 datasets presented in 2.1.2 and simulated 4Pi-SMLM particles.

2.2.1 3D SMLM averaging pipeline

In collaboration with Drs. Shyamal Mosalaganti and Martin Beck at EMBL, Heidelberg, I established an initial 3D SMLM averaging pipeline (Fig.2-4) that consists of:

1. *Rendering of the 4Pi-SMLM localizations into an image z-stack* (Fig.2-4 A). Here, 3D histograms of the detected localizations are rendered into an image z-stack with the appropriate pixel size (selected accordingly to the 3D SMLM microscope of choice) and assigned with 8-bit grayscale values.
2. *Automatic particle picking of individual NPCs from the z-stacks* (Fig.2-4 B). For versatility, two different automatic particle picking modalities have been incorporated into the 3D SMLM averaging pipeline in collaboration with Dr. Jean-Karim Hériché. The first modality uses the DB scan algorithm (Ester

et al., 1996), which is a density-based clustering algorithm that can identify SMLM particles of irregular structure. This modality is preferential for most macromolecular complexes that do not have a ring-shape morphology. In addition, for regular ring-shape morphologies as the architecture of scaffold nucleoporins, an alternative algorithm based on Hough transforms (Duda and Hart, 1972) has also been incorporated into the pipeline (see Chapter 4: Materials and methods for further information about the particle picking parameters).

3. *Intensity normalization of particles* (Fig.2-4 C). Given the intrinsically exponential distribution of the number of blinking events per fluorophore in SMLM (Dempsey et al., 2011), the number of localizations obtained per voxel (and the assigned 8 bit intensity per voxel) will also follow this distribution. Thus, to normalize the fluorescence intensity signal in the picked particles z-stacks, I apply a principal square-root function applied prior to averaging (see Chapter 4: Materials and methods for details).
4. *Particle averaging and alignment by 3D cross-correlation (CC)* (Fig.2-4 D). Here, an initial reference image is generated by the sum of all 4Pi-SMLM particles. This reference image is further imposed with an 8-fold symmetry based on the known symmetry of the NPC. Subsequently, the 4Pi-SMLM particles are aligned by angular search (i.e. both rotational and translational shifts are calculated by 3D CC in Fourier space between the reference and individual 4Pi-SMLM) (see 1.4.2). After the 3D alignment, a new averaged reference image is generated. The entire process is iterated until no further improvement in alignment is seen (i.e. convergence of angular search; see Chapter 4: Materials and methods for a step-by-step description of averaging steps).
5. *3D reconstruction of the average photon density map* (Fig.2-4 E). The final reference image (i.e. final averaged image) contains precise information about the axial, lateral and rotational position of the NOI and can be interactively visualized and analyzed in diverse molecular modeling softwares (e.g. UCSF Chimera (Pettersen et al., 2004)). The isosurface

rendered representation of the photon density map was based on manually selected threshold values that expose the structure of interest.

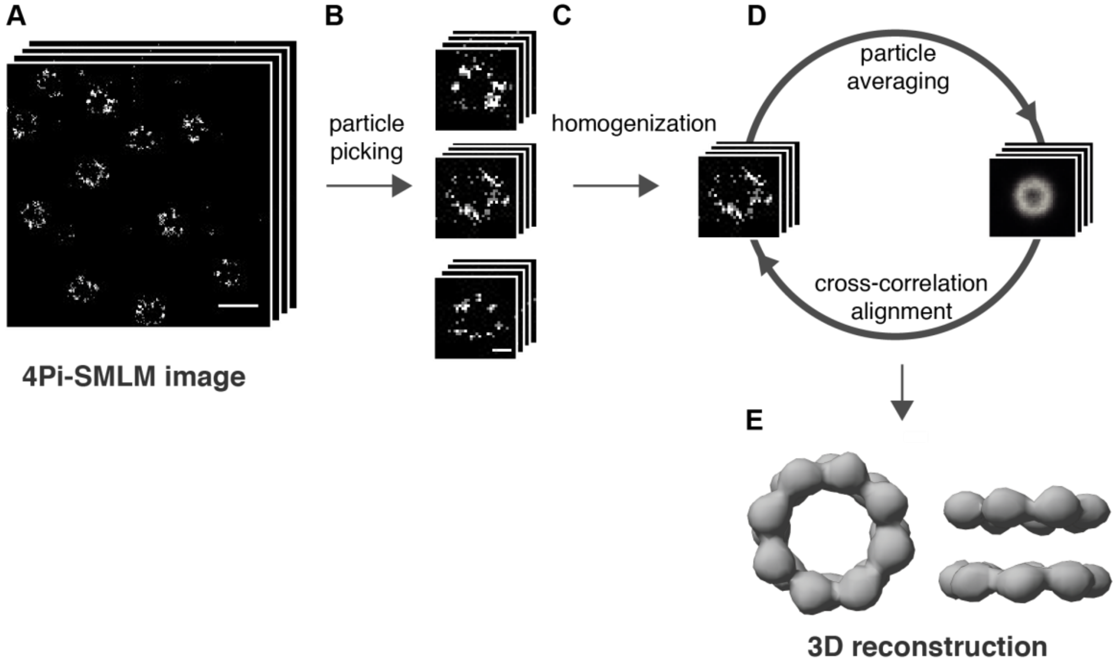

FIGURE 2-4. 3D averaging of 4Pi-SMLM images. A) A representation of a 4Pi-SMLM image stack of a 1.3 μm^2 area of the lower surface of the nucleus (scale bars indicate 200nm) of a U2OS cell, endogenously expressing SNAP-107, labeled with BG- AF 647. **B)** A representation of automatically picked individual image stacks of NPC particles (x2 magnification; scale bars indicate 50nm) from the lower surface of the nucleus. **C)** A homogenization transformation is applied to all individual NPC particles prior to averaging to obtain a more compact signal distribution. **D)** The first step in the averaging pipeline is the generation of an initial reference that derives form the sum of all individual particles. An 8-fold rotation is imposed on the reference due to the known symmetry of the NPC. The second step is the 3D alignmet of particles. Here, the reference will explore a predefined rotation space. At each rotation step a 3D cross-correlation function (CC) between the reference and each individual particle is calculated. The rotation step in which the reference obtains the highest CC values determines the correct rotation. The position of the CC peak determines the translation. The calculated rotations and translations are applied and a new sum image is generated to generate the subsequent reference. The entire process is iterated until no further improvement in alignment is calculated. **E)** From the final reference image a isosurface-rendered 3D reconstruction can be generated for visualization purposes (range: -0.199-28.2; threshold: 4).

This initial 3D averaging pipeline (1-5) successfully resulted in a well-refined 3D reconstruction, where both positions of Nup107 at the nucleoplasmic and cytoplasmic rings are shown, as well as their underlying relative symmetry (Fig.2-4 E). However, a more systematic assessment was needed in order to characterize the pipeline efficiency and explore existing caveats when subjected to a broad range of image quality parameters.

2.2.2 NPC particle simulations

To systematically evaluate the performance and robustness of the initially established 3D averaging pipeline with 4Pi-SMLM datasets of varying quality, I made use of simulated 4Pi-SMLM particles. In collaboration with Dr. Mark Bates, I generated simulated 4Pi-SMLM particles in which I could vary key SMLM image quality parameters including localization precision (LP) and degree of labeling (DOL; see Chapter 4: Materials and methods for details). Twelve simulated 4Pi-SMLM datasets were computed, each of which included five hundred NPC particles with the following ground truth parameters and image quality conditions:

i. Particle diameter: 100 nm
ii. Particle axial distance: 50nm
iii. Mean number of photons: 4000 (i.e. AF647)
iv. Architecture: double ring
v. Symmetry: 8-fold
vi. Random particle tilt: up to 30°
vii. Relative shift between NR-CR subunits: 8°
viii. LP: 5 nm, 10 nm and 20 nm
ix. DOL: 100%, 70%, 50% and 30%

All particles of each simulated 4Pi-SMLM dataset were independently submitted to the 3D averaging pipeline (see 2.2.1) (Fig.2-5). The averaged simulated particles with a LP of 5 nm and varying DOL (100%, 70% and 50%) (Fig.2-5 A) showed a

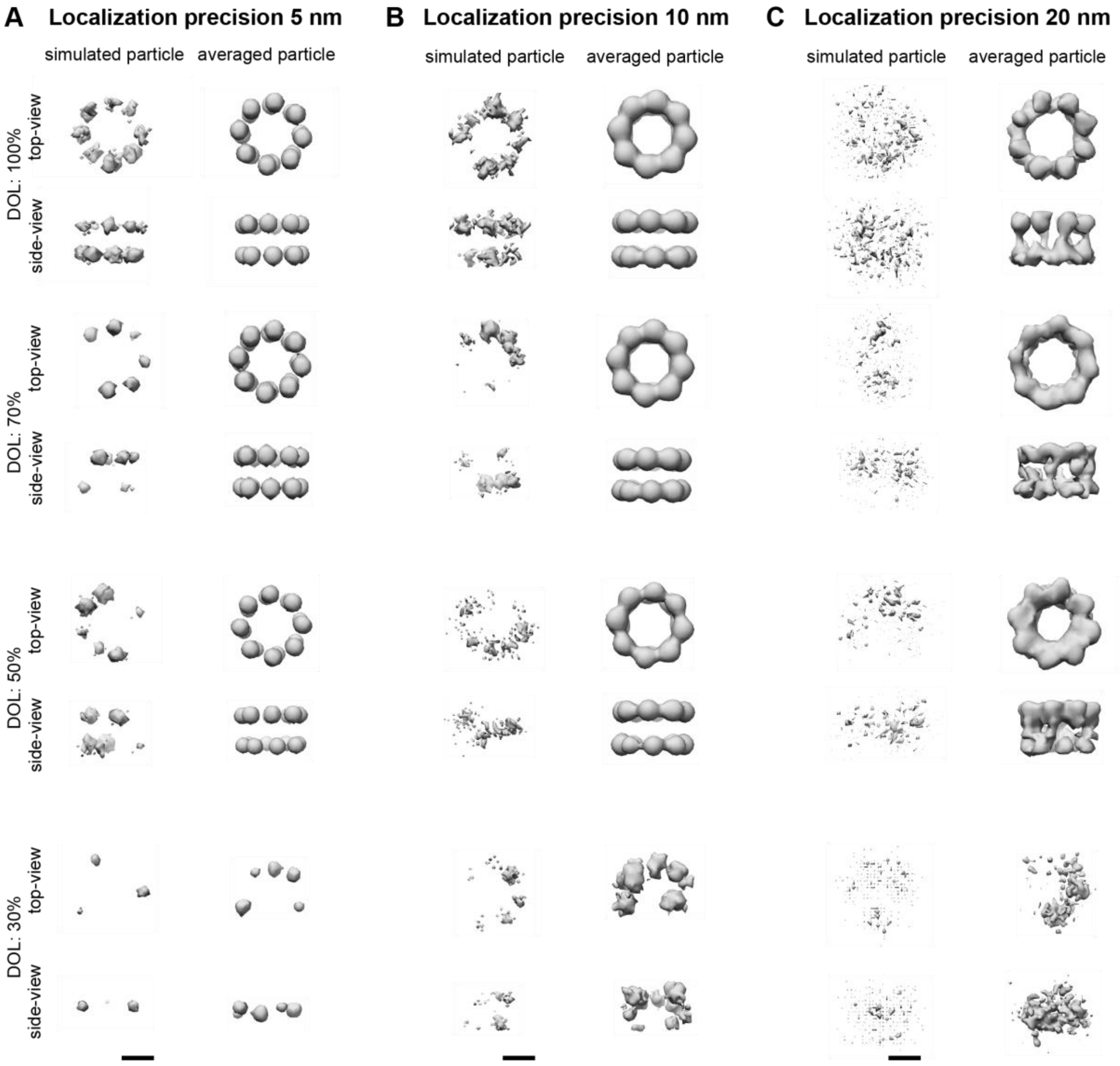

FIGURE 2-5. Evaluation of 3D averaging performance on simulated 4Pi-SMLM particles. An exemplery isosurface-rendered top- and side-view image of a 4Pi-SMLM simulated particle (based on Nup107 radial and axial distances; 50 nm for both) and the averaged reconstruction of 500 simulated particles of four different degrees of labelling (DOL; 100%, 70%, 50% and 30%) are shown for particles with a localization precision of 5 nm (A), 10 nm (B) and 20 nm (C). Each dataset was averaged by using the corresponding pipeline presented in Figure2-5. Scale bars, 50 nm (A-C).

superior refinement of subunit position compared to the Nup107 dataset in 2.2.1 and recovered both nucleoplasmic and cytoplasmic rings with their underlying relative symmetry. However, even with a LP of 5 nm, the particles that had a DOL of 30% failed to recover the ground truth conditions after 3D averaging. The particles with a LP of 10 nm and varying DOL (100%, 70% and 50%) (Fig.2-5 B) resembled in refinement the subunit position of the Nup107 dataset in 2.2.1. Similarly, only those datasets with a DOL of 50% and higher recovered both nucleoplasmic and cytoplasmic rings. Finally, all the conditions with a LP of 20 nm failed to recover the ground truth conditions after averaging (Fig.2-5 C).

In conclusion, the averaging of simulated 4Pi-SMLM particles demonstrated that the 3D averaging pipeline tolerated well particles of a LP of ~10 nm and below, while particles with a LP of 20 nm failed to average into a refined architecture, where both rings could be clearly separated from each other. From the particles with a LP of ~10 nm and below, a DOL of 50% was sufficient to achieve a refined average, while those particles with an inferior DOL (e.g. 30%) failed to average into a refined architecture. This analysis also suggests that the quality of our datasets resembled a LP of ~10 nm with a DOL ~50%, meaning that the previously optimized labeling, mounting and imaging conditions were sufficient to produce refined averages, where the presence of a particular NOI in a single or double ring should be distinguishable as well as their underlying symmetry.

2.2.3 NPC axial and lateral positioning

The 3D averages from the simulated 4Pi-SMLM particles provided a platform for testing the accuracy of the averaging pipeline and establishing a strategy for the determination of the axial and lateral position of nucleoporins.

In order to examine the accuracy and benefits of the 3D averaging pipeline, I used the simulated particles that resembled my experimental working conditions:

i. Particle diameter: 100 nm
ii. Particle axial distance: 50nm
iii. Mean number of photons: 4000 (i.e. AF647)
iv. Architecture: double ring
v. Symmetry: 8-fold

vi. Random particle tilt: up to 30°
vii. Relative shift between NR-CR subunits: 8°
viii. LP: 10 nm
ix. DOL: 50%

To determine the axial and lateral position of the 3D reconstructions of simulated 4Pi-SMLM particles, the axial and lateral projected intensity profiles were fit with a Gaussian function (Fig.2-6):

$$\boldsymbol{f(x)} = \sum_{i=1}^{n} a_i e^{\left[-\left(\frac{x-b_i}{c_i}\right)^2\right]}$$

where a is the amplitude, b the centroid position, c is related to the peak width and n the number of peaks to fit. For scaffold nucleoporins that are present in both nucleoplasmic and cytoplasmic rings, analogous to the simulated data in this section, $n = 2$. The centroid positions (b_1 and b_2) are further subtracted from each other to obtain the corresponding sub-pixel distance d between the axial and lateral position of the averaged image.

The first reference image (Fig.2-6 A) generated prior to the iterative alignment and averaging see 2.2.1, was produced from unregistered and tilted simulated 4Pi-SMLM particles, thus the calculated axial and lateral distance deviate from the ground truth distances, illustrating the need for the 3D averaging pipeline for refinement and precise distance estimation.

The last reference image (Fig.2-6 B), after 3D averaging, was generated from registered 4Pi- SMLM particles, correcting for existing tilts. Thus the calculated axial and lateral distances approximated the ground truth distances with high accuracy (considering the intrinsic 10nm LP of the simulated 4Pi-SMLM particles).

In conclusion, the fitting of Gaussian functions to the averaged reference axial and lateral intensity profiles allows accurate distance determinations and will be used throughout this work.

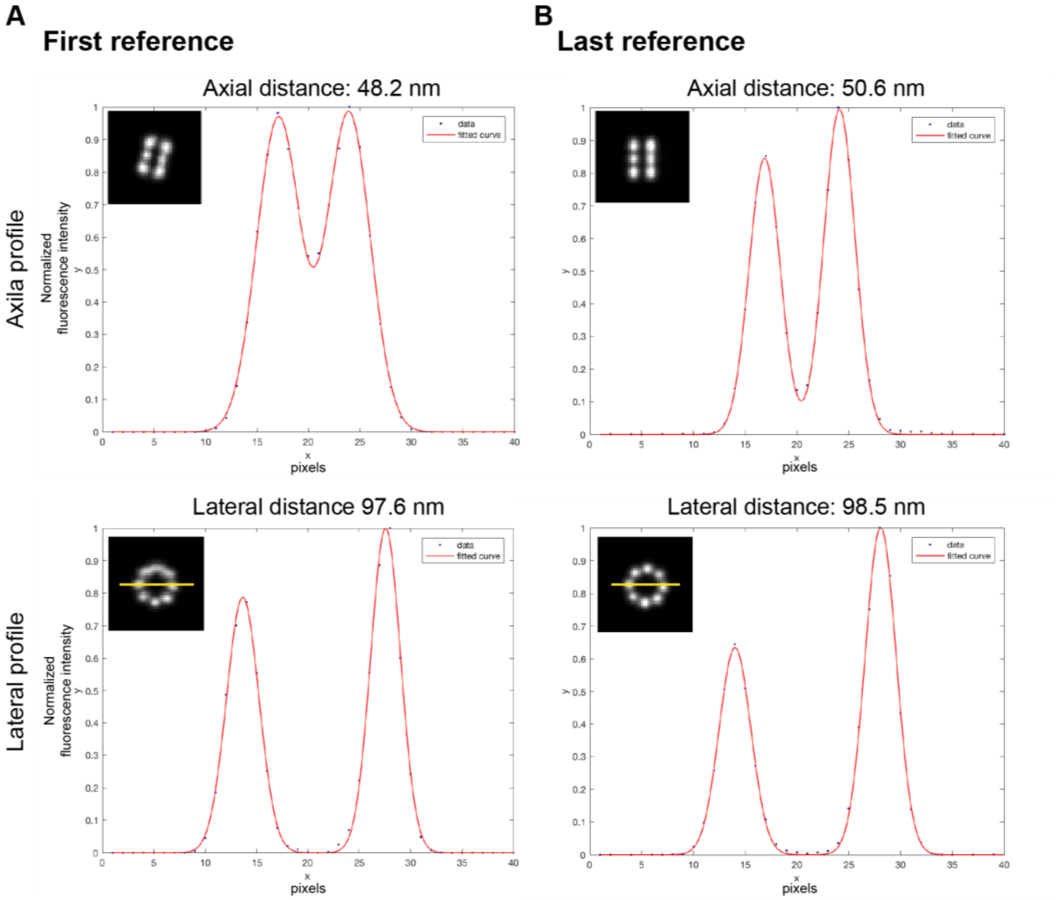

FIGURE 2-6. Averaged particle distance determination and validation. Five hundred simulated 4Pi-SMLM particles were generated (40x40x40 pixels; pixel size: 7nm; LP: 10nm; DOL: 50%; r = 50nm; h = 50nm, tilt = 30°) and averaged with the 3D averaging pipeline described in Figure2-5. Graphs show the normalized intensity axial profiles of the averaged simulated NPC 4Pi-SMLM particles that were calculated by the sum projection along the X-axis. Graphs below show the the normalized intensity lateral profiles that were calculated by the sum projection along the Z-axis. Image inset shows exemplary 2D greyscale images of the corresponding axial and lateral profiles. Both the axial and lateral distance estimation were calculated by fitting with a double Gaussian function to the axial and lateral profiles of the first averaged reference image generated prior to iterative cross-correlation alignment and averaging. **A)** The existing particle missalignment and tilt does not allow to recover the ground truth distances. The final averaged reference image generated after iterative cross-correlation alignment and averaging (iterations = 10). **B)** After implementing the 3D averaging pipeline the recovered distances are closer to the ground truth compared to the distances obtained prior to averaging.

2.2.4 Masks for averaging

The comparison of the axial intensity profile between the first and the last reference image (Fig.2-6 A-B), revealed that small differences in intensity distribution between rings are amplified by the 3D averaging causing a greater inequality in the intensity distribution between rings in the last reference images. I hypothesized that this effect could be driven by the incorrect alignment of a proportion of particles, where particles with drastically uneven ring intensities would preferentially align the ring with the strongest intensity to the reference ring with higher intensity. In order to validate this hypothesis, correct for the proportion of particles with incorrect alignment and allow an equal refinement of both rings during 3D averaging, I explored the possibility of averaging each ring independently. Once the references of both dependently and independently averaged rings were available, a systematic comparison analysis between the translational shifts that each particle undergoes throughout each averaging process should then allow me to test the hypothesis.

In order to average each ring independently, I used reference masks (see 1.4.2) and compared the final averaged references deriving from both dependently and independently averaged rings (Fig.2-7). The applied masks served to define a specific volume (e.g. spherical, elliptical, cylindrical, etc.) that was applied to the reference images to ignore signal outside the masked region throughout the averaging steps. Masks can be used to reduce background signal and to define a substructure of interest for alignment. In the latter case, the volume mask shape should resemble and encompass the substructure of interest only.

First, a spherical volume mask, which encompassed both rings of the initial reference image, was used for the dependent averaging of the rings (Fig.2-7 A; see Chapter 4: Materials and methods for details of the generation of spherical masks). Second, two elliptical masks were used separately during averaging of each independent ring (Fig.2-7 B). To have the option of generating elliptical masks for NOIs that are positioned at different volumes, I established an automatic volume masks generator that takes the axial positioning of each ring of the initial reference image into account (see Chapter 4: Materials and methods for detailed information about the automatic volume masks generator and the corresponding Matlab code).

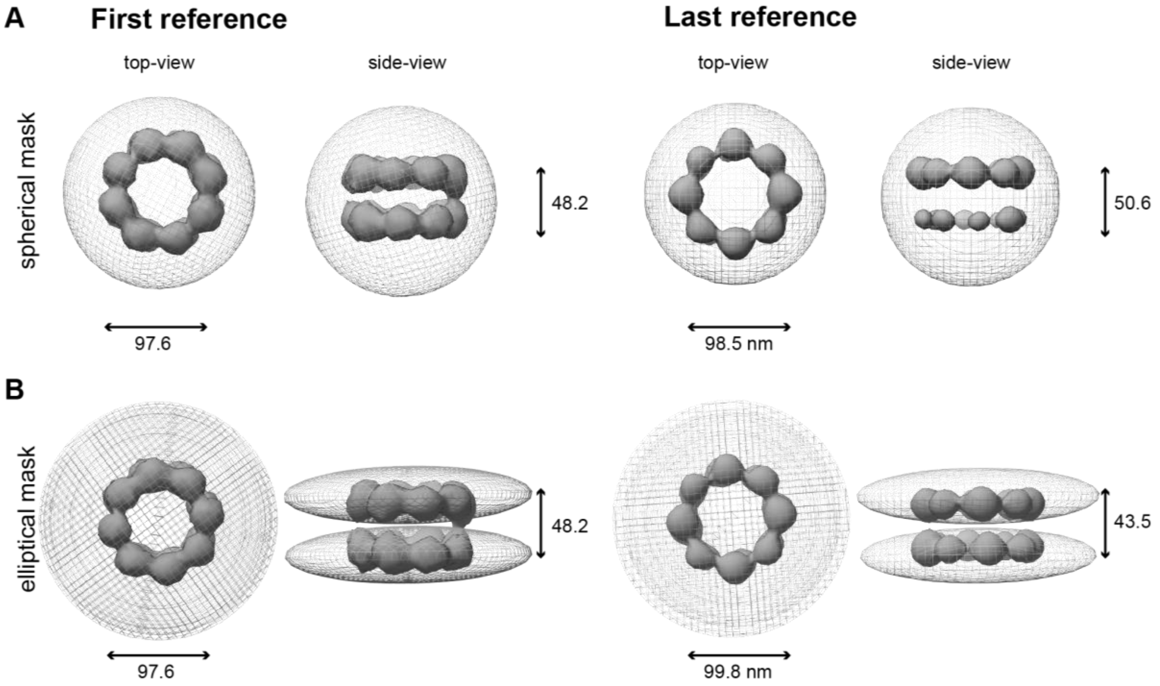

FIGURE 2-7. Nuclear and cytoplasmic masks for averaging. Representation of the use of spherical (A) and elliptical reference masks (B) during 3D averaging. Five hundred simulated 4Pi-SMLM particles were generated (40x40x40 pixels; pixel size: 7nm; LP: 10nm; DOL: 50%; r = 50nm; h = 50nm) and averaged with the 3D averaging pipeline discribed in Figure2-5. Isosurface-rendered representation of the reference images (first reference: Range: 0-154; Level: 35; last reference: Range: 0-0.1; Level: 0.09) together with the corresponding mesh-rendered masks. Axial and lateral distances (indicated in nm) were calculated by fitting a double Gaussian function to each axial and lateral profile of the first reference volume prior to averaging (left) and the final reference volume after averaging (right).

The 3D reconstruction of the last reference image averaged with the spherical mask, again exhibited larger differences in intensity distribution between rings after averaging (Fig.2-7 A). The 3D reconstruction from the averages that used separate elliptical masks for each ring, however, recovered equally refined rings compared to the rings averaged with the spherical mask (Fig.2-7 B). Thus, the implementation of elliptical masks during 3D averaging, provides an approach for the independent refinement of both nucleoplasmic and cytoplasmic rings of the NPC and is used subsequently for averaging of NOIs that are positioned in a double ring structure in the pore. For the NOIs that are asymmetrically positioned within the pore, spherical masks were systematically used for 3D averaging.

2.2.5 Axial system stability

The implementation of elliptical masks during 3D averaging confines the alignment of each of the rings of the pore independently, which improved the refinement of each ring. After the refinement steps, we observed that the lateral distance of the last reference averaged with elliptical masks compared to the last reference averaged with spherical masks improved in approximation (99.8 nm compared to 98.5 nm) to the ground truth distance (100 nm) described in 2.2.3 (Fig.2-7). On the other hand, the axial distance of the last reference averaged with elliptical masks compared to the last reference averaged with spherical masks deteriorated in approximation (43.5 nm to 50.5 nm) to the ground truth distance (50 nm) (Fig.2-7), suggesting that the use of elliptical masks introduces drifts in the z-plane.

To investigate if the use of elliptical masks compared to spherical masks introduces z-plane drifts between the independently masked volumes, I analyzed the total amount of translational shifts that each simulated particle experienced after 3D averaging (Fig.2-8). The analysis of translational shifts revealed that when using spherical masks, the majority of particles stably remain in the same z-plane, while a subset of particles underwent major shifts in the z-plane (Fig. 2-8 A), likely arising from misalignments due to the differences in intensities between rings (see 2.2.4). On the other hand, the use of elliptical masks diminished the proportion of misaligned particles, thus favoring the independent refinement of rings, but introduced global sub-pixel shifts (~3 nm) providing an explanation for the reduction in the measured axial distances (Fig. 2-8 B).

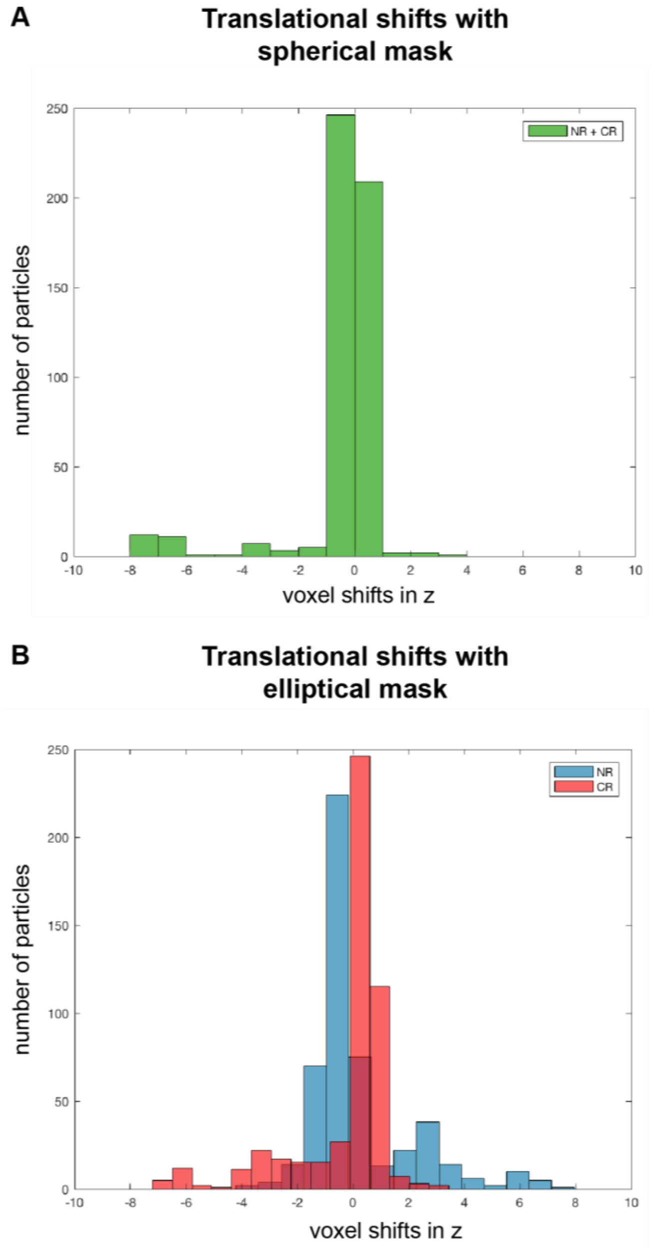

FIGURE 2-8. Translational system drifts analysis. Measurements of the translational shifts (in pixels) that each particle made after the final iteration (10 iterations) of the 3D averaging pipeline. Simulated 4Pi-SMLM particles from Figure2-7 were used for monitoring and calculating the translational shits. The histograms represent the amount and frequency of the translational shifts in the Z-axis by using a single spherical mask covering the entire volume of the reference (NR+CR) (see Figure 2-7) (A) and two independant elliptical masks covering the nuclear ring (NR) and cytoplasmic ring (CR) volume of the reference independantly (see Figure 2-7) (B). The use of a spherical mask (A) shows that the majority of particles do not drift in the Z-plane (0 shifts in pixels) and a small proporion of particles drifts significantly (>4 shifts in pixels). The use of independant elliptical masks (B) shows that each volume (NR and CR) has a minimal drift Z-plane (<1 shifts in pixels).

2.2.6 Axial reference interpolation

To preserve the improvements in refinement that result from the averaging with two elliptical masks, but correct for the axial shifts that they introduce during averaging, I developed a strategy for restoring the axial positions in the last reference images based on axial interpolation (Fig.2-9). This strategy consists of the following steps (for details see Chapter 4: Materials and methods):

1. 3D averaging with both spherical (S) and elliptical (E) masks and selection of the last reference (E) for interpolation (Fig.2-9 A)
2. Estimation of the axial difference (α) in position between S and E, by the difference in centroid positions extracted with the axial distance estimation approach described in 2.2.3 (Fig.2-9 B)
3. Interpolation of E based on α (Fig.2-9 C) to obtain the corrected averaged reference (I) following:

   for the cytoplasmic ring

   $$I_x = E_x(1-\alpha) + E_{x+1}\alpha$$

   for the nucleoplasmic ring

   $$I_x = E_x\alpha + E_{x+1}(\alpha - 1)$$

   where E_x and I_x are the intensity values of the position x within the reference images E and I, respectively.

4. Reconstruction of I, which contains both refined masked features and corrected axial positions (Fig.2-9 D)

The final reference generated from the simulated particles used in 2.2.3, which was averaged with both spherical and elliptical masks in 2.2.4 and analyzed for axial drift in 2.2.5, was further subjected to the axial interpolation strategy described throughout the steps 1-5. The resulting interpolated reference revealed a 3D reconstruction with well-refined nucleoplasmic and cytoplasmic rings and with improved axial (49.7 nm) and lateral (99.8 nm) distances that closely approximate the ground truth positions (axial: 50nm; lateral: 100nm) (Fig.2-9 D).

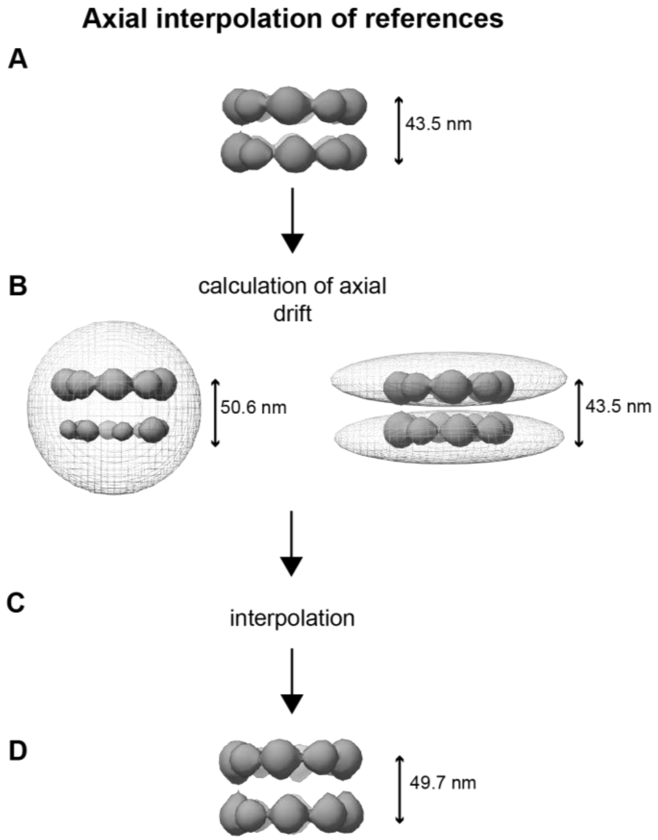

FIGURE 2-9. Correction of axial system drift with the interpolation of averaged references. Schematic representation of the axial system drift correction pipeline for references averaged with elliptical masks. **A)** Isosurface-rendered view of the final reference obtained obtained with the use of elliptical masks from Figure2-7. **B)** Calculation of the translational shift difference between the spherical (left; covering both nuclear and cytoplasmic ring) and elliptical (right; covering the nuclear and cytoplasmic ring independently) reference masks after 3D averaging (see Figure2-7). **C)** Correction of axial drift in the final reference (elliptical masks) with image interpolation (algorithm based on the axial drift difference). **D)** Isosurface-rendered view of the final reference after interpolation.

2.2.7 Rotational system stability

To completely validate the implementation of elliptical volume masks during 3D averaging for the independent refinement of nucleoplasmic and cytoplasmic rings and for the respective position estimation of the NOI under study, the absence of rotational drift in the resulting reconstructions needs to be tested. To compare if the use of elliptical masks compared to spherical masks introduces independent rotational shifts between the two masked volumes, which would indicate the presence of rotational system drift, I quantified the total amount of rotational shifts that each simulated particle used in 2.2.3, which was averaged with both spherical and elliptical masks in 2.2.4, experienced after 3D averaging (Fig.2-10).

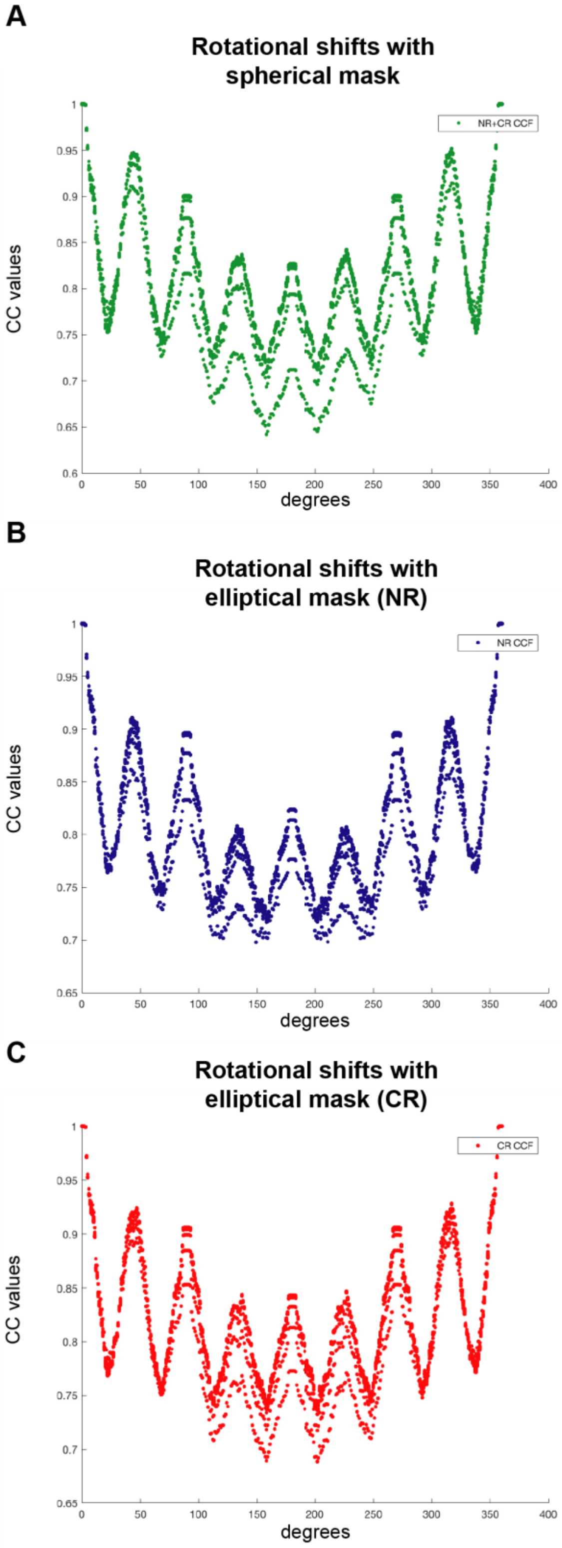

FIGURE 2-10. Analysis of rotational system drift. A correlation-based approach to calculate the rotational stability during 3D averaging. The rotational cross-correlation profile (across 360°) of each reference (10 iterations) is calculated from the simulated 4Pi-SMLM particles from Figure2-7. **A)** Rotational 3D CC functions from averages performed with a **A)** spherical mask, **B)** an elliptical mask covering the NR and **C)** an elliptical mask covering the CR. **(A-C)** The peaks in CC values are stable throughout iterations (i.e. at the same degree of rotation). (CC: cross-correlation; NR: nuclear ring; CR: cytoplasmic ring)

To estimate the amount of rotational shifts between averaged volumes and confirm the absence of rotational system drift during 3D averaging, I developed a strategy that examines the radial position of each reference image at each averaging iteration step that is based on rotational 3D CC functions. This approach measures the similarity between references that originated from the same volume mask, as a function of rotational displacement (i.e. the reference at each iteration step to the last refined reference). In this way an angular displacement of the periodic rotational 3D CC function would indicate the presence of rotational system drift (for details on the analysis of rotational system drift see Chapter 4: Materials and methods).

The analysis of rotational system drift revealed no angular displacement in the periodic rotational 3D CC function in both spherical (Fig.2-10 A) and elliptical volume masks (Fig.2-10 B-C), demonstrating that the radial position of each reference image at each averaging iteration step remained stable. Thus, the absence of rotational system drift during 3D averaging for the implementation of both spherical and elliptical volume masks was confirmed. In addition, the rotational system drift analysis displayed the increase in structural similarity (i.e. shown by higher values in rotational 3D CC) after each of the averaging iteration steps in both spherical (Fig.2-10 A) and elliptical volume masks, illustrating the convergence of the iterative averaging procedure (Fig.2-10 B-C).

In conclusion, the use of both spherical and elliptical volume masks allows for rotational refinement throughout the 3D averaging pipeline. Given that i) the implementation of elliptical volume masks, favors the independent refinement of both nucleoplasmic and cytoplasmic rings (see 2.2.4.) and that ii) a strategy for the correction of the observed axial system drift has been developed (see 2.2.6.), I incorporated these approaches into the 3D averaging pipeline in 2.2.1.

2.2.8 NPC rotational positioning

To establish a quantitative approach to measure the rotational differences between the nucleoplasmic and cytoplasmic positions of the NOI, I once more made use of rotational 3D CC functions. The implementation of rotational 3D CC functions, in addition to calculating the rotational drift that is present in particular averaging systems (see 2.2.7), can also be used to measure the rotational displacement between the nucleoplasmic and cytoplasmic positions of the NOIs. I thus established a methodology that measures the similarity between references that originated from different volume masks, as a function of rotational displacement (i.e. the last reference of the nucleoplasmic volume mask against the last reference of the cytoplasmic volume mask). In this way the angular displacement of the periodic rotational 3D CC function measures the degree of rotational offset between nucleoplasmic and cytoplasmic rings between individual eight-fold subunits (for details see Chapter 4: Materials and Methods).

To examine the established approach in its ability to reveal the presence of rotational displacement and validate the accuracy of the methodology in measuring the differences between the nucleoplasmic and cytoplasmic positions of the NOI, I analyzed the last references obtained from the averaging of simulated particles with elliptical volume masks (see 2.2.4-6). By comparing the relative rotational displacement in 360° between the nucleoplasmic and cytoplasmic rings (Fig.2-11 A) a clear shift between the periodic rotational 3D CC function of the cytoplasmic against the nucleoplasmic ring was observed. These results indicated the presence of rotational displacement between nucleoplasmic and cytoplasmic rings. To further investigate the degree of rotational displacement between individual eight-fold subunits, I independently examined 45° (one eighth) of the rotational 3D CC function (Fig.2-11 B). Likewise, a clear shift between the 45° of periodic rotational 3D CC function of the cytoplasmic against the nucleoplasmic ring was observed. To quantify the amount of rotational displacement between individual eight-fold subunits, I independently fitted a

Gaussian function to each 45° segment of the rotational 3D CC function and subtracted the centroid positions of each individual fit. The calculated rotational displacement between nucleoplasmic and cytoplasmic subunits (8°) recovered the exact ground truth rotational difference (8°) (see 2.2.3), validating with high accuracy the suitability of the established methodology to compare relative positions of subunits between the nuclear and cytoplasmic rings.

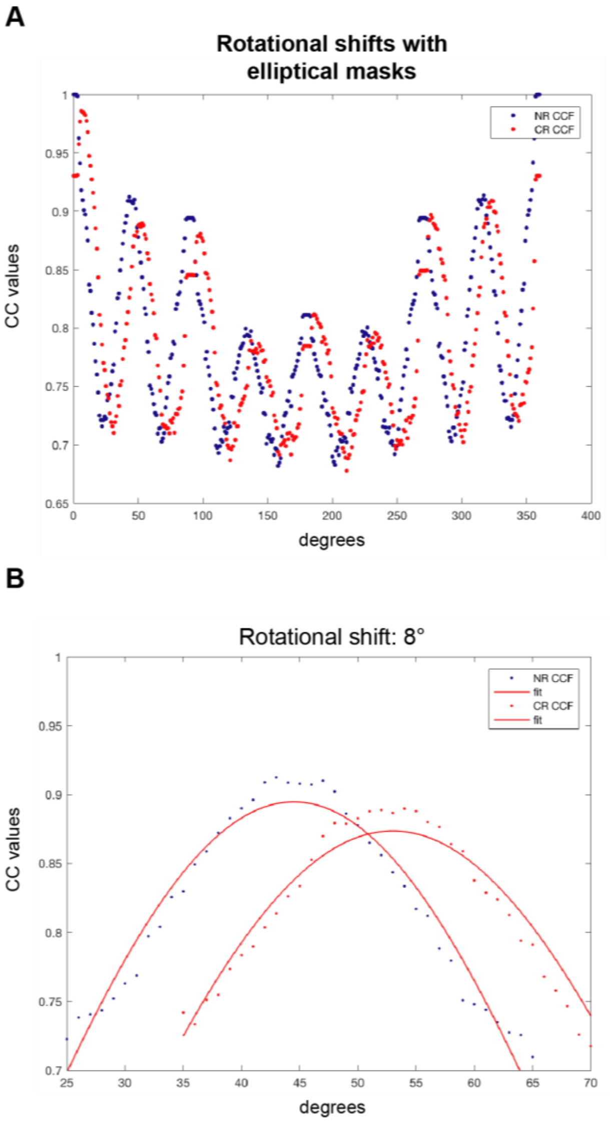

FIGURE 2-11. Rotational displacement between subunits. A correlation-based approach to calculate the rotational displacement (in degrees) between subunits of the NR and CR. Averaged simulated 4Pi-SMLM particles (with elliptical mask) from Figure2-7 were used for this analysis. **A)** Comparison between the rotational 3D CC profiles (across 360°) of the final averaged reference of the NR and the CR. The 3D CC profile of the CR appears shifted compared to the profile of the NR. **B)** Comparison between the rotational 3D CC profiles (across 45°) of the final averaged reference of the NR and the CR. The rotational distance difference of 8° was calculated by fitting with a Gaussian function to each 3D CC profile independantly.

2.3 Scaffold nucleoporins

Having established and optimized a 3D SMLM averaging pipeline and validated its use for determining the axial, lateral and rotational position of nucleoporins with high accuracy on simulated 4Pi-SMLM particles, I implemented the established tools to systematically determine the 3D architecture of scaffold NOIs as proof-of-principle and to further investigate the uncharacterized architecture of the tenth member of the Y-shape-subcomplex ELYS (see 2.1). To do so, I acquired single-color 4Pi-SMLM datasets of each scaffold NOI with the developed labeling, mounting and acquisition techniques described in 2.1.1-2. As expected for scaffold Nups forming part of the Y-shape-subcomplex pore, all four NOIs revealed a ring-shaped architecture in the 4Pi-SMLM images (Fig.2-12).

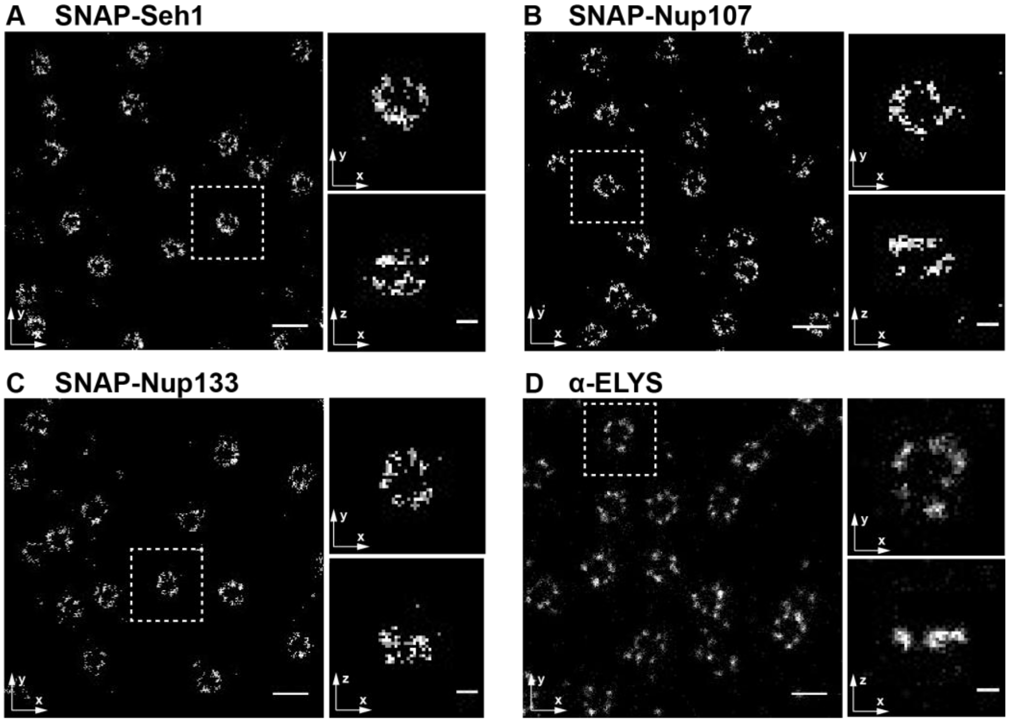

FIGURE 2-12. 4Pi-SMLM imaging of scaffold nucleoporins. A representative 1.75 µm^2 area of the lower surface of the nucleus (scale bars indicate 200nm) and a top- and side-view image of one exemplary pore (x2.5 magnification; scale bars indicate 50nm). **A)** U2OS cell, endogenously expressing SNAP-Seh1, labeled with BG- AF 647; **B)** U2OS cell, endogenously expressing SNAP-Nup107, labeled with BG- AF 647; **C)** U2OS cell, endogenously expressing SNAP-Nup133, labeled with BG- AF 647; **D)** U2OS cell, labeled with α-ELYS primary antibody and secondary coupled to BG- AF 647. The contrast in the images was adjusted for visualization.

Moreover, differences in the underlying architecture between the NOI were already apparent in the magnified top- and side-view images of single NPCs, e.g. ELYS formed larger and single rings (Fig.2-12 D), contrasting to the other three NOIs that formed smaller and double rings (Fig.2-12 A-C). In order to quantitatively compare the axial, lateral and rotational position between the Y-shaped complex NOIs, I analyzed the 4Pi-SMLM datasets acquired for each NOI with the 3D SMLM averaging pipeline I developed as described throughout section 2.2.

2.3.1 3D averaging of scaffold nucleoporins

All 4Pi-SMLM NOI datasets were subjected to 3D SMLM averaging and their axial, lateral and rotational distances were systematically quantified (Fig.2-13). The resulting 3D reconstructions (Fig.2-13 A) revealed that Seh1 had the smallest lateral distance (82 nm), the largest axial distance (57 nm) and rotational displacement (13°) between subunits, followed by Nup107 (lateral distance: 101 nm; axial distance: 57 nm and rotational displacement: 6°), Nup133 (lateral distance: 102 nm; axial distance: 38 nm and rotational displacement: 12°) and ELYS, which presented the largest lateral distance (128 nm) and only a single ring.

The architectural differences between these four proteins that I obtained by the 3D SMLM and particle averaging methodology I developed are consistent with current EM models of NPC structure (see 2.1) (Fig.2-13 B), where the positions of the docked crystal structures of Seh1, Nup107 and Nup133 recapitulate the decrease in axial distances and the increase in lateral distances between subunits of the corresponding NOI, respectively. This model also illustrates the presence of rotational displacement between nucleoplasmic and cytoplasmic subunits of the NOIs. In addition, current EM models predict that ELYS forms part of the nucleoplasmic ring of the pore only and suggest its position, through computational modeling, in the proximity of the NE (Fig.2-13 B). From the initial

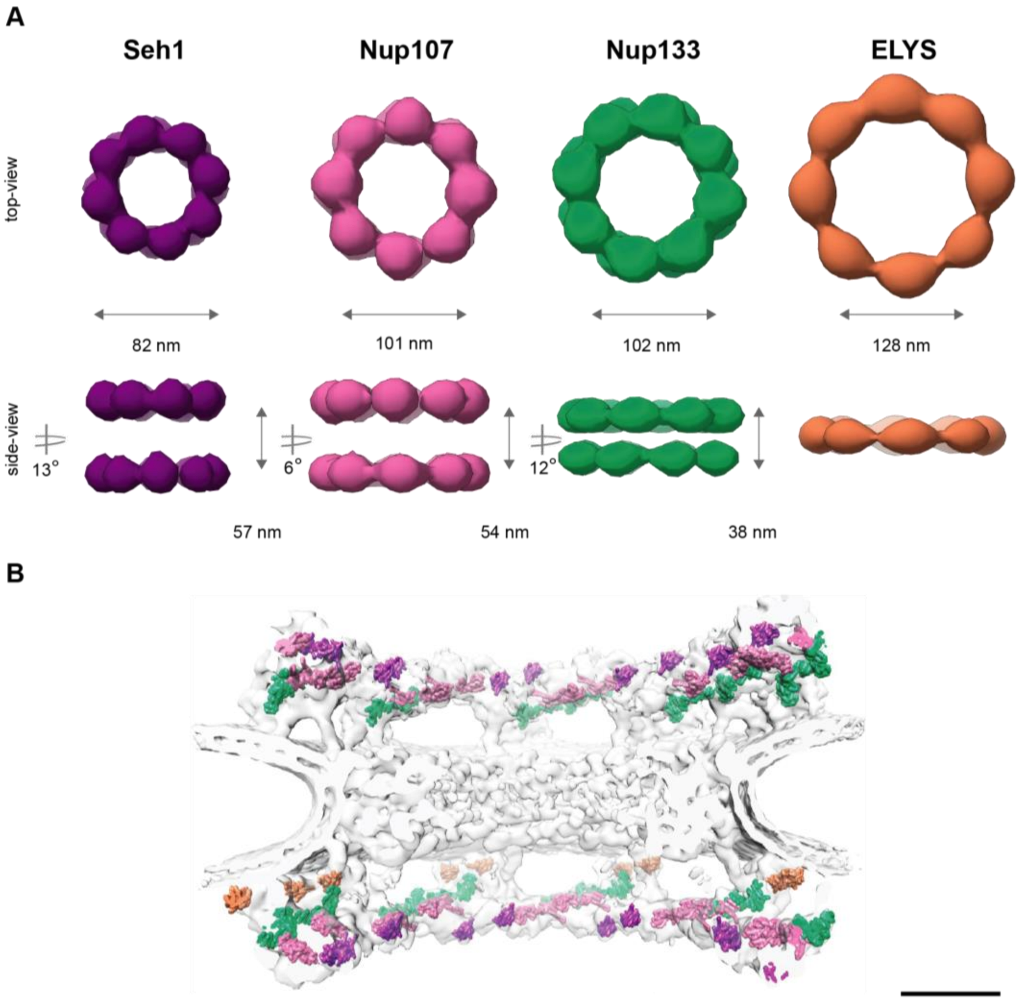

FIGURE 2-13. 3D averaging of 4Pi-SMLM scaffold nucleoporins. A) Isosurface-rendered density maps of the 3D averagings of 4Pi-SMLM datasets from Figure2-12 (Seh1: purple, range= -0.004 - 1.06, level =1.8; Nup107: pink, range= -0.002 - 0.316, level= 0.025; Nup133: green, range= -0.005 -1.11, level = 0.11 and ELYS: orange, range= -0.004 - 1.39, level = 1). The implemented 3D averaging pipeline (see Figure2-4) was used with elliptical masks (see Figure2-8). The axial system drift was corrected by the axial interpolation of references (see Figure 2-9). The axial and radial distances were calculated by fitting a double gaussin function to the corresponding intensity distribution profiles (see Figure2-6). The subunit rotational shifts were calculated by the rotational correlation-based approach (see Figure2-11). **B)** A model describing the architecture of the core region of the NPC with the predicted positions of the static Nups. This model incorporates the isosurface view (cut in half) of the core-region of the human NPC (EMDB 3103; light grey) and the estimated positions (docked crystal structures) of the nucleoporins Seh1 (purple), Nup107 (pink) and Nup133 (green) (Bui et al., 2013). The position of the β-propeller of the Nup ELYS (orange) has been predicted by crosslinking experiments and computational modeling (Bui et al., 2013, von Appen et al., 2015).

results I obtained in the 3D reconstructions of averaged 4Pi-SMLM ELYS particles, I validated that ELYS forms only one ring of the NPC compared to the rest of the NOI. However, to locate the exact position of ELYS relative to the rest of the NOI, the use of dual-color labeling is needed and implemented later in this work.

2.3.2 Validation of the positioning of scaffold nucleoporins

Even though the architectural differences, obtained from the 3D reconstructions (Fig.2-13 A) are in line with current EM models (see 2.1) (Fig.2-13 B), I set to obtain a more detailed comparison between the axial and lateral positions of the NOI derived from the 3D reconstructions of averaged 4Pi-SMLM particles and the docked crystal structures in current EM models. Ideally, to precisely compare the positions of the NOI derived from averaged 4Pi-SMLM particles to the docked crystal structures in current EM models, it would be necessary to take into consideration the distance offset produced by the labeling system and the exact location of the self-labeling protein-tag that was fused to the NOI by genome-editing. The size of the SNAP tag protein domain predicts an offset of ~ 5nm from the BG-dye pocket to the NOIs caused by my labeling system (see 2.1.1) and the endogenously tagged U2OS SNAP –Seh1, –Nup107 and –Nup133 cell lines used in this study all incorporated the SNAP-tag at the N-terminal domain of the protein. However, available crystal structured for Nup107 and Nup133 lack the N-terminal domain, restricting the precision of the comparison. In addition, the 3D reconstruction of ELYS was obtained from polyclonal antibody labeling and thus the comparative analysis would differ from the proposed estimation for the SNAP-tagged NOIs. Moreover, there is no available crystal structure for ELYS and this estimation would need to rely in the computationally predicted densities in current EM models.

An alternative solution to compare the axial and lateral positions between the 3D reconstructions of averaged 4Pi-SMLM particles and the docked crystal structures in current EM models is to compute density maps from the docked crystal structures at reduced resolution. Those density maps would mimic and approximate the positions of the 3D reconstructions of averaged 4Pi-SMLM particles and would provide a general platform to compare approximate distances between the mass centers of the available crystal structures at SRM resolution (for a detailed description on the generation of density maps and distance estimations for the axial and lateral position comparison between 3D reconstructions of averaged 4Pi-SMLM particles and the docked crystal structures in current EM models see Chapter 4: Materials and Methods).

The generated density maps (Fig.2-14) from the available docked crystal structures of the scaffold NOI (i.e. Seh1, Nup107 and Nup133) confirmed that Seh1 has the smallest lateral distance (~83 nm) and the largest axial distance (~58 nm), followed by Nup107 (lateral distance: ~99 nm and axial distance: ~54 nm) and finally Nup133 (lateral distance: ~105 nm and axial distance: ~45 nm). These results demonstrated that the axial and lateral positions obtained from the 3D reconstructions of averaged 4Pi-SMLM particles recapitulate the architectural differences between the NOI and highly approximate the axial and lateral positions assigned in current EM models (see discussion in Chapter 3). The axial distance obtained for Nup133 is more compressed in the 3D reconstructions obtained from 4Pi-SMLM data (see Fig.2-13 A) compared to the axial distance recovered from the generated density map of docked crystal structures of Nup133 (Fig.2-14). This could be explained by the position of the N-terminus of Nup133 (i.e. where the SNAP-tag is incorporated), which points towards the NE and thus could shift the signal from the fluorescent dye in comparison to the position of the docked crystal structure. In addition, the generated density maps from the available docked crystal structures of Seh1, Nup107 and Nup133 expose the presence of rotational displacement between nucleoplasmic and cytoplasmic subunits. This proof-of-principle comparative analysis of the previously characterized scaffold NOI, validates the use of 3D SMLM averaging outlined through section 2.2.1-8 and provides a framework to integrate structural information from orthogonal methodologies for the understanding of the architecture of the NPC.

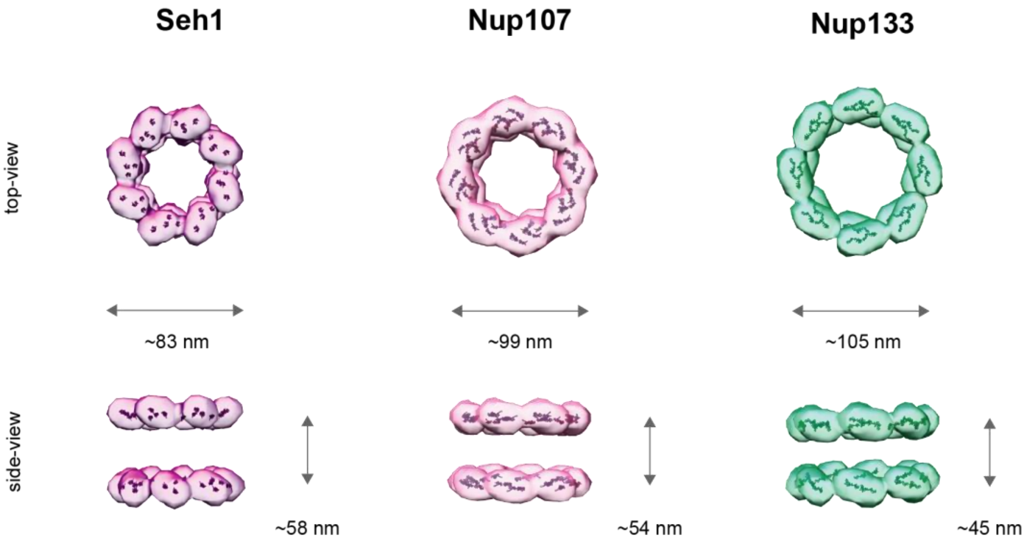

FIGURE 2-14. Validation of 3D 4Pi-SMLM averages of scaffold nucleoporins. Comparison of the axial and lateral distances between available structures of scaffold nucleoporins. Top-view and side-view density maps (Seh1: purple, range= 0 - 0.007 , level =0.0002; Nup107: pink, range= 0 -0.009, level = 0.0003, and Nup133: green, range= 0 -0.009, level = 0.0002) were generated from docked crystal structures (Bui et al., 2013, von Appen et al., 2015) at a 20nm resolution. Axial and radial distances were calculated by tracing the 3D volume of the generated density maps in the molecular modeling software UCSF Chimera (Pettersen et al., 2004).

2.3.3 Variability of scaffold nucleoporins

It is important to mention that current structural models of the NPC derive information mainly from cryo-ET techniques, which due to the inherent low signal-to-noise ratio present in individual particle sub-tomograms, rely greatly on averaging methods to improve the overall resolution and contrast in order to resolve the structure of the macromolecular assembly of interest. While the averaging of cryo-ET data resolves structural features in exquisite detail, the obtained reconstructions depict a static average of the structure of interest and thus struggle to obtain information about the intrinsic variability of the structure of interest. On the other hand, SMLM techniques while being more limited in spatial resolution have the complementary advantage of higher signal-to-noise ratio within individual particle SMLM z-stacks and the strength of specifically labeling a desired protein of interest within a macromolecular complex, thus are likely able to capture the intrinsic variability of the structure of interest in individual images.

After having successfully validated the use of 3D SMLM averaging for the study of the architecture of the NPC by obtaining comparable axial and lateral positions to current EM maps for the scaffold NOIs, I investigated the intrinsic axial, lateral and rotational variability within the scaffold NOI that is captured within my 4Pi-SMLM data. To this end, I first quantified the axial and lateral distances in each individual 4Pi-SMLM NPC for those scaffold NOIs, which form part of both nucleoplasmic and cytoplasmic rings of the pore (for details see section 2.2.3 and Chapter 4: Materials and Methods). The resulting distributions of the axial and lateral distances of all individual 4Pi-SMLM particles (Fig.2-15 A) revealed that Seh1 had a lateral distance that ranges from 50 nm to 120 nm with a median lateral distance of 84 nm and an axial distance that varied from 40 nm to 80 nm with a median axial distance of 58 nm. Nup107 had a lateral distance that ranging from 80 nm to 130 nm with a median lateral distance of 100 nm and an axial distance that varied from 30 nm to 70 nm with a median axial distance of 54 nm. Finally, Nup133 had a lateral distance that ranged from 80 nm to 140 nm with a median lateral distance of 102 nm and an axial distance that varied from 20 nm to 65 nm with a median axial distance of 38 nm. These results illustrate that the median values of the axial and lateral single NPC derived distance distributions are consistent with the distances extracted directly from the averaged images and in addition, highlight the intrinsic axial and lateral variability that exists within individual scaffold NOI (see Chapter 3: Discussion for further details).

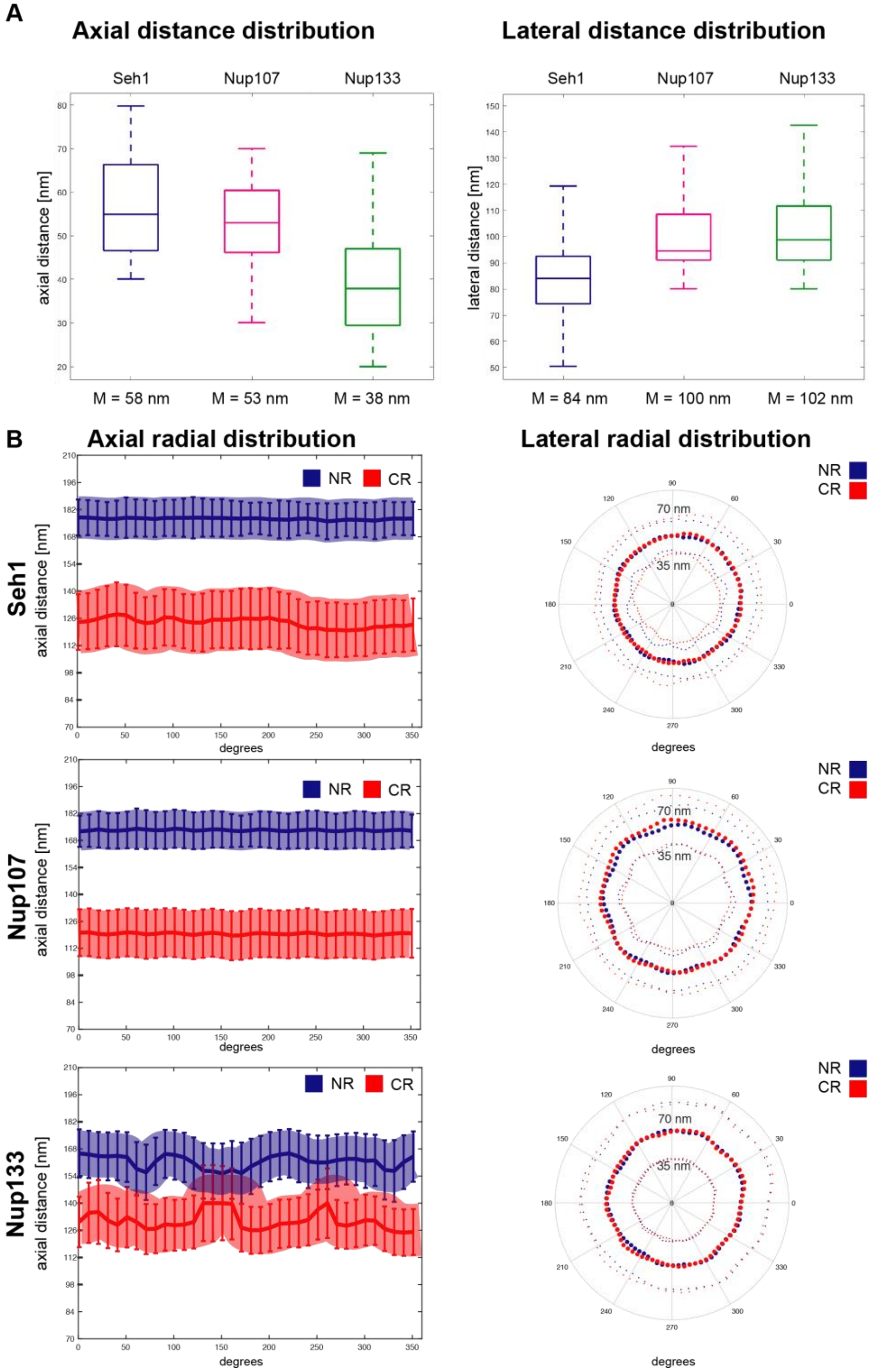

FIGURE 2-15. Variability of static nucleoporins. A) Distribution of the axial and lateral distance positions of individual 4Pi-SMLM static Nups (Seh1: purple, Nup107: pink and Nup133: green). Distance estimations were performed on the axial and lateral profiles of 4Pi-SMLM particles by fitting a double Gaussian function. The median (M) of each boxplot distribution is indicated. **B)** Mean and SD of the axial and lateral distance of the radial position in the NR and CR of Seh1 (top), Nup107 (middle) and Nup133 (bottom). (SD: standard deviation; NR: nuclear ring; CR: cytoplasmic ring). Analysis performed in collaboration with Julius Hossain (B).

To further investigate the axial and lateral variability within individual eight-fold subunits and explore how each of the analyzed particles is positioned with respect to the final averaged image, the mean and standard deviation of the axial and lateral variability at each individual rotational position (across 360°) of the NR and CR was calculated independently (Fig.2-15 B; for details see Chapter 4: Materials and Methods). This analysis illustrated the extent of positional dispersion across the entire circumference of both NR and CR in individual particles compared against the mean position retrieved after 3D SMLM averaging for Seh1 (NR: mean axial SD: ±9.1 nm; mean lateral SD: ±11.3 nm and CR: mean axial SD: ±14.4 nm; mean lateral SD: ±15.3 nm), Nup107 (NR: mean axial SD: ±9.3 nm mean lateral SD: ±13.6 nm and CR: Axial: mean axial SD: ±12.5nm; mean lateral SD: ±16.4 nm) and Nup133 (NR: mean axial SD: ±13.5 nm; mean lateral SD: ±21.8 nm and CR: mean axial SD: ±13.9 nm; mean lateral SD: ±22.2 nm). These results highlight the existing degree of variability across the entire circumference of both NR and CR in the scaffold NOIs and suggest the presence of different conformational states within the scaffold of the NPC (for further details see Chapter 3: Discussion).

2.3.4 Unsupervised structure-based classification of scaffold nucleoporins

Based on the observed axial and lateral variability within the scaffold NOI that form part of both nucleoplasmic and cytoplasmic rings, I hypothesized that unsupervised classification methodologies might be able to cluster individual NPCs into particles representing similar conformational states of an overall surprisingly dynamic core scaffold in an unbiased manner. In collaboration with Dr. Jean-Karim Hériché, I explored novel variable features within the scaffold NOIs through an unsupervised classification methodology that is based on topological data analysis. Here, individual 4Pi-SMLM particles are represented as 3D point clouds, from which topological signatures are extracted in the form of persistence diagrams (Edelsbrunner et al., 2002). Persistence diagrams encode the topology of the 3D point cloud space in a reduced dimensionality and with robustness to noise and can quantify the shape and structure of the analyzed data. The distance between persistence diagrams allows the clustering and subsequent classification of the 4Pi-SMLM particles (for details see Chapter 4: Materials and Methods).

To validate the use of persistence diagrams for the clustering and subsequent classification of 4Pi-SMLM particles, I first tested if this methodology can distinguish the different scaffold NOIs from each other based on their underlying characteristic topologies that lead to significantly different average structures. To verify this, I mixed individual 4Pi-SMLM particles of all scaffold NOIs, which were represented as persistence diagrams and calculated their relative distances. The resulting distance matrix (Fig.2-16 A) exhibited the characteristic checkerboard pattern of distance matrices clusters, confirming the presence of clusters of similar particles. To further inspect the cluster groups, their distances were represented in a tree diagram (Fig.2-16 B), whose second hierarchy branching illustrated that the persistence diagrams of individual 4Pi-SMLM particles of all scaffold NOIs clustered into at least four major groups (Fig.2-16 B). Each cluster contained one dominant NOI, showing that the unsupervised structure based clustering can recover differences between different NOIs. In addition, based on their topological similarity, the persistence diagrams revealed that the group of ELYS particles clustered further apart from the rest of the NOIs, while the groups of Nup107, Nup133 and Seh1 particles, clustered closely together, consistent with the single versus double ring differences between these groups. Within the double ring NOIs, Nup133 and Seh1 were most similar in their persistence diagrams, while Nup107 was clustered further apart, which could be explained by Nup107 having the smallest difference in rotational displacement compared to the rest of double ringed NOIs. This analysis demonstrated the capability of persistence diagrams to distinguish NOIs from each other based on their underlying topological signatures and validates the use of persistence diagrams for the structure-based clustering and classification of 4Pi-SMLM particles.

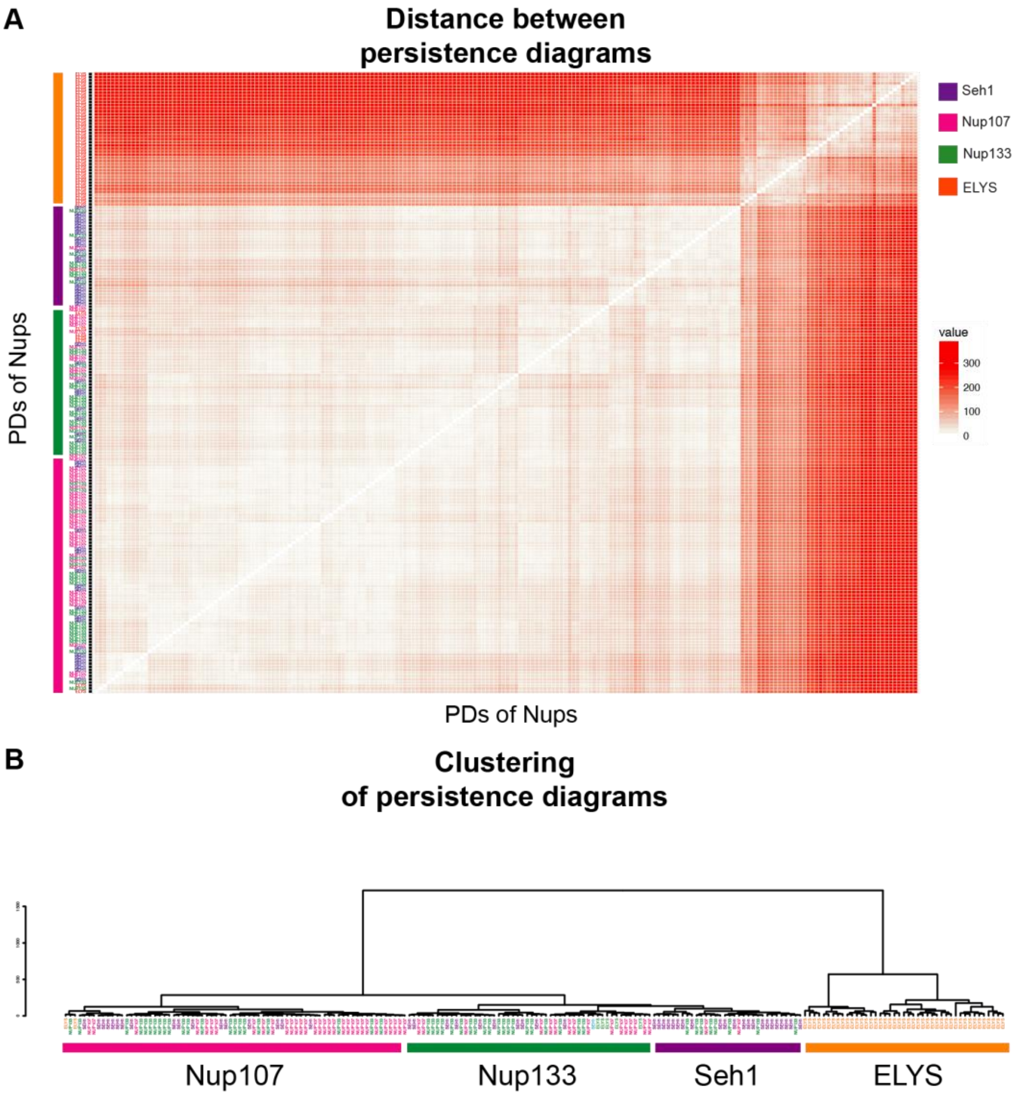

FIGURE 2-16. Clustering of persistence diagrams of static nucleoporins. A) Distance matrix between the peristence diagrams (PDs) of static nucleoporins (Seh1:purple; Nup107: pink; Nup133: green; ELYS: orange) showing the characteristic checkboard pattern of clusters in distance matrices. See Chapter 4: Materials and Methods for details on the algorithm of the clustering of persistence diagrams. **B)** Dendrogram of the persistence homology clustering of the 4Pi-SMLM particles of static nucleoporins (see Figure2-4). Each of the four major clusters was assigned the identity of the dominant Nup represented in it. The majority of nucleoporins cluster in their own representative cluster group (Seh1: purple; Nup107: pink; Nup133: green and ELYS: orange). See Chapter 4: Materials and Methods for details on clustering of persistence homology clusters and tree diagram. In collaboration with Jean-Karim Hériché.

Next, to investigate the variability within individual NOI that can be distinguished through the similarity of their topological signatures, the 3D point clouds of all single NPCs within each NOI were further analyzed based on their persistence diagram distances. For each NOI, a tree diagram that represented the persistence diagram distances of the corresponding 4Pi-SMLM particles was created (e.g. illustrated for Seh1 in Fig.2-17 A). Based on the tree branching, clusters were defined as the three most separated groups (Fig.2-17 A). To investigate the 3D structural differences between these intra-NOI clusters, the three classes for each NOI were then subjected separately to the 3D SMLM averaging pipeline (Fig.2-17 B).

The 3D reconstructions resulting from the 3D SMLM averaging of the different classes that were identified through unsupervised clustering revealed that the major architectural feature defining each class is the varying rotational positioning between subunits (Fig.2-17 B). Nucleoporins Seh1, Nup107 and Nup133 that form part of both nucleoplasmic and cytoplasmic rings of the NPC were used to verify the rotational differences between the corresponding subunits within the nuclear and cytoplasmic rings. These results indicate that all scaffold NOIs, in addition to having a highly variable axial and lateral position also exhibit highly variable rotational positioning within NPCs, revealing a surprisingly large degree of structural flexibility within the scaffold of the NPC.

2.4 Flexible nucleoporins

Having established a strategy that combined the unsupervised structure based classification of single 4Pi-SMLM particles with subsequent 3D SMLM particle averaging to uncover the structurally different arrangements of one NOI, I decided, to next apply these established tools to systematically determine the 3D architecture of flexible NOIs in the NPC (see 2.1). For this, I acquired single-color 4Pi-SMLM datasets of each flexible NOI with the previously developed labeling, mounting and acquisition techniques described in 2.1.1-2.

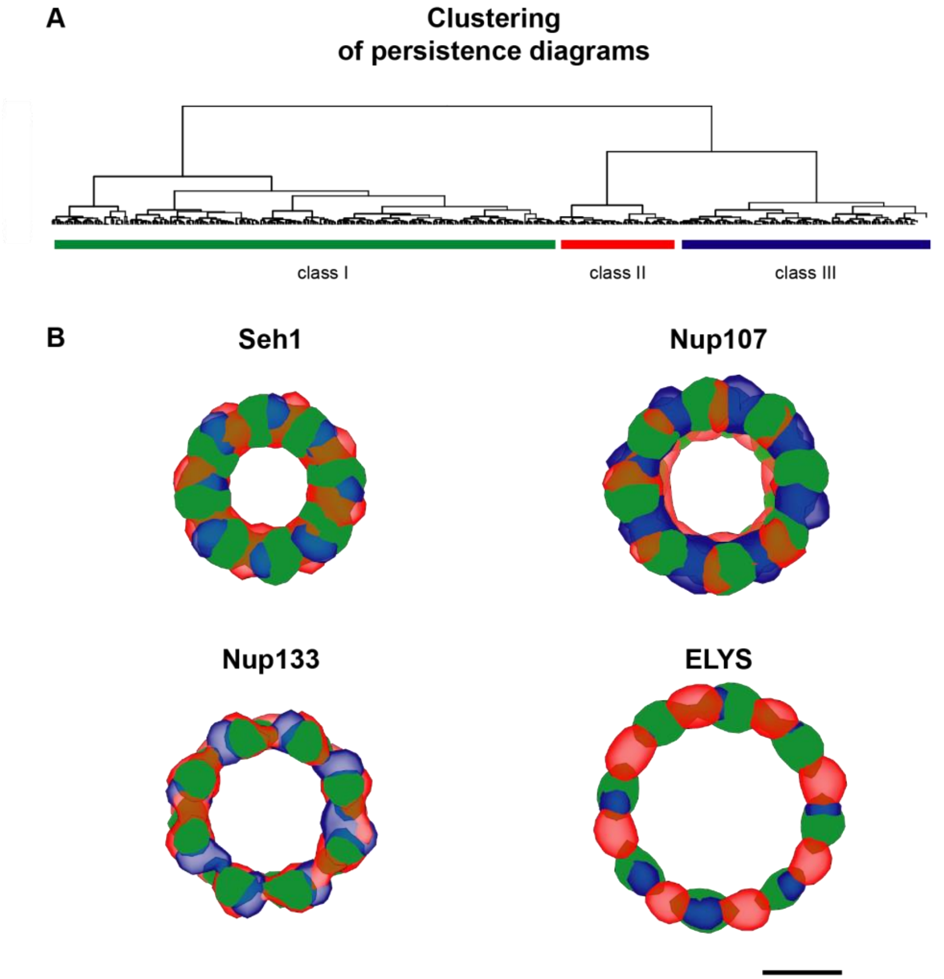

FIGURE 2-17. Rotational variability of static nucleoporins. A) Dendrogram illustrating the 4Pi-SMLM persistance homology clustering (see Figure2-16) of a particular nucleoporin dataset (exemplary clustering of Seh1 particles; see Figure2-4). Each cluster class selected for further 3D averaging is color-coded (class 1 = green; class 2 = red and class 3 = blue). **B)** The combined top-view density maps of the 3D averagings (4Pi-SMLM dataset of Figure2-4) of the three most represented clusters (class I = green; class II = red and class II = blue) of Seh1 (top-left); Nup107 (top-right); Nup133 (bottom-left) and ELYS (bottom-right). Scale bars indicate 50nm. In collaboration with Jean-Karim Hériché.

The flexible NOIs revealed a more irregular architecture compared to the scaffold NOIs in the 4Pi-SMLM images (Fig.2-18). While the 4Pi-SMLM images of Nup358/RanBP2 included pores with ring-shaped structures, they also included pores of a more filled disk signal distribution (Fig.2-18 A). In addition, the magnified top-view and side-view 4Pi-SMLM images illustrate that the different pore structures present in the images were mainly localized at the same z-position of the NPC (Fig.2-18 A i-ii). On the other hand, the 4Pi-SMLM images of TPR revealed an even greater variety of shapes, most of which resembled ring-shapes, disk-shapes or a combination of both (Fig.2-18 B). In addition, the magnified top-view and side-view 4Pi-SMLM images illustrate that the different pore structures presented in the images were localized at very different z-position of the NPC (Fig.2-18 B i-ii).

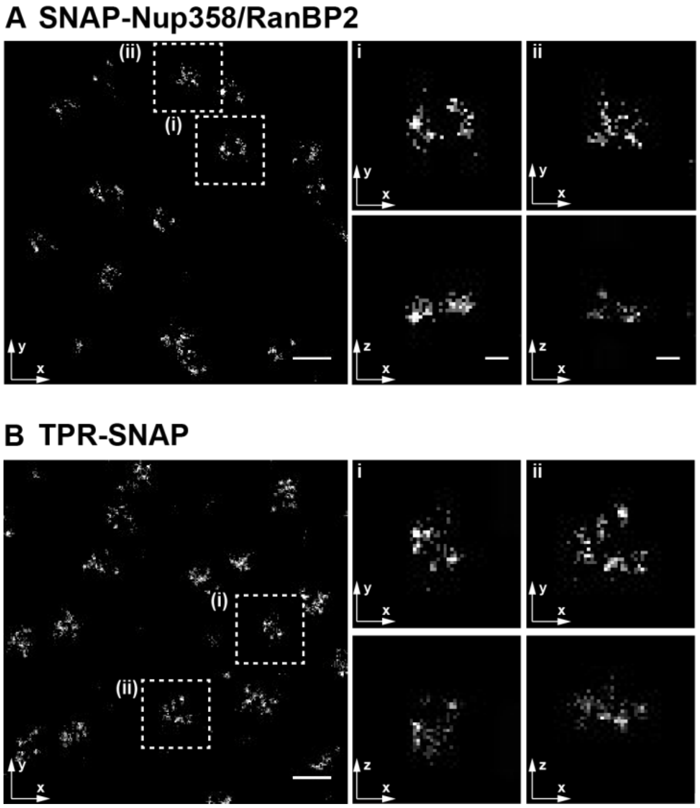

FIGURE 2-18. 4Pi-SMLM imaging of flexible nucleoporins. A representative 1.75 µm^2 area of the lower surface of the nucleus (scale bars indicate 200nm) and (i-ii) a top- and side-view image of one exemplary pore (x2.5 magnification; scale bars indicate 50nm). **A)** U2OS cell, endogenously expressing SNAP-Nup358/RanBP2, labeled with BG- AF 647; **B)** U2OS cell, endogenously expressing TPR-SNAP, labeled with BG- AF 647. The contrast in the images was adjusted for visualization.

In order to explore the intrinsic variability in shape of the flexible NOIs observed in the 4Pi-SMLM images, and determine their relative axial, lateral positional differences, I subjected the single particle based 3D point clouds for each flexible NOI to persistence diagram clustering (see 2.3.4) and subsequently independently averaged each representative class (see 2.2) (Fig.2.19).

2.4.1 3D averaging of flexible nucleoporins

The clustering of Nup358/RanBP2 persistence diagrams revealed the presence of at least two main classes (for details see Chapter 4: Materials and Methods), which were further subjected independently into the 3D SMLM averaging pipeline. Likewise, the clustering of TPR persistence diagrams indicated the presence of at least three main classes (for details see Chapter 4: Materials and Methods) that were independently averaged as well. Given the large size of the flexible NOIs (RanBP2: 358 MDa; TPR: 267 kDa) and their proposed roles in the formation of elongated and flexible filamentous structures (Cordes et al., 1997; Delphin et al., 1997), it is very important to consider the position of the incorporated SNAP-tag. While Nup358/RanBP2 was endogenously tagged at the N-terminus, TPR was tagged at the C-terminus. Thus, the 3D reconstructions that results from the described analysis represents the corresponding positional information of Nup358/RanBP2 N-terminus and TPR C-terminus.

The 3D reconstructions of the two main classes of Nup358/RanBP2 revealed that Nup358/RanBP2 particles formed both ring-shaped and globular shape architectures (Fig.2-19 A). The averaging of the first class of Nup358/RanBP2 particles recovered pores that included both a ring-shaped and a small central sphere-shaped structure, reaching a lateral distance of ~75 nm and an axial distance of ~30 nm calculated by the FWHM of the axial intensity profile distribution. The averaging of second class of Nup358/RanBP2 particles recovered pores that comprised a sphere-shaped structure only, with a lateral distance of ~33 nm and an axial distance of ~31 nm, both calculated by the FWHM of the lateral and axial intensity profile distribution. These results suggest that Nup358/RanBP2 N-terminus, which has been proposed to compose part of the cytoplasmic filaments close to the cytoplasmic ring of the pore (Fig.2-19 C), arranges into two main conformations within the NPC. The first conformation (i.e. represented by class I) forms a ring-shaped structure, suggesting its potential association to the cytoplasmic ring of the pore. The second major conformation (i.e. represented by class II) forms a sphere-shaped structure, suggesting either the ability of Nup358/RanBP2 to be present in an open and closed conformation, or the coexistence of Nup358/RanBP2 in the cytoplasmic ring and central lumen of the pore (for further details see Chapter 3: Discussion).

The 3D reconstructions of the three main classes of TPR revealed that TPR particles formed both highly flexible structures with features that resemble ring-shapes and sphere-shapes at drastically distant axial locations (Fig.2-19 B). The averaging of the first class of TPR particles recovered pores that contained a ring-shape structure and a small distal sphere-shape separated by an axial distance of ~85 nm from each other. The ring-shape structure can reach a lateral distance of ~65 nm. The averaging of the second class of TPR particles recovered pores that included an elongated sphere-shape architecture with an axial distance of ~45 nm and lateral distance of ~40 nm. Finally, the third class of TPR particles resolved pores with both a ring-shape and a small central sphere-shape structure and another distal sphere-shape structure separated by an axial distance of ~95 nm from each other. The ring-shape structure can reach a lateral distance of ~70 nm. These results suggest that TPR C-terminus, which is known to form part of the nuclear basket (Fig.2-19 C), arranges into highly flexible ring-shape and sphere-shape conformations, with an axial distances that can span from ~45-95 nm (Fig.2-19 B) (see Chapter 3: Discussion for further details). Two of the major classes (i.e. class I and III) of TPR included a ring-shape conformation, hinting into its potential positioning in the proximity of the nucleoplasmic ring of the pore compared to the distal sphere-shape conformation found in all major TPR conformations (Fig.2-19 B). In addition, one of TPR's conformations (i.e. class II) comprises sphere-shape structures positioned in close proximity to each other, suggesting the presence of an intermediate conformational state between the highly distantly positioned subunits within the rest of TPR's conformations (for further details see Chapter 3: Discussion).

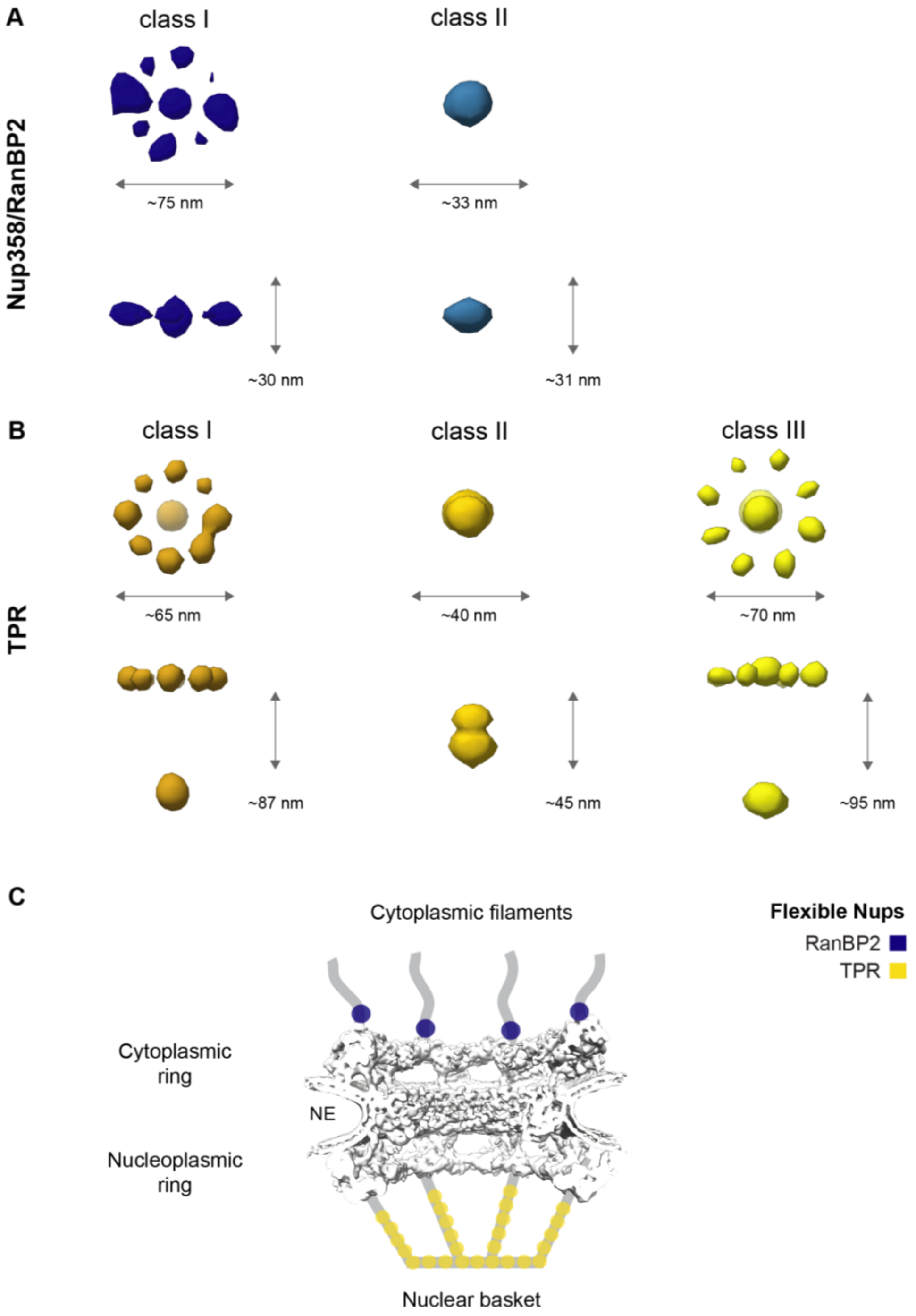

FIGURE 2-19. 3D averaging of 4Pi-SMLM flexible nucleoporins. Isosurface-rendered density maps of the most represented persistance homology clusters (see Figure2-17) of the 4Pi-SMLM datasets from Figure2-18. The implemented 3D averaging pipeline (see Figure2-4) was used with spherical masks (see Figure2-7). The axial and radial distances were calculated by fitting a double Gaussian function or FWHM to the corresponding intensity distribution profiles (see Figure2-6) of RanBP2 (RanBP2: class I: dark blue; class II: light blue) (A) and TPR (TPR: class I: dark yellow; class II: yellow; class III: light yellow) (B). **C)** A model describing the architecture of the NPC with the predicted positions of the flexible Nups.

2.5 3D mapping of the NPC

After accomplishing the aim of characterizing the 3D architecture of both scaffold and flexible NOIs with 3D SRM, as well as examining their intrinsic variability and conformational states, the next aim encompassed the integration of the architectural features retrieved from the averaging of single-color 4Pi-SMLM data into an overall 3D NPC map. This 3D map would allow us to obtain novel information about the relative positioning of uncharacterized NOIs within the NPC and fill this gap in our knowledge about the structure of the NPC.

Ideally, to obtain the position of each NOI relative to each other, all NOIs should be imaged simultaneously. However, as described in 1.3.3.3, multi-color imaging is much less straightforward in SMLM as in conventional light microscopy, given its limitation of the availability of compatible dyes for SMLM. Thus, multi-color SMLM is most effectively applied on only two molecular targets at a time. Due to this limitation, it was necessary to design an alternative strategy to retrieve the relative positions between many NOIs. In the proposed strategy ELYS serves as reference Nup and is systematically imaged in a pairwise fashion together with each of the other NOIs (see 2.1). The resulting dual-color images are further subjected to 3D averaging. Finally, the 3D dual-color reconstructions are integrated into a single 3D SMLM NPC map by overlaying the position of the reference Nup ELYS.

2.5.1 Dual-color SMLM strategies

To identify the dual-color labeling and imaging strategy that would provide us with the highest quality 4Pi-SMLM images that meet the quality control requirements for 3D averaging, I tested the efficiency of two different dual-color SMLM approaches: the activator-reporter and the ratio-metric approach (described in detail in 1.3.3.3). The selection of these dual-color SMLM approaches was guided by the compatibility of available dyes for SNAP-tag coupling and SMLM and the possibilities for modifications of the imaging system.

First, to minimize the modifications to the imaging system, I explored the use of the activator-reporter approach, which applies dye pairs; an “activator” dye and the a photoswitchable “reporter” dye as an individual probe (Bates et al., 2007). Here, the activator dye is excited with its appropriate wavelength and facilitates the photoswitching of the reporter dye, which will be the one detected. By using the same reporter dye in combination with different activator dyes, it is possible to separate the different colors with the use of alternating excitation wavelengths while keeping the emission wavelength constant. The activator-reporter technique has previously been demonstrated with the use of antibodies as a labeling methodology. For this approach, antibodies are labeled with the same proportion of “activator” and “reporter” dyes, which is possible as several dyes can be coupled to one antibody molecule chemically. However this established approach only works for the reference Nup ELYS, which is detected via specific antibodies, while most NOIs investigated in my study have an endogenously expressed SNAP-tag that only allows one-to-one stoichiometry between benzylguanine coupled dye and tag, requiring me to establish a new BG-ligand activator-reporter system for use with the SNAP-tag (Fig. 2-20 A). The first challenge was to screen for suitable activator-reported tandem-dyes that could be coupled to BG and would react with the SNAP-tag. In collaboration with the Facility for Synthetic Chemistry at the Max Plank Institute for Biophysical Chemistry in Göttingen, I screened and optimized the labeling conditions of a variety of SNAP-tag substrates coupled to tandem-dyes (from here on referred to as tandem SNAP-tag substrates) for their use in the activator-reporter approach (see Chapter 4: Materials and Methods for further details on the optimizations). The following tandem SNAP-tag substrates were tested:

- BG – A405-Cy5
- BG – Cy3-Cy5

- BG-peg – A647-A405
- BG-peg – A647-Cy3
- BG – A647-cadaverine-Cy3
- BG – A647-cadaverine-A405

The screening and optimization of all of the above listed tandem SNAP-tag substrates produced SMLM images of much inferior quality, compared to single-color SMLM images of the respective NOI, i.e. most produced a very high level of background, presumably due to poor molecular specificity. This might be due to their comparatively large size, which restricted the access to the nuclear compartment or compromises the reaction with the SNAP enzyme and/or their negative charge, which could cause higher non-specific binding events and consequently result in the observed high background signal. To improve the quality of SMLM images, I optimized the labeling protocols by increasing the permeability of the cell membrane and substantially lowering the working concentration of the tandem SNAP-tag substrates (for details see Chapter 4: Materials and Methods). Finally, the use of BG – A647-cadaverine-A405 at 200 nM of working concentration in the optimized labeling protocol produced dual-color SMLM images of improved quality (Fig. 2-20 A). While the obtained dual-color SMLM images showed significantly decreased background and improved labeling efficiency of NPCs, the number of localizations obtained from the tandem SNAP-tag substrates was still much lower compared to single color labeling with BG-A647, and below the quality criteria I had established for particle averaging. Thus, I explored alternative dual-color SMLM strategies that could produce higher quality SMLM images with less laborious and time-consuming labeling protocols.

As an alternative dual-color SMLM approach, I tested the use of the ratio-metric approach described in 1.3.3.3, together with SNAP-tag labeling. However to implement this strategy, some optical modifications had to me implemented on imaging system, for which I collaborated with Dr. Mark Bates. Here, the simultaneous acquisition of different fluorophores is achieved by using the same excitation wavelength but detecting different emission spectra (Lampe et al., 2012; Testa et al., 2010) (Fig. 2-20 B). For this, the different dyes have to be carefully selected to ensure overlap of the excitation but still separable emission spectra.

To separate the spectrally partially overlapping emissions into two detection paths, a custom dichroic mirror is used. Thus, the selection of each pair of dyes requires the selection of an appropriate custom dichroic mirror for the correct separation of signal as well optimization of the blinking buffer composition. Based on the ratio of each single molecule signal intensities in each detector, the color can be assigned to each localization event. For this strategy, I tested the following dye pairs coupled to either the SNAP-tag substrate or a secondary antibody in combination with long-pass (LP) dichroic mirrors and blinking buffer compositions (Table 1; for details see Chapter 4: Materials and Methods):

Optional dye pairs	Optional mirrors	Optional thiols for blinking buffer
IgG – A647 with BG – CF680	671 nm, 678 nm and 685 nm LP	10 mM MEA or 143 mM βME
IgG – CF680 with BG – A647	671 nm, 678 nm and 685 nm LP	10 mM MEA or 143 mM βME
IgG – A647 with BG – Cy5.5	671 nm, 678 nm and 685 nm LP	10 mM MEA or 143 mM βME
IgG – Cy5.5 with BG – A647	671 nm, 678 nm and 685 nm LP	10 mM MEA or 143 mM βME

Table 1: Tested conditions for dual-color ratio-metric imaging

The screening and labeling optimization of the above listed dye pairs together with the LP dichroic mirrors and blinking buffer compositions produced SMLM images of greater quality compared to the ones obtained with the activator-reporter approach. From the tested conditions, the highest quality images were achieved when cells were stained with IgG – CF680 with BG – A647 and IgG – A647 with

BG – Cy5.5, using a 678 nm LP dichroic. While the photoswitching properties of the dyes used in both staining conditions performed well when imaged with 10 mM MEA, the combination of A647 with Cy5.5 performed even better when used together with 143 mM βME. Thus, the condition IgG – A647 with BG – Cy5.5 together with a blinking buffer containing 143 mM βME and incorporating a 678 LP dichroic mirror was selected for dual-color 4Pi-SMLM imaging in this work (Fig. 2-20 B).

2.5.2 Dual-color SMLM imaging of the NPC

After successfully selecting and optimizing the dual-color SMLM technique suitable for imaging the NOI, I acquired dual-color 4Pi-SMLM datasets of the scaffold NOIs with the previously optimized labeling strategy, buffer composition and setup modification described in 2.5.1.

As expected from my previous single-color results on scaffold NOIs, the dual-color 4Pi-SMLM images revealed two ring-shape architectures arising from the reference Nup ELYS and a second scaffold NOI (Fig.2-21). The 4Pi-SMLM images show that the reference ring of ELYS has a comparatively larger diameter to Seh1 (Fig.2-21 A) and Nup107 (Fig.2-21 B), corroborating the results obtained from single-color 4Pi-SMLM imaging. Moreover, the magnified top-view and side-view images (Fig.2-21 A-B) recapitulated the identified architectures of scaffold NOIs, i.e. ELYS forms one single ring within the NPC, while the rest of NOIs form two rings of different heights within the NPC. In addition, the dual-color 4PI-SMLM images reveal the uncharacterized position of the reference Nup ELYS relative to the rest of the NOIs, showing that ELYS is positioned in proximity to the nucleoplasmic ring of scaffold NOIs.

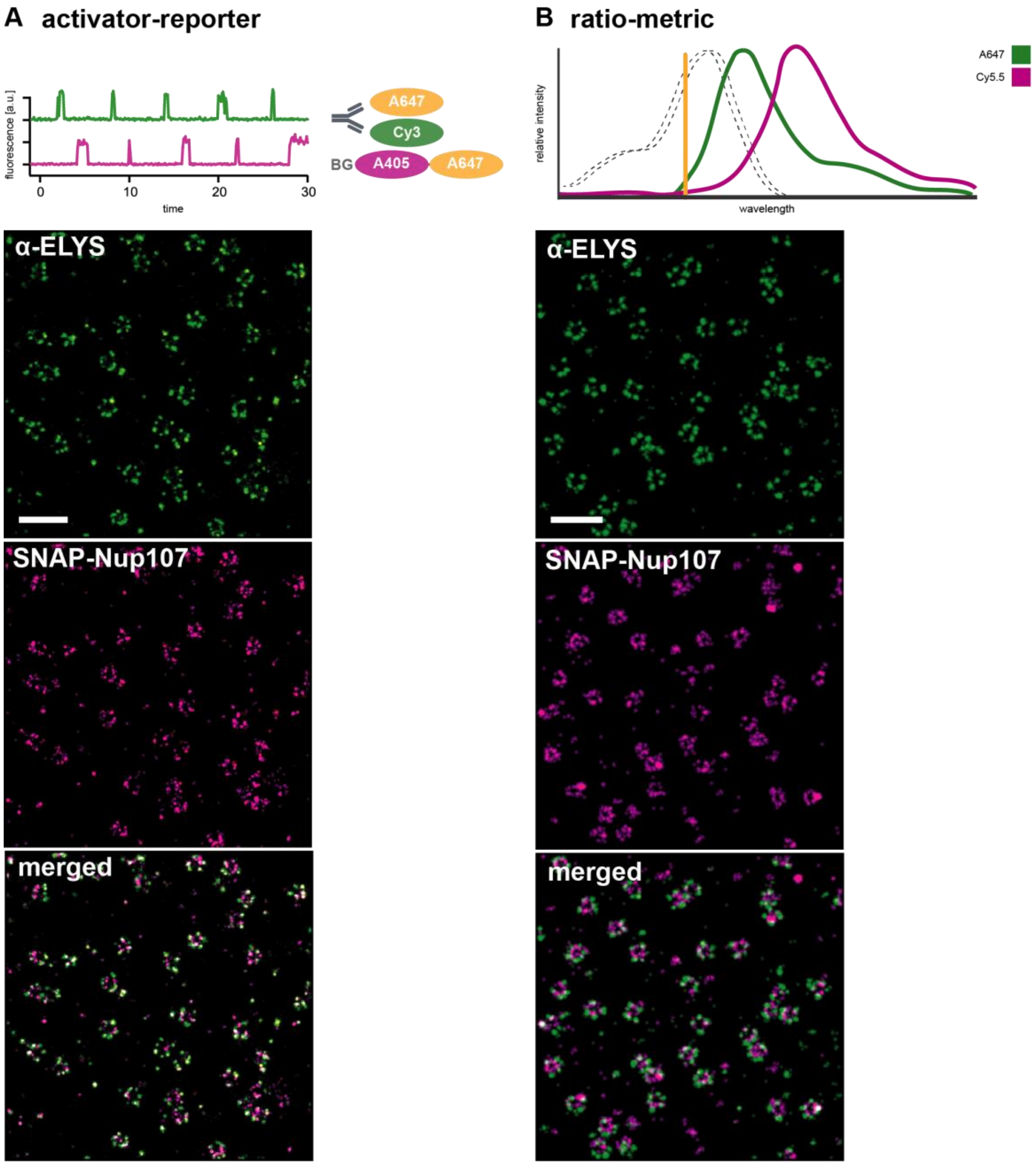

FIGURE 2-20. Dual-color SMLM optimization. A) Schematic representation of the activator-reporter approach for dual SMLM imaging (adapted from Bates, 2007). Dual-color gallery view of a U2OS cell, endogenously expressing SNAP-Nup107, labeled with BG-A647-cadaverine-A405 and an antibody against ELYS with the secondary antibody simultaneously coupled to AF647 and Cy3. **B)** Schematic representation of the ratio-metric approach for dual SMLM imaging. Dual-color gallery view of a U2OS cell, endogenously expressing SNAP-Nup107, labeled with BG-Cy5.5 and an antibody against ELYS with a secondary antibody coupled to AF647. Scale bars indicate 500 nm.

2.5.3 Relative averaging of scaffold nucleoporins

In order to obtain quantitative relative axial, lateral and rotational distance positions between the pairs of NOIs, I first adapted the 3D SMLM averaging pipeline for dual-color 4Pi-SMLM. Here, each dual-color 4Pi-SMLM dataset is split into separate 4Pi-SMLM color channels (i.e. the channel of the reference and of the targeted NOI). The dual-color 3D SMLM averaging pipeline uses the channel of the reference NOI (i.e. the ELYS channel) to automatically select the 4Pi-SMLM particles from both color channels (see 2.2.1). All particles from a particular color channel are then subjected to the 3D SMLM averaging pipeline and the resulting 3D reconstructions are combined for visualization and analysis purposes into a photon density map (see Chapter 4: Materials and Methods). From the combined dual-color 3D reconstructions, novel relative distance measurements (i.e. lateral, axial and rotational displacements) between the reference and the targeted NOI were extracted. For analyzing the relative rotational displacements between the subunits of the reference against the targeted NOI, the angular rotations were performed clockwise along the direction of the transport axis.

The resulting relative 3D reconstructions from averaged dual-color 4Pi-SMLM datasets (Fig.2-22) confirmed that ELYS forms a single ring within the NPC with a lateral distance that reaches ~ 145 nm in diameter. The distance estimations of the relative 3D reconstructions of Seh1 together with ELYS (Fig.2-22 A) show that Seh1 forms a double ring-shape structure with the smallest lateral distance (80 nm) and the largest axial distance (58 nm), compared to Nup107. In addition, the relative distance measurements revealed that the nucleoplasmic ring of Seh1 is positioned in very close proximity (14 nm) to the single ring formed by ELYS and the eight-fold subunits of Seh1 exhibits a relative displacement of 18° to the subunits of ELYS.

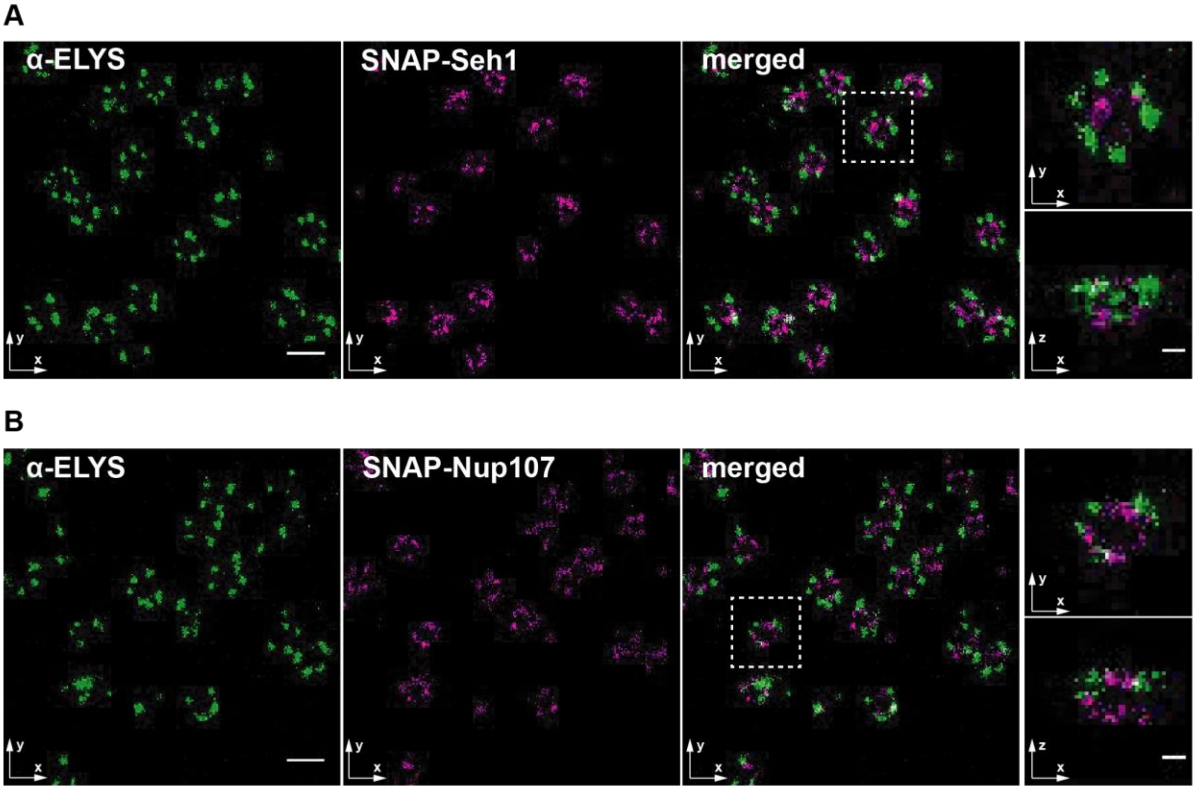

FIGURE 2-21. Dual-color 4Pi-SMLM imaging of static nucleoporins. A representative 1.75 μm^2 area of the lower surface of the nucleus (scale bars indicate 200nm) and a top- and side-view image of one exemplary pore (x2.5 magnification; scale bars indicate 50nm). **A)** U2OS cell, endogenously expressing SNAP-Seh1, labeled with BG- AF 647 and an antibody against ELYS; **B)** U2OS cell, endogenously expressing SNAP-Nup107, labeled with BG- AF 647 and an antibody against ELYS.

Similarly, the relative 3D reconstructions of Nup107 together with ELYS (Fig.2-22 B) show that Nup107 has a larger lateral distance (98 nm) and a smaller axial distance (52 nm), compared to Seh1. The relative distance measurements between Nup107 and ELYS revealed that the nucleoplasmic ring formed by Nup107 is consistently positioned in close proximity (16 nm) to the single ring formed by ELYS and the eight-fold subunits of Nup107 have a relative displacement of 17° to the subunits of ELYS.

With the positional information obtained from the relative 3D reconstructions of averaged dual-color 4Pi-SMLM particles I i) corroborated the architectural differences between the scaffold NOIs obtained from the 3D reconstructions of averaged single-color 4Pi-SMLM images and ii) obtained novel information about the precise axial, lateral and rotational position of ELYS with respect to the rest of the scaffold NOIs (for further details see Chapter 3: Discussion), demonstrating directly for the first time its position at the peripheral base of the nucleoplasmic ring, quite close to the inner nuclear membrane.

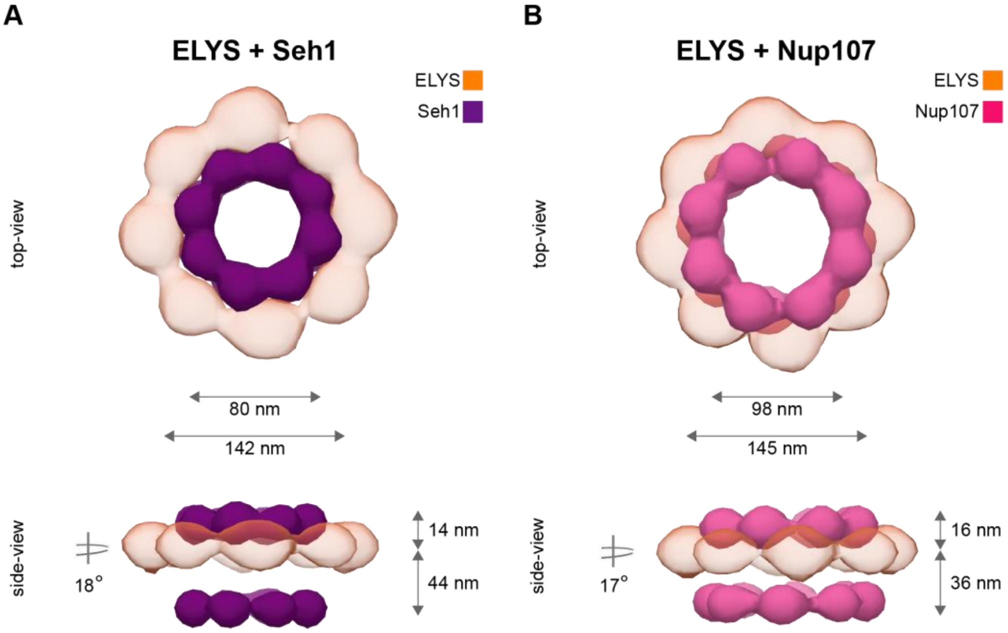

FIGURE 2-22. 3D averaging of dual-color 4Pi-SMLM static nucleoporins. Isosurface-rendered density maps of the top and side-view 3D averagings of the dual-color 4Pi-SMLM datasets from Figure2-21 (Seh1: purple, Nup107: pink and ELYS: orange). The implemented 3D averaging pipeline (see Figure2-5) was used with elliptical masks (see Figure2-7). The axial system drift was corrected by the axial interpolation of references (see Figure 2-9). The axial and radial distances were calculated by fitting a double Gaussian function to the corresponding intensity distribution profiles (see Figure2-6). The subunit rotational shifts were calculated by the rotational correlation-based approach (see Figure2-11) for ELYS and Seh1 (A) and ELYS and Nup107 (B).

2.5.4 3D mapping of scaffold nucleoporins

Finally, to consolidate the relative positional information obtained from the averaging of dual-color 4Pi-SMLM into a single 3D molecular map of the NPC, I aligned each dual-color averaged reference based on the relative positioning of the reference nucleoporin ELYS. For this, I calculated the relative axial, lateral and rotational differences between the positions of the reference nucleoporin ELYS present within each independent dual color dataset with the strategies described in 2.2.3 and 2.2.8 (for details see Chapter 4: Materials and Methods).

The relative position of ELYS between the two different dual-color 4Pi-SMLM datasets revealed that ELYS was stably located at the same axial and lateral position but exhibited an arbitrary rotational displacement of 6°, as both datasets were 3D averaged independently. To align both of the dual-color averaged references to each other, I first selected one of the dual-color averaged references as the template reference to which the second reference was registered. The second dual-color averaged reference was then interpolated in the rotational-plane by the amount of displacement (6°) obtained from the above-described measurements (for details see Chapter 4: Materials and Methods).

The position of the reference nucleoporin ELYS in the newly interpolated volume co-localized with the reference nucleoporin in the template volume, thus confirming the successful alignment between dual-color 4Pi-SMLM averaged references. Lastly, a 3D reconstruction was created, by combining the dual-color template reference image with the newly interpolated image, which depicts the relative positions of the NOI analyzed in 2.4.3 in a proof-of-principle 3D molecular map of the NPC (Fig.2-23).

The established 3D molecular map of the NPC integrates structural and positional information about NOIs from two independent pairwise measurements with a common reference. Thus, this map represents a scalable pipeline that opens the possibility for exploring the relative architectural features between any number of NOIs, analyzed relative to the same reference. From this infrastructure, new positional information can also be extracted between the independently measured NOIs, which remained inaccessible in individual protein 3D reconstructions of dual-color SMLM images. This strategy can be further implemented to position the rest of scaffold and flexible NOI as well as integrate the newly discovered flexible conformational states that each NOI was shown to possess.

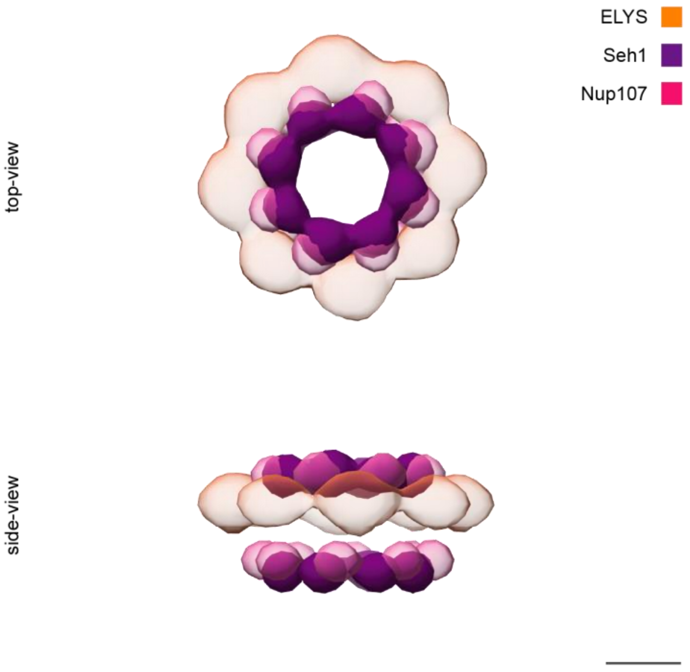

FIGURE 2-23. 3D mapping of static nucleoporins. Isosurface-rendered density maps of the top and side-view 3D averagings of the combined dual-color 4Pi-SMLM datasets (Seh1: purple, range= -0.000617-0.255, level = 0.065 ; Nup107: pink range= , level = and ELYS: orange, range= -0.00124-0.754 , level = 0.077) from Figure2-22. The positioning between the density maps was calculated by rotational correlation-based differences between ELYS subunits and applied for visualization. Scale bar indicates 50 nm.

3 Discussion

During my PhD studies, I have implemented 3D SMLM to study the architecture of the NPC in human cells. For this, I first systematically optimized the sample labeling, embedding and imaging conditions to acquire high quality images on a 4Pi-SMLM. I next established and validated a 3D SMLM averaging pipeline that incorporates information of hundreds of pores to resolve with great precision the 3D architecture of each of the nucleoporins under study and allows the extraction of quantitative information regarding their position inside the NPC. I further applied these methodologies to study how individual nucleoporins, which form part of both the static scaffold and the flexible periphery of the pore, are structurally organized within the NPC and what the different conformations are that they exhibit *in situ*, which indicates a surprisingly dynamic nature of the NPC architecture. Finally, I established a complementary strategy that combines two-color 3D SMLM with averaging, which allowed me to integrate and position the nucleoporins under study into a multiprotein 3D molecular map of the NPC. In this chapter, I will discuss how these efforts have advanced the application of 3D SMLM combined with averaging for the understanding of the dynamic architecture of the NPC and the characterization of its flexible regions that had remained inaccessible for atomic-resolution methodologies previously.

3.1 The 3D molecular organization of the NPC revealed by 4Pi-SMLM

The structure of the NPC has been studied throughout the last six decades mainly with atomic-resolution techniques. State-of-the-art NPC models have docked a large range of available crystal structures of individual Nups and partial sub-complexes into recent high-resolution cryo-ET density maps of the scaffold of the NPC with the aid of modeling approaches (von Appen et al., 2015; Bui et al., 2013; Kim et al., 2018; Kosinski et al., 2016; Lin et al., 2016). While current NPC models have characterized the consensus scaffold structure of the pore in great detail, the nucleoporins that localize asymmetrically or have a flexible architecture have been dismissed from the reconstructions. In addition, existing models illustrate an averaged snapshot of the pore scaffold and do not provide information about the dynamic conformational landscape it could explore natively. Therefore, during my PhD work I set out to investigate the architecture and conformational landscape of scaffold, asymmetrically positioned and flexible Nups. To this end, I implemented SRM-based techniques as these have the advantage of combining molecular specificity and high signal to noise, which can capture the underlying variability and flexibility of molecular components, with nanoscale high-resolution imaging.

2D SMLM techniques have previously been shown to provide complementary structural information about specific molecular components of the pore (Löschberger et al., 2012; Szymborska et al., 2013). To achieve high localization precision in all dimensions and in order to investigate asymmetrically positioned and flexible Nups, which could exhibit more complex conformations, a 3D SMLM technique was needed. The 4Pi-SMLM microscope was used for this study due to its inherent superior resolution in 3D compared to other currently available 3D SRM approaches (Aquino et al., 2011). The implementation of 4Pi-SMLM and imaging optimizations were performed in collaboration with Dr. Mark Bates and Prof. Dr. Stefan Hell at the Department of NanoBiophotonics at the Max Plank Institute for Biophysical Chemistry in Göttingen.

During the initial phase of my PhD work, I established and optimized the necessary labeling and imaging conditions to obtain high quality single-color 4Pi-SMLM images of the NPC. To achieve this, it was important to select a compatible labeling strategy that combines specific labeling, low background and a small size to decrease the risk of functional perturbation and achieve a minimal offset to the protein of interest. The choice of the fluorescent dye is also critical for the performance of SMLM, thus I selected the organic dye AF647 to be used consistently throughout all single-color 4Pi-SMLM optimizations and experiments, as this dye has been thoroughly studied and reported to have very good photo-switching properties (Dempsey et al., 2011). Initially, I compared indirect labeling strategies (i.e. antibodies and nanobodies) against the use of a direct labeling (i.e. SNAP-tag), as all of these labeling strategies are compatible with a wide choice of dyes for multicolor imaging. I compared the quality of 4Pi-SMLM images resulting from α-GFP antibody labeling, α-GFP nanobody labeling and SNAP-tag labeling in endogenously expressing GFP-Nup107 or SNAP-Nup107 human cell lines (Fig.2-2). My results are in line with previous studies (Ries et al., 2012; Szymborska et al., 2013), showing that α-GFP indirect immunofluorescence labeling produces a high density of labeling, which is likely due to signal amplification by the use of primary and secondary polyclonal antibodies and the possibility of coupling multiple dyes per secondary antibody. However, this approach presents high background noise, likely due to unspecific binding and results in the highest offset to the NOI (Fig.2-2 A). α-GFP nanobody labeling showed the lowest labeling specificity and highest background noise, but due to its relative small size compared to conventional antibodies, reduced the offset of the NOI (Fig.2-2 B). Finally, my results on SNAP-tag labeling revealed that this labeling method has high specificity but a low density of labeling compared to previous conditions, which likely results from the lack of AF647 signal amplification due to 1:1 covalent binding between the self-labeling genetically fused protein tag and the benzylguanine-dye molecule. This condition revealed no background noise and the smallest offset to the NOI (Fig.2-2 C). Based on these qualitative comparisons I selected SNAP-tag labeling as the strategy of choice given its high labeling specificity, low background noise and better approximation to the molecular position of the NOI, compared to the indirect affinity labeling reagents I tested. In addition, as a labeling system for multicolor imaging, I selected the use of specific primary antibody detected by labeled secondary antibody against one reference NOI (ELYS) because this strategy produced higher quality 4Pi-SMLM images compared to nanobody labeling, could be combined well with SNAP-tag labeling and as the reference served for data integration only, the offset was not an obstacle in this case.

The embedding medium and acquisition conditions were subsequently optimized for obtaining high quality 4Pi-SMLM images in endogenously expressing SNAP-Nup107 human cell lines (Fig. 2.3). Given that the sample mounting for 4Pi-SMLM, allows only a small volume of up to ~30 µl it was important to test which blinking buffer would not become exhausted and provide good photoswitching behavior over the prolonged acquisition times necessary to obtain many localization events and high localization precision. I thus tested the performance and durability of AF647 in reported blinking buffers containing 10 mM MEA or 143 mM βME with an oxygen removal system (Dempsey et al., 2011) for 4Pi-SMLM. Both tested blinking buffers produced good AF647 photoswitching and resulted in high-quality 4Pi-SMLM images, however, after a period of 3h, the photoswitching of AF647 deteriorated significantly in the presence of 143 mM βME compared to 10 mM MEA, thus I selected MEA as the primary thiol of choice in the blinking buffer used for single-color 4Pi-SMLM experiments. During buffer optimizations for multicolor imaging, I identified an incompatibility of βME with the curing agent of choice (picodent) for the embedding of the sample, which explains the difference in durability. Finally, the 4Pi-SMLM imaging of NPC was further optimized by illuminating the sample with a highly inclined beam of excitation light (HiLo) (Tokunaga et al., 2008). In line with the described advantages reported by Tokunaga et al., our results using 'HiLo' illumination show an increased signal-to-noise ratio and improved single-molecule detection during 4Pi-SMLM imaging due to less out of focus signal contribution.

In conclusion, the performed labeling, embedding and imaging optimizations resulted in high-quality 4Pi-SMLM images of the NPC, which clearly revealed in 3D a dual ring-like architecture for Nup107 (Fig.2-3 B-E), which is consistent with current models of the scaffold pore structure (von Appen et al., 2015; Bui et al., 2013).

3.2 The architecture of the NPC revealed by 3D SMLM averaging

The localization density of individual NPCs in 4Pi-SMLM images depends on the switching properties of the dye and the completeness of labeling, which can present a substantial degree of variation. Thus, it is difficult to draw objective structural conclusions from single NPCs present in 4Pi-SMLM images as missing information could bias such interpretations. To overcome this systematic under-labeling limitation and enhance the signal-to-noise ratio present in the 4Pi-SMLM images, I implemented a 3D SMLM averaging approach in collaboration with Dr. Shyamal Mosalaganti and Dr. Martin Beck. Averaging methods are routinely used in the field of EM to integrate information from a large number of copies of a specific molecular assembly to increase the signal-to-noise ratio and resolution of the image containing the structure of interest. However, its incorporation in the field of SRM is fairly recent and the existing pipelines are very specific for each macromolecular complex of interest and the specific SRM technique in use. Due to this scarcity of generally applicable particle averaging methods for SRM, I developed a new 3D averaging method that allows me to analyze 3D SMLM images to determine the underlying 3D architecture of the NOI and extract quantitative 3D information about their spatial positioning.

3.2.1 3D SMLM averaging of nucleoporins

I established an initial 3D SMLM averaging pipeline that included i) automatic picking of hundreds of 4Pi-SMLM particles of a particular NOI, ii) homogenization of the AF647 signal distribution prior of averaging, iii) iterative generation of references with 8-fold symmetry and iv) 3D particle alignment (Fig.2-4 A-D). This pipeline generated an initial 3D reconstruction of Nup107 with well-refined nucleoplasmic and cytoplasmic rings (Fig.2-4 E).

In addition, I systematically evaluated how the 3D SMLM pipeline handles a broad range of image quality parameters. For this, I made use of simulated 4Pi-SMLM particles and varied key SMLM image quality parameters that can be optimized experimentally, such as localization precision (LP) and degree of labeling (DOL). From the analysis of averaged images of simulated 4Pi-SMLM particles with a combination of LP (5 nm, 10nm and 20 nm) and DOL (30%, 50% and 100%) I concluded that particles with a LP of 10 nm and below and DOL of 50% and above are suited for 3D SMLM averaging and will result in reconstructions where both rings formed by scaffold Nups will be well resolved (Fig.2-5). This could be due to the fact that with decreasing DOL and increasing LP it is more difficult to create an initial reference that would contain sufficient constraints for a stably converging alignment. Also, while the DOL tolerated by the SMLM averaging pipeline is likely to be a general limitation for most structures of interest, the limit in LP will depend on the size of the particular macromolecular complex under study and should be re-evaluated for different structures of interest. For the case of the NPC, while it has been reported that images with a LP ~20-30 nm can resolve in 2D the ring-shape architecture of the NPC (i.e. diameter of ~80-120 nm) (Szymborska et al., 2013), smaller LPs are needed to discriminate the axial positions of the NOI in 3D as their axial distances are significantly shorter (i.e. ~30-50 nm), which explains the need for stringent LP and DOI parameters for the 3D SMLM pipeline.

3.2.2 The axial and lateral organization of the NPC

I further set up a strategy for extracting precise axial and lateral positions from the averaged 4Pi-SMLM particles based on the Gaussian fitting of the averaged axial and lateral intensity profiles and validated its accuracy and performance on averaged simulated 4Pi-SMLM particles. The calculated axial and lateral distances of the averaged simulated 4Pi-SMLM particles highly approximated the ground truth positions set in the simulations (Fig.2-6). As discussed above, it is important to remember that the LP and DOL influence the particle alignment and averaging and thus the quality of the 3D reconstructions obtained from SMLM images, which subsequently also affects the precision of the axial and lateral positions determination. Thus, the lateral distance offset seen in on averaged simulated 4Pi-SMLM particles (Fig.2-6 B) could arise from particle misalignment. In addition, when comparing the axial intensity profile between the first and the last reference image (Fig.2-6 A-B), it became clear that a proportion of particles which were present in the nuclear ring prior to alignment were absent in the axial intensity profile of the last reference image, supporting the hypothesis of misaligned particles. In conclusion, the axial and lateral position extraction strategy allowed highly accurate distance determinations and was incorporated into the analysis pipeline in this work, however the distance determination strategy on averaged simulated 4Pi-SMLM also suggested the presence of misaligned particles, which I further investigated and resolved.

3.2.3 Optimization of NPC averaging

In order to further investigate the proportion of misaligned particles during 3D SMLM averaging and to find an optimization solution to correct and allow an equal refinement between nuclear and cytoplasmic ring (NR and CR), I averaged each ring independently. For this, I used masks, which confine the reference to a specific volume (e.g. spherical, elliptical, cylindrical, etc.) allowing me to ignore likely unspecific signal from outside the masked region throughout the averaging steps. Masks are routinely used in EM averaging steps to reduce background noise or to define a substructure of interest. I compared the resulting averaged images from references masked with a spherical volume mask (i.e. encompassing both NR and CR) or two elliptical volume masks (i.e. encompassing only the NR or CR) (Fig.2-7). The averaged image with a spherical mask retained the difference in intensity distribution between the NR and CR, while the averaged image with the elliptical mask recovers more equally refined rings, indicating that this confinement restricts particle misalignment. These results are in line with the hypothesis that the observed misalignment is most likely caused by the preferential alignment of rings to the reference ring with higher intensity, which in some cases will cause a mismatch between NR and CR during averaging. Thus, the more restrictive volume confinement of particles to the NR and CR elliptical masks prevents alignment mismatch during averaging and improves the final 3D reconstruction.

With this analysis, I showed that the use of elliptical masks during averaging improves the refinement of both the NR and CR independently and results in a better approximation of the ground truth lateral distances set in the simulation of the 4Pi-SMLM particles (Fig.2-7). However, I also demonstrated that while the averages from independent elliptical masks (i.e. NR and CR) results in an improved refinement due to restriction of particle misalignment, they lack the axial stability seen in averages with spherical masks and the two rings can drift independently from each other in the z-plane (Fig.2-8). This can be explained by the fact that the elliptical masks ignore the signal outside the masked region throughout the averaging steps and thus align each ring independently from each other and can potentially incorporate independent shifts in the z-plane, which can change the original axial distance between the masked particle regions.

To retain the improved average rings with elliptical volume masks and correct for the axial position drift, I developed a strategy that uses the information of references averaged with both a spherical and two elliptical masks and restores the axial positions based on interpolation (Fig.2-9). I validated this strategy by demonstrating that the resulting interpolated 3D reconstruction recovered axial (49.7 nm) and lateral (99.8 nm) distances very close to the ground truth positions (axial: 50 nm; lateral: 100 nm) (Fig.2-9 D) and integrated this analysis step into the established 3D SMLM analysis pipeline.

3.2.4 The radial organization of the NPC

To entirely validate the use of independent elliptical volume masks during 3D averaging, I further verified that the use of elliptical masks during averaging does not lead to independent rotational shifts between the two rings. For this, I compared the rotational intensity profiles of the resulting simulated averaged images from references masked with a spherical volume mask or two elliptical volume masks throughout each iteration step (Fig.2-10). The rotational intensity profiles measure the similarity between references through rotational 3D CC functions, as a function of rotational displacement and thus can indicate the presence of rotational system drifts. My analysis detected no rotational displacements in references averaged with either spherical (Fig.2-10 A) or elliptical volume masks (Fig.2-10 B-C), validating the use of independent elliptical volume masks during 3D averaging.

Moreover, I further applied rotational 3D CC functions to analyze the differences between the NR and CR rotational positions on averaged simulated 4Pi-SMLM particles. For this purpose, I established an approach that measures the similarity between references that originated from different elliptical volume masks, as a function of rotational displacement (i.e. volume of the NR against the CR). My analysis on the rotational intensity profiles across 360° revealed a clear rotational shift between NR and CR (Fig.2-11 A). I then divided the rotational intensity profiles in 45°-segments to calculate the degree of rotational displacement between individual eight-fold subunits between the NR and CR by fitting a Gaussian function to each 45° segment of the rotational 3D CC function. My calculations determined a rotational displacement of 8° between subunits of the NR and CR for simulated Nup107 particles (Fig.2-11 B), which are in line with the ground truth rotational difference (i.e. 8°). My strategy for determining the differences between the NR and CR rotational positions on averaged simulated 4Pi-SMLM particles demonstrated precision in quantifying rotational differences and was methodically included in the analysis workflow.

Taken together, I have set up a 3D SMLM averaging pipeline that generates refined 3D reconstructions of molecular components of the NPC from many individual pores extracted from 3D SMLM images. In addition, I established an analysis workflow that quantifies the lateral, axial and rotational position of the averaged molecular component under study. I validated both the 3D SMLM averaging and analysis workflow by subjecting simulated 4Pi-SMLM NPC particles into the pipeline and recovering the pre-determined ground truth positions. While I optimized the 3D SMLM averaging pipeline for the averaging of the NPC and used 4Pi-SMLM datasets, it can conceptually be applied to other large protein complexes and with datasets that have been derived from alternative 3D SMLM techniques, with only minor modifications. The main parameter potentially requiring adaptation for other imaging technologies being the localization precision and for other macromolecular structures the shape of the employed masks during averaging, if necessary. I envision that numerous future biological studies could benefit greatly from obtaining quantitative high-resolution molecular 3D information of macromolecular protein complexes by my averaging and analysis pipeline. In addition, my workflow can be further combined with time- or perturbation-dependent studies to gain mechanistic insights into the structure function relationship of the protein complexes under study *in situ*. I will exemplify in the next Discussion sections the potential of my methodology in gaining novel structural information by investigating the architecture of both scaffold and flexible molecular components of the NPC.

Finally, given the differences in image formation between cryo-EM and 3D SMLM, traditional subtomogram averaging routines might not be optimal analysis tools for SMLM data. Thus, I envision that in the near future 3D SMLM analysis frameworks will further develop algorithmically and move away from EM-based approaches, to become more powerful and generic tools for the study of structural biology *in situ*. Initial efforts in finding alternative methodologies for the registration of SMLM particles (Broeken et al., 2015) started to appear during the course of my doctoral work. However, the 3D reconstructions obtained with these alternative methodologies have not reached the quality of reconstruction obtained from traditional subtomogram averaging routines, and thus additional methodological improvements will be needed in the field.

3.3 Structural organization of scaffold nucleoporins

I first studied the 3D organization of scaffold NOIs as some of these (Seh1, Nup107 and Nup133) have been mapped in current EM models and consequently offer the opportunity to compare results from orthogonal methodologies and provide an additional validation for my pipeline. To this end I produced U2OS cells endogenously expressing the SNAP-tagged version of the NOI and acquired single-color 4Pi-SMLM datasets of each scaffold NOI (Fig.2-12). The top-view 4Pi-SMLM images revealed a ring-shaped architecture for scaffold NOI of varying diameters, consistent with previous findings performed with 2D SMLM techniques (Szymborska et al., 2013). However, when inspecting the 4Pi-SMLM images form a side-view perspective I could identify novel features about scaffold Nups that previous SMLM experiments were unable to capture. For instance, ELYS formed a single NPC ring compared to the other NOIs (Fig.2-12), which is atypical within the group of scaffold Nups. To obtain a quantitative comparison of the differences observed in the 4Pi-SMLM images of scaffold NOIs, I applied my 3D SMLM averaging analysis pipeline to each NOIs' 4Pi-SMLM dataset.

The resulting 3D reconstructions recapitulate the observed differences between scaffold Nups in 4Pi-SMLM images and determined their axial, lateral and rotational distances (Fig.2-13). My analysis revealed that Seh1 has the smallest diameter rings with the largest axial separation, followed by Nup107, Nup133 and ELYS, whose single ring has the largest diameter. In addition, it illustrated that the radial register shift between the NR and CR range from 6° found between Nup107 subunits to 13° found in Seh1 subunits. My results support the conclusion that the arm of the Y-shape-subcomplex in which Seh1 is located, is positioned closer in the lateral plane to the NPC cavity and further apart in the axial plane from the NE, compared with the stem and tail of the Y-shape-subcomplex where Nup107 and Nup133 are positioned respectively, which was determined to be in a more peripheral position in the lateral plane and a closer position the NE in the axial plane. This architectural arrangement of the Y-shape-subcomplex is consistent with current EM models (von

Appen et al., 2015; Bui et al., 2013) (Fig.2-13 B). Similarly, the smallest axial separation observed between Nup133 rings is also in line with its proposed interaction with the NE (Kim et al., 2014). In addition, my results confirm the suggested single-ring architecture of ELYS and indicate its position at the farthest periphery of the NPC.

The overall organization of scaffold NOIs was in line with the organization predicted in current EM models, providing strong validation for my experimental and computational pipeline. I then set out to compare the similarity between the axial and lateral positions of scaffold NOIs derived from these two orthogonal methodologies in more detail. Ideally, a comparison of positions obtained from averaged 4Pi-SMLM particles and positions obtained from docked crystal structures in current EM models requires consideration of the distance offset produced by both the labeling system and by the protein-tag that was incorporated at the N-terminus of the NOI during genome-engineering. While I could estimate the offset distance resulting from the labeling system, the crystal structures of the majority of the NOIs lack the N-terminal domain and thus did not allow me to predict the direction of the offset in the 3D structure model of the NPC. As an alternative, I implemented a different comparison strategy, where I created density maps from available docked crystal structures of each NOI at a resolution that would mimic that of my reconstructions obtained from the 3D SMLM averaging pipeline. The downsampled density maps allowed me to extract their approximate lateral and axial distances (Fig.2-14) and compare them to my SMLM derived parameters. The distance analysis performed on the downsampled density maps of the docked crystal structures confirmed the architectural differences between Seh1, Nup107 and Nup133 that were obtained by the 3D SMLM averaging and analysis pipeline. In addition, the axial and lateral distances of Seh1 and Nup107 obtained from the generated density maps were in very good agreement with the distances recovered from averaged 4Pi-SMLM images. In the case of Nup133, the lateral positions were also consistent, however the axial distance of Nup133 was smaller in the 4Pi-SMLM images (Fig.2-14). These differences in Nup133 axial ring distance could be explained by the position of the incorporated probe at the N-terminus of Nup133 (i.e. pointing in the direction of the NE), which could shift the signal from the fluorescent dye, and thus the averaged position, in the direction of the NE in comparison to the position of the docked crystal structure, which lacks the N-terminus of Nup133. In conclusion, the very good consistency between positions obtained from generated density maps and averaged 4Pi-SMLM images in my comparative analysis, validates the use of 3D SMLM averaging and analysis to determine structural parameters of the NPC and furthermore provides a strategy to integrate structural information from orthogonal methodologies for the understanding of the architecture of the NPC.

3.3.1 Heterogeneity in scaffold Nucleoporins

Current models of the NPC scaffold have been determined through fitting and modeling of available crystal structures into a tomographic map (von Appen et al., 2015; Bui et al., 2013; Kim et al., 2018; Kosinski et al., 2016). These tomographic maps are obtained by averaging tens of thousands of cryo-ET subtomograms on the asymmetric unit level (i.e. one-eighth of the pore volume) to improve the intrinsically low signal-to-noise ratio of cryo-EM. After averaging, the reconstructed asymmetric unit is duplicated eight times and stitched back together to compose the entire volume of the NPC. While with this strategy current tomographic maps of the NPC have reached astonishing resolution and resolved the scaffold of the pore in great detail, they represent an asymmetric unit average and thus cannot capture the biological variability that the scaffold of the pore could contain. From another point of view, SMLM techniques have the complementary advantage of specifically visualizing known target proteins with a high signal-to-noise ratio but are limited in resolution by the number of photons obtained from the fluorescent label on the protein. Due to the higher signal-to-noise ratio in individual SMLM particles, the whole NPC volume can be averaged with a ten-fold smaller number of particles compared to subtomogram averaging. As a result, the 3D reconstructions generated from SMLM averaging should in principle be able to capture more of the biological variability within the structure of the pore.

Following this rationale, I explored if the scaffold NOIs of the NPC, which are generally viewed as very stable in the field, show signs of conformational dynamics. To this end, I explored the extent of axial, lateral and rotational variability within the scaffold NOIs captured in 4Pi-SMLM particles. First, I estimated the amount of axial and lateral intensity profile variability with the scaffold NOIs that are present in both the nucleoplasmic and cytoplasmic rings of the pore. The distribution of axial and lateral intensity profile distances (Fig.2-15 A) reflected a broad distribution but recovered median values, which are consistent with the axial and lateral distances from average reconstructions. These results suggest that the distances that are recovered from averaged references correspond to one of many possible states of the pore and hint towards positional variability of scaffold NOIs within the NPC.

To investigate in more detail the extent of variability within the analyzed scaffold NOIs, the axial and lateral position of each NOI particle was compared to the averaged position at each radial step within the nucleoplasmic and cytoplasmic ring of the pore and the standard deviation was calculated (Fig.2-15 B). These results illustrate in greater detail the extent of positional variation of scaffold NOIs across the entire circumference of the pore and support the notion of a high degree of axial and lateral flexibility (i.e. reaching a mean axial SD of ± 14 nm and mean lateral SD of ± 22 nm) within the whole NPC circumference. While these results highlight the degree of positional variability within the NPC, it is important to keep in mind that this analysis does not eliminate all technical variability that may be present in the data. Thus, to quantify the biological variability more precisely, more simulations of NPC particles with variable structure and their analysis with the pipeline I developed will be needed in the future.

3.3.2 Structure based classification of scaffold Nucleoporins

It is assumed that the scaffold of the NPC forms a stable and static coat of the membrane pore and anchors the rest of the NPC architecture (i.e. cytoplasmic filaments and nuclear basket) and transport machinery (reviewed in (Knockenhauer and Schwartz, 2016)) that is believed to be more flexible. This notion derives from currently available NPC maps (von Appen et al., 2015; Kim et al., 2018; Kosinski et al., 2016; Lin et al., 2016), which portray a highly averaged consensus ‘snapshot’ for the shape, position and most of the known biochemical interactions within the scaffold of the pore. Nevertheless, a recent structural study in yeast has identified flexible connectors that hold the scaffold of the pore together (Kim et al., 2018) and speculated that these connectors might give the scaffold a certain degree of flexibility in response to deformation. In line with this hypothetical flexibility, my results revealed a wide range of variable positions that the scaffold of the NPC can occupy and suggest that the scaffold of the pore might actually have a much more flexible architecture than previously anticipated (Fig.2-15).

To further explore without any structure model imposed bias which variable features are present in the scaffold NOIs, I implemented an unsupervised classification method that is based on topological data analysis in collaboration with a theoretician in my group. For this analysis, topological signatures from the raw individual NPC 3D SMLM particles of scaffold NOIs were extracted, converted into persistence diagrams and their relative distances were used for clustering into different structural classes (Fig.2-16). To validate the use of this classification method for structure based classification, I first performed clustering and classification of a mixed set of 4Pi-SMLM particles from different NOIs, to test if the different proteins could be distinguished. To this end, 4Pi-SMLM particles from all scaffold NOIs were represented as persistence diagrams and their relative distances were calculated and represented in a distance matrix (Fig.2-16 A). The distance matrix revealed the presence of multiple clustering groups, which were further analyzed and represented in a tree diagram (Fig.2-16 B). The tree diagram illustrated at least four major cluster groups, which were assigned with the identity of the most abundant NOI. It is important to note, that while this classification method could very clearly distinguish NOIs that have lower topological similarities (e.g. ELYS compared to the scaffold Nups), it performs with more uncertainty when clustering NOIs that have more similar topological signatures (e.g. Nup133, Nup107 and Seh1). Nevertheless, by using the most abundant identity cluster assignment, the classification was able to partition each major cluster to a unique NOI, validating the use of persistence diagrams for structure based clustering and classification of 4PI-SMLM particles.

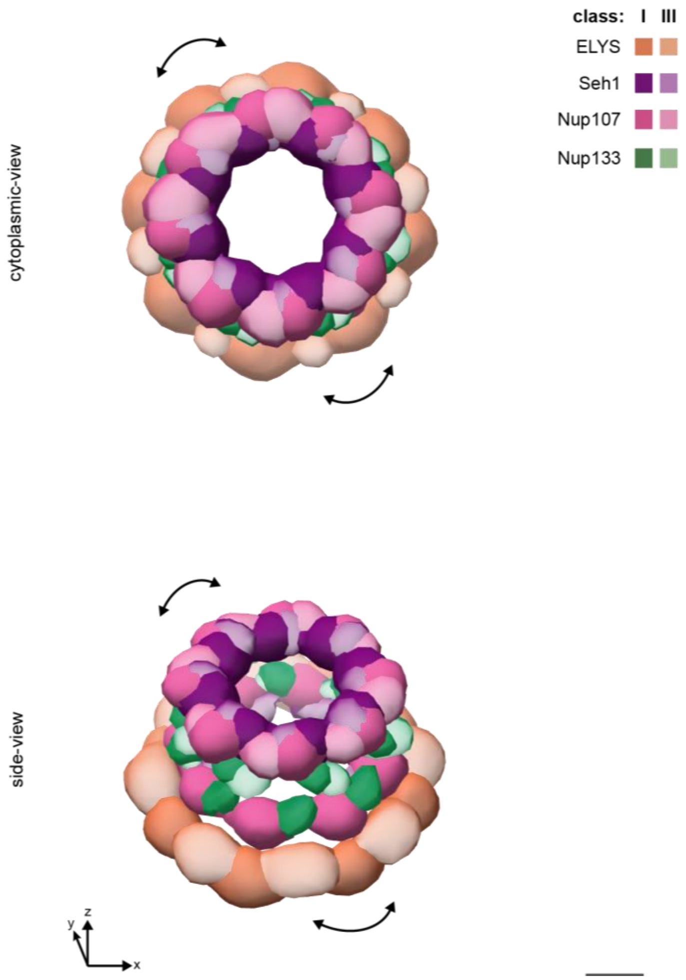

FIGURE 3-1. Flexible architecture of the scaffold of the NPC. Isosurface-rendered density maps of the cytoplasmic- and side-view 3D averagings of the combined single-color 4Pi-SMLM datasets of representative clusters from Figure 2-17 (Seh1 class I and III: purple; Nup107 class I and III: pink; Nup133 class I and III: green and ELYS class I and III: orange). Scale bar indicates 25 nm.

Subsequently, I wanted to test if this approach could identify different structural classes within particles of the same NOI. To this end, each individual scaffold NOI was further analyzed based on its persistence diagrams to uncover variable architectural features and define their conformational classes. For this, each scaffold NOI was represented in a tree diagram and divided into clusters based on the degree of branching (Fig.2-17 A). The particles of the resulting classes were then subjected to averaging and reconstruction to uncover their underlying architectural differences. Very interestingly, the resulting 3D reconstructions revealed that a major variable architectural feature that distinguished each class from each other was the variability in rotational offset between subunits of the cytoplasmic and nuclear rings within the three double ring scaffold NOIs (Fig.2-17 B).

Taken together, my unsupervised structure based classification results provide further evidence for the unexpectedly high flexible nature (i.e. variable axial, lateral and rotational position) of scaffold NOIs that have been impossible to observe so far. While an initial structural study has hinted at the existence of more flexible ties (i.e. flexible connectors) holding scaffold of the pore together (Kim et al., 2018), it lacked direct or quantitative structural evidence of flexibility. Results from my 3D SMLM experiments thus provide the first quantitative insight into the inherent flexibility of the scaffold of the NPC (Fig.3-1). Excitingly, it will now be possible to test if this surprising structural variability corresponds to molecular rearrangements that underlie different functional states of the NPC, by combining my approach with targeted perturbation studies.

3.4 Structural organization of the nuclear basket and the cytoplasmic filaments

While the classification of the scaffold of the pore exposed an unforeseen high degree of variability in its conformational states, we anticipated for the architectural analysis of the nuclear basket as well as the cytoplasmic filaments the presence of even more flexible conformations. Due to the absence of a clear average structure from higher resolution approaches, that could guide masks and be used to validate results of 3D particle averaging, I directly implemented the unsupervised classification methods based on persistence homology to analyze the architecture of flexible NOIs.

For this I first acquired single-color 4PI-SMLM datasets of each of the flexible NOIs with optimized labeling and imaging conditions. The resulting 4Pi-SMLM images already exposed a more irregular architecture for the flexible NOIs compared to the ring-shaped scaffold NOIs (Fig.2-18). The cytoplasmic filament Nup358/RanBP2 exhibited pores that resembled the characteristic ring-shape of the scaffold of the pore, but also included particles that formed a more spherical architecture in a confined axial range (Fig.2-18 A). These results suggest that Nup358/RanBP2 could exhibit at least two different conformations on the cytoplasmic side of the pore. Furthermore, the nuclear basket filament TPR exposed an even broader range of shapes within the 4Pi-SMLM images, from ring-shapes, spherical shapes and the combination of both across a wide axial range (Fig.2-18 B). These results suggest that TPR could form an even larger number of different conformations, which might span across the entire nucleoplasmic face of the pore.

3.4.1 Conformational states of Flexible Nucleoporins

To characterize the architecture of the observed variable conformational states of flexible NOIs and determine their relative positional differences, each flexible NOI dataset was classified and each resulting class was then averaged independently (Fig.2-19).

Both Nup358/RanBP2 and TPR have been proposed to form long and flexible filamentous structures composed of their predicted coiled-coil domains and to be the major constituents of the cytoplasmic filaments and nuclear basket, respectively

(Cordes et al., 1997; Delphin et al., 1997). Due to their large size (Nup358/RanBP2: 358 kDa and TPR: 267 kDa) and proposed threadlike architecture, it is especially important to keep the site where the fluorescent probe was incorporated in mind when interpreting the averaged 4Pi-SMLM data. The reconstructions that resulted from the classification and averaging of 4Pi-SMLM datasets reflect the position of Nup358/RanBP2's SNAP-tagged N-terminus and of TPR's SNAP-tagged C-terminus.

The classification of Nup358/RanBP2 recovered two major classes and their 3D reconstructions revealed that these classes consist of a small ring- (~75 nm in diameter) and sphere-shaped (~33 nm in diameter) architectures (Fig.2-19 A). These results suggest that the N-terminus of Nup358/RanBP2, which has been proposed to interact with the scaffold of the pore (Bui et al., 2013) and stabilize the oligomerization of the Y-shape-subcomplex (von Appen et al., 2015), can be present in at least two different conformations on the cytoplasmic face of the pore. The ring-shaped conformation (i.e. class I) would be in line with its proposed role in stabilizing the Y-shaped subcomplex (von Appen et al., 2015) and positioned close to the scaffold of the pore. The sphere-shaped conformation (i.e. class II), however, suggests that Nup358/RanBP2 might have an unanticipated position inside the NPC's central channel, which might potentially interact with the transport machinery. This conformation suggests that the N-terminal domain of Nup358/RanBP2 might have a dynamic conformational nature and can exist in an open and closed conformation, which one could speculate being involved in the regulation of the transport machinery (Fernandez-Martinez et al., 2016).

The structure based clustering of TPR SMLM particles revealed three major classes. The 3D reconstructions of these classes exposed highly flexible structural features that resembled ring- (reaching up to ~70 nm in diameter) and sphere-shapes (reaching up to ~40 nm in diameter) at distant axial positions (spanning from ~45-95 nm from each other) (Fig.1-19 B). Two of the recovered conformations (i.e. class I and III) are composed of both a ring- and a sphere-shape architecture simultaneously, suggesting that some of the TPR C-termini in one NPC can be positioned in proximity to the nucleoplasmic ring of the pore, while other TPR molecules have their C-terminus located in a distal spherical structure. Earlier evidence in the literature had mapped the distribution of TPR's C-terminus with immunogold label to a distal distance of ~ 100 nm apart from the pore's scaffold (Krull et al., 2004), and thus it has been widely assumed that the NPC basket is formed by eight flexible filaments that converge in a distal ring-like structure. Contrary to this assumption, my results unexpectedly revealed that TPR's C-termini are actually positioned simultaneously at the two distal ends of the presumed nuclear basket. This unexpected architectural feature could be explained by the ability of TPR's coil-coiled structure to form antiparallel tetramers (Pal et al., 2017), which could ultimately position the more disordered C-terminus at two different ends of the nuclear basket. Interestingly, the nuclear basket has been reported to possess different functions including transport, chromatin and also membrane remodeling capacity (Mészáros et al., 2015). While this last role has not been directly conferred to TPR, based on the ring-shaped architectural arrangement revealed though my classification analysis, it would be of great interest to investigate if TPR's C-terminus could interact with the NE and might even possess membrane bending ability.

Finally, the existence of a conformational state (i.e. class III), which contains both a ring- and sphere-shape structure at the same axial position, suggests that either the distal end of the basket might be able to move enormous distances or that the ring close to the membrane could also have an open and a closed conformation that could be linked to its reported role in nucleo-cytoplasmic transport (reviewed in (Wente and Rout, 2010)).

3.5 An integrated 3D molecular map of the NPC

After characterizing the 3D architecture of both scaffold and flexible NOIs, as well as investigating the surprising degree of inherent variability of the scaffold and the presence of major very different conformational states of the flexible NOIs, I envisioned the integration of all obtained information into a single 3D molecular map of the NPC architecture. This map would provide the foundation for in addition extracting relative architectural information between all NOIs and would allow a global interpretation of their positions within the NPC. To this end, I developed a conceptual strategy where the pairwise imaging of the NOIs together with a constant reference NOI (i.e. ELYS), would provide all necessary coordinates for such map.

Multicolor 4Pi-SMLM, however, had not been broadly implemented and was limited by the availability of compatible dyes and the microscope's design. Due to this, I first examined previously reported dual-color SMLM approaches (i.e. activator-reporter (Bates et al., 2007) and ratio-metric (Testa et al., 2010)) and evaluated their performance on the 4-Pi-SMLM. After selecting the most suitable dual-color 4Pi-SMLM approach, I optimized the labeling and imaging conditions and acquired dual-color data of selected NOI's. Finally, I expanded the 3D SMLM averaging pipeline to integrate dual-color SMLM data and obtain 3D reconstructions containing relative distance positions.

3.5.1 Dual-color 4Pi-SMLM imaging of the NPC

The selection of the dual-color approach I tested was based on the compatibility of available dyes for SMLM and the technically possible modifications to the 4Pi microscope. I explored the performance of the activator-reporter and the ratio-metric dual-color approaches in the 4Pi-SMLM.

Implementing the activator-reporter approach seemed appealing, as this would decrease the amount of modifications needed in the microscope. However, as this approach uses tandem SNAP-tag substrates, which are commercially unavailable, I relied on collaboration with the Facility for Synthetic Chemistry at the Max Plank Institute for Biophysical Chemistry in Göttingen, which provided me with a variety of tandem SNAP-tag substrates, which I screened for dual-color SMLM performance (section 2.5.1). The quality of labeling of all tandem SNAP-tag substrates produced SMLM images of inferior quality (i.e. high background levels and inferior molecular specificity) compared to those labeled with only BG-AF647. These results suggest that tandem SNAP-tag substrates might have difficulty to access the nuclear compartment due to their large size and/or negative charge, or that their reactivity with the SNAP-tag was decreased. While my optimization efforts (i.e. using the tandem SNAP-tag substrate BG – A647-cadaverine-A405) resulted in reasonable quality dual-color SMLM images (i.e. substantially decreased background noise and improved labeling efficiency) (Fig.2-20 A), the number of localizations obtained from this strategy was still too low to obtain good reconstructions based on averaging and I therefore moved on to exploring alternative approaches.

For implementing the ratio-metric dual-color approach in the 4Pi-SMLM, I tested four different dye combinations in combination with different suitable long-pass (LP) dichroic mirrors and blinking buffer compositions and evaluated their performance for dual-color SMLM imaging (Table 1). My initial screening results produced images of improved quality compared to the ones obtained with the activator-reporter approach. Finally, after selecting and optimizing the best suitable condition (i.e. using IgG – A647 with BG – Cy5.5 a 678 LP dichroic mirror and a blinking buffer based on βME), I obtained high labeling quality dual-color SMLM images (Fig. 2-20 B) and selected this arrangement for all dual-color 4Pi-SMLM imaging in this work. In conclusion, the ratio-metric approach for dual-color 4Pi-SMLM imaging proved to be advantageous compared to the activator-reporter, as it benefits from using the better performing standard SMLM dyes and ends up using the majority of detected localizations for the final reconstructed dual-color image.

3.5.2 Relative mapping of nucleoporins

After successful selection and optimization of the dual-color strategy for 4Pi-SMLM, I systematically acquired dual-color datasets of the scaffold NOIs together with the selected reference NOI (i.e. ELYS). My results consistently revealed the expected ring-shape architectures that were previously observed in single-color images for scaffold NOIs (Fig.2-21). However, in addition to reinforcing previously made observations, the dual-color images revealed novel features about the relative architecture of the NOIs, showing for example that the reference NOI ELYS is positioned as a single ring in close proximity to the nucleoplasmic ring of scaffold NOIs (Fig.2-21). The sub-stoichiometric occurrence of ELYS compared to the rest of the Nups of the Y-shape-subcomplex (Ori et al., 2013) and its absence in available density maps (von Appen et al., 2015; Bui et al., 2013), hinted to its existence as an asymmetric scaffold Nup. In addition, its role as a chromatin binding protein (Rasala et al., 2006), suggested that ELYS might be localized to the nucleoplasmic ring of the pore. However, my results show for the first time directly localization of ELYS relative to other members of the Y-shape-subcomplex and support the notion of its asymmetrical position at the nucleoplasmic ring of the NPC.

To analyze in greater detail the positioning of ELYS relative to the analyzed scaffold NOIs, I further adapted the 3D SMLM averaging pipeline for processing dual-color 4Pi-SMLM particles. From the resulting 3D dual-color reconstructions, I quantified the relative axial, lateral and rotational distance positions between the analyzed pairs of scaffold NOIs (Fig.2-22). My 3D reconstructions revealed that ELYS unique ring is positioned in very close proximity to the nucleoplasmic rings of the analyzed members of the Y-shape-subcomplex. Moreover, ELYS exhibited a significantly larger diameter than even the most peripheral members of the Y-shape-subcomplex.

Taking these observations together, my results provide quantitative evidence of the asymmetric position of ELYS to the nuclear ring of the pore and its relative architecture suggests that it might interact with the nuclear membrane at the periphery of the scaffold of the pore, which might explain ELYS' reported role in regulating NE's subdomain protein composition (Clever et al., 2012) and in the differential NPC assembly mechanisms (Otsuka and Ellenberg, 2017). In addition, ELYS has been reported to have a role as a chromatin binding protein during postmitotic NPC assembly (Rasala et al., 2006, 2008). Given the peripheral position of ELYS (Fig.2-22) that my results revealed, one could speculate that this localization could confer an easier access to stable ELYS-chromatin interactions without interfering with the transport machinery and which could potentially be maintained even after the NPC has fully assembled. As the DNA binding capacity is provided by the large disordered C-terminal domain of ELYS (~150 kDa) (Rasala et al., 2008), it would be of great interest in the future to further investigate, by my approach correlated with live cell imaging, how far this flexible domain can stretch into the nucleus and if it could mediate genomic rearrangements involved in transcriptional regulation and chromatin organization (reviewed in (Ibarra and Hetzer, 2015)).

Finally, I constructed a 3D molecular map of the NPC based on the relative positional information obtained from the dual-color 4Pi-SMLM averages (Fig.2-23). For this, I used the reference ELYS to align (i.e. in the axial, lateral and rotational plane) the different dual-color reconstructions and the interpolated averages were combined into a single 3D reconstruction.

My 3D molecular map of the NPC integrates architectural information of NOIs that were obtained from separate measurements and thus allows for the drawing of new observations and positional quantitation about any of the included NOIs, which was inaccessible on previous reconstructions (Fig.2-23). Following this strategy, any other nucleoporins and their different conformational states can be integrated into this molecular map, thus providing a unique framework to position asymmetric Nups, the architectural information of which had been inaccessible with existing methodologies. To illustrate the power of the information content in a

3D map containing both scaffold and flexible NOIs, I integrated the obtained single-color reconstructions into their predicted positions (Fig. 3-2). Such a map would provide novel information about how the nuclear basket and cytoplasmic filaments are positioned within the entire architecture of the pore and how the different conformational states could functionally relate to each other. For example, to understand if the revealed sphere-shape conformations of Nup358/RanBP2 (i.e. class I-II) are positioned inside the NPC’s central lumen and if the exposed conformations can dynamically change between an open and closed state to regulate the transport machinery. To investigate if TPR’s C-terminus is positioned in proximity to the nucleoplasmic ring of the pore and if this ring-shape structure could also interact with the NE to mediate transport and membrane remodeling functions. If combined with functional perturbation studies this strategy opens exciting possibilities to gain access to a mechanistic understanding of the flexible molecular architecture of the NPC inside cells.

3.6 Perspective

In this work, I have established a methodology that combines 4Pi-SMLM imaging of the molecular components of the NPC with 3D SMLM subvolume averaging to obtain 3D reconstructions from which precise quantitative positional information can be extracted. Moreover, I integrated a novel unsupervised structure based classification approach into this methodology, which allowed me to examine the existing structural dynamics within both scaffold and flexible regions of the pore. Finally, I developed an integrative approach based on dual-color imaging with a constant reference nucleoporin to construct a 3D molecular map, which allows for a global architectural and positional interpretation of any of the molecular components of the NPC. While this combined experimental and computational approach has been optimized to study the architecture of the NPC, it can in principle be applied to other macromolecular machines and organelles within cells.

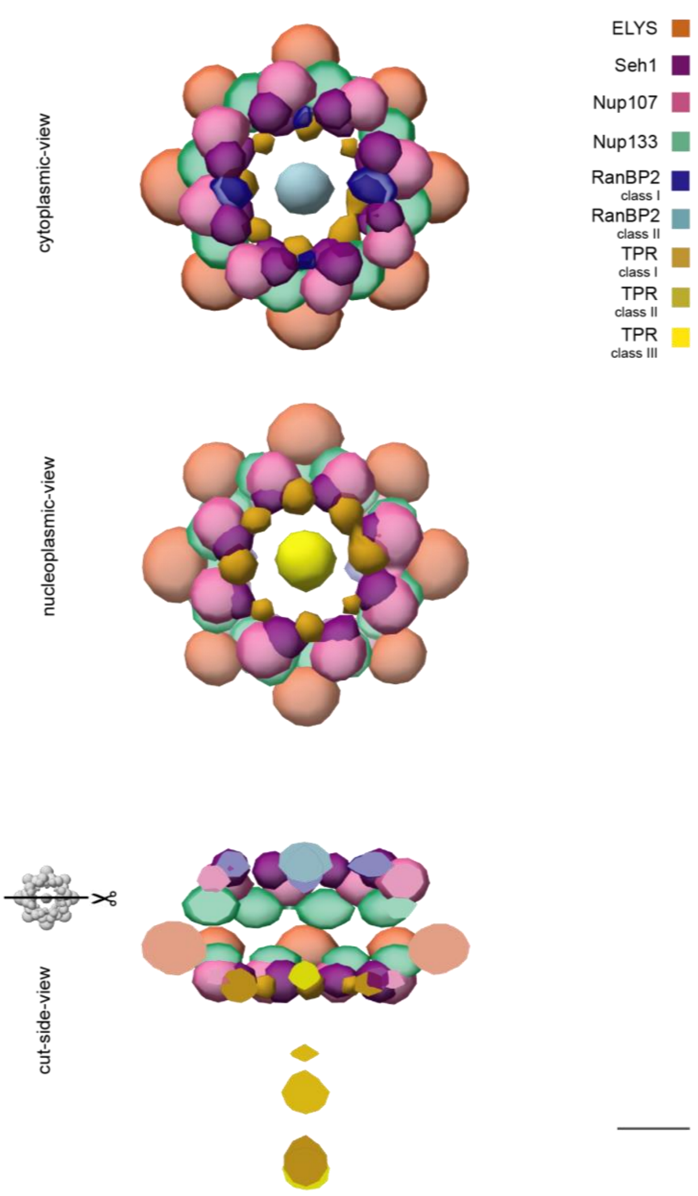

FIGURE 3-2. 3D confomational map of the NPC. Isosurface-rendered density maps of the cytoplasmic-, nucleoplasmic- and cut-in-half side-view 3D averagings of the combined dual-color 4Pi-SMLM datasets (Seh1: purple ; Nup107: pink and ELYS: orange) from Figure2-23 and manually positioned single-color 4Pi-SMLM datasets (Nup133: green ; RanBP2 class I-II: blue and TPR class I-III: yellow) from Figure2-13 and Figure2-19 respectively. The positioning of the single-color 4Pi-SMLM datasets was manually selected for visualization based on their hypothesized location. Scale bar indicates 50 nm.

In the near future systematic implementation of the established methodology should allow me to integrate more molecular components into the 3D map of the NPC to study the organization of further uncharacterized nucleoporins within the pore (Fig.3-2). This strategy could complement EM methodologies and help fit currently available crystal structures to uncharacterized regions of the NPC. I expect that this framework will allow me to understand in greater detail the positioning of the different conformational states that the nuclear basket and the cytoplasmic filaments possess. Also, this approach could serve to explore the organizations of the FG-Nups and give insights into the so far enigmatic architecture of the transport machinery of the pore. Moreover, this approach can be combined with both functional and cell cycle studies to provide mechanistic information about the architectural rearrangements during transport and the different assembly processes by which cells build the NPC. For example, it would be of great interest to identify key NPC assembly intermediates, by acutely removing nucleoporins with degron-tags (i.e. degron (AID) system) and characterizing the architecture and molecular components present in stalled intermediate states with my dual-color 3D SMLM averaging approach. It would also be very significant to the field to further inspect with this strategy, which of the key NPC assembly intermediates possess membrane-bending and dilation capacity to mediate the first steps in NPC assembly. Furthermore, to gain access to the architectural rearrangements during transport, it would be possible to interfere with the transport competence of the pore with well-established inhibitors (e.g. disrupting with 1,6-hexanediol (HD) or blocking with wheat germ agglutinin (WGA)) and re-examining the structure of NOIs to identify key conformational rearrangements produced during transport disruption.

My analysis on the biological variability and structure based classification of different conformational states provided a first insight into the so far uncharacterized dynamic nature of both the scaffold and flexible regions of the NPC. Thus, it will be of great interest in the future to further investigate the functional implications of the dynamic nature of the NPC structure and to understand if differences in the composition of the pore have an influence in its structure and ultimate function. A first step towards this will be to carry out the structure based classification in dual-color data, to understand if and which different structural classes of different NOIs correlate with each other, which would indicate coordinated movements. While the characterization of the biological variability was performed in the same cell type, it will be very interesting to implement this analysis for different cell types to investigate how the composition, architecture and function of the NPC varies between different cell lineages. Finally, with ongoing advancements in the field of super-resolution (e.g. live-cell SRM and cryo-SRM) and electron microscopy (near atomic resolution cryo-EM) and with developing correlative methodologies (e.g. correlative live-SRM and SRM-cryo-EM), it will soon become possible to study the dynamic ultrastructural rearrangements of multi-molecular machines inside cells during their functional cycle.

4 Materials and Methods

4.1 Genome-engineered cell lines

4.1.1 Cell culture

HeLa Kyoto (HK) cells (RRID: CVCL_1922) were kindly provided by S. Narumiya (Kyoto University). The human osteosarcoma U2OS (RRID: CVCL_0042) cells were purchased from ATCC (Wesel, Germany). HK cells were cultured in 1x high glucose Dulbecco's modified eagle medium (DMEM; Thermo Fisher Scientific, cat.# 41965039). U2OS cells were cultured 1x high glucose McCoy's 5A modified medium (McCoy; Thermo Fisher Scientific, cat.# 26600023). Both DMEM and McCoy media were supplemented with 10% (v/v) fetal bovine serum (FBS; Thermo Fisher Scientific; cat.#10270106; qualified, E.U.-approved, South America origin), 100 U/ml penicillin-streptomycin (Thermo Fisher Scientific; cat.# 15140122), 2 mM L-glutamine (Thermo Fisher Scientific; cat.# 25030081) and 1 mM sodium pyruvate (Thermo Fisher Scientific; cat.# 11360070). In addition, the McCoy media was supplemented with 10% MEM nonessential amino acids (Thermo Fisher Scientific; cat.# 11140050). Cells were grown on culture dishes (ThermoFisher) at 37 °C and 5% CO_2 in a cell culture incubator. Cells were passaged at a confluence of around 80% every 3 days by trypsinization (Trypsin-ethylenediaminetetraacetic acid (EDTA; 0.05%), phenol red (Thermo Fisher Scientific; cat.# 25300054)). Tests confirming the absence of mycoplasma were performed every 2 months.

4.1.2 Cell line generation

Genome editing was carried out in both HK and U2OS cells in order to express endogenously tagged NOIs. Zinc finger nucleases (ZFNs) were used to tag Nup107 at the N-terminus with the monomeric enhanced GFP (mEGFP) (Otsuka et al., 2016) in HK cells and with SNAPf-tag in U2OS cells. ZFNs DNA binding sequences are listed in Table 3-1, which were purchased from Sigma Aldrich. The donor plasmids are listed in Table 3-3 and consist of the mEGFP and SNAPf-tag cDNA sequence flanked by left and right homology arms. The transfection of ZFN pairs and the donor plasmid into HK and U2OS cells was performed as described in previous reports (Koch et al., 2018; Mahen et al., 2014).

Cell line	**ZFN binding sequences (5'-3')**
HK ZFN mEGFP-Nup107 #z26z31	TCAGTACTGATG and GCTGAGCCCGAAGTC
U2OS ZFN SNAP-Nup107 #294	TCAGTACTGATG and GCTGAGCCCGAAGTC

Table 3-1. ZFN binding sequences

For tagging Seh1, Nup133, Nup358/RanBP2 at the N-terminus and TPR at the C-terminus with SNAP-tag paired CRISPR/Cas9D10A nickases were used. The design of guide RNAs (gRNAs) was carried out using the Feng Zhang Lab's Target Finder (http://crispr.mit.edu/) or Benchling (https://benchling.com/crispr) as described previously in (Koch et al., 2018; Mahen et al., 2014) and listed under Table 3-2. The gRNAs were cloned into 2A-EGFP containing pX335 (Cong et al., 2013). The CRISPR-Cas9 nickases with gRNAs and the donor plasmid were transfected using Fugene6 reagent (Promega, Madison, WI) in U2OS cells, according to the manufacture's protocol. 2–3 days after transfection, cells were sorted with a MoFlo Legacy cell sorter (Beckman Coulter, Brea, CA) as described in (Koch et al., 2018; Mahen et al., 2014). After the first round of genome-editing homozygous clones were achieved from Nup107, Seh1, Nup133 and Nup358/RanBP2 and heterozygous clones for TPR tagged expression. A second round of genome editing was performed on the heterozygously-tagged TPR expressing clones after confirming with Sanger sequencing the absence of mutations in the wild-type alleles.

Cell line	Sequence encoding antisense gRNA (5'-3')	Sequence encoding sense gRNA (5'-3')
U2OS CR SNAP-Seh1 #238	CCACAAACATGGTTTCCGTC	CAGCATCGCGGCGGACCACA
U2OS CR SNAP-Nup133 #80	GAGCAGCGACTAGGACAGCG	TCTCCGCGGACCCCGGTAC
U2OS CR SNAP-Nup358/RanBP2 #721	GGCGCGTGAGACCAGCGCTC	GAGGCGCAGCAAGGCTGACG
U2OS CR TPR-SNAP #266-554	CTCCTCTCCCTCCCATTGCA	CAGAGGAAATATTAATTAAA

Table 3-2. gRNA sequences

Donor plasmid	**Transcript ID (ENSEMBL)**	**Donor Sequence (5'-3')**
pmEGFP-Nup107_Donor	ENST00000229179	AAAAGACTATATCAACAGGCTTATTAAACGGATAAACTGAAGCATCTAACATTATTTTTGTAATCTGGTCAGTTAATAGCCAGTCACTACTTTCAAACTGGAAAAAACAAAAACCAAAACAAAAATGTGACTGACTCCTTCAAGACCAAAATACACCACTTTTTGCCTAGACGGCACTTTGAAATAGAGGGCAATACCATCATATTTCACGCTTGCCTTTCTACTTTTTAATACAGGTGAACTTTTTCTCCTTAATAGGAAAGAACACCAAGTAAAGAACAAATAGCAGTTATGGAAAATAGTTGCAAAAACTGCAGGGGGCTACAGAACAAAGGACTGAGTGTAGGCAGAGAGATAGAGATCCCCGAGGTGTGGGGCAGAGCCCACGCATCTGAATTCCAAGAACAGGCGCTTTCTGACAGAGAATACCAGGAAATGACTTCACATTTTTCCAGACTATCAACATACTTCATTCTTCCCAGTAGGAGAACCCAGGGCCTGTTCCACGCCCACAGACTTTGGTCAGGCAAAGCGGCCGCAGGGCGTCTGGGCTAAACGCAACCAGGAACACATTGGCAAACTTTTGCGCCTGCGCCCACCGGGCGTGCACCTGTAGGCTGAAGTCGCGCATGCGCTAGATGGGAACGTTGTTTCTTCTCCCCTACCCCTTTTCTGTGGGTCTGTTTTAGGGACAGACTGCTTCCGGGTCGAAGGGCTTGCTTCCGGAGAGCGGGAAGGCTAAAACGCGGTAGCTAAACTGCAGCCAACTTTGGTTGTGTGTGGAAAAGGCTTTAGCCACTAGTATGGTGAGCAAGGGCGAGGAGCTGTTCACCGGGGTGGTGCCCATCCTGGTCGAGCTGGACGGCGACGTAAACGGCCACAAGTTCAGCGTGTCCGGCGAGGGCGAGGGCGATGCCACCTACGGCAAGCTGACCCTGAAGTTCATCTGCACCACCGGCAAGCTGCCCGTGCCCTGGCCCACCCTCGTGACCACCCTGACCTACGGCGTGCAGTGCTTCAGCCGCTACCCCGACCACATGAAGCAGCACGACTTCTTCAAGTCCGCCATGCCCGAAGGCTACGTCCAGGAGCGCACCATCTTCTTCAAGGACGACGGCAACTACAAGACCCGCGCCGAGGTGAAGTTCGAGGGCGACACCCTGGTGAACCGCATCGAGCTGAAGGGCATCGACTTCAAGGAGGACGGCAACATCCTGGGGCACAAGCTGGAGTACAACTACAACAGCCACAACGTCTATATCATGGCCGACAAGCAGAAGAACGGCATCAAGGTGAACTTCAAGATCCGCCACAACATCGAGGACGGCAGCGTGCAGCTCGCCGACCACTACCAGCAGAACACCCCCATCGGCGACGGCCCCGTGCTGCTGCCCGACAACCACTACCTGAGCACCCAGTCCGCCCTGAGCAAAGACCCCAACGAGAAGCGCGATCACATGGTCCTTAAGGAGTTCGTGACCGCCGCCGGGATCACTCTCGGCATGGACGAGCTGTACAAGTCCGGACTCAGATCTCGAGCTCAAGCTTCGAATTCCGACAGGTCAGTACTGATGGTGGCAGCCGAGCCAGAAGTCTTGCCCGTCTCGCCTGTTGGCGAAACGAAATAGGTGAAACTAGACTCCCAGAAGAAGCCAAGGAGGTCCCGGGTGCTTCCCCTAAGGCTCCTTCCCCATGCCGGGAAATTTGGCCACAAATGGGGAAAAAGCCGCTTGGCGTGCGTCGGGGTGGGGTACAGATCATAATAGTCCCTTACTTTCCCACTACGTTCTGCGATCTATTCGGCGCTTTGGGGCAGCAACACTGTTCGCTCCTGGGGTGGGCGGGGTAGGTAGCGCGGCGTTCGAAATGCTAAGTGACCAGCCTGAGATCACAAAGCCAGTCAGTGAAGATACTGGGATCTCAGCCCAGACTTTCTGATTACAAGTGCCAGCATCAGATTCTGAGTTCCCTCTATGATCTGGGTACTGTGCTAGCCGCCTACAACAAAGATCAGTTATTCAAGATCCTTCCCCTCGGGGAATTAGTTGTGTAATGGAGACAACCAAGCAGTGTAAAGTGGTAAGTGTTTGGGGGCGATTAAGTCTCCTTGTCACTGTAACTATCAGGAAGACCCCTCAAAGAAGGTAACTTTCTAGCTGGTCTTTGAATAATAAGAGTACATTATTCGTACTCCAAACATTGAGTACCTACTATGTGACTGCCATTGTTCTAAAGGCGTTGAATATATATTATTAGCTTATTTAATCTTCAGAACAAGAAAAATCCTATGAGATGGGTACTGTTATCCTTTTTTCATATATAACACTGAGACTAAAAGAGGTTAAGGAACTTGCTGAAAGTTCGGAAGCTAATAAATACA

pSNAPf-Nup107_Donor	ENST00000229179	CBB ID#1363 AAAAGACTATATCAACAGGCTTATTAAACGGATAAACTGAAGCATCTAACATTATTTTTGTAATCT GGTCAGTTAATAGCCAGTCACTACTTTCAAACTGGAAAAAACAAAAACCAAAACAAAAATGTGAC TGACTCCTTCAAGACCAAAATACACCACTTTTTGCCTAGACGGCACTTT GAAATAGAGGGCAATACCATCATATTTCACGCTTGCCTTTCTACTTTTTAATACAGGTGA ACTTTTTCTCCTTAATAGGAAAGAACACCAAGTAAAGAACAAATAGCAGTTATGGAAAAT AGTTGCAAAAACTGCAGGGGGCTACAGAACAAAGGACTGAGTGTAGGCAGAGAGATAGAG ATCCCCGAGGTGTGGGGCAGAGCCCACGCATCTGAATTCCAAGAACAGGCGCTTTCTGAC AGAGAATACCAGGAAATGACTTCACATTTTTCCAGACTATCAACATACTTCATTCTTCCC AGTAGGAGAACCCAGGGCCTGTTCCACGCCCACAGACTTTGGTCAGGCAAAGCGGCCGCA GGGCGTCTGGGCTAAACGCAACCAGGAACACATTGGCAAACTTTTGCGCCTGCGCCCACC GGGCGTGCACCTGTAGGCTGAAGTCGCGCATGCGCTAGATGGGAACGTTGTTTCTTCTCC CCTACCCCTTTTCTGTGGGTCTGTTTTAGGGACAGACTGCTTCCGGGTCGAAGGGCTTGC TTCCGGAGAGCGGGAAGGCTAAAACGCGGTAGCTAAACTGCAGCCAACTTTGGTTGTGTG TGGAAAAGGCTTTAGCCACTAGTATGGACAAAGACTGCGAAATGAAGCGCACCACCCTGG ATAGCCCTCTGGGCAAGCTGGAACTGTCTGGGTGCGAACAGGGCCTGCACCGTATCATCT TCCTGGGCAAAGGAACATCTGCCGCCGACGCCGTGGAAGTGCCTGCCCCAGCCGCCGTGC TGGGCGGACCAGAGCCACTGATGCAGGCCACCGCCTGGCTCAACGCCTACTTTCACCAGC CTGAGGCCATCGAGGAGTTCCCTGTGCCAGCCCTGCACCACCCAGTGTTCCAGCAGGAGA GCTTTACCCGCCAGGTGCTGTGGAAACTGCTGAAAGTGGTGAAGTTCGGAGAGGTCATCA GCTACAGCCACCTGGCCGCCCTGGCCGGCAATCCCGCCGCCACCGCCGCCGTGAAAACCG CCCTGAGCGGAAATCCCGTGCCCATTCTGATCCCCTGCCACCGGGTGGTGCAGGGCGACC TGGACGTGGGGGGCTACGAGGGCGGGCTCGCCGTGAAAGAGTGGCTGCTGGCCCACGAGG GCCACAGACTGGGCAAGCCTGGGCTGGGTTCCGGACTCAGATCTCGAGCTCAAGCTTCGA ATTCCGACAGGTCAGTACTGATGGTGGCAGCCGAGCCAGAAGTCTTGCCCGTCTCGCCTG TTGGCGAAACGAAATAGGTGAAACTAGACTCCCAGAAGAAGCCAAGGAGGTCCCGGGTGC TTCCCCTAAGGCTCCTTCCCCATGCCGGGAAATTTGGCCACAAATGGGGAAAAAGCCGCT TGGCGTGCGTCGGGGTGGGGTACAGATCATAATAGTCCCTTACTTTCCCACTACGTTCTG CGATCTATTCGGCGCTTTGGGGCAGCAACACTGTTCGCTCCTGGGGTGGGCGGGGTAGGT AGCGCGGCGTTCGAAATGCTAAGTGACCAGCCTGAGATCACAAAGCCAGTCAGTGAAGAT ACTGGGATCTCAGCCCAGACTTTCTGATTACAAGTGCCAGCATCAGATTCTGAGTTCCCT CTATGATCTGGGTACTGTGCTAGCCGCCTACAACAAAGATCAGTTATTCAAGATCCTTCC CCTCGGGGAATTAGTTGTGTAATGGAGACAACCAAGCAGTGTAAAGTGGTAAGTGTTTGG GGGCGATTAAGTCTCCTTGTCACTGTAACTATCAGGAAGACCCCTCAAAGAAGGTAACTT TCTAGCTGGTCTTTGAATAATAAGAGTACATTATTCGTACTCCAAACATTGAGTACCTAC TATGTGACTGCCATTGTTCTAAAGGCGTTGAATATATATTATTAGCTTATTTAATCTTCA GAACAAGAAAAATCCTATGAGATGGGTACTGTTATCCTTTTTTCATATATAACACTGAGA CTAAAAGAGGTTAAGGAACTTGCTGAAAGTTCGGAAGCTAATAAATACA
pSNAPf-Seh1_Donor	ENST00000399892	CBB #1405 CTGATCCTTTCCTCCCCGTCCAGCCTTCGCTCTTAGGCTACCGAGCCTGGACTGCTTGTCATCC CCTCAGGCGTCTCCCCGGCCCTCCCTGCTCTTCAGCCGTCCCGACGGAGCGCGGCTCCTGAC CAAACCCACGGTTCGCCTTCTCCACCTGCTCCGCGCGCCTCGCATGTGTCTGGGGGGAAACAC ATCCAAACGTCGACTTAAATGATTCAGGGCCGAGGACCGTGAGAGGCAGTCTTCACTTTTTCAT CTTTCTTCATTTGCACAGTATACCAATAAGCTCTTACTACTTCTCAGCACAGGTAACTCGCCTTTT GCAGAGCACCCTCCGCCGCCGAACGGTCAGAGCCTGGAGGAACCCGCACCAGGATCGTAGGG CATGACGGGCCGGGGGCGGGACGAGGATTGACGAGCCGGGAACAGGGCGGGGCTTGAGGG GGCGGGAGGGTGGGGCGAGGCATGACGGCTCTGGTGGGAGGGTAGGCGGGGCTTGACGGG CCTGGGGGCGGGGCGGGGCTTGAGGGACCGGAAGGTGGGGCGAGTCATGACGGGCCGGGG CGTGGGCAGGGCTTGAGGGGCCAGGGGACTGTGTGGGGCCTGACGGGCCGGTGGGTGGGG CGGGGCTTGAAGGACCGGAGGGTGTGTGGGCGGGGCTTGATAGGCAGGGGCGGTGCGGGGG CGTGGGCAGCACAAGCCGTGCGCTCCCGGGCTGCGAGGTCTGGCTAGGCTACGGGCCACGC GCCGCCGCCGCTGCCGCCGCCACTGTCCTCTTCGGAGGCGCGGGCCCGACGGAAACCACTAG TATGGACAAAGACTGCGAAATGAAGCGCACCACCCTGGATAGCCCTCTGGGCAAGCTGGAACT GTCTGGGTGCGAACAGGGCCTGCACCGTATCATCTTCCTGGGCAAAGGAACATCTGCCGCCGA CGCCGTGGAAGTGCCTGCCCCAGCCGCCGTGCTGGGCGGACCAGAGCCACTGATGCAGGCCA CCGCCTGGCTCAACGCCTACTTTCACCAGCCTGAGGCCATCGAGGAGTTCCCTGTGCCAGCCC TGCACCACCCAGTGTTCCAGCAGGAGAGCTTTACCCGCCAGGTGCTGTGGAAACTGCTGAAAG TGGTGAAGTTCGGAGAGGTCATCAGCTACAGCCACCTGGCCGCCCTGGCCGGCAATCCCGCC GCCACCGCCGCCGTGAAAACCGCCCTGAGCGGAAATCCCGTGCCCATTCTGATCCCCTGCCAC CGGGTGGTGCAGGGCGACCTGGACGTGGGGGGCTACGAGGGCGGGCTCGCCGTGAAAGAGT GGCTGCTGGCCCACGAGGGCCACAGACTGGGCAAGCCTGGGCTGGGTTCCGGACGGACTCA GATCTCGAGCTCAAGCTTCGAATTCTGCAGTCGACGGTACAAGTCCGGACTCAGATCCGCTAG

		CTTTGTGGCTCGCAGCATCGCGGCGGACCACAAGGATCTCATCCACGATGTCTCTTTCGACTTCCACGGGCGGCGGATGGCAACCTGCTCCAGCGATCAGAGCGTTAAGGTGCGCGCGGCGCTTGCGGGCGGGGCCGACCCCGGAAGGAAGGAAGGGGAGTGGGTGGGCGGCGCGGGGAACGGGGCTGTGTCTTGGTTCAGTGACGCCGCTGGAAGCTGTGGGGTGGCGGGCGAGCCCTGGCTGGACTGAGCGGAAGCCCTCCCCGCCCGCGTATTGTGGGGTCACGGCGGCCTCGCGGGCCGCCCTCCCGTGCGCCTGCGCAGCTGGTGCCACGTGCGCGCTCCCGCCCGCAGGGTACGCCGGGCCCTCTCCCAGGCCGCGCTGCCGGGGCTGCGGGCGGGAACCCAGGGGCATCCCACCGTCAGCCTCGGCGTCGTGGGTCTTGCCCGCGCTGTTCACCCGACGACCTGCAGTGGGACCTGGTGGGAGACTTTGCCTGGCTGGCGCTGCGTCGAGTTCTGTGCCCCGCCGGTGTTCTCTCACCAGGGCACATGGTTTTCTCCGTGGGTTCAGAGCAGAAGCTCACTTTGTTACGCCGAGGAAGAAAAATACAAACCATTTACATCCAATGATTTCCCTGCTTGCTGCCCAGGAATCGGAGGGTTTGTTTCTTGAAGTTCCCGTAAACGTCTGTAGACACTTCCGAC
pSNAPf-Nup133_Donor	ENST00000261396	**Cbb id#1366** ACAGACACGTAGGACCTTACAACGTATACCATGATCTTAGGGTGGAGGTAGGTGTGAGGGATGACTGCAGATAGAGCTCTTCTCTTTGCCTTGGACAACTGGCCAGTTTTACCAAGCTGGAACAGAGATGGTGGTAGGAGAGGGGTCCTAAAGGAAAACATGAATGCGCTTTTCATAAGTGGATTGTGAGGAGTTCGCAGGACTTCCAGCTGAAATTGTCCCCTAGGGAGCTGAATGATAGGGGTCTGGGGGTTTTGAGCTGGATCCAGGTTAGAGACACGGATTTGTGGCGTCATCAGCGTGGATGAGACTGCGCAAAGTTGAATGGGAAAATGGCAAACCTAGAAAACAACAAATATCACAGTGCGATACCAGTGTCAGCTTTACGGCTTTTCTCCGTCCTCAGCTTGGAATGAGGAACATCTTTCATTTCACAAGAGGTTCAGGAACTACCAGTGTGAAAAGAGGCTACGTTCAAGCTGCTGGAGGGCCAGTTCCACCTAGGCGCAGTCAAGAAGGGCGCCTGGCTTTCCGGCTTCACGTCCCTGGAAGCTCGGCACTGCAGCGGTTCTAGATCTGGGGCCGCCGGCTGCCTTCCCGACCTACCTCGCTGACTGGGCACCGCCCTTAACGTCACGATCCCGCCCCCGCCAGCGCTCCGACCACAACCCGCGGGAGCCATTGCGTTTGACGTCATCATCGCGCGCCATCTCTTCCCTTAGGTGTTTAAGTTCCGCGCGCAGGCCAGGCTGCAACCTGACGGCCAGATCCCTCGCTGTCCTAGTCGCTGCTCCTTGGAGTCGTTAACATGGACAAAGACTGCGAAATGAAGCGCACCACCCTGGATAGCCCTCTGGGCAAGCTGGAACTGTCTGGGTGCGAACAGGGCCTGCACCGTATCATCTTCCTGGGCAAAGGAACATCTGCCGCCGACGCCGTGGAAGTGCCTGCCCCAGCCGCCGTGCTGGGCGGACCAGAGCCACTGATGCAGGCCACCGCCTGGCTCAACGCCTACTTTCACCAGCCTGAGGCCATCGAGGAGTTCCCTGTGCCAGCCCTGCACCACCCAGTGTTCCAGCAGGAGAGCTTTACCCGCCAGGTGCTGTGGAAACTGCTGAAAGTGGTGAAGTTCGGAGAGGTCATCAGCTACAGCCACCTGGCCGCCCTGGCCGGCAATCCCGCCGCCACCGCCGCCGTGAAAACCGCCCTGAGCGGAAATCCCGTGCCCATTCTGATCCCCTGCCACCGGGTGGTGCAGGGCGACCTGGACGTGGGGGGCTACGAGGGCGGGCTCGCCGTGAAAGAGTGGCTGCTGGCCCACGAGGGCCACAGACTGGGCAAGCCTGGGCTGGGTTCCGGACTCAGATCTCGAGCTCAAGCTTCGAATTCTGCAGTCGACTTCCCAGCCGCCCCTAGCCCGCGGACACCGGGAACCGGGTCCCGAAGGGGCCCGCTGGCCGGACTCGGGCCCGGCTCCACGCCCCGGACGGCTAGCAGGAAGGGTCTGCCCCTGGGGTCTGCAGTCAGCTCCCCAGTGCTCTTCTCGCCGGTCGGCCGGCGTAGCTCGCTAAGCTCGCGGTAAGTGATCTCCCTGGTTGGGTCTGGCAACCAACAGCCTCACGGGCCGCAGTGGGCCGGATAGGTTGTTGTCTTTAGAAGCCTTTGGAACCGGGGCGGCGGAATAGAATGCCACAGTATTGGAAAATAGACCTTTTCCACTGCTGCAGGTAGTATCTGCTTCGTTTTGATTATCAGTTGATCAGTTGATTCCCCACTTTGCATTTTTCATGGATACCTTTGTGCAGAAGTGAAGTACAAACTGGATTTGCATCAGTGTTTACCTACTTCCCACCTACTACCCGTGTGATCTGGTGTAAGTCACTCGTGATTTTCTTCATCTGTGAAATGGCGATAATATATCTCACCTGAGCCAGAGGAGTTATTATGAATTGCCACGATGCAGATGTAAGGTGATGGTGATAATGAGGACCTACAACCCTGAAAGATCATTGTTTAATGCCTAACATACCAACTGACATTAATATCTGATGATTGGTAATTAAAGGGTTTCTAGCTACGGAATTTAACTTTCTAGGTAAATTATAAGGAAAAGGCTTTACATAAGTGAGCTAAGAGTACTGTGATAGTTTAGTTACTAAAACTGCTCGTTTGGAGCACCAGTAAAATCATCACACACAC
pSNAPf-RANBP2_Donor	ENST00000283195	CBB #1408 TCCCTCTGTCGCCCAGACGGCGCAATCTCGGCTCACTGCAACCTCCGCCTCCCGGGTTCAAGCGATTCTCCTGCCTTAGCCTCCGGAGTAGCTGGGACTACAGGCGTCCGACACCACGGCCGGCTAATTTTTTGTATTTTTGGTAGAGATGGGGTTTCCCTGTGCTAGCCAGGATGGTCTCGATTTCCTGACCTCATGATCCGCCCGCCGTGGCCTCTCAAAGTGCTGGGATTACAGGCGTGAGCCACCACGCCTGGCCCTCATTTAATAAGATATGAATTTAAAAATGTATGCTTTAGTATTCACACATGTCCGATGCAACGTATTTAACCAGTCATCTCCAGAAACTTTGTTCCAATTTACACGTTCACCAAATTGGCCTGAGTGCTTTTTTTCTTCCAATGCATTGCGCACTTATAATTTAGAACAAGTGACCAAAACGCTTAAGAGCCCATCACGCAAATTGTTATCTGCTGGAAATCTACGCCCTAGGCTGTGGACACTGGCGGCCGAAATCTGATCCCGGCTTGCCAAGACACCCTCAGAGCACGCGGCGCTGCCAAGAGCCTGGCCGAGTGCAGCTCGAGCGCCGACGTCGCCAACGTGGCGCACACTGCTGACGCAGTACGCAAGTTCGTCACAGTGGTCCTCCGCCGGCTGCGCCGCAAGTTCGTCACAGTGGTCCTCCGCCGGCTACGGCG

		CTGCGTCACTGGTTTGCAGGCGCTTTCCTCTTGGAAGTGGCGACTGCTGCGGGCCTGAGCGCTGGTCTCACGCGCCTCGGGAGCCAGGTTGGCGGCGCGACTAGTATGGACAAAGACTGCGAAATGAAGCGCACCACCCTGGATAGCCCTCTGGGCAAGCTGGAACTGTCTGGGTGCGAACAGGGCCTGCACCGTATCATCTTCCTGGGCAAAGGAACATCTGCCGCCGACGCCGTGGAAGTGCCTGCCCCAGCCGCCGTGCTGGGCGGACCAGAGCCACTGATGCAGGCCACCGCCTGGCTCAACGCCTACTTTCACCAGCCTGAGGCCATCGAGGAGTTCCCTGTGCCAGCCCTGCACCACCCAGTGTTCCAGCAGGAGAGCTTTACCCGCCAGGTGCTGTGGAAACTGCTGAAAGTGGTGAAGTTCGGAGAGGTCATCAGCTACAGCCACCTGGCCGCCCTGGCCGGCAATCCCGCCGCCACCGCCGCCGTGAAAACCGCCCTGAGCGGAAATCCCGTGCCCATTCTGATCCCCTGCCACCGGGTGGTGCAGGGCGACCTGGACGTGGGGGGCTACGAGGGCGGGCTCGCCGTGAAAGAGTGGCTGCTGGCCCACGAGGGCCACAGACTGGGCAAGCCTGGGCTGGGTTCACTCTCGGCATGGACGAGCTGTACAAGTCCGGACTCAGATCTCGAGCTCAAGCTTCGAATTCTGCAGTCGACGGTACCGCGGGCCGCTTTTTTTTTTTTTGTTAACAGGCGCAGCAAGGCTGACGTGGAGCGGTACATCGCCTCGGTGCAGGGCTCCACCCCGTCGCCTCGACAGGTGAGTGGGTCTCGAAGAGACCGACGGCCTCGACCTGGCCGGGCGGCGGCCTCGCGCTGCTCAGGCGTCATGGCTCCCGACGGGCGCTGCTCCCTGGCGCGCTCTGTTGAGGCGCCGGCCGGCTGGCGCAGTCCTGTGGGCGGCGTGGCGCTTGCAAGCGCATGAAGAGTCCTGGGGGGACAGCGGTGGGCGGGAGACCTTTGGCGCCGGCGCTTCCTCTTTCTCCCGGCTTGTTCCCGACGCTTGTTCCCGACGGTGCTCGCTCCTGGGGCCGCCCTGGCCCGGGCTTTCTGGCCGATCGCGCACCCCGTAGTACCCGCGCGGCCTAGTTCTCGGGGGCTTGGGCACCCGGGTGCTGTATCGGCGGGTTTCTTCCCATCTCCTGGACATATACTTTATATGCTGCGGCGGAGGTCGTACCTCCTTGGCCTGGAGGAACCCAGTGGGGACTGACGCAGCTCCGGGTGAGCTTTGGCGGCTGCGTCGAGTGACAAGGTAGGCATCTCAGCGCGGACATTTGCAATGGCCCGACGGCGCAAATGACACGGAAAGTCCCCTTGTTTTGAGTATGAGGTGTTTGTCGCTGTCCCTTTGTAAGGGTCCAGCTCCACTCCACTCCTCATACTCACCTCCCTCGCCCCCCTCCCCGCCCGGAAC
pTPR-SNAPf_Donor	ENST00000367478	CBB #1409 CTTTCTCATTTTTTCACTTGCTTTTCTTTTATCTTAATGTTTTTCTTAGATACTAGTAGTAGTCAACCAAAGCCTTTCAGACGAGTAAGACTTCAGACAACATTGAGACAAGGTGTCCGTGGTCGTCAGTTTAACAGACAGAGAGGTGAATTTCTGACATAACTGGATTACATGATAGAATGTGGAATAGTAATAAATGGAACAAGTTTTCTAATCCTTAAGCCTCCAATTTATTTTTTTAATGTTCCAAAGTTTTATTAAATAATTACATGTTGAGCAGGTGATATTTACCAATCTGTAAACTTCATGTAGACAGATTTGTATACCTTAGATATATAATAAATATGTGCTTATATTTTATATTTATTGATTTCTTCCTTAAATCCAAATTAAGATTTGGAAAATATGAAGTGTTATAGTGTTATATTCATTTGTTGTATCTCTACCTATTGCCATTATATTGTTAATTTTTTTATACAACACGATAAAGCTTTGTGATTATGTTTTAGCTAGTAAAAGTGTAAAATTTTAATATTTCCATGTTTTCCAATATAACTTTTAGATTGTACTTGTGTCACAAAAAGAGGGATTAATCTGCTTGTAATAATTTCCATTGAAGTTGTAGAATACCCAACAGTTTTATATCCACAATGCCTAGATATTTTTTATAATGAACTAGGGTAAGTGAATACACTAGTTTTGAATTCTTAAAAGATATATTCAATTTGATTCTTTTTTCTTTTACAGGTGTGAGCCATGCAATGGGAGGGAGAGGAGGAATAAACAGAGGAAATATTAATAGATCTGGCGGAGGAGGCGGAGACAAAGACTGCGAAATGAAGCGCACCACCCTGGATAGCCCTCTGGGCAAGCTGGAACTGTCTGGGTGCGAACAGGGCCTGCACCGTATCATCTTCCTGGGCAAAGGAACATCTGCCGCCGACGCCGTGGAAGTGCCTGCCCCAGCCGCCGTGCTGGGCGGACCAGAGCCACTGATGCAGGCCACCGCCTGGCTCAACGCCTACTTTCACCAGCCTGAGGCCATCGAGGAGTTCCCTGTGCCAGCCCTGCACCACCCAGTGTTCCAGCAGGAGAGCTTTACCCGCCAGGTGCTGTGGAAACTGCTGAAAGTGGTGAAGTTCGGAGAGGTCATCAGCTACAGCCACCTGGCCGCCCTGGCCGGCAATCCCGCCGCCACCGCCGCCGTGAAAACCGCCCTGAGCGGAAATCCCGTGCCCATTCTGATCCCCTGCCACCGGGTGGTGCAGGGCGACCTGGACGTGGGGGGCTACGAGGGCGGGCTCGCCGTGAAAGAGTGGCTGCTGGCCCACGAGGGCCACAGACTGGGCAAGCCTGGGCTGGGTTGAGATATCATGGTCTGTAAACAATAACAACTGTGAATAAGATTATCAAATCTGTTTTAGTGTAATGATTGTCAAGTTTAAAAACATTTTTATATATAAACTGGTATACTCATGTCAATATTCTTTATTAATAAAATGTTTTTCAGTGTCAAAATTTATTATTCATTTCTTCATTAGTTGACTCCTCCTTTGCTCATCAGTCTAAGGACAGTTGTACCAGACTTTGGATAAGGTCTGCCCAGAACGAGTAGTAATTGCTCTTGCTGTTCTACTAGGCACATCAATGTTATAGTATTGATCTAAATGGAAGAGAAAACATTTTTTTAGTTAAAAAGAAAACAATGCCCAAACTAAAAAATAACTTATGTTGACTATTATGCTCAAAGACAATGTTTATCATTTTAATAGAGATGTTTTTACTAATTAATTTGAACTTTATAACAAAAAGAAAAACAATTGCCTAGACTTTTCAGCTTTTTTGATGTTTCAAAAGATTGACATTTCACCATCTTTTTGTAAAATCAGGTTCAGCTCTCCTTTATGAAGTAAACATTAAAGAGTAACCAAGTTTGAAAAATAATTTACTTGGGGTTATTCCTTTTAAAAAATACATGCCAATGTCATTCATATTATGAAATTACAGGCAGAATAACTTAGATTTCTGGGCATTTCAAAGAAAAGCATCCTGAGTAATATAATTTAATTAATAAAATTAGTTTCTCAGGAACTTCTTTCTGATCTTACAGACTCTGCAGTGATGCAAATCATTATAACCTTGTGCCAAACAAGGTATCTGTTAAATGCCACA

Table 3-3. Donor plasmids for genome editing. *ENSEMBL release 75 (August 2017)

4.1.3 Cell line validation

All endogenously tagged cell lines were validated by our standard validation pipeline described in (Koch et al., 2018). For this junction PCRs were performed to test the integration and homozygosity (primers are listed in Table 3-4). Western Blot (WB) analysis was performed to test the protein expression of homozygously tagged proteins (antibodies are listed in Table 3-5). Southern Blot (SB) analysis was carried out with endogenous and tag-specific probes (GFP and SNAP-tag) to test for correct genomic integration and off-target integrations (SB probes listed in Table 3-6). Correct subcellular localization of tagged proteins was confirmed with confocal microscopy. For the localization of SNAP-tagged cell lines, live cells were stained with either 1µM SNAP-Cell® 647- SiR or 100 nM SNAP-Cell® TMR-Star Ligand (NEB; cat.# S9102S; S9105S). Cells were incubated with the substrate for 30 min in pre-warmed complete McCoy medium at 37 °C and 5% CO2 and washed three times with pre-warmed complete McCoy medium. Cells were left in complete McCoys media for a further 30 minutes to allow unbound dye to diffuse out. Cells were then imaged using imaging medium (CO2-independent imaging medium (custom order from Thermo Fisher Scientific; based on cat.# 18045070; without phenol red); supplemented with 20% (v/v) FBS (Thermo Fisher Scientific; cat.# 10270106), 2 mM L-glutamine (Thermo Fisher Scientific; cat.# 25030081) and 1 mM sodium pyruvate (Thermo Fisher Scientific; cat.# 11360070)) under the confocal microscope. Finally, Sanger sequencing was used to confirm the integrity of the tag and gene DNA sequence after genome engineering.

Gene	**Forward primer (sequence 5’-3’)**	**Reverse primer (sequence 5’-3’)**
mEGFP-Nup107	Mito 89 ATTAATAAAAGGTATAAATGCCAGCAACAG	Mito 90 CACCTGGTCAACAACTACTTACTCCT

SNAP-Nup107 (SNAP integration)	Mito 89 ATTAATAAAAGGTATAAATGCCAGCAACAG	CBB 2018 GAACTTCACCACTTTCAGCAGTTTC
SNAP-Nup107 (het/homo)	Mito 89 ATTAATAAAAGGTATAAATGCCAGCAACAG	Mito 90 CACCTGGTCAACAACTACTTACTCCT
SNAP-Seh1	N/A	N/A
SNAP-Nup133 (SNAP integration)	CBB 2077 CAGTGGTTGAGGGAAAGGTAAG	CBB 2018 GAACTTCACCACTTTCAGCAGTTTC
SNAP-Nup133 (het/homo)	CBB 2077 CAGTGGTTGAGGGAAAGGTAAG CBB 2074 ACAGAGATGGTGGTAGGAGAG	CBB 2076 AAATCGAACAGGTTACGAGCAT CBB 2075 CTGCACAAAGGTATCCATGAAA
SNAP-Nup358/RanBP2 (SNAP integration)	Mito 498 GCATAAGACGGTGGTTCTGGAACCAATC	CBB 2018 GAACTTCACCACTTTCAGCAGTTTC
SNAP-Nup358/RanBP2 (het/homo)	Mito 501 TTGTTATCTGCTGGAAATCTACGCCCTAGG	Mito 502 GTCTCTTCGAGACCCACTCACCTGTC
TPR-SNAP	Mito 728 ATTTCCATTGAAGTTGTAGAATACCCAACAG	Mito 729 CCTTATCCAAAGTCTGGTACAACTGTCC
mEGFP	Mito 374 TCAAGGAGGACGGCAACATC	Mito 002 GATGTTGCCGTCCTCCTTGA
SNAP	Mito 292 AAAGACTGCGAAATGAAGCGCAC	Mito 293 AGATGTTCCTTTGCCCAGGAAGAT

Table 3-4. Primers for junction PCR.

AB against	Supplier	Catalog #	Host	Dilution
Nup107	ABCAM Glavy Lab	ab178399 N/A	Rabbit Rabbit	1:10,000 1:1000
Seh1	Mattaj Lab	N/A	Guinea Pig	1:1000
Nup133	Abcam	Ab155990	Rabbit	1:2000

RanBP2	N/A	N/A	N/A	N/A
TPR	N/A	N/A	N/A	N/A
mEGFP	Roche	11814460001	Mouse	1:1000
SNAP	NEB	P9310S	Rabbit	1:1500

Table 3-5. Antibodies for WB analysis.

Gene	**Probe (5'-3')**
Nup107	TTCTATGTGGTTGTTTCCCATACTTTCCTGCTGAAGGAATATCTGAAGGTTTTAAGTGGAGGAAAAGCATATTAGATTCTTGTCTTAAACACAGGCCTTTTAGTCCGCACAATTTAGTTTCTAGACCTTTGAGTGAAACTGACAGGGAGTGTTGTGATGGGACAGGAGACCTCCTGGGTTGAAATAACTTGAAGGGTCATTTTGCTCCAATTTACCACAATTCT
Seh1	N/A
Nup133	AGTCTATGGGATTGAAGCCAAGTTTTCCTAAATCCTGTTTTGTTTTTTTTTTACATGAAAAATATTACATTTAATTACATGGTAAATATGAGCCAGTGTTAATTTTTTTCAAAGAACTCCTTACTGTGAAAATATATACATAAAAAATTAGGATAATGGAGAATTTTAAGTTACAAGTAAGGTAATATAGACTCTTTTCTTTAGGGGAACACCAACACGAATGTTCCCACACCACTCCATAACTGAGTCTGTGAACTATGATGTGAAAACGTTTGGATCTTCTCTTCCTGTTAAAGTCATGGAAGCCCTAACATTGGCTGAAGGTAGGTGTCATCTTTCCA
Nup358/RanBP2	TTTGGCATAAGACGGTGGTTCTGGAACCAATCCCCCGCCGAGATGACTGTTTAAAAAATTGTAATTGTCCAAAACTTAATATTTGTGGTCTTTTTCATTATGCAGTTCTAAATCTCCCTT
TPR	CACAGCAATTAGAATAAGTACCGTAGTGTAACTTCTCACATTCAGTCATCATTGCAGCCAGCATTTTTACTTTATCTTCATGTTTTCACAAATGATATCACCTCCTTGGGAAACTGTTAGTTAATACCTTACCTTTAGAAAAGGCATAGTAATCATAGCCGTCAGGTTTTCTGATGTTGGGCAGTGATATAGCTGAGGTAACCACATTTGGAAGTCCTCTCCACAGTATACTC
mEGFP	CACATGAAGCAGCACGACTTCTTCAAGTCCGCCATGCCCGAAGGCTACGTCCAGGAGCGCACCATCTTCTTCAAGGACGACGGCAACTACAAGACCCGCGCCGAGGTGAAGTTCGAGGGCGACACCCTGGTGAACCGCATCGAGCTGAAGGGCATCGACTTCAAGGAGGACGGCAACATCCTGGGGCACAAGCTGGAGTACAACTACAACAGCCACAACGTCTATATCATGGCCGACAAGCAGAAGAACGGCATCAAGGTGAACTTCAAGATCCGCCACAACATCGAGGACGGCAGCGTGCAGCTCGCCGACCACTACCAGCAGAACACCC

SNAP	AAAGACTGCGAAATGAAGCGCACCACCCTGGATAGCCCTCTGGGCAAGCTGGAACTGTCTGGGTGCGAACAGGGCCTGCACCGTATCATCTTCCTGGGCAAAGGAACATCT

Table 3-6. Probes for SB analysis.

4.2 Single molecule localization microscopy

4.2.1 Sample preparation

Seeding cells

The homozygously expressing tagged-NOIs U2OS or HK cells were seeded on 18 mm #1.5 round coverslips, for 2D SMLM or 4Pi-SMLM respectively, which had been sterilized in 70% ethanol, dried and washed three times with 1x PBS in 6-well plates (Thermo Fisher Scientific; cat.# 140685). All coverslips used for 4Pi-SMLM were coated with a mirror-reflective aluminum film over one quarter of their surface, for the purpose of alignment in the 4Pi microscope. Mirror coating was accomplished using a thermal evaporator at the Optics Workshop of the Max Planck Institute for Biophysical Chemistry, Göttingen. Seeded cells were allowed to attach overnight at 37°C and 5% CO_2 in a cell culture incubator. All samples were fixed with the same fixation protocol and subsequently stained using one of the staining protocols described below. The incubations were carried out at room temperature (RT), unless otherwise stated. All samples were protected from light with aluminum foil.

Fixation

The coverslips containing the homozygously expressing SNAP-NOIs cells were rinsed twice with PBS and pre-fixed with 2,4% paraformaldehyde (PFA; Electron Microscopy Sciences; cat.# 15710) in 1x PBS (+Ca^{2+}/Mg^{2+}) for 30 seconds, to keep cells attached to the coverslip during subsequent permabilization and washing steps. The cells were then immediately permeabilized with 0.5% Triton X-100 (Sigma-Aldrich; cat.# T8787) in 1x PBS (+Ca^{2+}/Mg^{2+}) for 10 min and directly fixed afterwards with 2,4% paraformaldehyde (PFA; Electron Microscopy Sciences; cat.# 15710) in

1x PBS (+Ca^{2+}/Mg^{2+}) for another 30 minutes. After fixation, the samples were rinsed three times with 1x PBS and quenched for remaining fixative with 50 mM NH_4Cl for 5 min. After quenching, the sample was rinsed three times with 1xPBS and washed three times for 5 min with 1x PBS in a rocker. The fixed samples were immediately stained using one of the protocols described below.

4.2.1.1 NPC labeling with anti-GFP antibody

After fixation (4.2.1), samples were blocked with 5% Normal Goat Serum (NGS; Sigma-Aldrich; cat.# G9023) in 1x PBS (+Ca^{2+}/Mg^{2+}) for 1 hour. The primary anti-GFP antibody (polyclonal rabbit anti-GFP-antibody; MBL; cat.# 598; 1:500) was diluted in blocking solution (5% (w/v) NGS in 1x PBS) and incubated with the sample for 1 hour. The sample was then rinsed three times with 1xPBS and washed three times for 5 min with 1x PBS on a rocker. The secondary antibody coupled to AF647 (polyclonal $F(ab')^2$ fragment of goat anti-rabbit; Thermo-Fisher; cat.#A21246; 1:500) was also diluted in blocking solution (5% (w/v) NGS in 1x PBS) and incubated with the sample for 1 hour. This was followed by a final round of three rinsing and 5min washing steps.

4.2.1.2 NPC labeling with anti-GFP nanobody

After fixation (4.2.1), samples were blocked with a few drops of Image-iT FX Signal Enhancer (Thermo-Fisher; cat.# I36933) for 30 min. The anti-GFP nanobody (monoclonal anti-GFP nanobody; Chromotek; cat.# gt-250; 1:1000), which had been coupled to AF647 using NHS-ester chemistry, was kindly provided by Dr. Jonas Ries (Ries et al., 2012) and was diluted in blocking solution (2% (w/v) BSA in 1x PBS) and incubated with the sample for 1 hour. This was followed by a final round of three rinsing and 5min washing steps.

4.2.1.3 NPC labeling with SNAP-tag

After fixation (4.2.1), samples were blocked with a few drops of Image-iT FX Signal

Enhancer (Thermo-Fisher; cat.# I36933) for 30 min. The benzylguanine (BG)-conjugated AF647 (SNAP-Surface; NEB; cat.# S9136S) was diluted to 1 µM in blocking solution (0,5% (w/v) BSA, 1 mM DTT in 1x PBS) and incubated with the sample for 1 hour. This was followed by a final round of three rinsing and 5 min washing steps.

4.2.1.4 Dual-color NPC labeling

a) *Dual-color labeling for the Ratio-metric approach*

After fixation (4.2.1), samples were blocked with a few drops of Image-iT FX Signal Enhancer (Thermo-Fisher; cat.# I36933) for 30 min. The benzylguanine (BG)-conjugated Cy5.5 was synthesized and kindly provided by the Chemical Facility of the Max Plank Institute in Göttingen. The BG-Cy5.5 was diluted to 200 nM in blocking solution (0,5% (w/v) BSA, 1 mM DTT in 1x PBS) and incubated with the sample for 2 hours. Next, the sample was rinsed three times with 1x PBS and washed three times for 5 min with 1x PBS on a rocker. The samples were then blocked again with 5% Normal Goat Serum (NGS; Sigma-Aldrich; cat.# G9023) in 1x PBS (+Ca^{2+}/Mg^{2+}) for 1 hour. The primary anti-ELYS antibody (polyclonal rabbit anti-AHCTF1-antibody; Sigma-Aldrich; cat.# HPA031658; 1:30) was diluted in blocking solution (5% (w/v) NGS in 1x PBS) and incubated with the sample for 1 hour. The sample was then rinsed three times with 1xPBS and washed three times for 5 min with 1x PBS in a rocker. The secondary antibody coupled to AF647 (polyclonal F(ab')^2 fragment of goat anti-rabbit; Thermo-Fisher; cat.#A21246; 1:500) was also diluted in blocking solution (5% (w/v) NGS in 1x PBS) and incubated with the sample for 1 hour. This was followed by a final round of three rinsing and 5min washing steps.

b) *Dual-color labeling for the activator-reporter approach*

After fixation (4.2.1), samples were blocked with a few drops of Image-iT FX

Signal Enhancer (Thermo-Fisher; cat.# I36933) for 30 min. The benzylguanine (BG)-conjugated A647-cadaverine-A405 was synthesized and kindly provided by the Chemical Facility of the Max Plank Institute in Göttingen. The BG-A647-cadaverine-A405 was diluted to 200 nM in blocking solution (0,5% (w/v) BSA, 1 mM DTT in 1x PBS) and incubated with the sample for 2 hours. Next, the sample was rinsed three times with 1x PBS and washed three times for 5 min with 1x PBS in a rocker. The samples were then blocked again with 5% Normal Goat Serum (NGS; Sigma-Aldrich; cat.# G9023) in 1x PBS (+Ca^{2+}/Mg^{2+}) for 1 hour. The primary anti-ELYS antibody (polyclonal rabbit anti-AHCTF1-antibody; Sigma-Aldrich; cat.# HPA031658; 1:30) was diluted in blocking solution (5% (w/v) NGS in 1x PBS) and incubated with the sample for 1 hour. The sample was then rinsed three times with 1xPBS and washed three times for 5 min with 1x PBS on a rocker. The secondary antibody, which had been coupled to AF647 and Cy3 using NHS-ester chemistry (IgG of goat anti-rabbit; Invitrogen; cat.# 31210; 1:500) was diluted in blocking solution (5% (w/v) NGS in 1x PBS) and incubated with the sample for 1 hour. This was followed by a final round of three rinsing and 5min washing steps.

4.2.1.5 Fluorescent beads

The stained samples were additionally covered with 0.1 µm Fluorescent Microspheres, (Red fluorescent, 690nm/720nm, Molecular Probes, cat.#F-8798). For this, beads were sonicated for 10 minutes in a water-bath sonicator. The beads were then diluted in 1x PBS at 1:1000000 and vortexed extensively. The diluted beads were applied immediately to the surface of the sample and incubated for 5 minutes. Immediately after the incubation, a buffer solution containing 50mM $MgCl_2$ was added to the sample and incubated for another minute. The sample was then rinsed three times and washed another three times for 10 minutes. The sample was stored in a dark place until needed.

4.2.1.6 Imaging Buffers

The blinking buffer used for SMLM was composed of:

I. TN buffer (50 mM Tris (Sigma-Aldrich; cat.# T1503), pH8; 10 mM NaCl (Merck; cat.# 106404); 10% (w/v) D-glucose (Merck; cat.# 104074))
II. Oxygen scavenger system (0.5 mg/mL pyranose oxidase (Sigma-Aldrich; cat.# P4234); 40 μg/mL catalase (Sigma-Aldrich; cat.# C100))
III. A primary thiol, either β-Mercaptoethylamine (MEA, Sigma-Aldrich, cat.# 30070) at a 10 mM concentration or β-Mercaptoethanol (βME, Sigma-Aldrich, cat.# M6250) at a 143 mM concentration.

The MEA was stored as a 1 M stock solution in PBS and the pH was adjusted with HCl to 8. The βME was stored as a pure solution. The solutions were kept at 4°C and used within a month of preparation. For experiments, the thiol solutions and the oxygen scavenger system were diluted immediately before imaging to the final concentrations indicated above. This blinking buffer changes pH over time, due to acidification with gluconic acid as one of the products of the enzymatic reaction. Given that the switching properties of SMLM dyes depend on the pH, the sample was exchanged every 2 hours.

4.2.1.7 Sample mounting

The samples were wet mounted using either an 18mm round coverslip mounted over a depression slide (neoLab; cat.# 1-6293) for 2D SMLM, or an 18mm round coverslip placed over a larger 30mm round coverslip for 4Pi-SMLM, to which I will refer to as mounting slide from here on. Next, ~300 μl blinking buffer (4.2.1.6) was added to the middle of the mounting slide and the stained sample was suspended on the blinking buffer with cells facing the mounting slide. Using a vacuum aspirator the volume of imaging buffer was carefully lowered until only a thin layer of buffer remained and the sample was immobilized. Finally, the mounted sample was sealed around the edges of the 18mm round coverslip using Picodent Twinsil glue (Picodent; cat.# 13001000).

4.2.2 Microscopes for Single molecule Localization

All SMLM measurements were performed using two microscopes, which were custom-built by Dr. Mark Bates at the MPI of Biophysical Chemistry in Göttingen, Germany. The first microscope (2D SMLM) was used for all 2D measurements while the second microscope (4Pi-SMLM) was used for all 3D measurements.

4.2.2.1 2D SMLM

The microscope is based on an Olympus IX-71 inverted microscope stand, and equipped with a UPLANSAPO 100X NA 1.4 oil-immersion objective lens. Laser illumination sources used for SMLM imaging included a red laser for imaging (642nm CW, 1.5W, MPB Communications Inc.) and UV and green lasers for molecule re-activation (405nm CW, 100mW, Coherent, and 561nm, CW, 5W, MPB Communications Inc.). Excitation light was controlled and modulated either directly via the laser controller or via an acousto-optic tunable filter (Crystal Technologies, AOTF-PCAOM). Variable angle TIRF or near-TIRF illumination was achieved using a custom light path entering through the rear port of the microscope. Excitation light was separated from fluorescence using a dichroic beam-splitter in the filter cube turret (650DCXR, Chroma Technology Corp.) and an emission filter in the detection path (ET700/75, Chroma). Fluorescence light was collected by the objective lens, passed through an optical relay, and focused to form an image on a back-illuminated EMCCD camera (Andor Ixon+, DU860). For dual-color SMLM, the fluorescence was split using a 678 nm (AF 647/Cy5.5) long pass dichroic mirror and imaged onto two halves of the camera chip. The microscope was equipped with a motorized sample stage (Märzhäuser Wetzlar), and the objective lens was mounted on a piezoelectric objective positioner (Piezo Jena). During image acquisition, the objective Z position was continuously adjusted to maintain a constant focus position. This focus-lock system was based on an infra-red laser beam introduced into the microscope via the right-side port below the filter turret and combined into the optical path using a short-pass dichroic mirror (900DCSP, Chroma). The focus lock laser (980nm, Thorlabs) was aligned to focus at the back focal plane of the objective lens and reflect from the glass-water interface of the sample. The position of the reflected beam was detected using a quandrant photodiode (Silicon Sensor Intl., QP50), which was monitored via a DAQ card (National Instruments). All microscope control and data acquisition was performed using custom software written in Labview (National Instruments).

4.2.2.2 4Pi-SMLM

The starting point for the 4Pi-SMLM microscope was an earlier design published by Aquino et al. (Aquino et al., 2011), and this design was extensively modified to achieve significantly higher image quality. Specifically, the design was changed to incorporate feedback systems to maintain the sample focus position, higher NA objectives to collect more light, a completely redesigned sample stage allowing for fast and reliable sample mounting and linear translation when adjusting the sample position, a redesigned 4Pi image cavity allowing for maintenance of the beam path alignment, and new acquisition and control software to allow accurate control of the numerous instruments involved in the system and acquisition of the raw image data. The laser illumination sources used for SMLM imaging included a red laser for imaging (642nm CW, 2W, MPB Communications Inc.) and UV and green lasers for molecule re-activation (405nm CW, 100mW, Coherent, and 561nm, CW, 5W, MPB Communications Inc.). Excitation light was controlled and modulated either directly via the laser controller or via an acousto-optic tunable filter (AA Opto Electronic). Variable angle TIRF or near-TIRF illumination was achieved by coupling all light sources through an optical fiber, whose output was positioned in an optical plane conjugate to the objective lens back focal plane. By placing the output of the fiber on a motorized translation stage, the illumination angle could be continuously varied for optimal signal to background ratio. The 4Pi microscope cavity was based on two high-NA objective lenses (Leica, 100x, oil immersion, NA 1.46). One objective was fixed in position on a mounting block while the other was adjustable in three dimensions using a 3-axis piezo stage (Physik Instrumente, P-733.3). The adjustable objective was also adjustable in tip/tilt and XYZ via micrometer screws for coarse positioning and alignment. Illumination and control beams were introduced into the 4Pi cavity and brought out again via dichroic mirrors (ZT405-488-561-640-950RPC, Chroma). The detected fluorescence from the two objectives was recombined at a 50:50 beam-splitter (Halle). Prior to the beam-splitter each detected beam passed through a quarter wave plate (Halle) and a custom Babinet-Soleil compensator made of quartz and BK7 glass, one of which with an adjustable thickness of quartz glass, which allowed a precise phase delay to be introduced between the P- and S- polarized fluorescence light. The remainder of the detection path consisted of an optical relay to crop and focus the overlaid P- and S- polarized images onto four quadrants of an EMCCD camera (Andor Ixon DU897) as previously described. Before the camera, the light was filtered with fluorescence emission filters (Semrock LP647RU, Semrock FF01-770SP) and optionally a dichroic mirror (Semrock FF685-Di02), which allowed the fluorescence in one polarization channel to be filtered selectively for two-color 4Pi-SMLM imaging. Control systems included the sample focus control and the objective alignment control, and each of these was based on an infra-red laser beam introduced into the 4Pi cavity. The sample focus control was based on a design similar to that used in the 2D SMLM microscope: an infrared beam (830nm laser diode, Thorlabs) was reflected from the sample-glass interface, and the position of the reflected beam was detected on a photodetector. Fine control of the sample position was maintained with a linear piezo stage (Physik Instrumente, P-752) mounted underneath the top section of the three-axis linear stage used for sample positioning (Newport, M-462-XYZ-M). For the objective alignment control, a second infra-red beam (940nm laser diode, Thorlabs) was collimated and passed through the two objective lenses, focusing at the sample plane. Any motion of the two objectives with respect to each other resulted in a lateral shift in the transmitted beam, or a change in the collimation of the transmitted beam. The lateral shift was continuously monitored via a quadrant photodiode, and the transmitted beam collimation was monitored by splitting the beam and focusing it onto two pinholes positioned on either side of the focus, with photodetectors behind each pinhole. These signals were measured using a DAQ card (National Instruments), and a software-based feedback loop was then used to adjust the position of the movable objective lens to keep it aligned with the fixed objective lens. All microscope control and data acquisition was performed using custom software written in Labview (National Instruments).

4.2.3 Image acquisition

The sample was illuminated with 642 nm excitation light in order to switch off the fluorophores and cause them to blink. The emitted light was filtered spectrally (see above) and detected at the EMCCD camera, running at a frame rate of 101 Hz. Typically, around 100,000 image frames were acquired in a single measurement. During the experiment, the power of the 405 nm laser (and also the green 561nm laser, in the case of activator-reporter based two-color imaging) was manually adjusted to keep the number of localizations per frame constant. Optical stabilization of the z-focus (focus-lock) was engaged before starting each recording, in order to minimize sample drift during the measurement. The imaging procedure was similar for 2D and 4Pi SMLM measurements, with the main differences being the microscope configuration and the sample preparation. Prior to each set of 4Pi measurements, images of a fluorescent bead located on the sample were recorded as the bead was scanned in the Z-dimension, in order to create a calibration scan which was used in post-processing analysis of the 4Pi SMLM image data. For 4Pi and dual-color ratiometric 2D SMLM measurements, images of beads located at different positions in the sample plane were recorded, in order to generate a coordinate mapping which allowed the coordinate systems of the different image channels to be mapped onto each other.

4.2.4 Image reconstruction

2D and 4Pi SMLM data were analyzed using custom software packages written by Dr. Mark Bates (unpublished). The 4Pi SMLM data was also analyzed using previously developed software written by Dr. Daniel Aquino (briefly described in Aquino et al., 2011). In general, SMLM image analysis and reconstruction follows a standard approach based on peak finding and localization (Bates et al., 2013b). Two-color imaging via the activator-reporter method was analyzed as described previously (Bates et al, Science, 2007). Two color imaging via the ratio-metric method was analyzed as described previously (Aquino et al., 2011; Testa et al., 2010). Correction of sample drift in post-processing was done based on image correlation of the SMLM data with itself over multiple time windows. SMLM images were rendered as summed Gaussian spots (2D imaging) or as localization histograms (3D imaging) with a bin size typically chosen to be 7nm.

4.3 Image Analysis

All analysis was performed using Matlab R2012b and R2017b (Mathworks) and R version 3.4.2 (R Foundation for Statistical Computing, 2018). The averaging operations were carried out with TOM (Nickell et al., 2005) and av3 (Forster et al., 2005) toolboxes in Matlab. The complete list of Matlab and R functions can be found in the following open source repository:
https://git.embl.de/sabinina/PhD_Thesis

4.3.1 NPC particle picking

The individual NPC particles were selected from the 4Pi-SMLM image-stacks by an automatic particle-picking pipeline, which was developed by Dr. Jean-Karim Hériché and is written in the R programming language (R Foundation for Statistical Computing, 2018). The automatic particle-picking pipeline implements two different algorithms for identifying NPC particles within the 4Pi-SMLM images: a density-based clustering algorithm (DBSCAN) (Ester et al., 1996) and a template-matching algorithm (circle Hough transform) (Duda and Hart, 1972). After detecting all possible NPCs within a 4Pi-SMLM image-stack, the selected particles are cropped into image-stacks of 40x40x40 voxels, where each voxel corresponds to 7nm.

The DBSCAN modality can be used to identify NPC particles of irregular structures. This algorithm was used to automatically select flexible NOIs in single-color 4Pi-SMLM images. The DBSCAN algorithm is controlled by two parameters: the distance ε (*eps*) defining a neighbourhood and the minimum number of points in the eps region (*MinPts*) (Ester et al., 1996). Both *MinPts* and *eps* were selected heuristically for each NOIs (RanBP2: *MinPts* = 8, *eps* = 15 ; TPR: *MinPts* = 7, *eps* = 12) as described in the literature (Ester et al., 1996).

The circle Hough transform modality is better suited to identify NPC particles with ring-shaped structures. This algorithm was used to automatically select scaffold NOIs in single- and dual-color 4Pi-SMLM images. The Hough transform algorithm can be adjusted with two main parameters: a circle radius (*r*) (or a range of radii) and a detection score threshold (*t*). A range of radii *r* was selected heuristically for each NOIs (Seh1: *r* = 5:8 pixels; Nup107: *r* = 6:10 pixels; Nup133: *r* = 7:10 pixels; ELYS: *r* = 9:12 pixels) and the threshold *t* was set to 0.4 for all cases. The dual-color images were all selected with the Hough transform modality based on the channel of the reference NOI (ELYS: *r* = 9:12 pixels).

4.3.2 3D SMLM averaging

All automatically selected 4Pi-SMLM particles (i.e. 40x40x40 voxel image-stacks, where each voxel corresponds to 7nm; Table 3-7.) were normalized by applying a principal square-root function to their fluorescence intensity profile. Subsequently, the initial reference image was generated by the sum of all 4Pi-SMLM particles. Following this, an iterative averaging algorithm was used for aligning the particles and to refine the initial reference (Beck et al., 2004). Briefly, the alignment was performed by angular search of the 4Pi-SMLM particles (i.e. both rotational and translational shifts are calculated by 3D cross correlation (CC) in Fourier space), to generate the subsequent references. Here, the orientation of each particle is described by the Euler angles φ, ψ, and θ. An initial averaging model of the NOIs was generated using a random distribution of the polar angle φ. During the iterative refinement, eight-fold symmetry along φ was imposed (i.e. based on the known NPC symmetry) in order to improve the SNR. Ideally, this algorithm takes into account the ‘missing wedge’ present for each of the sub volumes (tomograms) (Beck et al., 2004; Forster et al., 2005) and given that 4Pi-SMLM data contains no ‘missing wedge’, this parameter was supplemented with full angular coverage of -90° to 90°. To take into account the structural plasticity between the NR and CR (Beck et al., 2007), the NOIs that form part of both rings were masked with an elliptical mask whereas asymmetric NOIs were masked with a spherical mask during the SMLM alignment procedure. Ten iteration cycles were sufficient for angular search convergence.

The final reconstructions incorporated 661 particles for Seh1, 2021 particles for Nup107, 1741 particles for Nup133 and 2540 particles for ELYS. The final scaffold classes incorporated 341, 175 and 84 particles for Seh1 I-III; 564, 211 and 225 for Nup107 I-III; 442, 348 and 210 for Nup133 I-III and 200, 446 and 235 for ELYS I-III, respectively. The final flexible classes incorporated 222 and 91 particles for Nup358/RanBP2 I-II and 364, 253 and 383 for TPR I-II, respectively. Finally, the dual-color reconstructions incorporated 458 particles for ELYS with Seh1 and 514 particles for ELYS with Nup107.

For visualization purposes and generation of the photon density maps the final reconstructions were interactively visualized and analyzed in the molecular modeling software UCSF Chimera (Pettersen et al., 2004).

4.3.3 Distance estimation

The axial and lateral positions of the 4Pi-SMLM averaged 3D reconstructions were calculated by fitting a Gaussian function to their axial and lateral profiles. The axial profile was generated by the sum projection along the *X* and *Y* axis of the averaged image. The lateral profile was generated by the central line profile parallel to the *X* axis, in the sum projection along the *Z* axis of the averaged image.

$$\boldsymbol{f}(\boldsymbol{x}) = \sum_{i=1}^{n} a_i e^{\left[-\left(\frac{x-b_i}{c_i}\right)^2\right]}$$

where a is the amplitude, b the centroid position, c is related to the peak width and n the number of peaks to fit. For scaffold nucleoporins that are present in both nucleoplasmic and cytoplasmic rings, analogous to the simulated data in this section, $n = 2$. The centroid positions (b_1 and b_2) are further subtracted from each other to obtain the corresponding sub-pixel distance d between the axial and lateral position of the averaged image (Fig.2-6).

4.3.4 Generation of volume masks

Volume masks were automatically generated with the following equation:

$$1 = \frac{(x - xc)^2}{xr^2} + \frac{(y - yc)^2}{yr^2} + \frac{(z - zc)^2}{zr^2}$$

where the center $(xc, yc, zc) = (20, 20, C)$ with C as the axial centroid position obtained with the Gaussian Fit methodology described in 4.3.3, the radius $(xr, yr, zr) = (13, 13, 3)$ for an elliptical and $(xr, yr, zr) = (13, 13, 13)$ for a spherical mask in a 40x40x40 voxel size volume (Fig.2-7).

4.3.5 Reference interpolation

To correct the axial positions in the final averaged reference, an axial interpolation strategy was implemented (Fig.2-9). Here, the final averaged references with both spherical (S) and elliptical (E) masks are used for calculating the axial shift (α) (Fig.2-9 B), obtained from the difference in centroid positions from the Gaussian Fit methodology described in 4.3.3. The final averaged references obtained from the averaging with elliptical mask (E) was interpolated to obtain the corrected averaged reference (I) as following (Fig.2-9 C):

for the cytoplasmic ring

$$I_x = E_x(1-\alpha) + E_{x+1}\alpha$$

for the nucleoplasmic ring

$$I_x = E_x\alpha + E_{x+1}(\alpha - 1)$$

where E_x and I_x are the intensity values of the position x within the reference images E and I, respectively. The resulting interpolated averaged reference I contains both refined masked features and corrected axial positions (Fig.2-9 D)

4.3.6 Rotational position estimation

Rotational stability

For analyzing the rotational stability throughout the averaging iterations steps, the cross correlation (CC; $\otimes$) between the initial reference f against the iterated reference g was calculated along τ_φ (0° - 360°):

$$(f \otimes g)(\tau_{\varphi})$$

The resulting CCF analysis illustrates the rotational displacements of the periodic rotational 3D CC function at each iteration step. The presence of rotational displacements would indicate a rotational instability during the alignment procedure (Fig.2-10).

Rotational displacements between subunits

To determine rotational shifts between NR and CR subunits, a sum projected image along the Z axis was generated for each NR and CR volume. For a given iteration, the auto-cross-correlation (CC; $\otimes$) of the NR reference f and the cross-correlation (CC; $\otimes$) between the NR reference f against the CR reference g was calculated along τ_{φ} (0° - 360°). After this, each CCF was fitted with a Gaussian function to extract the centroid positions (see. 4.3.3). The subtraction of centroid positions corresponds to the rotational shifts between NR and CR subunits (Fig.2-11).

4.3.7 Radial NPC analysis on variability

Stacks containing the upper and the lower rings of average NOIs were sum projected along the *Z*-axis. Projected images were then transformed using its polar coordinate representation. The mean lateral (radial) distribution was computed by fitting a Gaussian to the polar image to detect the intensity peak in sub pixel accuracy along 1 to 360° angles. Each registered NOI was also projected and represented using the polar coordinate systems in similar way. An adaptive threshold value was determined using Otsu method and pixels having intensity value lower than 1/5 of the threshold was considered insignificant and removed for further analysis. Radial distances of individual nucleoporins were computed and angles without any labeled particle were not considered to compute lateral variations.

The mean axial position of the upper and the lower rings were computed by fitting a Gaussian along the Z direction through the pixel closest to the peak intensity detected for mean lateral distributions. This was done for each lateral angle (1 to 360°). Axial positions of individual nucleoporins were also computed in the similar way where pixels without any labeled particles were not taken into consideration for computing axial variations.

4.3.8 Persistence homology analysis

We view distinguishing between different conformations adopted by a given NOI inside a nuclear pore as a clustering problem, i.e. for each NOI, we would like to cluster nuclear pores based on structural similarity. As each nuclear pore is represented by a point set defined by the 3D Cartesian coordinates of the localization signals of the NOI in a 40x40x40 region, standard similarity or distance measures do not capture meaningful structural differences between such SMLM point sets because they are sensitive to rotation, missing data and noise. Therefore we sought a method that could robustly characterize differences in conformations of structures represented by 3D point sets and turned our attention to topological data analysis.

One way of deriving a topological signature from a point set is through the notions of homology groups and of persistent homology (Edelsbrunner and Harrer, 2010). The k-dimensional homology group characterizes the topological feature seen in that dimension, i.e. 0-dimensional homology characterizes connected components, 1-dimensional homology characterizes loops (or equivalently holes inside loops) and 2-dimensional homology characterizes voids (i.e. bubbles). Persistent homology efficiently computes homology groups at multiple scales. To this end, each point set is converted into a simplicial complex based on a proximity parameter t . Recording the appearance and disappearance of topological features over a range of values of t produces a persistence diagram.

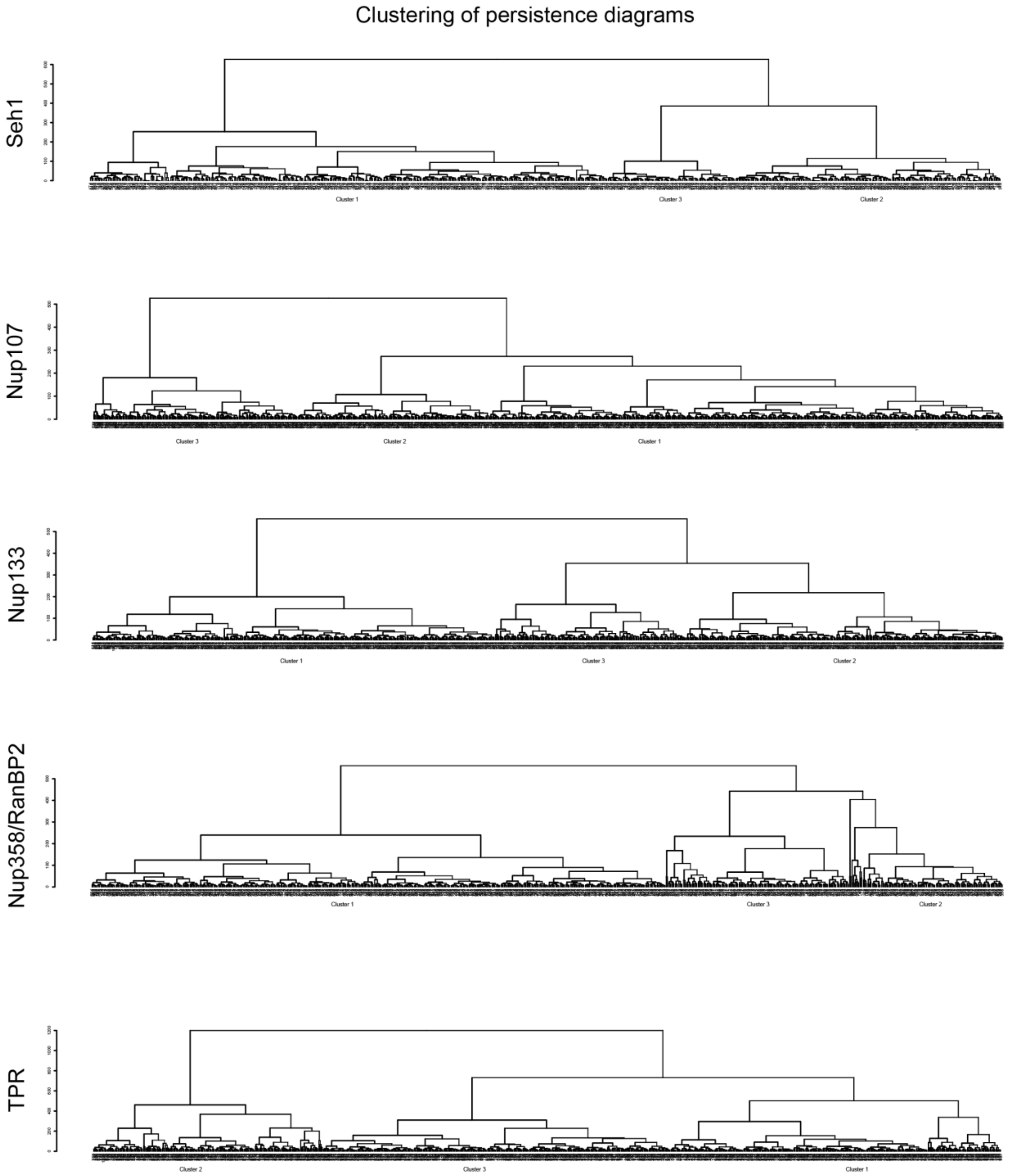

FIGURE 4-1. Clustering of Persitence diagrams. Each 4Pi-SMLM particle for a given NOI is represented by a persistence diagram and their similarities measured by the sliced Wasserstein distance (Carrière et al., 2017). Hierarchical clustering with Ward’s criterion was applied to the resulting distance matrix to create the persistence diagram trees for Seh1, Nup107, Nup133, Nup358/RanBP2 and TPR.

We further use the Euclidean distance as proximity measure between points in a set and compute 0- and 1-dimensional homology groups from Vietoris-Rips simplicial complexes and persistence diagrams for t ranging from 0 to 10 using the R package TDA (Fasy et al., 2014). Thus, each 4Pi-SMLM particle for a given NOI is represented by a persistence diagram. Finally, to measure topological similarity between nuclear pores, we next compute the sliced Wasserstein distance between the corresponding persistence diagrams (Carrière et al., 2017). Clustering is then performed by hierarchical clustering with Ward’s criterion applied to the resulting distance matrix (Fig.4-1).

5 Bibliography

Abbe, E. (1873). Beiträge zur Theorie des Mikroskops und der mikroskopischen Wahrnehmung. Arch. Für Mikroskopische Anat. *9*, 413–418.

Aitchison, J.D., and Rout, M.P. (2012). The yeast nuclear pore complex and transport through it. Genetics *190*, 855–883.

Akey, C.W., and Goldfarb, D.S. (1989). Protein import through the nuclear pore complex is a multistep process. J. Cell Biol. *109*, 971–982.

Alber, F., Dokudovskaya, S., Veenhoff, L.M., Zhang, W., Kipper, J., Devos, D., Suprapto, A., Karni-Schmidt, O., Williams, R., Chait, B.T., et al. (2007a). The molecular architecture of the nuclear pore complex. Nature *450*, 695–701.

Alber, F., Dokudovskaya, S., Veenhoff, L.M., Zhang, W., Kipper, J., Devos, D., Suprapto, A., Karni-Schmidt, O., Williams, R., Chait, B.T., et al. (2007b). Determining the architectures of macromolecular assemblies. Nature *450*, 683–694.

Amlacher, S., Sarges, P., Flemming, D., Van Noort, V., Kunze, R., Devos, D.P., Arumugam, M., Bork, P., and Hurt, E. (2011). Insight into structure and assembly of the nuclear pore complex by utilizing the genome of a eukaryotic thermophile. Cell *146*, 277–289.

Ando, D., Colvin, M., Rexach, M., and Gopinathan, A. (2013). Physical Motif Clustering within Intrinsically Disordered Nucleoporin Sequences Reveals Universal Functional Features. PLoS One *8*.

Antonin, W., Franz, C., Haselmann, U., Antony, C., and Mattaj, I.W. (2005). The integral membrane nucleoporin pom121 functionally links nuclear pore complex assembly and nuclear envelope formation. Mol. Cell *17*, 83–92.

Antonin, W., Ellenberg, J., and Dultz, E. (2008). Nuclear pore complex assembly through the cell cycle: Regulation and membrane organization. FEBS Lett. *582*, 2004–2016.

von Appen, A., and Beck, M. (2015). Structure Determination of the Nuclear Pore Complex with Three-Dimensional Cryo electron Microscopy. J. Mol. Biol.

von Appen, A., Kosinski, J., Sparks, L., Ori, A., DiGuilio, A.L., Vollmer, B., Mackmull, M.-T., Banterle, N., Parca, L., Kastritis, P., et al. (2015). In situ structural analysis of the human nuclear pore complex. Nature *526*, 140–143.

Aquino, D., Schönle, A., Geisler, C., Middendorff, C. V, Wurm, C.A., Okamura, Y., Lang, T., Hell, S.W., and Egner, A. (2011). Two-color nanoscopy of three-dimensional volumes by 4Pi detection of stochastically switched fluorophores. Nat. Methods *8*, 353–359.

Asally, M., Yasuda, Y., Oka, M., Otsuka, S., Yoshimura, S.H., Takeyasu, K., and Yoneda, Y. (2011). Nup358, a nucleoporin, functions as a key determinant of the nuclear pore complex structure remodeling during skeletal myogenesis. FEBS J. *278*, 610–621.

Bailer, S.M., Siniossoglou, S., Podtelejnikov, A., Hellwig, A., Mann, M., and Hurt, E. (1998). Nup116p and Nup100p are interchangeable through a conserved motif which constitutes a docking site for the mRNA transport factor Gle2p. EMBO J. *17*, 1107–1119.

Bailer, S.M., Balduf, C., Katahira, J., Podtelejnikov, A., Rollenhagen, C., Mann, M., Panté, N., and Hurt, E. (2000). Nup116p associates with the Nup82p-Nsp1p-Nup159p nucleoporin complex. J. Biol. Chem. *275*, 23540–23548.

Bailer, S.M., Balduf, C., and Hurt, E. (2001). The Nsp1p carboxy-terminal domain is organized into functionally distinct coiled-coil regions required for assembly of nucleoporin subcomplexes and nucleocytoplasmic transport. Mol. Cell. Biol. *21*, 7944–7955.

Basel-Vanagaite, L., Muncher, L., Straussberg, R., Pasmanik-Chor, M., Yahav, M., Rainshtein, L., Walsh, C.A., Magal, N., Taub, E., Drasinover, V., et al. (2006). Mutated nup62 causes autosomal recessive infantile bilateral striatal necrosis. Ann. Neurol. *60*, 214–222.

Bates, M., Huang, B., Dempsey, G.T., and Zhuang, X. (2007). Multicolor super-resolution imaging with photo-switchable fluorescent probes. Science *317*, 1749–1753.

Bates, M., Dempsey, G.T., Chen, K.H., and Zhuang, X. (2012). Multicolor super-resolution fluorescence imaging via multi-parameter fluorophore detection. ChemPhysChem *13*, 99–

107.

Bates, M., Jones, S.A., and Zhuang, X. (2013a). Stochastic optical reconstruction microscopy (STORM): A method for superresolution fluorescence imaging. Cold Spring Harb. Protoc. *8*, 498–520.

Bates, M., Jones, S.A., and Zhuang, X. (2013b). Stochastic optical reconstruction microscopy (STORM): A method for superresolution fluorescence imaging. Cold Spring Harb. Protoc. *8*, 498–520.

Bayliss, R., Littlewood, T., and Stewart, M. (2000). Structural Basis for the Interaction between FxFG Nucleoporin Repeats and Importin-β in Nuclear Trafficking. Cell *102*, 99–108.

Beck, M., and Hurt, E. (2017). The nuclear pore complex: Understanding its function through structural insight. Nat. Rev. Mol. Cell Biol. *18*, 73–89.

Beck, M., Förster, F., Ecke, M., Plitzko, J.M., Melchior, F., Gerisch, G., Baumeister, W., and Medalia, O. (2004). Nuclear pore complex structure and dynamics revealed by cryoelectron tomography. Science *306*, 1387–1390.

Beck, M., Lŭí, V., Förster, F., Baumeister, W., and Medalia, O. (2007). Snapshots of nuclear pore complexes in action captured by cryo-electron tomography. Nature *449*, 611–615.

Belgareh, N., Snay-Hodge, C., Pasteau, F., Dagher, S., Cole, C.N., and Doye, V. (1998). Functional characterization of a Nup159p-containing nuclear pore subcomplex. Mol. Biol. Cell *9*, 3475–3492.

Betzig, E., Patterson, G.H., Sougrat, R., Lindwasser, O.W., Olenych, S., Bonifacino, J.S., Davidson, M.W., Lippincott-Schwartz, J., and Hess, H.F. (2006). Imaging intracellular fluorescent proteins at nanometer resolution. Science *313*, 1642–1645.

Bilokapic, S., and Schwartz, T.U. (2012). 3D ultrastructure of the nuclear pore complex. Curr. Opin. Cell Biol. *24*, 86–91.

Bock, H., Geisler, C., Wurm, C.A., Von Middendorff, C., Jakobs, S., Sch??nle, A., Egner, A., Hell, S.W., and Eggeling, C. (2007). Two-color far-field fluorescence nanoscopy based on photoswitchable emitters. Appl. Phys. B Lasers Opt. *88*, 161–165.

Boehmer, T., Enninga, J., Dales, S., Blobel, G., and Zhong, H. (2003). Depletion of a single nucleoporin, Nup107, prevents the assembly of a subset of nucleoporins into the nuclear pore complex. Proc. Natl. Acad. Sci. *100*, 981–985.

Boehmer, T., Jeudy, S., Berke, I.C., and Schwartz, T.U. (2008). Structural and Functional Studies of Nup107/Nup133 Interaction and Its Implications for the Architecture of the Nuclear Pore Complex. Mol. Cell *30*, 721–731.

Bourg, N., Mayet, C., Dupuis, G., Barroca, T., Bon, P., Lécart, S., Fort, E., and Lévêque-Fort, S. (2015). Direct optical nanoscopy with axially localized detection. Nat. Photonics *9*, 587–593.

Briggs, J.A.G. (2013). Structural biology in situ-the potential of subtomogram averaging. Curr. Opin. Struct. Biol. *23*, 261–267.

Broeken, J., Johnson, H., Lidke, D.S., Liu, S., Nieuwenhuizen, R.P.J., Stallinga, S., Lidke, K.A., and Rieger, B. (2015). Resolution improvement by 3D particle averaging in localization microscopy. Methods Appl. Fluoresc. *3*.

Brohawn, S.G., and Schwartz, T.U. (2009). Molecular architecture of the Nup84-Nup145C-Sec13 edge element in the nuclear pore complex lattice. Nat. Struct. Mol. Biol. *16*, 1173–1177.

Brohawn, S.G., Leksa, N.C., Spear, E.D., Rajashankar, K.R., and Schwartz, T.U. (2008). Structural evidence for common ancestry of the nuclear pore complex and vesicle coats. Science *322*, 1369–1373.

Brohawn, S.G., Partridge, J.R., Whittle, J.R.R., and Schwartz, T.U. (2009). The Nuclear Pore Complex Has Entered the Atomic Age. Structure *17*, 1156–1168.

Bui, K.H., Von Appen, A., Diguilio, A.L., Ori, A., Sparks, L., Mackmull, M.T., Bock, T., Hagen, W., Andrés-Pons, A., Glavy, J.S., et al. (2013). Integrated structural analysis of the human nuclear pore complex scaffold. Cell *155*, 1233–1243.

Burns, S., Avena, J.S., Unruh, J.R., Yu, Z., Smith, S.E., Slaughter, B.D., Winey, M., and Jaspersen, S.L. (2015). Structured illumination with particle averaging reveals novel roles for yeast centrosome components during duplication. Elife *4*.

Buss, F., and Stewart, M. (1995). Macromolecular interactions in the nucleoporin p62 complex of rat nuclear pores: Binding of nucleoporin p54 to the rod domain of p62. J. Cell Biol. *128*, 251–261.

Carrière, M., Marco, C., and Steve, O. (2017). Sliced Wasserstein Kernel for Persistence Diagrams. Proc. 34th Int. Conf. Mach. Learn. 664–673.

Chacko, J.V., Zanacchi, F.C., and Diaspro, A. (2013). Probing cytoskeletal structures by coupling optical superresolution and AFM techniques for a correlative approach. Cytoskeleton *70*, 729–740.

Chadrin, A., Hess, B., San Roman, M., Gatti, X., Lombard, B., Loew, D., Barral, Y., Palancade, B., and Doye, V. (2010). Pom33, a novel transmembrane nucleoporin required for proper nuclear pore complex distribution. J. Cell Biol. *189*, 795–811.

Chen, B.C., Legant, W.R., Wang, K., Shao, L., Milkie, D.E., Davidson, M.W., Janetopoulos, C., Wu, X.S., Hammer, J.A., Liu, Z., et al. (2014). Lattice light-sheet microscopy: Imaging molecules to embryos at high spatiotemporal resolution. Science (80-.). *346*.

Chmyrov, A., Keller, J., Grotjohann, T., Ratz, M., D’Este, E., Jakobs, S., Eggeling, C., and Hell, S.W. (2013). Nanoscopy with more than 100,000 “doughnuts.” Nat. Methods *10*, 737–740.

Chow, K.H., Elgort, S., Dasso, M., and Ullman, K.S. (2012). Two distinct sites in Nup153 mediate interaction with the SUMO proteases SENP1 and SENP2. Nucl. (United States) *3*, 11.

Chug, H., Trakhanov, S., Hülsmann, B.B., Pleiner, T., and Görlich, D. (2015). Crystal structure of the metazoan Nup62•Nup58•Nup54 nucleoporin complex. Science (80-.). *350*, 106–110.

Clever, M., Funakoshi, T., Mimura, Y., Takagi, M., and Imamoto, N. (2012). The nucleoporin ELYS/Mel28 regulates nuclear envelope subdomain formation in HeLa cells. Nucleus *3*, 49–48.

Cong, L., Ran, F.A., Cox, D., Lin, S., and Barretto, R. (2013). Multiplex genome engineering using CRISPR/Cas systems. Mult. Genome Eng. Using Cris. Syst. *339*, 819–823.

Cook, A., Bono, F., Jinek, M., and Conti, E. (2007). Structural Biology of Nucleocytoplasmic Transport. Annu. Rev. Biochem. *76*, 647–671.

Cordes, V.C., Reidenbach, S., and Franke, W.W. (1995). High content of a nuclear pore complex protein in cytoplasmic annulate lamellae of Xenopus oocytes. Eur J Cell Biol *68*, 240–255.

Cordes, V.C., Reidenbach, S., Rackwitz, H.R., and Franke, W.W. (1997). Identification of protein p270/Tpr as a constitutive component of the nuclear pore complex-attached intranuclear filaments. J. Cell Biol. *136*, 515–529.

Cronshaw, J.M., Krutchinsky, A.N., Zhang, W., Chait, B.T., and Matunis, M.J. (2002). Proteomic analysis of the mammalian nuclear pore complex. J. Cell Biol. *158*, 915–927.

D’Angelo, M.A., and Hetzer, M.W. (2008). Structure, dynamics and function of nuclear pore complexes. Trends Cell Biol. *18*, 456–466.

D’Angelo, M.A., Raices, M., Panowski, S.H., and Hetzer, M.W. (2009). Age-Dependent Deterioration of Nuclear Pore Complexes Causes a Loss of Nuclear Integrity in Postmitotic Cells. Cell *136*, 284–295.

D’Angelo, M.A., Gomez-Cavazos, J.S., Mei, A., Lackner, D.H., and Hetzer, M.W. (2012). A Change in Nuclear Pore Complex Composition Regulates Cell Differentiation. Dev. Cell *22*, 446–458.

Dabauvalle, M.C., Loos, K., and Scheer, U. (1990). Identification of a soluble precursor complex essential for nuclear pore assembly in vitro. Chromosoma *100*, 56–66.

Daigle, N., Beaudouin, J., Hartnell, L., Imreh, G., Hallberg, E., Lippincott-Schwartz, J., and Ellenberg, J. (2001). Nuclear pore complexes form immobile networks and have a very low turnover in live mammalian cells. J. Cell Biol. *154*, 71–84.

Dasso, M. (2002). The Ran GTPase: Theme and variations. Curr. Biol. *12*.

Dawson, T.R., Lazarus, M.D., Hetzer, M.W., and Wente, S.R. (2009). ER membrane-bending proteins are necessary for de novo nuclear pore formation. J. Cell Biol. *184*, 659–675.

Debler, E.W., Ma, Y., Seo, H.S., Hsia, K.C., Noriega, T.R., Blobel, G., and Hoelz, A. (2008). A Fence-like Coat for the Nuclear Pore Membrane. Mol. Cell *32*, 815–826.

Delphin, C., Guan, T., Melchior, F., and Gerace, L. (1997). RanGTP targets p97 to RanBP2, a filamentous protein localized at the cytoplasmic periphery of the nuclear pore complex. Mol. Biol. Cell *8*, 2379–2390.

Dempsey, G.T., Vaughan, J.C., Chen, K.H., Bates, M., and Zhuang, X. (2011). Evaluation of fluorophores for optimal performance in localization-based super-resolution imaging. Nat. Methods *8*, 1027–1036.

Denning, D.P., Patel, S.S., Uversky, V., Fink, A.L., and Rexach, M. (2003). Disorder in the nuclear pore complex: The FG repeat regions of nucleoporins are natively unfolded. Proc. Natl. Acad. Sci. *100*, 2450–2455.

Deschamps, J., Mund, M., and Ries, J. (2014). 3D superresolution microscopy by supercritical angle detection. Opt. Express *22*, 29081.

Devos, D., Dokudovskaya, S., Alber, F., Williams, R., Chait, B.T., Sali, A., and Rout, M.P. (2004). Components of coated vesicles and nuclear pore complexes share a common molecular architecture. PLoS Biol. *2*.

Devos, D., Dokudovskaya, S., Williams, R., Alber, F., Eswar, N., Chait, B.T., Rout, M.P., and Sali, A. (2006). Simple fold composition and modular architecture of the nuclear pore complex. Proc. Natl. Acad. Sci. *103*, 2172–2177.

Doucet, C.M., and Hetzer, M.W. (2010). Nuclear pore biogenesis into an intact nuclear envelope. Chromosoma *119*, 469–477.

Doucet, C.M., Talamas, J.A., and Hetzer, M.W. (2010). Cell cycle-dependent differences in nuclear pore complex assembly in metazoa. Cell *141*, 1030–1041.

Doye, V., and Hurt, E. (1997). From nucleoporins to nuclear pore complexes. Curr. Opin. Cell Biol. *9*, 401–411.

Duda, R.O., and Hart, P.E. (1972). Use of the Hough transformation to detect lines and curves in pictures. Commun. ACM *15*, 11–15.

Dultz, E., and Ellenberg, J. (2010). Live imaging of single nuclear pores reveals unique assembly kinetics and mechanism in interphase. J. Cell Biol. *191*, 15–22.

Dultz, E., Zanin, E., Wurzenberger, C., Braun, M., Rabut, G., Sironi, L., and Ellenberg, J. (2008). Systematic kinetic analysis of mitotic dis- and reassembly of the nuclear pore in living cells. J. Cell Biol. *180*, 857–865.

Dultz, E., Huet, S., and Ellenberg, J. (2009). Formation of the nuclear envelope permeability barrier studied by sequential photoswitching and flux analysis. Biophys. J. *97*, 1891–1897.

Edelsbrunner, H., and Harrer, J. (2010). Computational Topology: An Introduction.

Edelsbrunner, H., Letscher, D., and Zomorodian, A. (2002). Topological persistence and simplification. Discret. Comput. Geom. *28*, 511–533.

Ester, M., Kriegel, H.P., Sander, J., and Xu, X. (1996). A Density-Based Algorithm for Discovering Clusters in Large Spatial Databases with Noise. Proc. 2nd Int. Conf. Knowl. Discov. Data Min. 226–231.

Fasy, B.T., Kim, J., Lecci, F., and Maria, C. (2014). Introduction to the R package TDA. arXiv:1411.1830v2 1–8.

Fath, S., Mancias, J.D., Bi, X., and Goldberg, J. (2007). Structure and Organization of Coat Proteins in the COPII Cage. Cell *129*, 1325–1336.

Fernandez-Martinez, J., Phillips, J., Sekedat, M.D., Diaz-Avalos, R., Velazquez-Muriel, J., Franke, J.D., Williams, R., Stokes, D.L., Chait, B.T., Sali, A., et al. (2012). Structure-function mapping of a heptameric module in the nuclear pore complex. J. Cell Biol. *196*, 419–434.

Fernandez-Martinez, J., Kim, S.J., Shi, Y., Upla, P., Pellarin, R., Gagnon, M., Chemmama, I.E., Wang, J., Nudelman, I., Zhang, W., et al. (2016). Structure and Function of the Nuclear Pore Complex Cytoplasmic mRNA Export Platform. Cell *167*, 1215–1228.e25.

Finlay, D.R., Meier, E., Bradley, P., Horecka, J., and Forbes, D.J. (1991). A complex of nuclear pore proteins required for pore function. J. Cell Biol. *114*, 169–183.

Fischer, J., Teimer, R., Amlacher, S., Kunze, R., and Hurt, E. (2015). Linker Nups connect the nuclear pore complex inner ring with the outer ring and transport channel. Nat. Struct. Mol. Biol. *22*, 774–781.

Flemming, D., Sarges, P., Stelter, P., Hellwig, A., Bottcher, B., and Hurt, E. (2009). Two structurally distinct domains of the nucleoporin Nup170 cooperate to tether a subset of nucleoporins to nuclear pores. J. Cell Biol. *185*, 387–395.

Fölling, J., Bossi, M., Bock, H., Medda, R., Wurm, C.A., Hein, B., Jakobs, S., Eggeling, C., and Hell, S.W. (2008). Fluorescence nanoscopy by ground-state depletion and single-molecule return. Nat. Methods *5*, 943–945.

Forster, F., Medalia, O., Zauberman, N., Baumeister, W., and Fass, D. (2005). Retrovirus envelope protein complex structure in situ studied by cryo-electron tomography. Proc. Natl. Acad. Sci. *102*, 4729–4734.

Frey, S., and Görlich, D. (2007). A Saturated FG-Repeat Hydrogel Can Reproduce the Permeability Properties of Nuclear Pore Complexes. Cell *130*, 512–523.

Frey, S., Richter, R.P., and Görlich, D. (2006). FG-rich repeats of nuclear pore proteins form a three-dimensional meshwork with hydrogel-like properties. Science (80-.). *314*, 815–817.

Fried, H., and Kutay, U. (2003). Nucleocytoplasmic transport: Taking an inventory. Cell. Mol. Life Sci. *60*, 1659–1688.

Funakoshi, T., Clever, M., Watanabe, A., and Imamoto, N. (2011). Localization of Pom121 to the inner nuclear membrane is required for an early step of interphase nuclear pore complex assembly. Mol. Biol. Cell *22*, 1058–1069.

Gall, J.G. (1967). Octagonal nuclear pores. J. Cell Biol. *32*, 391–399.

Galy, V., Antonin, W., Jaedicke, A., Sachse, M., Santarella, R., Haselmann, U., and Mattaj, I. (2008). A role for gp210 in mitotic nuclear-envelope breakdown. J. Cell Sci. *121*, 317–328.

Gest, H. (2004). The discovery of microorganisms by Robert Hooke and Antoni van Leeuwenhoek, Fellows of The Royal Society. Notes Rec. R. Soc. *58*, 187–201.

Goldberg, M.W., and Allen, T.D. (1992). High resolution scanning electron microscopy of the nuclear envelope: Demonstration of a new, regular, fibrous lattice attached to the baskets of the nucleoplasmic face of the nuclear pores. J. Cell Biol. *119*, 1429–1440.

Görlich, D., and Kutay, U. (1999). Transport between the cell nucleus and the cytoplasm. Annu. Rev. Cell Dev. Biol. *15*, 607–660.

Grandi, P., Doye, V., and Hurt, E. (1993). Purification of NSP1 reveals complex formation with “GLFG” nucleoporins and a novel nuclear pore protein NIC96. EMBO J. *12*, 3061–3071.

Grandi, P., Emig, S., Weise, C., Hucho, F., Pohl, T., and Hurt, E.C. (1995a). A novel nuclear pore protein Nup82p which specifically binds to a fraction of Nsp1p. J. Cell Biol. *130*, 1263–1273.

Grandi, P., Schlaich, N., Tekotte, H., and Hurt, E. (1995b). Functional interaction of Nic96p with a core nucleoporin complex consisting of Nsp1p, Nup49p and a novel protein Nup57p. EMBO J. *14*, 76–87.

Grandi, P., Dang, T., Pané, N., Shevchenko, A., Mann, M., Forbes, D., and Hurt, E. (1997).

Nup93, a vertebrate homologue of yeast Nic96p, forms a complex with a novel 205-kDa protein and is required for correct nuclear pore assembly. Mol. Biol. Cell *8*, 2017–2038.

Griffis, E.R. (2003). Nup98 Localizes to Both Nuclear and Cytoplasmic Sides of the Nuclear Pore and Binds to Two Distinct Nucleoporin Subcomplexes. Mol. Biol. Cell *14*, 600–610.

Grossman, E., Medalia, O., and Zwerger, M. (2012). Functional Architecture of the Nuclear Pore Complex. Annu. Rev. Biophys. *41*, 557–584.

Guan, T., Müller, S., Klier, G., Panté, N., Blevitt, J.M., Haner, M., Paschal, B., Aebi, U., and Gerace, L. (1995). Structural analysis of the p62 complex, an assembly of O-linked glycoproteins that localizes near the central gated channel of the nuclear pore complex. Mol. Biol. Cell *6*, 1591–1603.

Gustafsson, M.G.L. (2000). Surpassing the lateral resolution limit by a factor of two using structured illumination microscopy. J. Microsc. *198*, 82–87.

Gustafsson, M.G.L. (2005). Nonlinear structured-illumination microscopy: Wide-field fluorescence imaging with theoretically unlimited resolution. Proc. Natl. Acad. Sci. *102*, 13081–13086.

Gustafsson, M.G.L., Shao, L., Carlton, P.M., Wang, C.J.R., Golubovskaya, I.N., Cande, W.Z., Agard, D.A., and Sedat, J.W. (2008). Three-dimensional resolution doubling in wide-field fluorescence microscopy by structured illumination. Biophys. J. *94*, 4957–4970.

Hawryluk-Gara, L.A., Shibuya, E.K., and, and Wozniak, R.W. (2005). Vertebrate Nup53 Interacts with the Nuclear Lamina and Is Required for the Assembly of a Nup93-containing Complex. Mol. Biol. Cell *16*, 2382–2394.

Hawryluk-Gara, L. a, Platani, M., Santarella, R., Wozniak, R.W., and Mattaj, I.W. (2008). Nup53 is required for nuclear envelope and nuclear pore complex assembly. Mol. Biol. Cell *19*, 1753–1762.

Heilemann, M., Van De Linde, S., Schüttpelz, M., Kasper, R., Seefeldt, B., Mukherjee, A., Tinnefeld, P., and Sauer, M. (2008). Subdiffraction-resolution fluorescence imaging with conventional fluorescent probes. Angew. Chemie - Int. Ed. *47*, 6172–6176.

Hein, B., Willig, K.I., and Hell, S.W. (2008). Stimulated emission depletion (STED) nanoscopy of a fluorescent protein-labeled organelle inside a living cell. Proc. Natl. Acad. Sci. *105*, 14271–14276.

Heintzmann, R., and Gustafsson, M.G.L. (2009). Subdiffraction resolution in continuous samples. Nat. Photonics *3*, 362–364.

Hell, S.W. (2003). Toward fluorescence nanoscopy. Nat. Biotechnol. *21*, 1347–1355.

Hell, S.W. (2009). Microscopy and its focal switch. Nat. Methods *6*, 24–32.

Hell, S.W., and Wichmann, J. (1994). Breaking the diffraction resolution limit by stimulated emission: stimulated-emission-depletion fluorescence microscopy. Opt. Lett. *19*, 780.

Hess, S.T., Girirajan, T.P.K., and Mason, M.D. (2006). Ultra-high resolution imaging by fluorescence photoactivation localization microscopy. Biophys. J. *91*, 4258–4272.

Hinshaw, J.E., Carragher, B.O., and Milligan, R. a (1992). Architecture and design of the nuclear pore complex. Cell *69*, 1133–1141.

Hoelz, A., Debler, E.W., and Blobel, G. (2011a). The Structure of the Nuclear Pore Complex. Annu. Rev. Biochem. Vol 80 *80*, 613–643.

Hoelz, A., Debler, E.W., and Blobel, G. (2011b). The structure of the nuclear pore complex. Annu. Rev. Biochem. *80*, 613–643.

Hoelz, A., Glavy, J.S., and Beck, M. (2016). Toward the atomic structure of the nuclear pore complex: when top down meets bottom up. Nat. Struct. Mol. Biol. *23*, 624–630.

Hofmann, M., Eggeling, C., Jakobs, S., and Hell, S.W. (2005). Breaking the diffraction barrier in fluorescence microscopy at low light intensities by using reversibly photoswitchable proteins. Proc. Natl. Acad. Sci. *102*, 17565–17569.

Hu, T., Guan, T., and Gerace, L. (1996). Molecular and functional characterization of the p62 complex, an assembly of nuclear pore complex glycoproteins. J. Cell Biol. *134*, 589–

601.
Huang, B., Wang, W., Bates, M., and Zhuang, X. (2008). Three-dimensional super-resolution imaging by stochastic optical reconstruction microscopy. Science *319*, 810–813.
Huang, F., Sirinakis, G., Allgeyer, E.S., Toomre, D., Booth, M.J., Correspondence, J.B., Schroeder, L.K., Duim, W.C., Kromann, E.B., Phan, T., et al. (2016). Ultra-High Resolution 3D Imaging of Whole Cells In Brief Ultra-High Resolution 3D Imaging of Whole Cells. Cell *166*, 1–13.
Huebner, A., Kaindl, A.M., Knobeloch, K.P., Petzold, H., Mann, P., and Koehler, K. (2004). The triple A syndrome is due to mutations in ALADIN, a novel member of the nuclear pore complex. In Endocrine Research, pp. 891–899.
Hülsmann, B.B., Labokha, A.A., and Görlich, D. (2012). The permeability of reconstituted nuclear pores provides direct evidence for the selective phase model. Cell *150*, 738–751.
Ibarra, A., and Hetzer, M.W. (2015). Nuclear pore proteins and the control of genome functions. Genes Dev. *29*, 337–349.
Isgro, T.A., and Schulten, K. (2007a). Association of Nuclear Pore FG-repeat Domains to NTF2 Import and Export Complexes. J. Mol. Biol. *366*, 330–345.
Isgro, T.A., and Schulten, K. (2007b). Cse1p-Binding Dynamics Reveal a Binding Pattern for FG-Repeat Nucleoporins on Transport Receptors. Structure *15*, 977–991.
Juette, M.F., Gould, T.J., Lessard, M.D., Mlodzianoski, M.J., Nagpure, B.S., Bennett, B.T., Hess, S.T., and Bewersdorf, J. (2008). Three-dimensional sub-100 nm resolution fluorescence microscopy of thick samples. Nat. Methods *5*, 527–529.
Kampmann, M., and Blobel, G. (2009). Three-dimensional structure and flexibility of a membrane-coating module of the nuclear pore complex. Nat. Struct. Mol. Biol. *16*, 782–788.
Kassube, S.A., Stuwe, T., Lin, D.H., Antonuk, C.D., Napetschnig, J., Blobel, G., and Hoelz, A. (2012). Crystal structure of the N-terminal domain of Nup358/RanBP2. J. Mol. Biol. *423*, 752–765.
Katta, S.S., Smoyer, C.J., and Jaspersen, S.L. (2014). Destination: Inner nuclear membrane. Trends Cell Biol. *24*, 221–229.
Kelley, K., Knockenhauer, K.E., Kabachinski, G., and Schwartz, T.U. (2015). Atomic structure of the Y complex of the nuclear pore. Nat. Struct. Mol. Biol. *22*, 425–431.
Keppler, A., Gendreizig, S., Gronemeyer, T., Pick, H., Vogel, H., and Johnsson, K. (2003). A general method for the covalent labeling of fusion proteins with small molecules in vivo.
Kim, S.J., Fernandez-Martinez, J., Sampathkumar, P., Martel, A., Matsui, T., Tsuruta, H., Weiss, T.M., Shi, Y., Markina-Inarrairaegui, A., Bonanno, J.B., et al. (2014). Integrative Structure–Function Mapping of the Nucleoporin Nup133 Suggests a Conserved Mechanism for Membrane Anchoring of the Nuclear Pore Complex. Mol. Cell. Proteomics *13*, 2911–2926.
Kim, S.J., Fernandez-Martinez, J., Nudelman, I., Shi, Y., Zhang, W., Raveh, B., Herricks, T., Slaughter, B.D., Hogan, J.A., Upla, P., et al. (2018). Integrative structure and functional anatomy of a nuclear pore complex. Nature *555*, 475–482.
Klar, T.A., and Hell, S.W. (1999). Subdiffraction resolution in far-field fluorescence microscopy. Opt. Lett. *24*, 954.
Klar, T.A., Jakobs, S., Dyba, M., Egner, A., and Hell, S.W. (2000). Fluorescence microscopy with diffraction resolution barrier broken by stimulated emission. Proc. Natl. Acad. Sci. *97*, 8206–8210.
Knockenhauer, K.E., and Schwartz, T.U. (2016). The Nuclear Pore Complex as a Flexible and Dynamic Gate. Cell *164*, 1162–1171.
Koch, B., Nijmeijer, B., Kueblbeck, M., Cai, Y., Walther, N., and Ellenberg, J. (2018). Generation and validation of homozygous fluorescent knock-in cells using CRISPR-Cas9 genome editing. Nat. Protoc. *13*, 1465–1487.
Kosinski, J., Mosalaganti, S., Von Appen, A., Teimer, R., Diguilio, A.L., Wan, W., Bui, K.H.,

Hagen, W.J.H., Briggs, J.A.G., Glavy, J.S., et al. (2016). Molecular architecture of the inner ring scaffold of the human nuclear pore complex. Science (80-.). *352*, 363–365.

Krull, S., Thyberg, J., Björkroth, B., Rackwitz, H.-R., and Cordes, V.C. (2004). Nucleoporins as components of the nuclear pore complex core structure and Tpr as the architectural element of the nuclear basket. Mol. Biol. Cell *15*, 4261–4277.

Lampe, A., Haucke, V., Sigrist, S.J., Heilemann, M., and Schmoranzer, J. (2012). Multi-colour direct STORM with red emitting carbocyanines. Biol. Cell *104*, 229–237.

Lehmann, M., Lichtner, G., Klenz, H., and Schmoranzer, J. (2016). Novel organic dyes for multicolor localization-based super-resolution microscopy. J. Biophotonics *9*, 161–170.

Lelek, M., Di Nunzio, F., Henriques, R., Charneau, P., Arhel, N., and Zimmer, C. (2012). Superresolution imaging of HIV in infected cells with FlAsH-PALM. Proc. Natl. Acad. Sci. U. S. A. *109*, 8564–8569.

Lemke, E.A. (2016). The Multiple Faces of Disordered Nucleoporins. J. Mol. Biol. *428*, 2011–2024.

Li, D., Shao, L., Chen, B.C., Zhang, X., Zhang, M., Moses, B., Milkie, D.E., Beach, J.R., Hammer, J.A., Pasham, M., et al. (2015). Extended-resolution structured illumination imaging of endocytic and cytoskeletal dynamics. Science (80-.). *349*.

Lim, R.Y.H., Huang, N.-P., Koser, J., Deng, J., Lau, K.H.A., Schwarz-Herion, K., Fahrenkrog, B., and Aebi, U. (2006). Flexible phenylalanine-glycine nucleoporins as entropic barriers to nucleocytoplasmic transport. Proc. Natl. Acad. Sci. *103*, 9512–9517.

Lim, R.Y.H., Fahrenkrog, B., Köser, J., Schwarz-Herion, K., Deng, J., and Aebi, U. (2007). Nanomechanical basis of selective gating by the nuclear pore complex. Science (80-.). *318*, 640–643.

Lim, R.Y.H., Aebi, U., and Fahrenkrog, B. (2008). Towards reconciling structure and function in the nuclear pore complex. Histochem. Cell Biol. *129*, 105–116.

Lin, D.H., Zimmermann, S., Stuwe, T., Stuwe, E., and Hoelz, A. (2013). Structural and functional analysis of the C-terminal domain of Nup358/RanBP2. J. Mol. Biol. *425*, 1318–1329.

Lin, D.H., Stuwe, T., Schilbach, S., Rundlet, E.J., Perriches, T., Mobbs, G., Fan, Y., Thierbach, K., Huber, F.M., Collins, L.N., et al. (2016). Architecture of the symmetric core of the nuclear pore. Science *352*, aaf1015.

van de Linde, S., Endesfelder, U., Mukherjee, A., Schüttpelz, M., Wiebusch, G., Wolter, S., Heilemann, M., and Sauer, M. (2009). Multicolor photoswitching microscopy for subdiffraction-resolution fluorescence imaging. Photochem. Photobiol. Sci. *8*, 465.

Los, G. V, and Wood, K. (2006). The HaloTag^{TM}: A Novel Technology for Cell Imaging and Protein Analysis. In Methods in Molecular Biology: High Content Screening: A Powerful Approach to Systems Cell Biology and Drug Discovery, pp. 195–208.

Löschberger, A., van de Linde, S., Dabauvalle, M.-C., Rieger, B., Heilemann, M., Krohne, G., and Sauer, M. (2012). Super-resolution imaging visualizes the eightfold symmetry of gp210 proteins around the nuclear pore complex and resolves the central channel with nanometer resolution. J. Cell Sci. *125*, 570–575.

Lupu, F., Alves, A., Anderson, K., Doye, V., and Lacy, E. (2008). Nuclear Pore Composition Regulates Neural Stem/Progenitor Cell Differentiation in the Mouse Embryo. Dev. Cell *14*, 831–842.

Lutzmann, M., Kunze, R., Buerer, A., Aebi, U., and Hurt, E. (2002). Modular self-assembly of a Y-shaped multiprotein complex from seven nucleoporins. EMBO J. *21*, 387–397.

Lutzmann, M., Kunze, R., Stangl, K., Stelter, P., Tóth, K.F., Böttcher, B., and Hurt, E. (2005). Reconstitution of Nup157 and Nup145N into the Nup84 complex. J. Biol. Chem. *280*, 18442–18451.

Macara, I.G. (2001). Transport into and out of the Nucleus. Microbiol. Mol. Biol. Rev. *65*, 570–594.

Mahen, R., Koch, B., Wachsmuth, M., Politi, A.Z., Perez-Gonzalez, A., Mergenthaler, J., Cai, Y., and Ellenberg, J. (2014). Comparative assessment of fluorescent transgene methods for quantitative imaging in human cells. Mol. Biol. Cell *25*, 3610–3618.

Maimon, T., Elad, N., Dahan, I., and Medalia, O. (2012). The human nuclear pore complex as revealed by cryo-electron tomography. Structure *20*, 998–1006.

Mans, B.J., Anantharaman, V., Aravind, L., and Koonin, E. V (2004). Comparative genomics, evolution and origins of the nuclear envelope and nuclear pore complex. Cell Cycle *3*, 1612–1637.

Mansfeld, J., Güttinger, S., Hawryluk-Gara, L.A., Panté, N., Mall, M., Galy, V., Haselmann, U., Mühlhäusser, P., Wozniak, R.W., Mattaj, I.W., et al. (2006). The Conserved Transmembrane Nucleoporin NDC1 Is Required for Nuclear Pore Complex Assembly in Vertebrate Cells. Mol. Cell *22*, 93–103.

Matsuura, Y., Lange, A., Harreman, M.T., Corbett, A.H., and Stewart, M. (2003). Structural basis for Nup2p function in cargo release and karyopherin recycling in nuclear import. EMBO J. *22*, 5358–5369.

Matunis, M.J., Coutavas, E., and Blobel, G. (1996). A novel ubiquitin-like modification modulates the partitioning of the Ran-GTPase-activating protein RanGAP1 between the cytosol and the nuclear pore complex. J. Cell Biol. *135*, 1457–1470.

Melčák, I., Hoelz, A., and Blobel, G. (2007). Structure of Nup58/45 suggests flexible nuclear pore diameter by intermolecular sliding. Science (80-.). *315*, 1729–1732.

Mészáros, N., Cibulka, J., Mendiburo, M.J., Romanauska, A., Schneider, M., and Köhler, A. (2015). Nuclear Pore Basket Proteins Are Tethered to the Nuclear Envelope and Can Regulate Membrane Curvature. Dev. Cell *33*, 285–298.

Mi, L., Goryaynov, A., Lindquist, A., Rexach, M., and Yang, W. (2015). Quantifying Nucleoporin Stoichiometry Inside Single Nuclear Pore Complexes In vivo. Sci. Rep. *5*.

Mitchell, J.M., Mansfeld, J., Capitanio, J., Kutay, U., and Wozniak, R.W. (2010). Pom121 links two essential subcomplexes of the nuclear pore complex core to the membrane. J. Cell Biol. *191*, 505–521.

Montpetit, B., Thomsen, N.D., Helmke, K.J., Seeliger, M.A., Berger, J.M., and Weis, K. (2011). A conserved mechanism of DEAD-box ATPase activation by nucleoporins and InsP6 in mRNA export. Nature *472*, 238–244.

Moore, M.S., and Blobel, G. (1994). Purification of a Ran-interacting protein that is required for protein import into the nucleus. Proc. Natl. Acad. Sci. U. S. A. *91*, 10212–10216.

Mosalaganti, S., Kosinski, J., Albert, S., Schaffer, M., Strenkert, D., Salomé, P.A., Merchant, S.S., Plitzko, J.M., Baumeister, W., Engel, B.D., et al. (2018). In situ architecture of the algal nuclear pore complex. Nat. Commun. *9*.

Mosammaparast, N., and Pemberton, L.F. (2004). Karyopherins: From nuclear-transport mediators to nuclear-function regulators. Trends Cell Biol. *14*, 547–556.

Nagy, V., Hsia, K.-C., Debler, E.W., Kampmann, M., Davenport, A.M., Blobel, G., and Hoelz, A. (2009). Structure of a trimeric nucleoporin complex reveals alternate oligomerization states. Proc. Natl. Acad. Sci. U. S. A. *106*, 17693–17698.

Nakano, H., Funasaka, T., Hashizume, C., and Wong, R.W. (2010). Nucleoporin translocated promoter region (Tpr) associates with dynein complex, preventing chromosome lagging formation during mitosis. J. Biol. Chem. *285*, 10841–10849.

Napetschnig, J., Blobel, G., and Hoelz, A. (2007). Crystal structure of the N-terminal domain of the human protooncogene Nup214/CAN. Proc. Natl. Acad. Sci. U. S. A. *104*, 1783–1788.

Neumann, N., Lundin, D., and Poole, A.M. (2010). Comparative genomic evidence for a complete nuclear pore complex in the last eukaryotic common ancestor. PLoS One *5*.

Nickell, S., Förster, F., Linaroudis, A., Del Net, W., Beck, F., Hegerl, R., Baumeister, W., and Plitzko, J.M. (2005). TOM software toolbox: Acquisition and analysis for electron tomography. J. Struct. Biol. *149*, 227–234.

Olivier, N., Keller, D., Gönczy, P., and Manley, S. (2013a). Resolution Doubling in 3D-STORM Imaging through Improved Buffers. PLoS One *8*.

Olivier, N., Keller, D., Rajan, V.S., Gönczy, P., and Manley, S. (2013b). Simple buffers for 3D STORM microscopy. Biomed. Opt. Express *4*, 885.

Onischenko, E., Stanton, L.H., Madrid, A.S., Kieselbach, T., and Weis, K. (2009). Role of the Ndc1 interaction network in yeast nuclear pore complex assembly and maintenance. J. Cell Biol. *185*, 475–491.

Ori, A., Banterle, N., Iskar, M., Andrés-Pons, A., Escher, C., Khanh Bui, H., Sparks, L., Solis-Mezarino, V., Rinner, O., Bork, P., et al. (2013). Cell type-specific nuclear pores: a case in point for context-dependent stoichiometry of molecular machines. Mol. Syst. Biol. *9*, 648.

Ori, A., Iskar, M., Buczak, K., Kastritis, P., Parca, L., Andrés-Pons, A., Singer, S., Bork, P., and Beck, M. (2016). Spatiotemporal variation of mammalian protein complex stoichiometries. Genome Biol. *17*.

Otsuka, S., and Ellenberg, J. (2017). Mechanisms of nuclear pore complex assembly - two different ways of building one molecular machine. FEBS Lett.

Otsuka, S., Szymborska, A., and Ellenberg, J. (2014). Imaging the Assembly, Structure, and Function of the Nuclear Pore Inside Cells. In Methods in Cell Biology, pp. 219–238.

Otsuka, S., Bui, K.H., Schorb, M., Julius Hossain, M., Politi, A.Z., Koch, B., Eltsov, M., Beck, M., and Ellenberg, J. (2016). Nuclear pore assembly proceeds by an inside-out extrusion of the nuclear envelope. Elife *5*.

Otsuka, S., Steyer, A.M., Schorb, M., Hériché, J.K., Hossain, M.J., Sethi, S., Kueblbeck, M., Schwab, Y., Beck, M., and Ellenberg, J. (2018). Postmitotic nuclear pore assembly proceeds by radial dilation of small membrane openings. Nat. Struct. Mol. Biol. *25*, 21–28.

Pal, K., Bandyopadhyay, A., Zhou, X.E., Xu, Q., Marciano, D.P., Brunzelle, J.S., Yerrum, S., Griffin, P.R., Vande Woude, G., Melcher, K., et al. (2017). Structural Basis of TPR-Mediated Oligomerization and Activation of Oncogenic Fusion Kinases. Structure *25*, 867–877.e3.

Patel, S.S., Belmont, B.J., Sante, J.M., and Rexach, M.F. (2007). Natively Unfolded Nucleoporins Gate Protein Diffusion across the Nuclear Pore Complex. Cell *129*, 83–96.

Patterson, G., Davidson, M., Manley, S., and Lippincott-Schwartz, J. (2010). Superresolution Imaging using Single-Molecule Localization. Annu. Rev. Phys. Chem. *61*, 345–367.

Pavani, S.R.P., Thompson, M.A., Biteen, J.S., Lord, S.J., Liu, N., Twieg, R.J., Piestun, R., and Moerner, W.E. (2009). Three-dimensional, single-molecule fluorescence imaging beyond the diffraction limit by using a double-helix point spread function. Proc. Natl. Acad. Sci. *106*, 2995–2999.

Perez-Terzic, C., Gacy, a M., Bortolon, R., Dzeja, P.P., Puceat, M., Jaconi, M., Prendergast, F.G., and Terzic, A. (1999). Structural plasticity of the cardiac nuclear pore complex in response to regulators of nuclear import. Circ. Res. *84*, 1292–1301.

Perez-Terzic, C., Behfar, A., Méry, A., Van Deursen, J.M.A., Terzic, A., and Pucéat, M. (2003). Structural adaptation of the nuclear pore complex in stem cell-derived cardiomyocytes. Circ. Res. *92*, 444–452.

Pettersen, E.F., Goddard, T.D., Huang, C.C., Couch, G.S., Greenblatt, D.M., Meng, E.C., and Ferrin, T.E. (2004). UCSF Chimera—A Visualization System for Exploratory Research and Analysis. J Comput Chem *25*, 1605–1612.

Port, S.A., Monecke, T., Dickmanns, A., Spillner, C., Hofele, R., Urlaub, H., Ficner, R., and Kehlenbach, R.H. (2015). Structural and Functional Characterization of CRM1-Nup214 Interactions Reveals Multiple FG-Binding Sites Involved in Nuclear Export. Cell Rep. *13*, 690–702.

Rabut, G., Doye, V., and Ellenberg, J. (2004). Mapping the dynamic organization of the nuclear pore complex inside single living cells. Nat. Cell Biol. *6*, 1114–1121.

R Foundation for Statistical Computing (2018). R: A language and environment for statistical computing. R A Lang. Environ. Stat. Comput.

Raices, M., and D'Angelo, M. a (2012). Nuclear pore complex composition: a new regulator of tissue-specific and developmental functions. Nat. Rev. Mol. Cell Biol. *13*, 687–699.

Rajanala, K., Sarkar, A., Jhingan, G.D., Priyadarshini, R., Jalan, M., Sengupta, S., and Nandicoori, V.K. (2014). Phosphorylation of nucleoporin Tpr governs its differential localization and is required for its mitotic function. J. Cell Sci. *127*, 3505–3520.

Rajoo, S., Vallotton, P., Onischenko, E., and Weis, K. (2018). Stoichiometry and compositional plasticity of the yeast nuclear pore complex revealed by quantitative fluorescence microscopy. Proc. Natl. Acad. Sci. U. S. A. 201719398.

Rasala, B.A., Orjalo, A. V., Shen, Z., Briggs, S., and Forbes, D.J. (2006). ELYS is a dual nucleoporin/kinetochore protein required for nuclear pore assembly and proper cell division. Proc. Natl. Acad. Sci. *103*, 17801–17806.

Rasala, B.A., Ramos, C., Harel, A., and Forbes, D.J. (2008). Capture of AT-rich Chromatin by ELYS Recruits POM121 and NDC1 to Initiate Nuclear Pore Assembly. Mol. Biol. Cell *19*, 3982–3996.

Ratner, G.A., Hodel, A.E., and Powers, M.A. (2007). Molecular determinants of binding between Gly-Leu-Phe-Gly nucleoporins and the nuclear pore complex. J. Biol. Chem. *282*, 33968–33976.

Rayleigh (1896). XV. On the theory of optical images, with special reference to the microscope. Philos. Mag. Ser. 5 *42*, 167–195.

Rego, E.H., Shao, L., Macklin, J.J., Winoto, L., Johansson, G.A., Kamps-Hughes, N., Davidson, M.W., and Gustafsson, M.G.L. (2012). Nonlinear structured-illumination microscopy with a photoswitchable protein reveals cellular structures at 50-nm resolution. Proc. Natl. Acad. Sci. U. S. A. *109*, E135-43.

Reichelt, R., Holzenburg, A., Buhle, E.L., Jarnik, M., Engel, A., and Aebi, U. (1990). Correlation between structure and mass distribution of the nuclear pore complex and of distinct pore complex components. J. Cell Biol. *110*, 883–894.

Ren, Y., Seo, H.-S., Blobel, G., and Hoelz, A. (2010). Structural and functional analysis of the interaction between the nucleoporin Nup98 and the mRNA export factor Rae1. Proc. Natl. Acad. Sci. *107*, 10406–10411.

Reverter, D., and Lima, C.D. (2005). Insights into E3 ligase activity revealed by a SUMO-RanGAP1-Ubc9-Nup358 complex. Nature *435*, 687–692.

Ribbeck, K., and Görlich, D. (2001). Kinetic analysis of translocation through nuclear pore complexes. EMBO J. *20*, 1320–1330.

Ries, J., Kaplan, C., Platonova, E., Eghlidi, H., and Ewers, H. (2012). A simple, versatile method for GFP-based super-resolution microscopy via nanobodies. Nat. Methods *9*, 582–584.

Rout, M.P., and Blobel, G. (1993). Isolation of the yeast nuclear pore complex. J. Cell Biol. *123*, 771–783.

Rout, M.P., Aitchison, J.D., Suprapto, A., Hjertaas, K., Zhao, Y., and Chait, B.T. (2000a). The Yeast Nuclear Pore Complex. J. Cell Biol. *148*, 635–652.

Rout, M.P., Aitchison, J.D., Suprapto, A., Hjertaas, K., Zhao, Y., and Chait, B.T. (2000b). The yeast nuclear pore complex: Composition, architecture, transport mechanism. J. Cell Biol. *148*, 635–651.

Rout, M.P., Aitchison, J.D., Magnasco, M.O., and Chait, B.T. (2003). Virtual gating and nuclear transport: The hole picture. Trends Cell Biol. *13*, 622–628.

Rust, M.J., Bates, M., and Zhuang, X. (2006). Sub-diffraction-limit imaging by stochastic optical reconstruction microscopy (STORM). Nat. Methods *3*, 793–795.

Sampathkumar, P., Kim, S.J., Upla, P., Rice, W.J., Phillips, J., Timney, B.L., Pieper, U., Bonanno, J.B., Fernandez-Martinez, J., Hakhverdyan, Z., et al. (2013). Structure, dynamics, evolution, and function of a major scaffold component in the nuclear pore complex. Structure

21, 560–571.

Schlaich, N.L., Häner, M., Lustig, A., Aebi, U., and Hurt, E.C. (1997). In vitro reconstitution of a heterotrimeric nucleoporin complex consisting of recombinant Nsp1p, Nup49p, and Nup57p. Mol. Biol. Cell *8*, 33–46.

Schrader, N., Stelter, P., Flemming, D., Kunze, R., Hurt, E., and Vetter, I.R. (2008). Structural Basis of the Nic96 Subcomplex Organization in the Nuclear Pore Channel. Mol. Cell *29*, 46–55.

Schwartz, T.U. (2005). Modularity within the architecture of the nuclear pore complex. Curr. Opin. Struct. Biol. *15*, 221–226.

Schwartz, T.U. (2016). The Structure Inventory of the Nuclear Pore Complex. J. Mol. Biol. *428*, 1986–2000.

Schwoebel, E.D., Talcott, B., Cushman, I., and Moore, M.S. (1998). Ran-dependent signal-mediated nuclear import does not require GTP hydrolysis by Ran. J. Biol. Chem. *273*, 35170–35175.

Seo, H.-S., Ma, Y., Debler, E.W., Wacker, D., Kutik, S., Blobel, G., and Hoelz, A. (2009). Structural and functional analysis of Nup120 suggests ring formation of the Nup84 complex. Proc. Natl. Acad. Sci. *106*, 14281–14286.

Shao, L., Kner, P., Rego, E.H., and Gustafsson, M.G.L. (2011). Super-resolution 3D microscopy of live whole cells using structured illumination. Nat. Methods *8*, 1044–1048.

Sharma, A., Solmaz, S.R., Blobel, G., and Melčák, I. (2015). Ordered regions of channel nucleoporins Nup62, Nup54, and Nup58 form dynamic complexes in solution. J. Biol. Chem. *290*, 18370–18378.

Shaulov, L., Gruber, R., Cohen, I., and Harel, A. (2011). A dominant-negative form of POM121 binds chromatin and disrupts the two separate modes of nuclear pore assembly. J. Cell Sci. *124*, 3822–3834.

Shtengel, G., Galbraith, J.A., Galbraith, C.G., Lippincott-Schwartz, J., Gillette, J.M., Manley, S., Sougrat, R., Waterman, C.M., Kanchanawong, P., Davidson, M.W., et al. (2009). Interferometric fluorescent super-resolution microscopy resolves 3D cellular ultrastructure. Proc. Natl. Acad. Sci. *106*, 3125–3130.

Siniossoglou, S., Lutzmann, M., Santos-Rosa, H., Leonard, K., Mueller, S., Aebi, U., and Hurt, E. (2000). Structure and assembly of the Nup84p complex. J. Cell Biol. *149*, 41–53.

Smith, A.E., Slepchenko, B.M., Schaff, J.C., Loew, L.M., and Macara, I.G. (2002). Systems analysis of ran transport. Science (80-.). *295*, 488–491.

Smythe, C., Jenkins, H.E., and Hutchison, C.J. (2000). Incorporation of the nuclear pore basket protein Nup153 into nuclear pore structures is dependent upon lamina assembly: Evidence from cell-free extracts of Xenopus eggs. EMBO J. *19*, 3918–3931.

Solmaz, S.R., Chauhan, R., Blobel, G., and Melčák, I. (2011). Molecular architecture of the transport channel of the nuclear pore complex. Cell *147*, 590–602.

Solmaz, S.R., Blobel, G., and Melcak, I. (2013). Ring cycle for dilating and constricting the nuclear pore. Proc. Natl. Acad. Sci. *110*, 5858–5863.

Solsbacher, J., Maurer, P., Vogel, F., and Schlenstedt, G. (2000). Nup2p, a yeast nucleoporin, functions in bidirectional transport of importin alpha. Mol. Cell. Biol. *20*, 8468–8479.

Stagg, S.M., LaPointe, P., Razvi, A., Gürkan, C., Potter, C.S., Carragher, B., and Balch, W.E. (2008). Structural Basis for Cargo Regulation of COPII Coat Assembly. Cell *134*, 474–484.

Starr, D.A., and Fridolfsson, H.N. (2010). Interactions Between Nuclei and the Cytoskeleton Are Mediated by SUN-KASH Nuclear-Envelope Bridges. Annu. Rev. Cell Dev. Biol. *26*, 421–444.

Stavru, F., Nautrup-Pedersen, G., Cordes, V.C., and Görlich, D. (2006). Nuclear pore complex assembly and maintenance in POM121- and gp210-deficient cells. J. Cell Biol.

173, 477–483.

Strahm, Y., Fahrenkrog, B., Zenklusen, D., Rychner, E., Kantor, J., Rosbash, M., and Stutz, F. (1999). The RNA export factor Gle1p is located on the cytoplasmic fibrils of the NPC and physically interacts with the FG-nucleoporin Rip1p, the DEAD-box protein Rat8p/Dbp5p and a new protein Ymr255p. EMBO J. *18*, 5761–5777.

Strawn, L. a, Shen, T., Shulga, N., Goldfarb, D.S., and Wente, S.R. (2004). Minimal nuclear pore complexes define FG repeat domains essential for transport. Nat. Cell Biol. *6*, 197–206.

Stuwe, T., Schada Von Borzyskowski, L., Davenport, A.M., and Hoelz, A. (2012). Molecular basis for the anchoring of proto-oncoprotein Nup98 to the cytoplasmic face of the nuclear pore complex. J. Mol. Biol. *419*, 330–346.

Stuwe, T., Correia, A.R., Lin, D.H., Paduch, M., Lu, V.T., Kossiakoff, A.A., and Hoelz, A. (2015a). Nuclear pores. Architecture of the nuclear pore complex coat. Science *347*, 1148–1152.

Stuwe, T., Bley, C.J., Thierbach, K., Petrovic, S., Schilbach, S., Mayo, D.J., Perriches, T., Rundlet, E.J., Jeon, Y.E., Collins, L.N., et al. (2015b). Architecture of the fungal nuclear pore inner ring complex. Science (80-.). *350*, 56–64.

Suntharalingam, M., and Wente, S.R. (2003). Peering through the pore: Nuclear pore complex structure, assembly, and function. Dev. Cell *4*, 775–789.

Sydor, A.M., Czymmek, K.J., Puchner, E.M., and Mennella, V. (2015). Super-Resolution Microscopy: From Single Molecules to Supramolecular Assemblies. Trends Cell Biol. *25*, 730–748.

Szymborska, A., de Marco, A., Daigle, N., Cordes, V.C., Briggs, J. a G., and Ellenberg, J. (2013). Nuclear pore scaffold structure analyzed by super-resolution microscopy and particle averaging. Science *341*, 655–658.

Talamas, J.A., and Hetzer, M.W. (2011). POM121 and sun1 play a role in early steps of interphase NPC assembly. J. Cell Biol. *194*, 27–37.

Testa, I., Wurm, C.A., Medda, R., Rothermel, E., Von Middendorf, C., Fölling, J., Jakobs, S., Schönle, A., Hell, S.W., and Eggeling, C. (2010). Multicolor fluorescence nanoscopy in fixed and living cells by exciting conventional fluorophores with a single wavelength. Biophys. J. *99*, 2686–2694.

Tokunaga, M., Imamoto, N., and Sakata-Sogawa, K. (2008). Highly inclined thin illumination enables clear single-molecule imaging in cells. Nat. Methods *5*, 159–161.

Ulrich, A., Partridge, J.R., and Schwartz, T.U. (2014). The stoichiometry of the nucleoporin 62 subcomplex of the nuclear pore in solution. Mol. Biol. Cell *25*, 1484–1492.

Ungricht, R., and Kutay, U. (2017). Mechanisms and functions of nuclear envelope remodelling. Nat. Rev. Mol. Cell Biol. *18*, 229–245.

Vaughan, J.C., Jia, S., and Zhuang, X. (2012). Ultrabright photoactivatable fluorophores created by reductive caging. Nat. Methods *9*, 1181–1184.

Verdet, E. (1869). Leçons d’optique physique.

Vetter, I.R., Nowak, C., Nishimoto, T., Kuhlmann, J., and Wittinghofer, A. (1999). Structure of a Ran-binding domain complexed with Ran bound to a GTP analogue: Implications for nuclear transport. Nature *398*, 39–46.

Vogelsang, J., Steinhauer, C., Forthmann, C., Stein, I.H., Person-Skegro, B., Cordes, T., and Tinnefeld, P. (2010). Make them blink: Probes for super-resolution microscopy. ChemPhysChem *11*, 2475–2490.

Vollmer, B., Schooley, A., Sachdev, R., Eisenhardt, N., Schneider, A.M., Sieverding, C., Madlung, J., Gerken, U., Macek, B., and Antonin, W. (2012). Dimerization and direct membrane interaction of Nup53 contribute to nuclear pore complex assembly. EMBO J. *31*, 4072–4084.

Vollmer, B., Lorenz, M., Moreno-Andrés, D., Bodenhöfer, M., De Magistris, P., Astrinidis, S.A., Schooley, A., Flötenmeyer, M., Leptihn, S., and Antonin, W. (2015). Nup153 Recruits the Nup107-160 Complex to the Inner Nuclear Membrane for Interphasic Nuclear Pore Complex Assembly. Dev. Cell *33*, 717–728.

W. Wan, J.A.G.B. (2016). Cryo-Electron Tomography and Subtomogram Averaging. In Methods in Enzymology, p.

Walther, T.C., Alves, A., Pickersgill, H., Loïodice, I., Hetzer, M., Galy, V., Hülsmann, B.B., Köcher, T., Wilm, M., Allen, T., et al. (2003). The conserved Nup107-160 complex is critical for nuclear pore complex assembly. Cell *113*, 195–206.

Weirich, C.S., Erzberger, J.P., Berger, J.M., and Weis, K. (2004). The N-terminal domain of Nup159 forms a β-propeller that functions in mRNA export by tethering the helicase Dbp5 to the nuclear pore. Mol. Cell *16*, 749–760.

Weis, K. (1998). Importins and exportins: How to get in and out of the nucleus. Trends Biochem. Sci. *23*, 185–189.

Weis, K. (2007). The Nuclear Pore Complex: Oily Spaghetti or Gummy Bear? Cell *130*, 405–407.

Wente, S.R., and Rout, M.P. (2010). The nuclear pore complex and nuclear transport. Cold Spring Harb. Perspect. Biol. *2*.

Wheelock, M.J., and Johnson, K.R. (2003). Cadherins as Modulators of Cellular Phenotype. Annu. Rev. Cell Dev. Biol. *19*, 207–235.

Whittle, J.R.R., and Schwartz, T.U. (2009). Architectural nucleoporins Nup157/170 and Nup133 are structurally related and descend from a second ancestral element. J. Biol. Chem. *284*, 28442–28452.

Whittle, J.R.R., and Schwartz, T.U. (2010). Structure of the Sec13-Sec16 edge element, a template for assembly of the COPII vesicle coat. J. Cell Biol. *190*, 347–361.

Winey, M., Yarar, D., Giddings, T.H., and Mastronarde, D.N. (1997). Nuclear pore complex number and distribution throughout the Saccharomyces cerevisiae cell cycle by three-dimensional reconstruction from electron micrographs of nuclear envelopes. Mol. Biol. Cell *8*, 2119–2132.

Xu, K., Babcock, H.P., and Zhuang, X. (2012). Dual-objective STORM reveals three-dimensional filament organization in the actin cytoskeleton. Nat. Methods *9*, 185–188.

Yamazumi, Y., Kamiya, A., Nishida, A., Nishihara, A., Iemura, S. ichiro, Natsume, T., and Akiyama, T. (2009). The transmembrane nucleoporin NDC1 is required for targeting of ALADIN to nuclear pore complexes. Biochem. Biophys. Res. Commun. *389*, 100–104.

Yaseent, N.R., and Blobel, G. (1999). GTP hydrolysis links initiation and termination of nuclear import on the nucleoporin Nup358. J. Biol. Chem. *274*, 26493–26502.

Yoshida, K., Seo, H.-S., Debler, E.W., Blobel, G., and Hoelz, A. (2011). Structural and functional analysis of an essential nucleoporin heterotrimer on the cytoplasmic face of the nuclear pore complex. Proc. Natl. Acad. Sci. *108*, 16571–16576.

Yuh, M.C., and Blobel, G. (2001). Karyopherins and nuclear import. Curr. Opin. Struct. Biol. *11*, 703–715.

Zhang, X., Chen, S., Yoo, S., Chakrabarti, S., Zhang, T., Ke, T., Oberti, C., Yong, S.L., Fang, F., Li, L., et al. (2008). Mutation in Nuclear Pore Component NUP155 Leads to Atrial Fibrillation and Early Sudden Cardiac Death. Cell *135*, 1017–1027.

Zhang, Z., Kenny, S.J., Hauser, M., Li, W., and Xu, K. (2015). Ultrahigh-throughput single-molecule spectroscopy and spectrally resolved super-resolution microscopy. Nat. Methods *12*, 935–938.

Zhou, X.X., and Lin, M.Z. (2013). Photoswitchable fluorescent proteins: Ten years of colorful chemistry and exciting applications. Curr. Opin. Chem. Biol. *17*, 682–690.